

**DOCTORATE  
DISSERTATION**



**東京大学**  
THE UNIVERSITY OF TOKYO

**Study on Waveguide Feeder Network of X-band  
Slot-Array Antenna for Synthetic Aperture  
Radar Compatible with Small Satellite**

**(小型衛星に搭載できる X-band 合成開口レーダ  
用スロットアレーアンテナのための導波管給電  
ネットワークの研究)**

**Supervisor: Prof. Hirobumi Saito**

**BUDHADITYA PYNE**

**Department of Electrical Engineering and Information Systems  
Graduate School of Engineering**

**June 2018**

---





# 博士論文 (要約)

## **Study on Waveguide Feeder Network of X-band Slot-Array Antenna for Synthetic Aperture Radar Compatible with Small Satellite**

**(小型衛星に搭載できる X-band 合成開口レーダ用スロットアレーアンテナのための導波管給電ネットワークの研究)**

指導教員 齋藤宏文

ブダディット パイン



**STUDY ON WAVEGUIDE FEEDER NETWORK OF X-BAND SLOT-  
ARRAY ANTENNA FOR SYNTHETIC APERTURE RADAR  
COMPATIBLE WITH SMALL SATELLITE**

(小型衛星に搭載できる X-band 合成開口レーダ用スロットアレーア  
ンテナのための導波管給電ネットワークの研究)

A Dissertation  
Presented to  
The Academic Faculty

by

BUDHADITYA PYNE  
University of Tokyo ID: 37-157291  
GSDM ID: 15202

In Fulfillment  
of the Requirements for the Degree  
DOCTORATE IN ELECTRICAL ENGINEERING AND INFORMATION SYSTEMS  
in the  
GRADUATE SCHOOL OF ENGINEERING

The University of Tokyo  
JUNE 2018

**COPYRIGHT © 2018 BY BUDHADITYA PYNE**





**STUDY ON WAVEGUIDE FEEDER NETWORK OF X-BAND SLOT-  
ARRAY ANTENNA FOR SYNTHETIC APERTURE RADAR  
COMPATIBLE WITH SMALL SATELLITE**

(小型衛星に搭載できる X-band 合成開口レーダ用スロットアレーア  
ンテナのための導波管給電ネットワークの研究)

Approved by:

Prof. HIROBUMI SAITO <sup>a,b</sup>, Ph.D. Advisor

<sup>a</sup> Department of Spacecraft Engineering  
Institute of Space and Astronautical Sciences  
*Japan Aerospace Exploration Agency*

<sup>b</sup> Department of Electrical Engineering and  
Information Systems  
Graduate School of Engineering  
*The University of Tokyo*

Prof. JIRO HIROKAWA, Ph.D. Advisor

Department of Electrical and Electronic Engineering  
Graduate School of Engineering  
*Tokyo Institute of Technology*

Dr. MARC RODRIGUEZ-CASSOLA, International  
Project Advisor

Department of Radar Concepts for SAR Missions  
Microwaves and Radar Institute  
*German Aerospace Center*

Dr. HIROKO NAKAMURA, GSDM Advisor

Department of Aeronautics and Astronautics  
Center for Aviation Innovation Research  
Graduate School of Engineering  
*The University of Tokyo*

Dr. ROBERTO ORSI, GSDM Advisor

Graduate School of Public Policy  
*The University of Tokyo*

Date Approved: June 2018





*To my parents Manimay Pyne and Ketaki Pyne for love,*

*encouragement, patience and support*

*To Maria Alexandrovna Borukha for inspiration, support*

*and laughter*



## ACKNOWLEDGEMENT

I would like to express my heartfelt gratitude to my Ph.D. advisors Prof. Hirobumi Saito and Prof. Jiro Hirokawa; International Project advisors Dr. Marc Rodriguez-Cassola and Prof. Alberto Moreira; and GSDM advisors Dr. Roberto Orsi and Dr. Hiroko Nakamura for their guidance, feedback, encouragement, and constant support. I would like to thank my JAXA colleagues Dr. Prilando Riziki Akbar, Dr. Vinay Ravindra, Dr. Tomoya Fukami and Dr. Hiromi Watanabe; DLR colleagues Mr. Jalal Matar and Dr. Felipe Queiroz de Almeida; GSDM SIP colleagues Mr. Marc- André Chavy-MacDonald, Mr. Quentin Verspieren, Mr. Goutham Karthikeyan, Mr. Giulio Coral and Ms. Hiya Roy for their contribution and assistance. I would like to thank Mr. Nakamura of Technosolver Ltd. for providing thermal deformation data of antenna surface. I acknowledge support of JAXA staff for remote access of JAXA Supercomputer System (JSS2) for conducting full-panel HFSS simulations and all members of JAXA, Tokyo Institute of Technology and Kyoto University for their assistance in antenna panel measurements. I would like to convey my gratitude to the Impulsing Paradigm Change Through Disruptive Technologies Program (ImPACT) of Cabinet Office, Government of Japan for funding this research and the Global Leader Program for Social Design and Management (GSDM) of the University of Tokyo for their financial support throughout my PhD.

Finally, I would like to thank my parents, Mr. Manimay Pyne and Mrs. Ketaki Pyne; close relatives especially Dr. Debasis Bhattacharya, Dr. Mahua Bhattacharya and Dr. Rahul Bhattacharya; and close friends especially Ms. Maria Alexandrovna Borukha for their love, encouragement and constant support.



# TABLE OF CONTENTS

<b>ACKNOWLEDGEMENT</b>	<b>iv</b>
<b>LIST OF TABLES</b>	<b>vii</b>
<b>LIST OF FIGURES</b>	<b>viii</b>
<b>LIST OF SYMBOLS AND ABBREVIATIONS</b>	<b>xviii</b>
<b>ABSTRACT</b>	<b>xx</b>
<b>CHAPTER 1. INTRODUCTION</b>	<b>1</b>
<b>1.1 Research Background</b>	<b>1</b>
<b>1.2 The MicroX-SAR Mission</b>	<b>3</b>
1.2.1 Background	3
1.2.2 Overview	5
<b>1.3 Dissertation Outline</b>	<b>7</b>
<b>CHAPTER 2. A BRIEF OUTLINE OF SAR CONCEPTS</b>	<b>9</b>
<b>2.1 SAR Operating Principle</b>	<b>9</b>
2.1.1 Operating Modes	10
2.1.2 Radar Range Equation	11
2.1.3 Image Resolution	12
2.1.4 Image Quality	14
2.1.5 Applications	17
<b>2.2 SAR Antenna Design Performance Metrics</b>	<b>18</b>
2.2.1 Signal to Noise Ratio	18
2.2.2 SAR Ambiguities and Artifacts	18
<b>2.3 Antenna Array Architecture</b>	<b>22</b>
2.3.1 Active Arrays	23
2.3.2 Passive Arrays	24
2.3.3 Digital Beamforming	25
<b>2.4 State of the Art Review</b>	<b>27</b>
<b>CHAPTER 3. MICROX-SAR ANTENNA NETWORK DESIGN</b>	<b>35</b>
<b>3.1 Feasibility Studies</b>	<b>35</b>
3.1.1 Selection of Antenna Panel Technology	35
3.1.2 Selection of Antenna Feeder Network	44
<b>3.2 Radiation Slots Design</b>	<b>46</b>
<b>3.3 Corporate Edge-feed Scheme</b>	<b>51</b>
3.3.1 Coupling Slots Design	55
3.3.2 Power Divider $\tau$ -junction Design	60
3.3.3 Edge Panel Feeder Design	63
3.3.4 Full Edge Panel Simulation Results	73
<b>3.4 Corporate Center-feed Scheme</b>	<b>78</b>

3.4.1	Coupling Slots Design	82
3.4.2	Edge Panel Feeder Design	87
3.4.3	Center Panel Feeder Design	91
3.4.4	$N\lambda$ Offset Tournament Feeder Network Design	98
3.4.5	Full Panel Simulation Results of All Panels	102
<b>3.4</b>	<b>Measurement Results</b>	<b>107</b>
3.4.1	Near-field Tests	109
3.4.2	Far-field Tests	113
3.4.2	Vector Network Analyzer Tests	119
<b>3.5</b>	<b>Post-Measurement Analysis</b>	<b>123</b>
3.5.1	Diagnosis of Reflection Degradation	123
<b>3.6</b>	<b>Summary</b>	<b>126</b>
<b>CHAPTER 4.</b>	<b>PERFORMANCE ANALYSIS OF EGG-CHOKE FLANGE</b>	<b>129</b>
<b>4.1</b>	<b>Background</b>	<b>129</b>
<b>4.2</b>	<b>Simulation Results</b>	<b>131</b>
4.2.1	Issues with Standard Circular Choke Flange	131
4.2.2	Egg-Choke Flange Design	134
<b>4.3</b>	<b>Measurement Results</b>	<b>138</b>
<b>4.4</b>	<b>Eigen Mode Analysis</b>	<b>141</b>
<b>4.4</b>	<b>Summary</b>	<b>158</b>
<b>CHAPTER 5.</b>	<b>CONCLUSION</b>	<b>151</b>
<b>5.1</b>	<b>Summary and Discussion</b>	<b>151</b>
<b>5.2</b>	<b>Future Work</b>	<b>153</b>
<b>APPENDIX A.</b>	<b>FFT-BASED ANTENNA PATTERN COMPUTATION TOOL</b>	<b>155</b>
<b>A.1</b>	<b>Background</b>	<b>155</b>
5.1.1	Duality between Space Domain and Frequency Domain	157
<b>A.2</b>	<b>Planar Arrays</b>	<b>159</b>
5.2.1	Case Study with MicroX-SAR Antenna	159
5.2.2	Considerations of Thermo-elastic Surface Deformation	161
5.2.3	Comparison with HFSS Simulations and Measurement Results	161
<b>A.3</b>	<b>Reflectors</b>	<b>164</b>
5.3.1	Combining Geometrical Optics and FFT	165
5.3.2	Offset and Non-Offset Feeds with Spillover	166
5.3.3	Separation of Co-polar and Cross-polar components	168
5.3.4	Beam-Center Approximation Technique	169
5.3.5	Case Study with Tandem-L Antenna	173
5.3.6	Comparison with GRASP Simulation Results	173
<b>A.4</b>	<b>Summary and Discussion</b>	<b>194</b>
<b>A.5</b>	<b>Future Work</b>	<b>195</b>
<b>LIST OF RELATED PUBLICATIONS AND PATENTS</b>		<b>197</b>
<b>REFERENCES</b>		<b>199</b>

## LIST OF TABLES

2.1	Summary of Antenna Technology for Space-borne SAR Missions	27
2.2	Challenges for Antenna Design for Small Satellites	31
2.3	Typical Power and Mass Allocation for different SAR systems	32
2.4	Strategy for Small SAR Satellites	33
3.1	MicroX-SAR Mission Parameters with Desired Specifications	36
3.2	Mass of MicroX-SAR Antenna Components	41
3.3	MicroX-SAR Antenna Structure Specifications	54
3.4	Edge-feed Scheme End-feed ‘N-1’ Slots Design Parameters	59
3.5	Modified $\tau$ -junction Design Parameters	62
3.6	$\tau$ -junction with Slot ‘N’ Design Parameters	64
3.7	Designed Parameters of Edge Feeders for Slot ‘N’	71
3.8	Designed Parameters of Slot ‘N’ with $\tau$ -junction of Center-feed Scheme	89
3.9	Design Parameters of Slot ‘N’ and Slot ‘N-1’ with $\tau$ -junction of Center-feed	89
3.10	Design Parameters of Slot ‘N’ with PMC-junction of Center-feed Scheme	92
3.11	Design Parameters of Slot ‘N’ and Slot ‘N-1’ with PMC-junction	93
3.12	Center Feeder Design Summary of Antenna Panels	98
3.13	Summary of Center-feed Full Panel Simulation Results	107
3.14	Summary of Center-feed Full Panel Measurement Results	122
3.15	Pros and Cons of Different Feeding Schemes	127
5.1	Performance Comparison of Proposed MicroX-SAR Antenna with Existing Research Work	153

## LIST OF FIGURES

1.1	ALOS 2 Satellite Antenna	3
1.2	NOVASAR-S Satellite Antenna	5
1.3	Overview of MicroX-SAR Mission	6
1.4	Doctorate Dissertation Outline	8
2.1	Operating Principle of Synthetic Aperture Radar	9
2.2	Overview of Mono-static Radar System	10
2.3	SAR Operating Modes	11
2.4	SAR Image Resolution Computation Geometry	13
2.5	SAR Images with Different SNR Levels	16
2.6	SAR Images with Different SNRR Levels	16
2.7	Timing Diagram of Polarimetric SAR Processing	17
2.8	SAR Image with Ambiguities	21
2.9	Active and Passive Array Antenna Architecture	24
2.10	Digital Beamforming Antenna Array Architecture	25
2.11	Typical SAR System Architecture	30
3.1	Mass vs Ground Resolution for SAR Satellites with NESZ = -20 dB	35
3.2	Waveguide-fed Parallel-plate Slot-array Antenna Configuration	37
3.3	LHCP Antenna with End-feed Waveguide Feeder	38
3.4	Dual Circular Polarization Antenna with End-feed Waveguide Feeder	39
3.5	Honeycomb Core Configuration in Parallel Plate	42

3.6	Measured Honeycomb Loss at 9.65 GHz	44
3.7	Series Feeding Network Scheme	45
3.8	Corporate Feeding Network Scheme	45
3.9	Comparison of Antenna Far-field Patterns for different Feeding Schemes	46
3.10	HFSS Design Model of Linear 1D Array of Radiation Slots	47
3.11	HFSS Design Model of Single Radiation Slot-pair	47
3.12	Reflection Coefficient of Designed Radiation Slots	50
3.13	Amplitude and Phase of Radiation Slot 1D Array before and after Optimization	50
3.14	Reflection Coefficient of Radiation Slot 1D Array before and after Optimization	51
3.15	Left Wing of Edge-feed Antenna Network Tournament Circuit	53
3.16	Edge-Feed Design Model Schematic of Antenna Panel 3	53
3.17	Side-view of Layered Structure of Edge-feed Antenna Panel 3	53
3.18	Coupling Factor for Linear 1D Array with Uniform Excitation	56
3.19	HFSS Single Slot Design Model of Edge-feed Scheme	57
3.20	HFSS Design Model of End-feed Array of 'N-1' Coupling Slots for Edge-feed Scheme	58
3.21	Modified HFSS Design Model of Coupling Slots 1, 2, 3 for Edge-feed Scheme	59
3.22	Reflection Coefficient of End-feed Array of 'N-1' Coupling Slots before and after Optimization for Edge-feed Scheme	60
3.23	HFSS Design Model of Original $\tau$ -junction	61
3.24	HFSS Design Model of Modified $\tau$ -junction	62
3.25	HFSS Design Model of Coupling Slot 'N' of Edge-feed Scheme	64
3.26	Reflection Coefficient of Coupling Slot 'N' of Edge-feed Scheme	65

3.27	Variation of Port Amplitude and Phase with Frequency	65
3.28	HFSS Design Model of Panel 3 Edge Feeder with '2N' Coupling Slots	67
3.29	HFSS Animation of Electric Field Propagation inside Edge-feed Waveguide	67
3.30	Simulation Amplitude Distribution of Edge Feeder for Panel 3	68
3.31	Simulation Phase Distribution of Edge Feeder for Panel 3	68
3.32	Simulation Reflection Coefficient of Edge Feeder for Panel 3	68
3.33	Fabricated Edge-feed Waveguide Feeder for Panel 3	69
3.34	Effect of Mirroring Coupling Slot Design along Azimuth	71
3.35	Comparison of HFSS Design Model for Slot 'N' of Left Feeder and Right Feeder of Panel 3 for Edge Feed Scheme	72
3.36	Simulation Amplitude Distribution of Left Feeder and Right Feeder for Panel 3	72
3.37	Simulation Phase Distribution of Left Feeder and Right Feeder for Panel 3	73
3.38	Simulation Reflection Coefficient of Left Feeder and Right Feeder for Panel 3	73
3.39	HFSS Simulation Model of Panel 3 with Edge-feed Waveguide Feeders	75
3.40	HFSS Simulation Amplitude and Phase of Panel 3 with Edge-feed Scheme	75
3.41	HFSS Simulation Reflection Coefficient of Panel 3 with Edge-feed Scheme	75
3.42	HFSS Simulation Elevation Pattern of Panel 3 with Edge-feed Scheme	76
3.43	HFSS Simulation Azimuth Pattern of Panel 3 with Edge-feed Scheme	76
3.44	HFSS Simulation Peak Gain vs Frequency of Panel 3 with Edge-feed Scheme	76

3.45	Effect of Metallic Wall on Poynting Vector Distribution of Coupling Slot ‘N’	77
3.46	Poynting Vector Distribution of Edge-feed Scheme of Panel 3	78
3.47	Deployed Configuration of MicroX-SAR Satellite with Antenna	79
3.48	Side-view of Layered Structure of Edge-feed Antenna Panel 3M	79
3.49	Center-feed Design Model Schematic of Antenna Panel 3P	81
3.50	Left Wing of Center-feed Antenna Network Tournament Circuit	81
3.51	Center-feed HFSS Full Panel Simulation Model of: (a) Panel 3M (b) Panel 0	82
3.52	Center-feed Single Coupling Slot HFSS Design Model	84
3.53	Reflection Coefficient of Designed Center-feed Coupling Slots	84
3.54	Variation of Coupling Slot Parameters with Coupling Factor for Center-feed Scheme	85
3.55	HFSS End-feed ‘N-1’ slots Design Model and Optimized Slot Separation for Center-feed Scheme	85
3.56	Phase Distribution of End-feed Array of ‘N-1’ Slots for Center-feed Scheme	86
3.57	Amplitude Distribution of End-feed Array of ‘N-1’ Slots for Center-feed Scheme	86
3.58	Reflection Coefficient of End-feed Array of ‘N-1’ Slots of Center-feed Scheme	86
3.59	HFSS Design Model with $\tau$ -junction for Center-feed Scheme of Slot ‘N’ and Slot ‘N-1’	88
3.60	Center-feed Full Feeder HFSS Design Model of Panel 3M	90
3.61	Center-feed Full Feeder Simulation Amplitude Distribution of Panel 3M	90
3.62	Center-feed Full Feeder Simulation Phase Distribution of Panel 3M	91
3.63	Simulation Reflection Coefficient of Center-feed Feeder of Panel 3M	91

3.64	HFSS Design Model with PMC-junction for Center-feed Scheme of Slot 'N' and Slot 'N-1'	92
3.65	HFSS Half-Feeder Design Model with PMC-junction for Center-feed Scheme	93
3.66	Center-feed Half Feeder Simulation Amplitude Distribution of Panel 0	94
3.67	Center-feed Half Feeder Simulation Phase Distribution of Panel 0	94
3.68	Center-feed Full Feeder HFSS Design Model of Panel 0	95
3.69	Center-feed Full Feeder Simulation Amplitude Distribution of Panel 0	95
3.70	Center-feed Full Feeder Simulation Phase Distribution of Panel 0	96
3.71	Simulation Reflection Coefficient of Center-feed Feeder of Panel 0	96
3.72	HFSS Animation of Electric Field Propagation inside Center-feed Waveguide for Panel 3M and Panel 0	97
3.73	Poynting Vector Distribution of Center-feed Scheme of Panel 3M	98
3.74	Schematic of Center-feed Power Divider Network Design with $\tau$ -junctions	99
3.75	Power Divider $\tau$ -junction $J_1$ Design Schematic	100
3.76	Optimized Design Parameters of Power Divider $\tau$ -junction $J_1$	100
3.77	Transmission S Parameters Amplitude and Phase of Designed Power Divider Network	101
3.78	HFSS Design Model of Power Divider Network with Coupling Slots	101
3.79	Simulation Phase Distribution of Designed Power Divider Network with Coupling Slots	101
3.80	Simulation Amplitude Distribution of Designed Power Divider Network with Coupling Slots	102
3.81	Simulation Reflection Coefficient of Designed Power Divider Network with Coupling Slots	102
3.82	Simulation Amplitude and Phase Distribution of Center-feed Panel 0	104



3.83	Simulation Amplitude and Phase Distribution of Center-feed Panel 1M	104
3.84	Simulation Amplitude and Phase Distribution of Center-feed Panel 2M	104
3.85	Simulation Amplitude and Phase Distribution of Center-feed Panel 3M	105
3.86	Simulation Elevation Pattern of Center-feed Antenna Panels	105
3.87	Simulation Azimuth Pattern of Center-feed Antenna Panels	106
3.88	Simulation Peak Directivity of Center-feed Antenna Panels	106
3.89	Simulation S Parameters of Center-feed Antenna Panels	107
3.90	Wilkinson Power Divider with Phase Shifter for Panel 0	108
3.91	Fabricated Center-feed Antenna Panels	108
3.92	Measured Cable Loss of Wilkinson Power Divider	109
3.93	Near-field Measurement Setup	110
3.94	Measurement Amplitude and Phase Distribution of Center-feed Panel 0	110
3.95	Measurement Amplitude and Phase Distribution of Center-feed Panel 1M	111
3.96	Measurement Amplitude and Phase Distribution of Center-feed Panel 2M	111
3.97	Measurement Amplitude and Phase Distribution of Center-feed Panel 3M	111
3.98	Measurement 1D Phase Distributions along Range and Azimuth at Different Frequencies of Panel 3M	112
3.99	Measurement Amplitude Distribution of Antenna Panel Array 1M-3M	112
3.100	Measurement Phase Distribution of Antenna Panel Array 1M-3M	112
3.101	Measurement Amplitude Distribution of Antenna Panel Array 0-3M	113
3.102	Measurement Phase Distribution of Antenna Panel Array 0-3M	113

3.103	Far-field Measurement Setup	115
3.104	Measured Gain Correction Factor for Far-field Measurement for All Panels	116
3.105	Measurement Elevation Pattern of Center-feed Antenna Panels	116
3.106	Measurement Azimuth Pattern of Center-feed Antenna Panels	117
3.107	Measurement Elevation and Azimuth Pattern of Antenna Panel Array	117
3.108	Measurement Elevation and Azimuth 3dB Beam-width for Panel 0, Panel 3M and 4-Panel Antenna Array	118
3.109	Measurement Peak Gain and Directivity of Center-feed Antenna Panels	118
3.110	Measurement Peak Gain and Directivity of Antenna Panel Array	119
3.111	VNA S Parameters Measurement Setup	120
3.112	Schematic of S Parameter Computation for Cascaded Antenna Panel Network	120
3.113	Schematic of S Parameter Calculation for Panel 1 and Panel 2	120
3.114	Measurement Reflection S Parameters of Each Isolated Panel and Panel Arrays	121
3.115	Measurement Transmission Power Dividing Ratio S Parameters of Panel 1M and Panel 2M	122
3.116	Simulation Reflection S Parameters for Parameter Variations	125
3.117	Simulation Transmission Power Dividing Ratio S Parameters for Parameter Variations	125
3.118	Fabricated New Panel 3M with SL = + 0.2 mm	126
4.1	MicroX-SAR Deployable Antenna with Choke Flange	130
4.2	HFSS Choke Flange Simulation Model	132
4.3	Transmission S Parameter of Circular Choke Flange for some cases	133

4.4	Circular Choke-Flange Resonance Frequency vs $\Delta z$ for several cases	133
4.5	HFSS Simulation Model Cross-sectional View of Standard Circular-choke and Proposed Egg-choke for $d=6$ mm	134
4.6	Choke Flange Resonance Frequency vs '2d' for $[\Delta x \Delta y \Delta z] = [1 \ 0 \ 0.5]$ mm	135
4.7	HFSS Simulation Transmission S Parameter of Egg-choke flange ( $d=6$ mm) with Linear and Rotational Misalignment	136
4.8	Choke Flange Measurement Setup	138
4.9	Measurement Transmission S Parameters of Egg-choke flange ( $d=6$ mm) with Linear and Rotational Misalignment	139
4.10	Electromagnetic Field Propagation Inside a Rectangular Waveguide	141
4.11	HFSS Eigen-Mode Simulation Model of Egg-choke Flange	143
4.12	Eigen-Mode Analysis of Egg-Choke Flange ( $d=6$ mm) for $[\Delta x \Delta y \Delta z] = [0 \ 0 \ 1]$ mm and $[\Delta x \Delta y \Delta z] = [0 \ 1 \ 1]$ mm	144
4.13	Simulation Excitation Mode Poynting Vector of Egg-choke Flange ( $d = 6$ mm) for $[\Delta x \Delta y \Delta z] = [0 \ 0 \ 1]$ mm and $[\Delta x \Delta y \Delta z] = [0 \ 1 \ 1]$ mm	147
4.14	Simulation Excitation Mode Electric Field Intensity of Egg-choke Flange ( $d = 6$ mm) for $[\Delta x \Delta y \Delta z] = [0 \ 0 \ 1]$ mm and $[\Delta x \Delta y \Delta z] = [0 \ 1 \ 1]$ mm	148
A.1	Planar Array Geometry	157
A.2	Thermo-elastic Surface Deformation of Space-borne Antenna	157
A.3	Antenna Configuration of MicroX-SAR Satellite	160
A.4	Fabricated Left Wing of Antenna Panel Array of MicroX-SAR Mission	160
A.5	3D Surface Deformation Profile of MicroX-SAR Antenna Array	161
A.6	2D Surface Deformation Profile of MicroX-SAR Antenna Array	161
A.7	MicroX-SAR 7-Panel Antenna Elevation Pattern with Thermal Deformation	161

A.8	MicroX-SAR 7-Panel Antenna Azimuth Pattern with Thermal Deformation	162
A.9	Comparison of MicroX-SAR 7-Panel Antenna 3dB Beam-width	162
A.10	Comparison of MicroX-SAR 7-Panel Antenna First Side-lobe Level	162
A.11	Effect of Thermal Deformation on Peak Gain of MicroX-SAR 7-Panel Antenna	163
A.12	Effect of Thermal Deformation on 2D Amplitude of MicroX-SAR 7-Panel Antenna	163
A.13	Effect of Thermal Deformation on 2D Phase of MicroX-SAR 7-Panel Antenna	163
A.14	Effect of Thermal Deformation on 3D Pattern of MicroX-SAR 7-Panel Antenna	164
A.15	Schematic of Reflector Antenna with Different Feed Positions	166
A.16	Co-polarization and Cross-polarization in Reflector Antenna	169
A.17	Schematic Showing Beam-Center Approach for Reflector Antenna Pattern Computation	171
A.18	Reflector Antenna Pattern Computation Algorithm	171
A.19	Demonstration of Tandem-L Reflector Concept	173
A.20	Tandem-L Co-polar Elevation and Azimuth Pattern for Non-Offset Feed Active $N_{az} = 1$	176
A.21	Tandem-L Co-polar Elevation and Azimuth Pattern for Non-Offset Feed Active $N_{az} = 0$	177
A.22	Tandem-L Co-polar Elevation and Azimuth Pattern for 9 meters Offset Feed Active $N_{az} = 1$	178
A.23	Tandem-L Co-polar Elevation and Azimuth Pattern for 9 meters Offset Feed Active $N_{az} = 2$	179
A.24	Tandem-L Co-polar 3dB Beam-width for Non-Offset Feed Active $N_{az} = 1$	180
A.25	Tandem-L Co-polar 3dB Beam-width for 9 meters Offset Feed Active $N_{az} = 2$	180

A.26	Tandem-L Co-polar First Side-lobe Level for Non-Offset Feed Active $N_{az} = 1$ Active $N_{el} = 16$	181
A.27	Tandem-L Co-polar First Side-lobe Level for 9 meters Offset Feed Active $N_{az} = 1$ Active $N_{el} = 16$	181
A.28	Tandem-L Co-polar 2D Pattern for Non-Offset Feed Active $N_{az} = 1$ Active $N_{el} = 16$	182
A.29	Tandem-L Co-polar 2D Pattern for Non-Offset Feed Active $N_{az} = 0$ Active $N_{el} = 0$	183
A.30	Tandem-L Co-polar 2D Pattern for 9 meters Offset Feed Active $N_{az} = 1$ Active $N_{el} = 16$	184
A.31	Tandem-L Co-polar 2D Pattern for 9 meters Offset Feed Active $N_{az} = 2$ Active $N_{el} = 32$	185
A.32	Tandem-L Cross-polar Elevation and Azimuth Pattern for Non-Offset Feed Active $N_{az} = 1$	186
A.33	Tandem-L Cross-polar Elevation and Azimuth Pattern for Non-Offset Feed Active $N_{az} = 2$	187
A.34	Tandem-L Cross-polar Elevation and Azimuth Pattern for 9 meters Offset Feed Active $N_{az} = 1$	188
A.35	Tandem-L Cross-polar Elevation and Azimuth Pattern for 9 meters Offset Feed Active $N_{az} = 0$	189
A.36	Tandem-L Cross-polar 2D Pattern for Non-Offset Feed Active $N_{az} = 1$ Active $N_{el} = 16$	190
A.37	Tandem-L Cross-polar 2D Pattern for Non-Offset Feed Active $N_{az} = 0$ Active $N_{el} = 32$	191
A.38	Tandem-L Cross-polar 2D Pattern for 9 meters Offset Feed Active $N_{az} = 1$ Active $N_{el} = 16$	192
A.39	Tandem-L Cross-polar 2D Pattern for 9 meters Offset Feed Active $N_{az} = 2$ Active $N_{el} = 0$	193

## LIST OF SYMBOLS AND ABBREVIATIONS

AASR	Azimuth Ambiguity to Signal Ratio
AUT	Antenna under Test
BBM	Bread Board Model
CNES	The Centre National D'études Spatiales
CSA	Canadian Space Agency
DLR	Deutsches Zentrum für Luft- und Raumfahrt
EM	Engineering Model
ESA	European Space Agency
FFT	Fast Fourier Transform
FM	Flight Model
GEO	Geostationary Orbit
GO	Geometrical Optics
HFSS	High Frequency Simulation Software
HH	Horizontal Polarization (transmission) Horizontal Polarization (reception)
HV	Horizontal Polarization (transmission) Vertical Polarization (reception)
IMPACT	Impulsing Paradigm Change Through Disruptive Technologies
ISAS	Institute of Space and Aeronautical Sciences
ISRO	Indian Space Research Organization
JAXA	Japan Aerospace Exploration Agency
JST	Japan Science and Technology Agency
LEO	Low Earth Orbit
LHCP	Left Hand Circular Polarization

LNA	Low Noise Amplifier
MEMS	Micro-electro-mechanical Systems
MEO	Medium Earth Orbit
NASA	National Aeronautics and Space Administration
NESZ	Noise Equivalent Sigma Zero
NF	Noise Figure
PBC	Periodic Boundary Condition
PEC	Perfect Electric Conductor
PMC	Perfect Magnetic Conductor
PO	Physical Optics
PRF	Pulse Repetition Frequency
RAR	Real Aperture Radar
RASR	Range Ambiguity to Signal Ratio
RCS	Radar Cross Section
RF	Radio Frequency
RHCP	Right Hand Circular Polarization
SAR	Synthetic Aperture Radar
SNR	Signal to Noise Ratio
SNRR	Signal to Nadir Echo Reflection Ratio
UKSA	United Kingdom Space Agency
VH	Vertical Polarization (transmission) Horizontal Polarization (reception)
VNA	Vector Network Analyzer
VV	Vertical Polarization (transmission) Vertical Polarization (reception)
XPd	Cross Polarization Discrimination
XPI	Cross Polarization Isolation

## ABSTRACT

This dissertation primarily studies the concept of a new waveguide feeding technique for wideband application of an X-band deployable rectangular parallel-plate slot-array antenna panel network for a synthetic aperture radar on-board a 100 kg class micro-satellite (MicroX-SAR Mission). First, the antenna design procedure in high-frequency structure simulator (HFSS) followed by its fabrication and measurement results are explained. Simulations and antenna array measurement results confirmed that the proposed feeding technique achieved wide-beam antenna gain 40.8 dBi with 75% aperture efficiency and 90% arraying efficiency within permissible reflection limit in 300 MHz bandwidth, thereby ensuring wideband operation. Next, the novel design concept of a contactless egg-shaped choke flange for wide-band applications in X-band is presented. Measurement results of the fabricated egg-choke flange confirmed wideband operability of 2.5 GHz with less than 0.1 dB transmission loss considering possible linear and rotational misalignments. Finally, it describes the methodology of computing antenna patterns for reflectors and planar arrays combining Geometrical Optics and FFT in Python, considering possible surface deformations. Comparison with GRASP and HFSS software simulation results of antenna patterns of MicroX-SAR planar array and Tandem-L reflector showed that the Python Pattern Tool is highly accurate within 0.1 dB and efficient with the computation time required only a few seconds compared to several hours for GRASP and HFSS. This dissertation work contributed to the successful realization of the Engineering Model antenna panel network for MicroX-SAR Mission.





# CHAPTER 1. INTRODUCTION

## 1.1 Research Background

Remote sensing is the acquisition of information about an object or phenomenon without making physical contact with the object in contrast to on site observation. Throughout the last few decades, it has been widely used to detect and classify objects on Earth (both on the surface, and in the atmosphere and oceans) by means of propagated signals (e.g. electromagnetic radiation). Radar is a very crucial component for remote sensing technology. The term ‘radar’ is a contraction of the words Radio Detection and Ranging [27]. It operates by radiating energy into space and detecting the echo signal reflected from the object. Radar consists of three parts: A transmitter, an antenna and a receiver. A transmitter generates an electromagnetic signal such as a short-pulsed sine-wave which is radiated into space by the antenna. A portion of the transmitted energy is intercepted by the target and re-radiated into space. The radiation directed back towards the radar is collected by the radar antenna which delivers it to the receiver. There it is processed to determine the presence of the target and its location. Environmental monitoring, earth-resource mapping, and military systems require broad-area imaging at high resolutions. Often, this imagery must be acquired at night or during inclement weather.

Synthetic Aperture Radar (SAR) provides such a capability. SAR systems take advantage of the long-range propagation characteristics of radar signals and the complex information processing capability of modern digital electronics to provide high resolution imagery. SAR complements photographic and other optical imaging capabilities because

it is not limited by the time of day or atmospheric conditions and because of the unique responses of terrain and cultural targets to radar frequencies. This is because electromagnetic waves at visible and near-visible spectrum is mostly either scattered or absorbed by clouds or dust particles. For these reasons, it is called an "all-weather instrument" [27].

Conventionally, SAR systems have been mounted on big satellite systems which weigh several tons like Seasat-SAR, TerraSAR-X. and ALOS-2. As a result, the project cost becomes very high and procurement and development time becomes very long. The re-visit time (i.e. the time interval between visits over the same geographical place by the satellite) is dependent on the incidence angle, beam mode and geographic location of the swath [36]. It is typically large for a single satellite (e.g. TerraSAR-X with 11-day repeat cycle [19], ERS-1/2 and ENVISAT with 35-day repeat cycles, RADARSAT-1/2 with 24-day repeat cycles and ALOS with 46-day repeat cycle [103]). Similar to the case of optical remote-sensing satellites, the re-visit time can be improved by having a constellation of satellites. For example, the Cosmo-SkyMed constellation (reconnaissance and civil applications) with four identical satellites and the SAR Lupe constellation (reconnaissance) with five identical satellites, have re-visit time of 7h and less than 10h respectively [36]. However, even the SAR satellites used in Cosmo-Sky Mode and SAR-Lupe constellations are of large class (1700 kg and 700 kg respectively [36]). Including the launch costs, the overall constellation mission becomes expensive. On the other hand, if a single small satellite SAR was realized, it could drastically cut down the costs associated in achieving near-real time, all-weather Earth observation system.

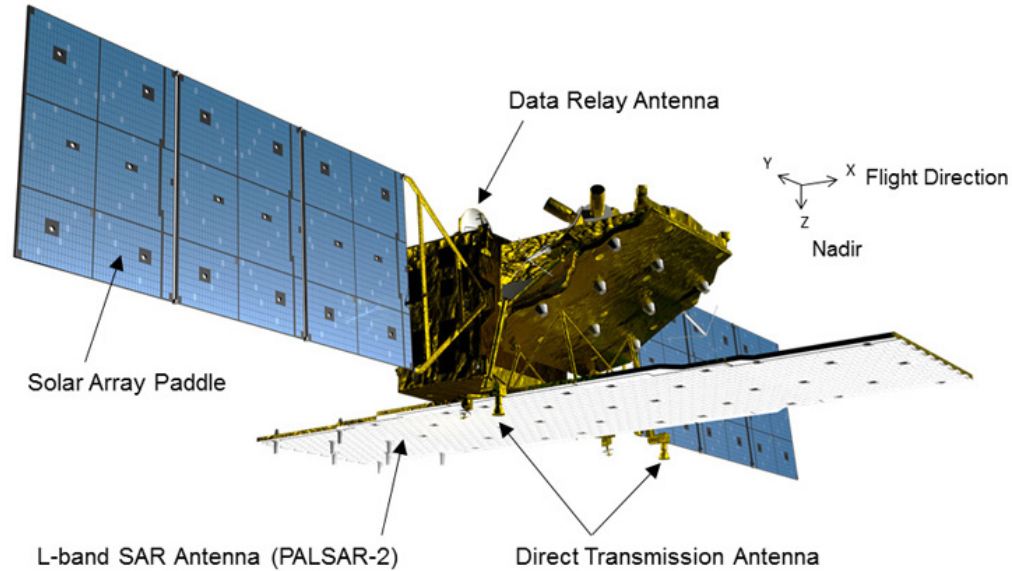


Fig. 1.1. ALOS 2 Satellite Antenna

## 1.2 The MicroX-SAR Mission

### 1.2.1 Background

Miniaturization of technology in general is desired since it can lead to lower volume, mass and easy handling of the end product. With respect to satellite technology, it has the added benefit that it lowers the launch cost of the satellite to orbit. Additionally, it allows launch of multiple satellites to orbit using the same rocket launcher. This is critical nowadays, since the number of rocket launches per year are relatively low. Another motivation for development of small satellites (<150kg) is that it makes a constellation mission comprising of distributed satellites affordable. In recent times with an ever-increasing threat of global climate change, there has been increasing work in the research and development of low-cost light-weight space-borne SAR systems for applications such as monitoring natural disasters like tsunamis, typhoons, landslides, and volcanic eruptions

especially in disaster-prone countries in the East and South-East Asia like Japan, Indonesia and the Philippines like NOVASAR-S Mission, which was launched by the UKSA with a payload of 430 kg capable of 6 meter resolution and swath-width of 20km in SAR Strip-map mode operation.

Small satellite is one of the fast-growing sectors in space industries. Small satellites usually refer to satellites below 500 kg, including minisatellite (100–500 kg), microsatellite (10–100 kg), nanosatellite (1–10 kg), pico-satellite (0.1–1 kg), and femto-satellite (<0.1 kg). Modern technology developments such as integrated circuits, miniaturization, and micro-electromechanical systems (MEMS) have improved their capabilities, enabling satellites to become small and capable. During recent years, small satellites have become increasingly important for space industries due to the advantages of low mass, fast development, flexibility, and low cost. There are numerous research programs on small satellite research and development worldwide. For example, the NASA Small Spacecraft Technology Program (SSTP) develops and demonstrates new capabilities employing the unique features of small satellites for science, remote sensing of Earth, exploration, and space operations [104]. JAXA has conducted a series of research and development programs on small low-cost satellites since the first small satellite “Micro-LabSat” was launched in 2002 [105]. Similar programs exist in the United Kingdom and Europe where the UKSA and ESA have many programs on small satellites and/or related technologies. Recently, small satellites, in particular the CubeSat, have shown explosive growth worldwide. As of January 2016, 45 countries have launched <50-kg satellites.

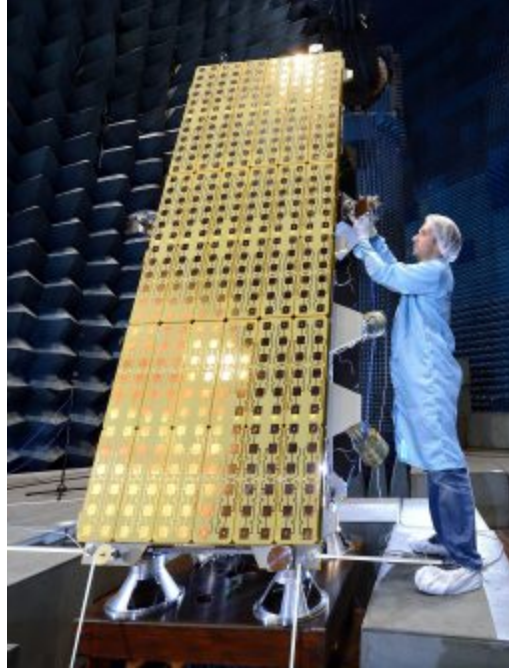


Fig. 1.2. NOVASAR-S Satellite Antenna

### *1.2.2 Overview*

The MicroX-SAR Mission is a brainchild of the Impulsing Paradigm Change Through Disruptive Technologies Program (ImPACT) of Cabinet Office, Government of Japan, which aims to develop a constellation of 100 kg class micro-satellites in Low Earth Orbit (LEO) with on-board SAR sensors capable of 1-meter resolution imagery for continuous Earth Observation for monitoring natural disasters in South-East Asia [101]. The estimated project cost per satellite is \$20 Million, which is only 1/10<sup>th</sup> of conventional SAR satellites. The proposed system enables worldwide coverage from ten minutes to several hours after launch irrespective of sunlight and weather conditions. The proposed launch is after 2020.

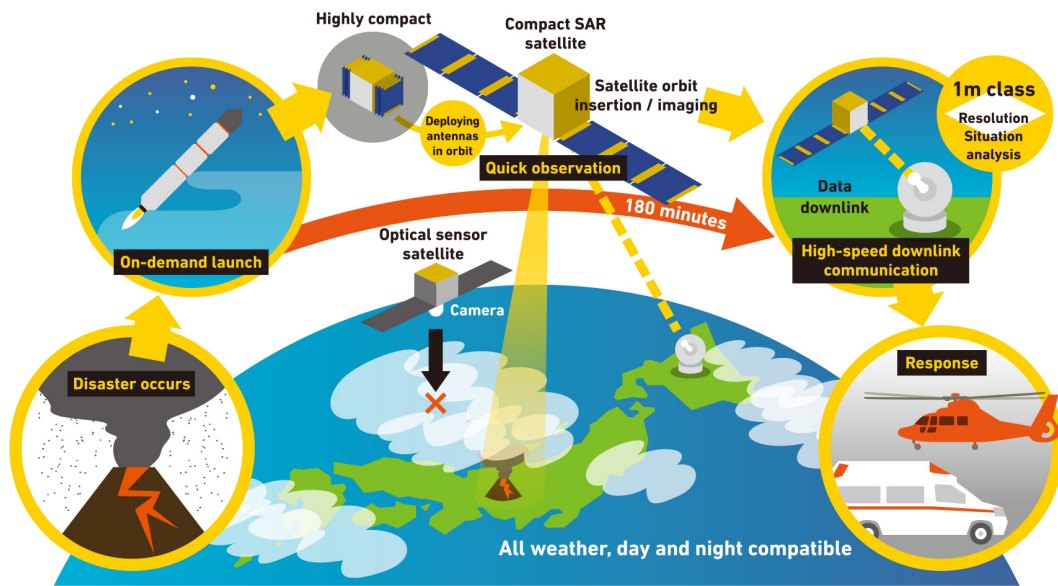


Fig. 1.3. Overview of MicroX-SAR Mission [101]

The MicroX-SAR (Small Synthetic Aperture Radar Satellite System for On-Demand Observation) Mission symbolizes disruptive innovation in the SAR industry being the first ever 100kg class micro-satellite capable of high resolution SAR image acquisition.

There are several key points for this major breakthrough:

- Selection of a new approach different from the two major methods used worldwide (active phased array antenna system and parabola antenna system) to achieve the world's most lightweight and compact SAR system.
- Development of the satellite bus (power source system and heat system) needed to achieve the compact SAR system.

- In terms of reliability, utilize the heritage of the Hodoyoshi satellite bus to create a compact, lightweight satellite not bound by the conventional approach to satellite development to achieve a 100 kg class small satellite system.
- Achievement of a high-speed data link capable of downlinking data in a single pass.
- Achievement of advanced automation through the use of advanced on-board software and an operation model.
- Continuous execution of benchmarks.

### 1.3 Dissertation Outline

The dissertation can be divided into two parts:

1. Research and Development of **MicroX-SAR Antenna System** conducted in Japan Aerospace Exploration Agency (JAXA) Sagami-hara, Japan under the guidance and supervision of Prof. Hirobumi Saito and Prof. Jiro Hirokawa (Oct 2015 – Sep 2018).
2. Research and Development of **Antenna Pattern Computation Tool** for SAR Processing in German Aerospace Center (DLR) Microwaves and Radar Institute, Oberpfaffenhofen, Germany under the guidance and supervision of Dr. Marc Rodriguez-Cassola (Dec 2017 – Mar 2018).

The dissertation is organized as follows: Chapter 2 provides a brief introductory summary of the important concepts of Synthetic Aperture radar, with focus on antenna design considerations and performance evaluation metrics. Chapter 3 provides a detailed



discussion on the concept, design methodology and measurement results of the proposed antenna feeder network. Chapter 4 discusses the background, design concept, performance analysis and measurement of the proposed egg-choke flange necessary for use in the antenna panel tournament circuit discussed in Chapter 3. Chapter 5 comprises of overall summary of Chapter 3 and Chapter 4. Appendix A demonstrates the concept, methodology and performance analysis of the Antenna pattern computation tool for efficient and accurate performance estimation of antennas for MicroX-SAR and Tandem-L missions.

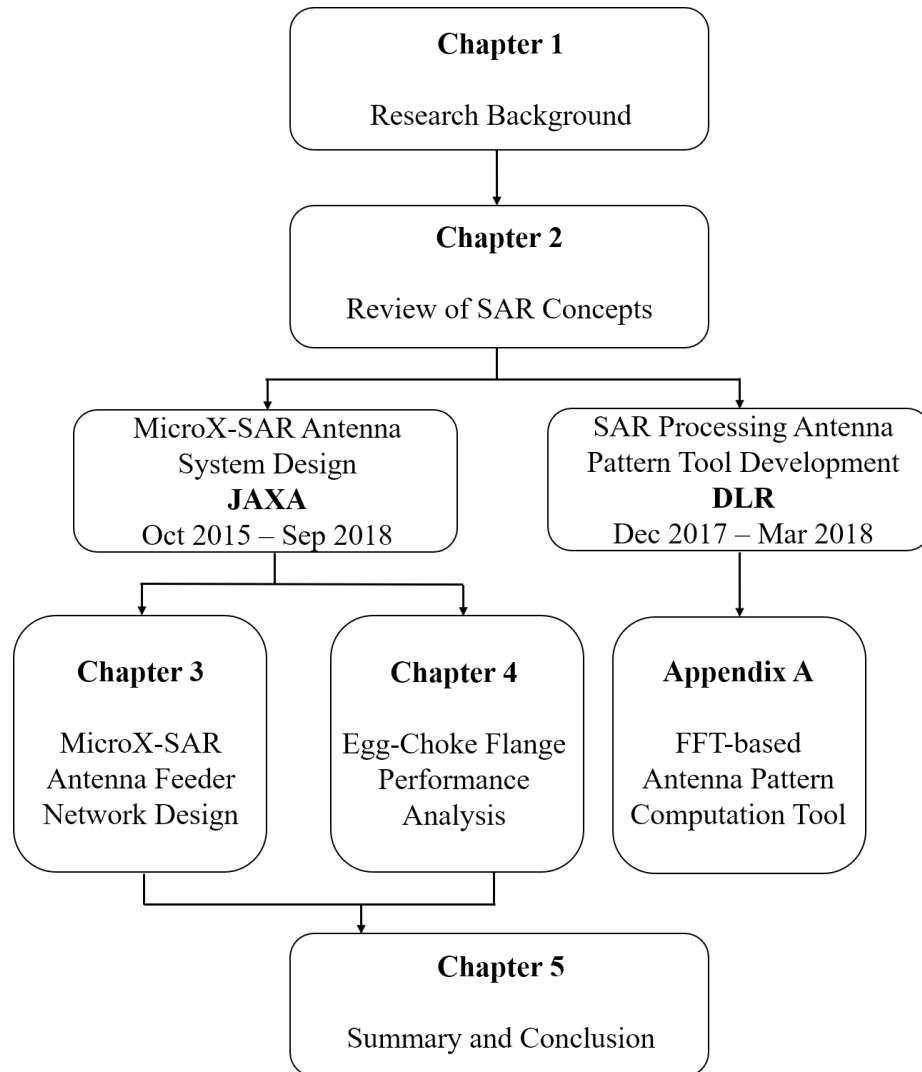


Fig. 1.5. Doctorate Dissertation Outline

## CHAPTER 2. A BRIEF OUTLINE OF SAR CONCEPTS

### 2.1 SAR Operating Principle

Synthetic Aperture Radar (SAR) is a coherent mostly airborne or space-borne side-looking radar system which utilizes the flight path of the platform to simulate an extremely large antenna or aperture electronically, and thereby generates a 2-D high-resolution remote sensing image [27]. The along-track direction is called the azimuth and the cross-track or radial direction is called the range. The working principle of SAR is similar to that of a phased array, but instead of a large number of the parallel antenna elements of a phased array, SAR uses one antenna in time-multiplex. The different geometric positions of the antenna elements are due to the moving platform. Swath width refers to the strip of the Earth's surface from which geographic data are collected and stored to create high resolution images of the terrain being over flown.

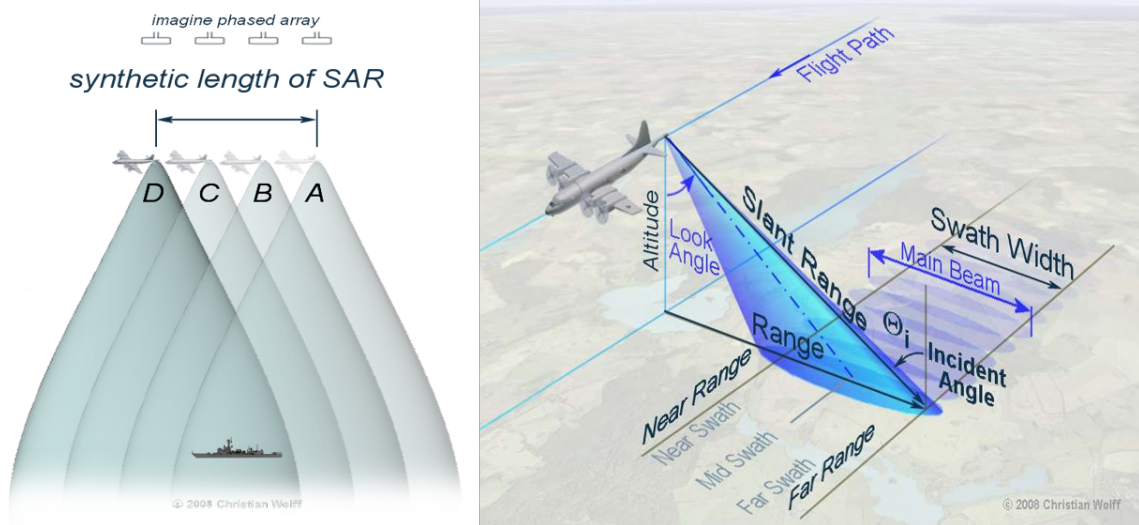


Fig. 2.1. Operating Principle of Synthetic Aperture Radar

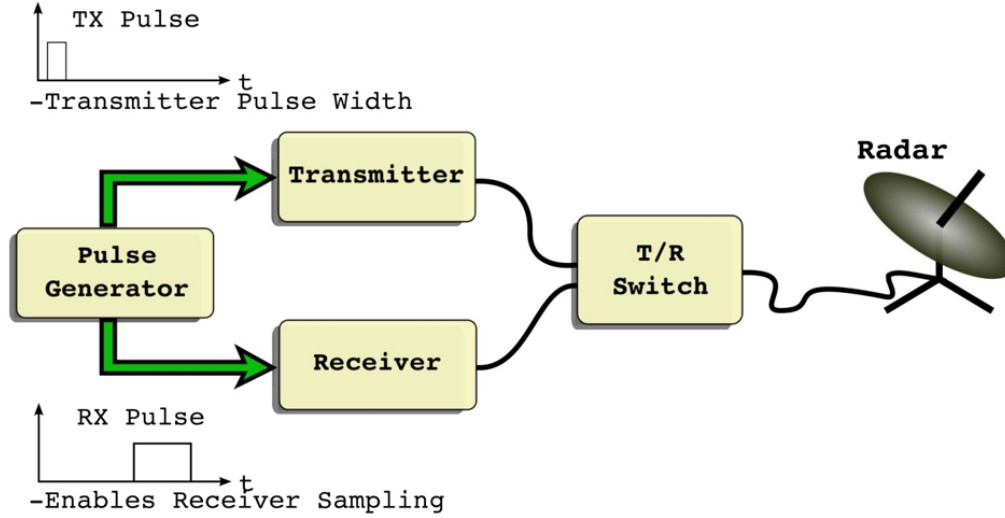


Fig. 2.2. Overview of Mono-static Radar System

### 2.1.1 Operating Modes

There are three basic modes of operation of SAR [27]:

Strip-map mode is the most conventional operating mode of SAR. It assumes a fixed pointing direction of the radar antenna broadside (the radar platform velocity and the antenna beam axis are perpendicular to each other) to the platform track, i.e. the nadir offset angle as well as the direction of the antenna beam is kept fixed. A strip map is an image formed in width by the swath of the SAR and follows the length contour of the flight line of the platform itself. It gives a moderate swath-width and a moderate azimuthal resolution.

Spotlight-SAR is a mode of SAR operation for obtaining high resolution images by steering the radar beam to keep the target within the beam for a longer time and thereby form a longer synthetic aperture. Spotlight SAR is capable of extending the high-resolution SAR imaging capability significantly. As more pulses are used, the azimuth resolution increases. This is achieved by keeping a target within the spotlight illumination of the radar beam for a longer time through electronic beam steering, resulting in a longer synthetic aperture, i.e. the nadir off-set angle is fixed but the antenna beam is steered to monitor the

same target region for a longer time to obtain a better azimuth resolution at the cost of lesser swath-width as other areas within a given accessibility swath of the SAR cannot be illuminated while the radar beam is spotlighting over a particular target area.

In Scan-SAR mode, while steering the antenna beam, the off-nadir angle is also changed at intervals of time to illuminate several sub-swaths. This mode has the capability to illuminate several sub-swaths by scanning its antenna off-nadir into different positions. It provides higher swath-width at the cost of azimuthal resolution.

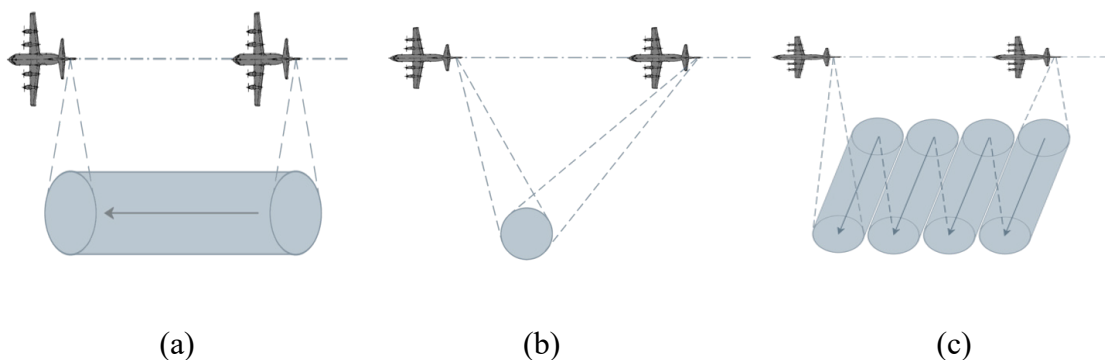


Fig. 2.3. SAR Operating Modes: (a) Strip-map (b) Spot-light (c) Scan-SAR

### 2.1.2 Radar-Range Equation

In a mono-static SAR, a single antenna functions as both the transmitter and receiver in time multiplex. Only a small fraction of the transmitted power is reflected to the receiver which depends on the radar cross-section (RCS) and only a fraction of the reflected power is intercepted by the receiving antenna which depends on the antenna area.

$$P_r = P_t \frac{\sigma}{4\pi r_1^2} G_t \frac{A_e}{4\pi r_2^2} \quad (2.1)$$

$$A_e = \frac{G_r \lambda^2}{4\pi} \quad (2.2)$$

$$r_1 = r_2 = \frac{ct}{2} = R = H \sec(\theta_N) \quad (2.3)$$

$$G_t = G_r = G \quad (2.4)$$

$$P_r = \frac{P_t G^2 \lambda^2 \sigma}{(4\pi)^3 R^4} \quad (2.5)$$

where,

$P_r$  is the received signal power

$P_t$  is the transmit power

$G_t$  is the transmit antenna gain

$G_r$  is the receive antenna gain

$r_1$  is the transmitter-to-target range

$r_2$  is the target-to-receiver range

$\lambda$  is the radar centre wavelength

$\sigma$  is the radar cross-section (RCS)

$A_e$  is the antenna area

$H$  is the satellite altitude

$\theta_N$  is the nadir off-set angle

$c$  is the speed of light in vacuum

$t$  is the time taken by the transmitted signal to return to the receiving antenna

### 2.1.3 SAR Image Resolution

SAR operates in broadside configuration, i.e. the radar antenna beam axis is perpendicular to the radar-platform radial velocity. It produces a 2-D image. The two

dimensions are called ground-range and azimuth or cross-range. Slant range is the distance between the antenna and the target area. Ground-range is the projection of the slant range on the earth's surface which depends on the angle of incidence. Azimuth or cross-range is the direction perpendicular to the direction of motion of the radar platform.

Range resolution denotes the ability of a SAR to distinguish between targets on the same azimuth but at different ranges. The ground-range resolution denotes the ability to distinguish between two targets on the Earth's surface. Azimuth resolution denotes the ability of a SAR to distinguish between targets on the same range but at different azimuth angles.

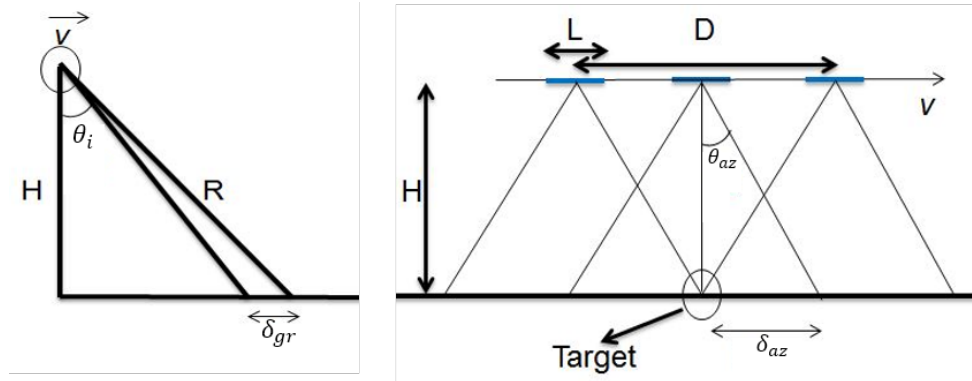


Fig. 2.4. SAR Image Resolution Computation Geometry

$$\delta_r = \frac{c}{2B} \quad (2.6)$$

$$\delta_{gr} = \frac{c}{2B \sin(\theta_i)} \quad (2.7)$$

$$\sin(\theta_i) = \left(1 + \frac{H}{R_E}\right) \sin(\theta_N) \quad (2.8)$$

$$\sin(\theta_{az}) \approx \theta_{az} = \frac{\lambda}{L} \quad (2.9)$$

$$D = 2\theta_{az}H \quad (2.10)$$

$$\delta_{\theta} = \frac{\lambda}{D} = \frac{L}{2H} \quad (2.11)$$

$$\delta_{az} = \delta_{\theta}H = \frac{L}{2} \quad (2.12)$$

where,

$\delta_r$  is the range resolution

$\delta_{gr}$  is the ground-range resolution

$B$  is chirp-bandwidth

$\theta_i$  is the incidence angle

$R_E$  is the mean radius of the earth

$\theta_{az}$  is the azimuthal angle

$L$  is the antenna length in azimuth

$D$  is the synthetic aperture length

$\delta_{\theta}$  is the angular resolution

$\delta_{az}$  is the azimuthal resolution

#### 2.1.4 SAR Image Quality

For SAR image, Signal to Noise Ratio (SNR) is defined in terms of the noise equivalent sigma zero ( $\sigma_{NEZ0}$ ), defined as the radar cross section which produces a received power equal to the thermal noise power, i.e. SNR of unity. Lower the  $\sigma_{NEZ0}$  the better is the SNR. Higher the ground-range resolution, worse the SNR, which needs to be compensated by increasing the antenna size and transmitted power.

$$\sigma_{NEZO} = \frac{8\pi R^3 \lambda v L_R k T_0 N_F}{P_t L_e^2 L_{az}^2 \epsilon_{ap}^2 \delta_{gr} D_p} \quad (2.13)$$

where,

$\lambda$  is the radar center wavelength

$R$  is the slant range

$T_0$  is the Standard Noise Temperature at Earth's surface

$v$  is the satellite orbital velocity

$P_t$  is the Peak power of RF Transmitter

$N_F$  is the Noise Factor

$L_e$  is the Antenna length is elevation

$L_{az}$  is the Antenna length is azimuth

$L_R$  is the Total radar system loss factor

$\epsilon_{ap}$  is the Antenna aperture efficiency

$c$  is the Speed of light in vacuum

$k$  is the Boltzmann's constant

$D_p$  is the Duty cycle of transmitted signal

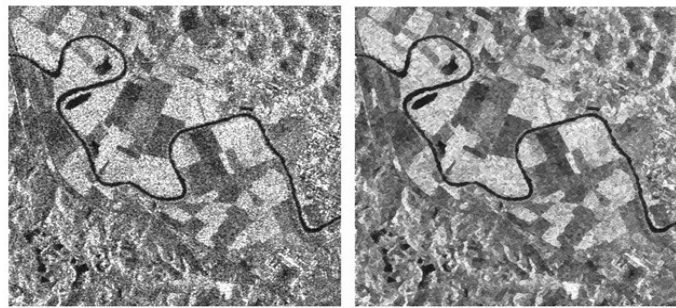
$G$  is the Antenna Gain

$\delta_{gr}$  is the Ground-range Resolution

The Nadir point is defined as the point on the Earth's surface with the minimum distance from the satellite. The Nadir return is a range ambiguous echo of a transmitted pulse which is to be considered in the timing calculation, since it might be very strong and may appear as a bright ambiguity in the processed SAR image. In order to mitigate its influence, it is important to determine the duration of the Nadir pulse depending on level



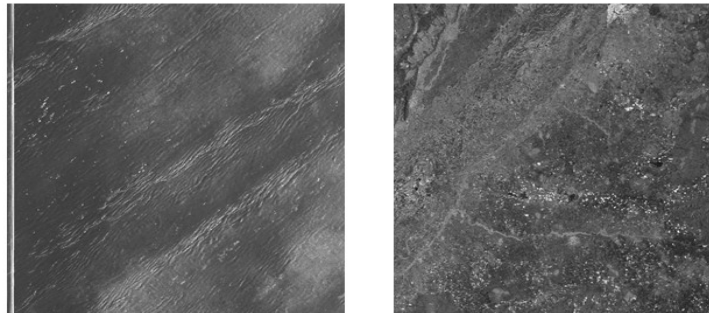
of the Signal to Nadir Ratio (SNRR). Higher SNRR implies better quality of the SAR image. Fig.2.10 below demonstrates this. The left image has low SNRR and the nadir return appears as a bright line in the left and thereby degrades the image quality. SNRR depends on the off-nadir angle, altitude and the ground reflectance properties. SAR operates in broadside configuration, i.e. the radar antenna beam axis is perpendicular to the radar-platform.



(a)

(b)

Fig. 2.5. SAR Images with Different SNR Levels: (a): High NESZ (b): Low NESZ



(a)

(b)

Fig. 2.6. SAR Images with Different SNRR: (a) Low SNRR (b) High SNRR

### 2.1.5 Applications of SAR

- Polarimetry
- Interferometry
- Single Aperture Moving Target Indication (MTI)
- Measurement of Target Height
- Foliage Penetration (F-OPEN SAR)
- Disaster Monitoring

In case of polarimetric imaging, scattering coefficients  $S_{xx}$ ,  $S_{xy}$ ,  $S_{yx}$ ,  $S_{yy}$  ( $x$ ,  $y$  stand for orthogonal polarization states) are measured.

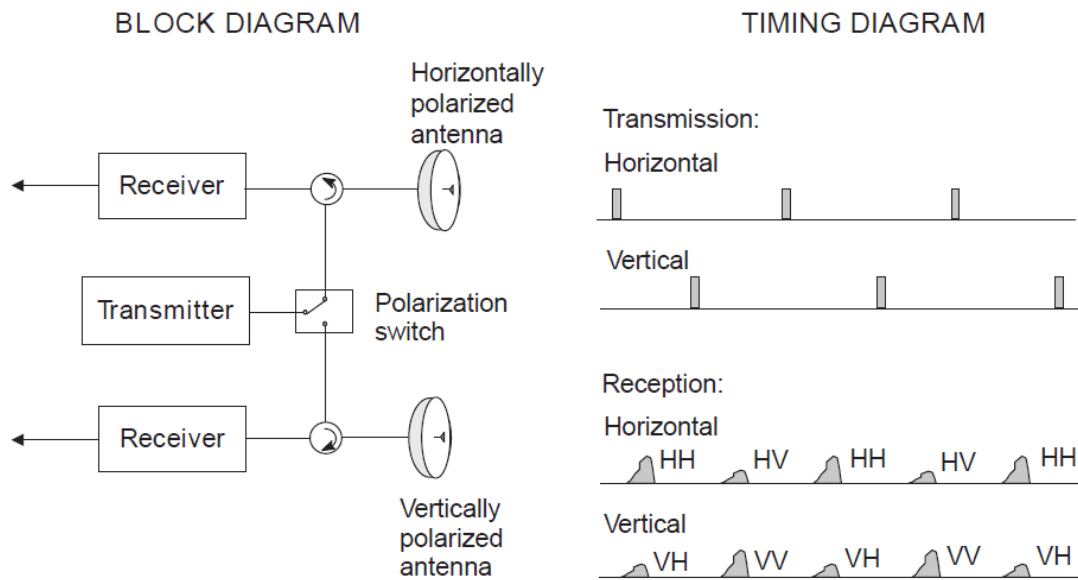


Fig. 2.7. Timing Diagram of Polarimetric SAR Processing

## 2.2 SAR Antenna Design Performance Metrics

### 2.2.1 *Signal to Noise Ratio (SNR)*

The SNR of a processed SAR image is proportional to the square of the realized gain of the antenna illuminating the desired target. Higher the SNR, brighter the image. Thus, it is desired to have high gain at the main-lobe of the antenna pattern. The target region is illuminated over a finite beam-width of the main lobe. The gain of the main beam falls off from the peak direction. As a result, at directions away from the peak, the SNR degrades. Thus, it is desired to have a wider beam-width to minimize this degradation.

### 2.2.2 *SAR Image Artifacts and Ambiguities*

- *Azimuth Ambiguity*

Azimuth ambiguities arise from the finite sampling of the azimuth frequency spectrum at the rate of the PRF. Since, we transmit pulsed signal, the SAR Doppler spectrum is not strictly band-limited due to the presence of the side-lobes in the antenna pattern. Thus, the desired signal band is contaminated by ambiguous signals from the adjacent spectra.

Azimuth ambiguity is commonly measured in terms of the Azimuth Ambiguity to Signal Ratio (AASR) which is defined as the ratio of the ambiguous signal to the desired signal within the SAR correlator azimuth processing bandwidth ( $B_P$ ). It is mathematically expressed as:

$$\text{AASR} = \frac{\sum_{n=-\infty}^{\infty} \int_{-B_P/2}^{B_P/2} G^2(f + n f_P) df}{\int_{-B_P/2}^{B_P/2} G^2(f) df} \quad n \neq 0, n = \pm 1, \pm 2, \pm 3, \dots \quad (2.14)$$

where  $G$  is the cross-range pattern at an azimuthal angle corresponding to Doppler frequency  $f$  and  $B_p$  is the processing bandwidth

AASR depends on the azimuth processing band-width. The wider the band-width, higher is the AASR. The processing band-width depends on the azimuth resolution requirement. The maximum achievable azimuthal resolution is equal to  $L_{az}/2$  where ' $L_{az}$ ' is the antenna length in azimuth. To achieve this maximum resolution, the azimuth processing band-width necessary is given by:

$$B_p = \frac{2V}{L_{az}} \quad (2.15)$$

where  $V$  is the velocity of the radar platform radial velocity.

- *Range Ambiguity*

In the range direction, desired echo reflections from the main-lobe from preceding and succeeding pulses can arrive at the receiving antenna simultaneously with the desired echo from the main-lobe of the present pulse. This is called range ambiguity. Thus, the PRF must be so selected to prevent this. Even if this situation is avoided, there is always the possibility of undesired pulse echoes from side-lobes overlapping with the desired pulse echoes from the main-lobe. This type of ambiguity is typically insignificant for airborne radars since the echo is received before the transmission of the next pulse due to low altitude. However, for space-borne radars, where several inter-pulse periods elapse between the transmission and reception of a pulse, the range ambiguities cannot be neglected.

The desired signal corresponds to the swath being imaged, while the undesired returns are from neighboring area whose returns coincide (in time) with the return from the imaging area. The extent of the ambiguity is usually quantified as the Integrated Range Ambiguity to Signal Ratio (RASR) and is given by:

$$RASR = \sum_{i=1}^N S_{ai} / \sum_{i=1}^N S_i \quad (2.16)$$

$$S_i = \sigma_{i0}^0 G_{i0}^2 / R_{i0}^3 \sin(\eta_{i0}) \text{ for } j=0 \quad (2.17)$$

$$S_{ai} = \sum_{j=-n_h}^{n_h} \sigma_{ij}^0 G_{ij}^2 / R_{ij}^3 \sin(\eta_{ij}) \text{ for } j \neq 0 \quad (2.18)$$

$$R_{ij} = \frac{c \left( t_i + \frac{j}{f_p} \right)}{2} \quad j = \pm 1, \pm 2, \dots, \pm n_h \quad (2.19)$$

where,

$j$  is the pulse number

$i$  is the time interval index of the data record window

$\eta_{ij}$  is the incidence angle

$R_{ij}$  is the Slant Range

$n_h$  is number of pulses to horizon

$G_{ij}$  is the range antenna gain

$N$  is total number of time intervals

$\sigma_{ij}^0$  is the normalized backscatter coefficient at given  $\eta_{ij}$

$\sum S_{ai}$  is the total ambiguous signal power from adjacent pulses

$\sum S_i$  is the total desired signal power

RASR can also be computed in the following way:

$$RASR = \frac{\sum_n \sum_{t_i}^{t_f} f(t + \frac{m}{f_p})}{\sum_{t_i}^{t_f} f(t)} ; m \neq 0, m = \pm 1, \pm 2, \pm 3, \dots \quad (2.20)$$

$$f = \frac{G^2}{R^3 \sin \theta_i} \quad (2.21)$$

where

$G$  is the antenna gain in elevation

$R$  is the slant-range

$\theta_i$  is the incidence angle

$f_p$  is the PRF

$[t_i t_f]$  denotes the receiving window

$t$  is time

The RASR depends on the duration of the receiving window, which depends on the desired observable swath-width. Greater the swath-width requirement, longer is the duration of the receiving window and hence higher is the RASR. The RASR also depends on the incidence angle, which depends on the nadir off-set angle. Larger the nadir off-set angle, larger is the incidence angle and hence higher is the RASR. Azimuth ambiguities arise from the finite sampling of the azimuth frequency spectrum at the rate of the PRF.

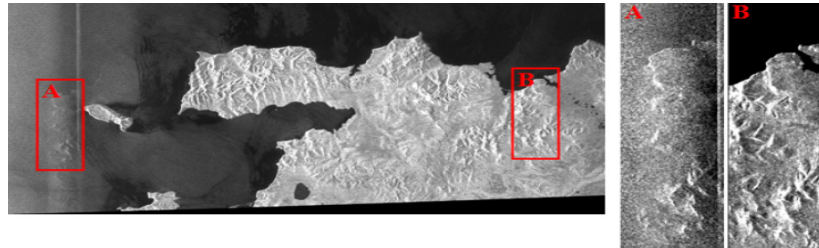


Fig. 2.8. SAR Image with Ambiguities: Range ambiguity (A) is seen on sea-surface due to echos from side-lobe in region (B). Bright strip in left part of image is due to nadir echo.

### 2.3 Antenna Array Architecture

The antenna gain is proportional to the size of the physical aperture of the antenna [26]. Thus, to form a high-gain antenna, a large aperture size is required. This can be made possible by simply enlarging the antenna physical dimensions as in the case of parabolic reflector antennas, where the diameter of the dish can be increased to achieve higher gain. Another way to enlarge the dimensions of the antenna, without necessarily increasing the size of individual elements, is to form an assembly of radiating elements in an electrical and geometrical configuration. Further the phase and amplitude at each individual element can be varied to synthesize a variety of beams from the same antenna. The trade-off is the increased complexity and cost of the system.

The simplest array architecture is shown in Fig.2.9(b). It has a centralized High-Power Amplifier (HPA) and RF feed network. The excitation amplitude and phase of the individual radiators are fixed and cannot be varied. This architecture has the least complexity and requires the least number of components. Example of this antenna architecture is the antenna system of Seasat-A and ERS-1. The challenge in implementing this simple architecture is the need of a centralized high-power RF source along with a low-loss power-divider network. For example, Seasat-A uses a central RF source made of SSPAs with peak power capability of 1kW and a low-loss air-filled coaxial cable power divider network. The use of conventional co-axial cables for the corporate feed network was ruled out due to high loss, and a corporate feed network using vacuum as the dielectric was developed. This corporate feed network used a solid center conductor in a rectangular structure suspended by solid supports [30]. Synthesizing beam by varying the amplitude and/or phase at the individual elements is called electronic scanning. This enhances the

capability of SAR by allowing synthesizing of different antenna patterns depending upon the imaging conditions. For example, imaging at higher incidence angles requires lesser main-lobe beam-width as compared to imaging at lower incidence angles without changing the swath-width. Electronic beam-steering may also be used in spotlight mode SAR as in ALOS-2 mission [43].

A phased array is a group of antennas whose effective (summed) radiation pattern can be altered by phasing the signals of the individual elements. By varying the phasing of the different elements, the radiation pattern can be modified to be maximized or suppressed in given directions, within limits determined by:

- (a) the radiation pattern of the elements
- (b) the size of the array
- (c) the configuration of the array

There are mainly two kinds of electronically scanning array (phased-array) antenna architectures as shown in Fig.2.9

### *2.3.1 Active Arrays*

In an active phased-array, a Transmission Receiver Module (TRM) is used for each element to provide amplitude and phase control. The RF power source is distributed throughout the array which reduces the requirement of power output of each power amplifier. There are numerous examples of active phased-array space-based SAR implemented in large satellites such as TerraSAR-X, RADARSAT-2 and RISAT-1.



Besides providing flexibility in amplitude and phase control for the array elements (and hence transmit/receive beam control), other advantages of active array architecture are as follows [102]: (1) The system sensitivity is increased because the system noise figure is set, and the RF power is generated at the aperture. (2) The feed networks need not be optimized for the lowest loss; thereby allowing design flexibility and the ability to minimize size (volume) and weight.

### 2.3.2 Passive Arrays

In passive phased-arrays, there is no element amplitude control; only bilateral phase shifters are used for each element to provide the required phase shift for scanning [102]. The RF power source is still centralized, and phase shifters are employed in the final carrier frequency stage. An example is the RADARSAT-1 antenna which provides ferrite-based phase shifters along one dimension of the rectangular array.

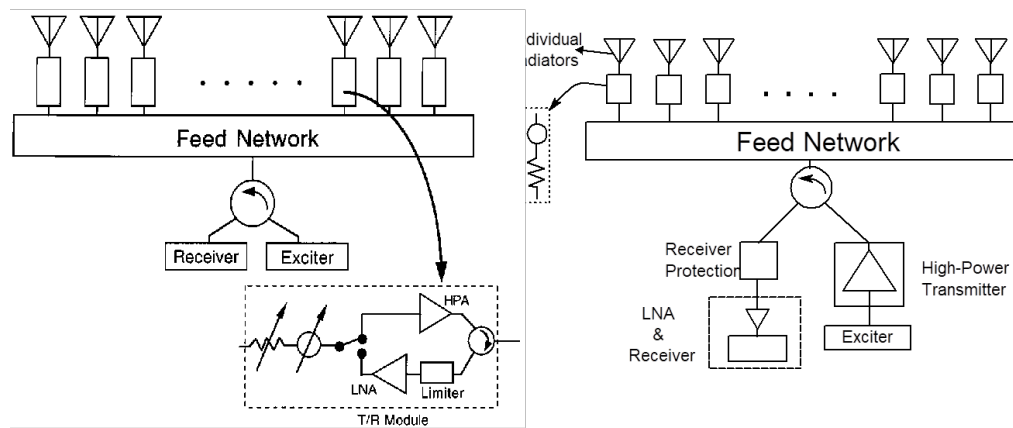


Fig. 2.9. Antenna Array Architecture: (a)Active Array and (b) Passive Array

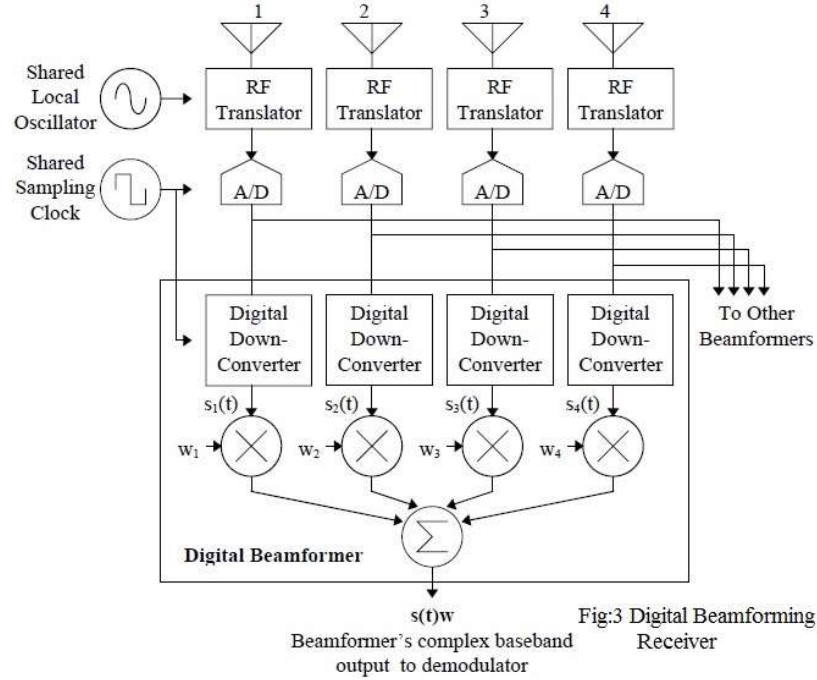


Fig. 2.10. Digital Beamforming Antenna Array Architecture

### 2.3.3 Digital Beamforming

Another architecture receiving much interest nowadays is Digital Beam Forming (DBF) (Fig.2.10). Here, the RF signal at each receiver element is digitized and stored. A transmit pattern with a large beam-width is sent during transmission, and later received signal recorded digitally at each radiator. Multiple received beams with high-gain and narrow beam-width can be synthesized in software. Nulls can be placed in the directions of strong interference (such as the nadir echo), thus reducing ambiguous energy. In this architecture, interference emanating from undesired directions is not canceled out after signal processing, therefore, all the elements, including the RF mixer and Analog to Digital Converter (ADC) and the Digital Signal Processing (DSP) unit must have sufficient dynamic range capable of handling the interference [100].

There are several advantages of phased-array systems:

- Does not require moving a large structure around the sky for pointing. (Less infrastructure)
- Fast steering. (Pulse-to-pulse)
- Distributed, solid-state transmitters as opposed to single RF sources. (Less warm-up time, no need for complex feed system, elimination of single-point failures)

These features allow:

- Remote operations
- Graceful degradation / continual operations
- Conformity of a phased array to the “skin” of a vehicle/ aircraft
- Surveillance/tracking - can both survey and track 1000s of objects
- Communication/downlink for small satellites

Although phased-array systems provide flexibility and more capability to SAR systems, they come at an expensive price:

- Increased cost.
- Increased weight
- Increased power consumption
- High complexity

All these factors are a consequence of using distributed architecture with multiple TRM modules. Design of TRM modules is also challenging since it requires fitting all RF

front-end components into a small package. The size requirement of the package is dictated by the inter-element spacing of array and hence wavelength of operation. Cooling solution has to be provided so that the amplifier efficiency is not degraded due to self-heating. Higher resolution of the digital phase-shifter in TRM module implies larger size and cost.

## 2.4 State of the Art Review

Table 2.1. Summary of Survey on Antenna Technology for Space-borne SAR Missions

<b>Mission</b>	<b>Freq- uency</b>	<b>Satellite Mass</b>	<b>Antenna Size</b>	<b>Polari- zation</b>	<b>Antenna Architecture</b>	<b>RF Feeder Network Architecture</b>	<b>Resolution, Swath- width, Cost</b>
SEASAT 1978 (NASA)	L-band 1.275 GHz	2300 kg	10.74m x 2.16m	HH	Passive Planar Microstrip Array [30]	Centralized with Co-Axial Cables	25 m, 100 km, N/A
Magellan 1989 (NASA)	S-band 2.385 GHz	3444 kg	3.7m diameter	HH	Passive Parabolic Dish	Centralized [31]	1 km, 35 km, \$680 Million
ERS-1 1991 (ESA)	C-band 5.3 GHz	8140 kg	10m x 1m	VV	Passive Slotted Waveguide Array [32]	Centralized Waveguide	30 m, 100 km, \$1.08 Billion
RADARSAT- 1 1995 (CSA)	C-band 5.3 GHz	2750 kg	15m x 1.5m	HH	Phased Array with Electronic Beam-steering	Centralized [33]	30 m, 100 km, \$500 Million

<b>Mission</b>	<b>Frequency</b>	<b>Satellite Mass</b>	<b>Antenna Size</b>	<b>Polarization</b>	<b>Antenna Architecture</b>	<b>RF Feeder Network Architecture</b>	<b>Resolution, Swath-width, Cost</b>
ALOS-1 2006 (JAXA)	L-band 1.27 GHz	4000 kg	8.9m x 3.1m	HH, VV, HV, VH	Planar Active Phased Array [34]	Distributed	14 m, 40 km, \$645 Million
SAR Lupe 2006 OHB	X-band 9.65 GHz	770 kg	3m diamet er	HH, VV, HV, VH	Parabolic Reflector [35]	Centralized	1 m, 8 km, \$300 Million
RADARSA T-2 2007 (CSA)	C-band 5.405 GHz	2300 kg	15m x 1.4m	HH, VV, HV, VH	Planar Active Phased Array [37]	Distributed Sub-array with Microstrip-line and waveguide	5 m, 105 km, \$300 Million
TecSAR 2008 (IAI)	X-band 9.59 GHz	295 kg	3m diamet er	HH, VV, HV, VH	Parabolic mesh Reflector with Beam- steering	Centralized with multiple feeders [39]	3 m, 40 km, \$200 Million
TerraSAR- X & Tandem-X 2007-2010 (DLR- Airbus)	X-band 9.65 GHz	1230 kg, 1340 kg	4.8m x 0.7m	HH, VV, HV, VH, LHCP, RHCP	Planar Active Phased Array [38] [40]	Distributed Sub-array with Microstrip power dividers	3 m, 50 km, \$356 Million

<b>Mission</b>	<b>Frequency</b>	<b>Satellite Mass</b>	<b>Antenna Size</b>	<b>Polarization</b>	<b>Antenna Architecture</b>	<b>RF Feeder Network Architecture</b>	<b>Resolution, Swath-width, Cost</b>
Cosmo Skymed 2010 (ASI)	X-band 9.6 GHz	1900 kg	5.7m x 1.4m	HH, VV, HV, VH	Planar Active Phased Array	Distributed [41]	3 m, 40 km, \$600 Million
RISAT-1 2012 (ISRO)	C-band 5.305 GHz	1858 kg	6m x 2m	HH, VV, HV, VH, LHCP, RHCP	Planar Active Phased Array [42]	Distributed	3 m, 25 km, \$60 Million
ALOS-2 2014 (JAXA)	L-band 1.2 GHz	2100 kg	10m x 3m	HH, VV, HV, VH	Planar Active Phased Array [43]	Distributed	3 m, 50 km, \$600 Million
NOVASA R-S 2018 (UKSA)	S-band 3.2 GHz	430 kg	3m x 1m	HH, VV, HV, VH	Microstrip Phased Array	Distributed [44]	6 m, 20 km, \$60 Million
CAPELLA -1 2018 (Capella Space)	N/A	24 kg	12U Cubes at [47]	N/A	N/A	N/A	N/A
NISAR 2021 (NASA - ISRO)	S/L-band 7.5, 3.75 GHz	2200 kg	12 m diamet er	HH, VV, HV, VH	Parabolic Reflector [46]	Distributed	3 m, 240 km, \$1.5 Billion
Tandem-L 2022 (DLR)	L-band 1.2575 GHz	1600 kg	15 m diamet er	HH, VV, HV, VH	Parabolic Reflector [45]	Distributed	7 m, 175 km, \$300 Million

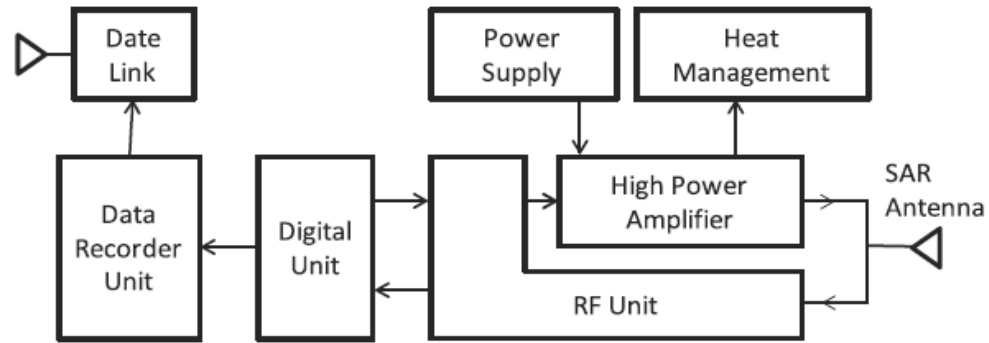


Fig. 2.11. Typical SAR System Architecture [4]

Antennas are key components that enable small satellites to receive and transmit electromagnetic signals. Onboard small satellites, there are a number of antennas for different functions. Due to limited volume onboard small satellites, it is important to optimize the antenna designs, which directly determine the performance of all wireless systems onboard satellites, such as telemetry, tracking, and control (TTC), high-speed data downlink, navigation, intersatellite communications, intrasatellite communications, wireless power transfer, radars and sensors, etc. Table 2.2 summarizes some of the key challenges of small satellite antennas development and the reasons. As shown, it is necessary to achieve miniaturization of antennas with optimum performance while the use of materials in antennas needs to take into account space environments. Table 2.3 shows typical power and mass requirements for typical SAR systems. Table 2.4 shows the strategy for small satellite missions.

Table 2.2. Challenges for Antenna Design for Small Satellites [100]

Challenge	Cause
High reliability	Risk of mission failure
Small stowage volume, low mass, low power, efficiency and cost	Satellite size is small
Mechanically robust	Must survive launch
Maintain stable electrical characteristics over large temperature variation	Antenna gets very hot or cold depending on solar illumination
Antennas able to survive harsh radiation environments in space	High radiation dosage from Van Allen radiation belts, solar proton events and solar energy particles, galactic cosmic rays can damage electronic components.
Materials capable to survive space environment	Thermal (CTE effects, low/high temperature failure of adhesives), Radiation (charging/degradation of dielectrics), atomic oxygen in LEO degrades material surfaces, Optical (emissivity/absorption)
Electromagnetic Compatibility (EMC) and mutual coupling between closely-spaced antennas	Degrades performance of antennas and electronic subsystems
Analyze entire satellite structure as integral part of antenna design	Structural radiation needs to be considered if physical size of small satellite often comparable to wavelength of RF signals
Control material outgassing (release of dissolved, trapped, frozen or absorbed gas)	Contaminates other spacecraft subsystems, leading to structural distortion and changed properties of materials
Electrostatic charging	Damage dielectric materials leading to abnormal behavior of electronic circuits
Multipaction and Ionization breakdown	Damages antenna and microwave components
Passive Intermodulation	Degrades wireless communication



Table 2.3. Typical Power and Mass Allocation for different SAR systems [4]

<b>Parameter</b>	<b>Large Sat</b>	<b>Medium Sat</b>	<b>Small Sat</b>	<b>Airborne</b>
Satellite Mass (kg)	200	500	150	-
Frequency Band	L	X	X	L, C, X, Ku
Resolution (m) at Altitude = 600 km	3	1	3-10	0.3-1
RF Average Power (W)	500	200	250	10
SAR DC Power (W)	6000	1000	1100	200
TX DC Power (W)	5000	900	1000	-
SAR Total Mass (kg)	900	200	75	20
Antenna	500	50	35	5
RF (TX/RX)	130	60	15	6
Digital Unit	200	40	15	4
Data Downlink	20	10	8	-
Cable etc.	50	40	2	5

Table 2.4. Strategy for Small SAR Satellite [4]

<b>Component</b>	<b>Large SAR Satellite</b>	<b>Small SAR Satellite</b>
SAR Antenna	*Active Phased Array (complex large stow size)  *Reflector (large stow size)	*Deployable, passive plane antenna  *Non-contact waveguide feeding with hinge support
TX RX Instrument	*Distributed TX/RX  *Centralized TWTA	*Centralized TX with GaN  *SSPA + Power Combiner
Power System	*Independent Solar Panel  *Large space battery	*Shared antenna/solar panel  *Fast dischargeable battery
Thermal System	*Complex distributed TX module on antenna panel	*GaN amplifier module on panel serving as radiator and heat sink
Digital Processing	*FPGA, Memory, DAC	*FPGA, Memory, DAC
Data Downlink	*1.2 Gbps X-band 8PSK  *RHCP/LHCP 2 channel  *200 Msps	1.5 – 4 Gbps in X-band  64-256 APSK  RHCP/LHCP 2 channel



## CHAPTER 3. MICROX-SAR ANTENNA NETWORK DESIGN

### 3.1 Feasibility Studies

#### 3.1.1 Selection of Antenna Panel Technology

Microstrip patch antennas are favoured at lower frequencies (S, L, C-Band) (eg: Seasat, RISAT-1, RADARSAT-2) because of their low profile and easy fabrication. At higher frequencies' slot-array waveguide antennas are preferred since they have lesser loss using only vacuum as the dielectric (eg: TerraSAR-X). The patch antenna, though it shows larger bandwidth and lower cost compared to waveguide antenna, at higher frequencies, it suffers from high ohmic losses and cross-polarization due to radiation from both patch and microstrip lines. Table 3.1 shows the MicroX-SAR Mission parameters. Fig. shows correspondence of SAR satellites mass and their ground resolutions. Fig.3.1 shows ground range resolutions for typical SAR missions of different size.

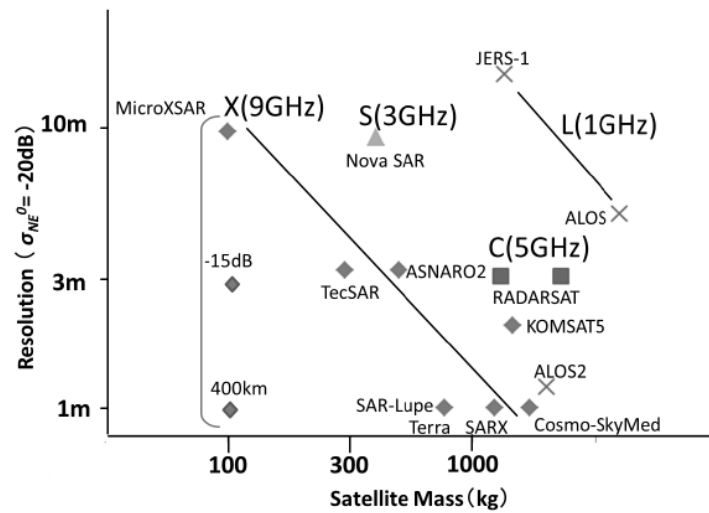


Fig. 3.1. Mass vs Ground Resolution for SAR Satellites with NESZ = -20 dB.

Table 3.1. MicroX-SAR Mission with Desired Specifications [11]

Parameter	SAR Mode	
	Strip-Map	Sliding Spotlight
Altitude	600 km	400 km
Resolution	3 m	1 m
Swath-width	25 km	10 km
Chirp Bandwidth	75 MHz	300 MHz
Center Frequency	9.65 GHz	
Antenna Size	4.9 m x 0.7 m	
Polarization	VV	
Antenna Panel Efficiency	> 50%	
TX Peak Power	1000 W – 1200 W	
TX Duty Cycle	25%	
System Loss	3.5 dB	
System Noise Figure	4.3 dB	
Pulse Repetition Frequency	3000 Hz – 8000 Hz	
NESZ	< - 15 dB	< -18 dB
Ambiguity to Signal Ratio	< -15 dB	

To reduce the weight of the system and manufacturing complexity, a rectangular parallel-plate slot-array antenna was chosen [82]. The first work on waveguide-fed

parallel-plate slot-array antenna is reported in. [86]. It has a very simple structure with radiating part being an upper conductor plate in which slot pattern is etched as shown in fig. 3.2. A plane transverse electromagnetic (TEM) wave is excited in the parallel plate by rectangular waveguide-fed coupling slots cut in the back conductor [86]. The TEM wave then couples to the radiating slot pairs, radiating linearly polarized waves.

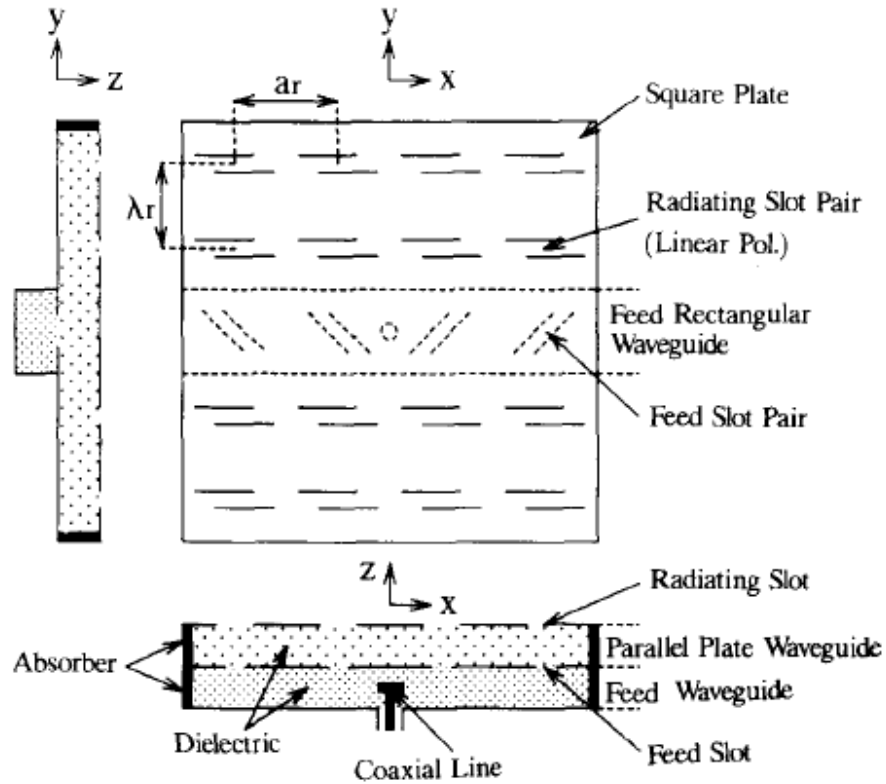


Fig. 3.2. Waveguide-fed Parallel-plate Slot-array Antenna Configuration

An X-band antenna with uniform aperture illumination employing single circular polarization (RHCP) was demonstrated with 54% aperture efficiency [6] and is shown in fig.3.3. Fig. 3.4 shows a dual circular polarization (LHCP and RHCP) rectangular slot-array antenna was designed and fabricated using Genetic Algorithm. The measurement

results showed an aperture efficiency of 49% and the center frequency was shifted to 9.77 GHz from designed 9.65 GHz [7].

In both cases, however, the desired SAR image resolution was 3 meters for strip-map mode operation and thus the required pulse frequency bandwidth was only 130 MHz. In the present state, as shown in Table 3.1, 1-meter resolution is desired for a standard nadir offset angle of 30 degrees, which means trebling the frequency bandwidth. In order to increase the bandwidth and at the same time achieve good NESZ and Ambiguity to Signal Ratio, the required RF power level increases. The peak power level achieved with dual circular polarization is 0.7 times that achieved with linear polarization. Thus, in the present case, we employ single linear vertical polarization for our antenna panel.

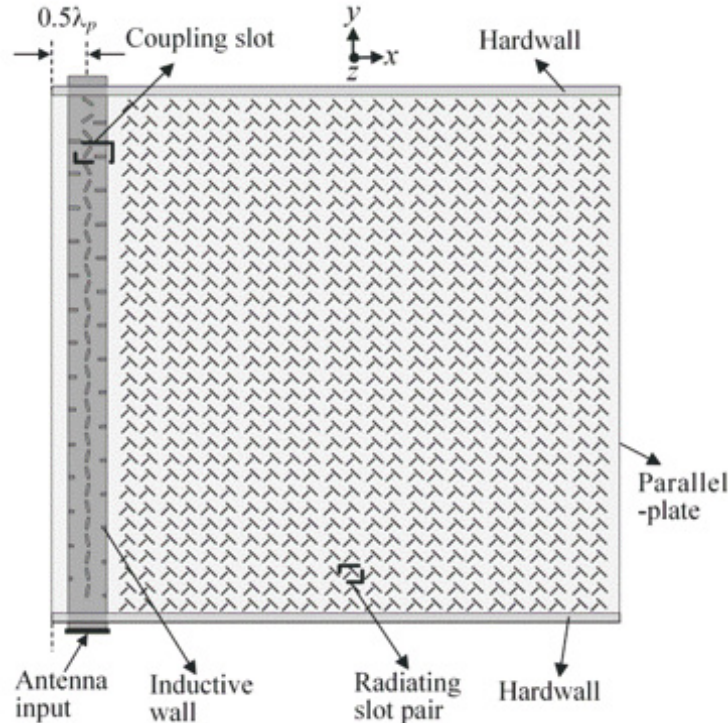


Fig. 3.3. LHCP Antenna with End-feed Waveguide Feeder

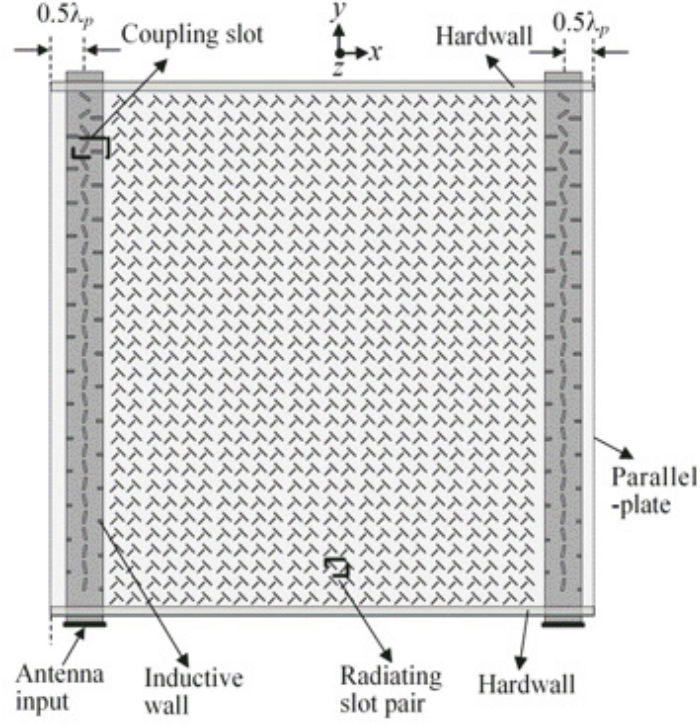


Fig. 3.4. Dual Circular Polarization Antenna with End-feed Waveguide Feeder

The rectangular slotted waveguide feeder (WR90) is installed underneath the lower conducting plate (not shown here). As in [6] and [7], a honeycomb core made from aramid paper (Nomex) is used as a spacer between two thin parallel plates made of aluminum. Two epoxy adhesive layers are used to bind the honeycomb core with the waveguide feeder and the parallel plate. In order to ensure quasi-TEM mode propagation inside the parallel-plate, two hard-wall layers are inserted on either side near the two edges of the parallel-plate. The radiating part (vertical polarization) is formed of horizontal slot-pairs placed at the upper parallel-plate to couple the propagated TEM wave in free space.

The width of hard surface wall,  $h_w$  is determined as [107]:



$$h_w = \frac{\lambda_0}{4\sqrt{\epsilon_{wall} - \epsilon_{eq}}}, \quad (3.1)$$

where  $\lambda_0$  is the wavelength in the free space and  $\epsilon_{wall}$  is the permittivity of hard surface wall. Here, polyimide ceramic hard surface wall (CEPLA) with  $\epsilon_{wall} = 3.6$  is applied. The  $\epsilon_{eq}$  is the equivalent permittivity of the dielectric materials that are stacked between parallel-plates. The value of  $\epsilon_{eq}$  is approximated as a series capacitance model as follows [108]:

$$\frac{2t_g + t_c}{\epsilon_{eq}} = \frac{2t_g}{\epsilon_g} + \frac{t_c}{\epsilon_{rc}}. \quad (3.2)$$

where,  $\epsilon_{rc}$  is the honeycomb permittivity. In this series capacitance model, 2 layers of adhesive sheet are applied.

$$\frac{1}{\lambda_g^2} + \frac{1}{(2a)^2} = \frac{1}{\lambda_0^2} \quad (3.3)$$

$$\lambda_g' = \frac{\lambda_0}{\sqrt{\epsilon_{eq}}} \quad (3.4)$$

where  $\lambda_0$  is the wavelength in free space corresponding to the center frequency,  $\lambda_g$  is the wavelength inside the waveguide of length 'a',  $\epsilon_{eq}$  is the equivalent relative permittivity of the layered structure and  $\lambda_a'$  is the wavelength inside the enclosure. For our case,  $\lambda_0=31.08$  mm,  $\lambda_g=42.35$  mm,  $\lambda_g' = 29.9$  mm and  $\epsilon_{eq}=1.08$ .

Table 3.2 Mass of MicroX-SAR Antenna Components

Component	Mass (gm)
Honeycomb core sheet	358
Upper parallel aluminum plate	344
Lower parallel aluminum plate	65
Adhesive sheet	138
Hard surface wall	57
Aluminum frame	24
Feeder waveguide	162
Total Antenna System	1148

- 
- *Honeycomb Properties*

Honeycomb layer with nominal density of 1.5lb/ft<sup>3</sup> and 1/4<sup>th</sup> inch cell size (about 1/5<sup>th</sup> of  $\lambda_0$ ) is used [6]. Fig.3.5 shows the honeycomb core configuration in the parallel plate. By applying this small cell size of honeycomb, a nearly isotropic propagation can be achieved [109]. For mechanical strength reason, the orientation of honeycomb core layer is arranged with ribbon direction (L direction) parallel to the y axis. Table 3.3 shows the antenna material specifications.

The permittivity of honeycomb  $\epsilon_{rc}$  is estimated from the result of phase measurement. Here, the phase measurement is conducted using inner field measurement method as described in [110].

$$\epsilon_{rc} = \left( \frac{\lambda_0 \beta}{2\pi} \right)^2 \quad (3.5)$$

where  $\beta$  is the measured phase constant from the field measurement. In this experiment, the value of  $\epsilon_{rc}$  is 1.0577.

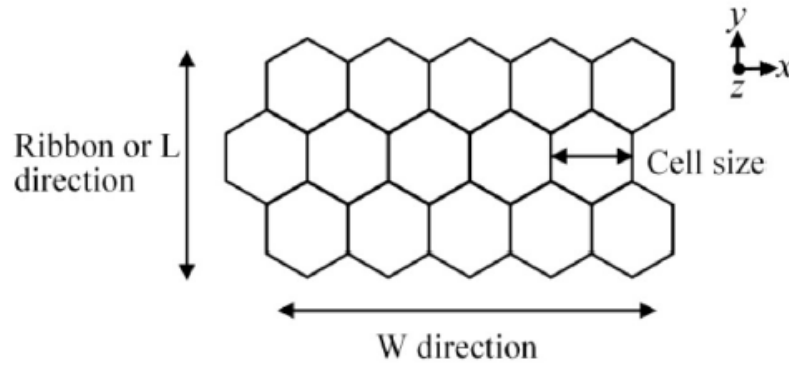


Fig. 3.5. Honeycomb Core Configuration in Parallel Plate

Another measurement is conducted to estimate the loss of honeycomb. Here, the loss of honeycomb is measured by inserting the honeycomb pieces into a WR90 waveguide. In the measurement, the empty waveguide is included at the calibration process. The width of the inserted honeycomb is same as the inner width of WR90 waveguide. However, due to the material unavailability, honeycombs with thickness less than the waveguide inner height are used in this measurement. Here, honeycombs with

thicknesses of 4.1 and 8.2 mm are used. Therefore, as to estimate the actual loss of honeycomb, filling factor is employed in this section.

The filling factor is defined as the ratio of the measured honeycomb thickness per inner height of the waveguide (10.16 mm). Then, the loss of the measured honeycomb is approximated as the measured  $|S_{21}|^2$  divided by the filling factor since the TE<sub>10</sub> mode is uniform along the height direction. The honeycomb with 4.1 mm thickness is measured with honeycomb lengths of 161 and 330 mm, while the honeycomb with 8.2 mm thickness is measured with honeycomb lengths of 161, 195, 330, and 390 mm. Fig.3.6 shows the data of the loss of honeycomb at 9.65 GHz. Moreover, the traveling distance of plain waves composing TE<sub>10</sub> mode is taken into account in this figure. The loss factor of honeycomb  $\alpha$  (dB/mm) is then derived by observing the gradient of loss curve. Here, the value of  $\alpha = 0.0023$  dB/mm is obtained. From this result, it is estimated that the applied honeycomb material has loss tangent (Formula) of about 0.0019 at 9.65 GHz. Here,  $\tan\delta$  is approximated as [43]:

$$\tan\delta = \frac{2c\alpha}{2\pi f} \sqrt{1 - \left(\frac{f_c}{f}\right)^2} \quad (3.6)$$

where  $c$  is the speed of light,  $f$  is the operational frequency, and  $f_c$  is the TE<sub>10</sub> mode cut-off frequency.

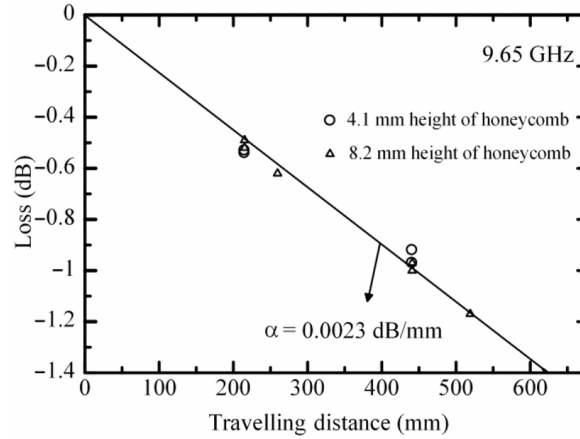


Fig. 3.6. Measured Honeycomb Loss at 9.65 GHz

### 3.1.2 Selection of Antenna Feeder Network

Feed network for microwave applications is a major design concern in terms of complexity and size [111]. Feed network depend on antenna type and geometry. There are two ways of feeding RF power to an array of passive antennas. Initially, feeder system configuration investigated by using a preliminary antenna model of MicroX-SAR system in the following way:

- *Series Feeding Network*

Fig.3.7 shows a typical series-fed network where the input signal, fed from one end of the feed network, is coupled serially to the antenna elements. The compact feed network of series-fed antenna arrays is one of the main advantages that make them more attractive than their parallel-fed counterparts. Beside compactness, the small size of series-fed arrays results in less insertion and radiation losses by the feed network. Usually series fed arrays are more efficient than corporate fed arrays. Series feed configurations suffer from narrow bandwidth and inherent phase difference caused by the differences in lengths of feed lines. As seen in fig. the feeder lengths from input to the feed point of each antenna panel all are not equal.

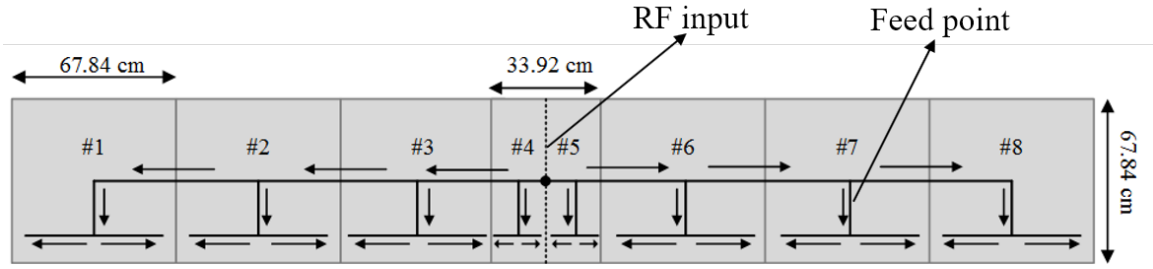


Fig. 3.7. Series Feeding Network Scheme

- *Corporate Feeding Network*

Corporate Feed integrates the RF feed network with the radiating elements on the same power source as shown in fig.3.8. Due to large number of the layers in corporate feed, it can be lossy due to long-line effect. However, losses are significantly reduced by using a waveguide feed network. The feeder lengths from input to the feed point of each antenna panel all are almost equal. As a result, corporate fed arrays have well-controlled aperture distribution.

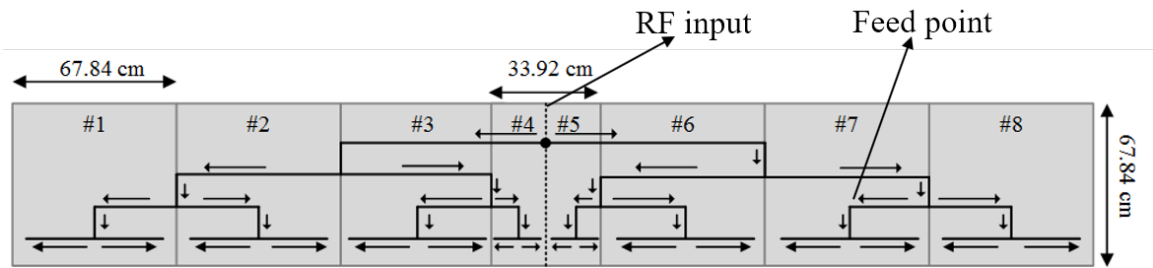


Fig. 3.8. Corporate Feeding Network Scheme

As seen in fig.3.9, employing series feed, the antenna patterns are significantly distorted at off-center frequencies, thereby making it unsuitable for wideband applications. On the contrary, using corporate feed, antenna patterns have minor degradations at off-center frequencies. Hence, corporate feeding is selected for MicroX-SAR antenna network.

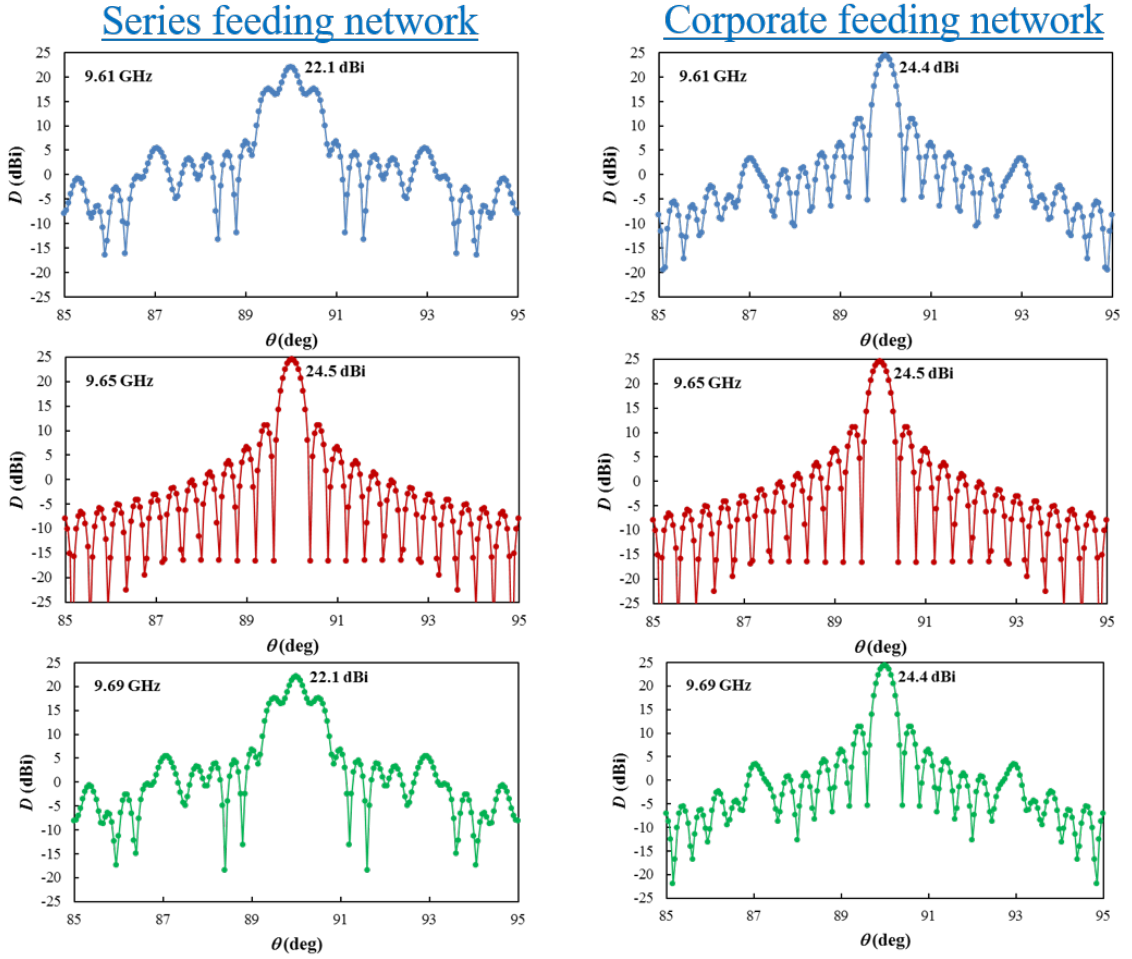


Fig. 3.9. Comparison of Antenna Far-field Patterns for different Feeding Schemes

### 3.2 Radiation Slots Design

Fig.3.10 shows a simplified model of one-dimensional (1-D) array of radiating slot with PBC.  $M$  total number of radiating slots are placed at the parallel plate. The radiating slot pair number ( $m$ ) is counted from the shorted-end of the parallel plate in  $x$  direction. To perform uniform excitation, the required coupling factor of each radiating slot pair is equal to  $1/m$ . At first single radiating slot pair is simulated to obtain the slot length and separation for each radiating slot pair.

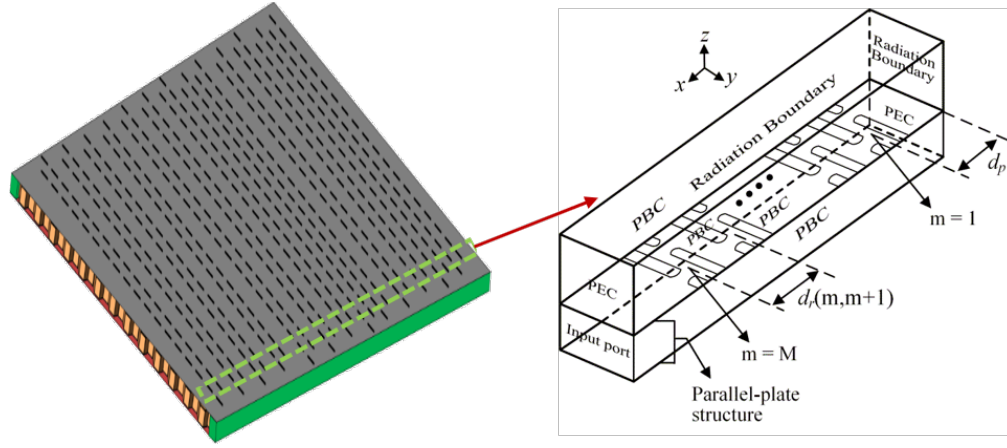


Fig. 3.10. HFSS Design Model f of Linear 1D Array of Radiation Slots

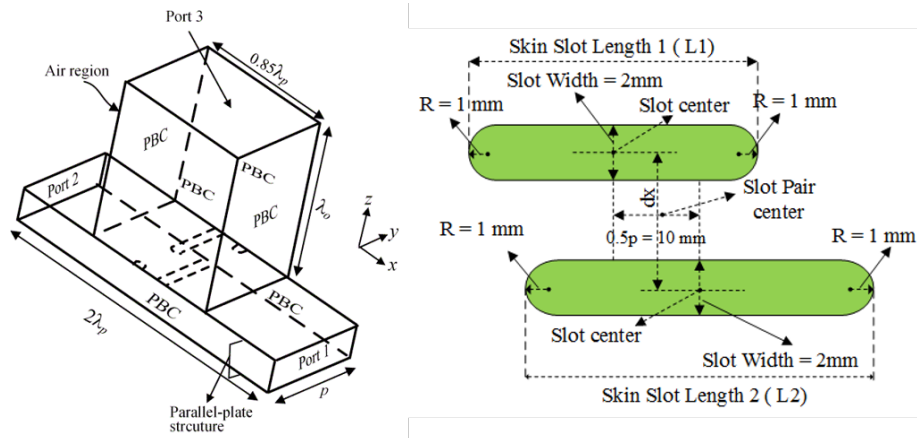


Fig. 3.11. HFSS Design Model of Single Radiation Slot-pair

Fig.3.11 shows the HFSS model with Periodic Boundary Condition (PBC) for one pair of radiating slot design. Here, this figure is a unit of radiating slot of 1-D radiating slot array as described in fig.3.10. In this model, port 1 is defined as the input port, while ports 2 and 3 are defined as the output ports. The coupled power is determined by the radiating slot length. A round-edged radiating slot with slot width of 2 mm and edge-curve radius of 1 mm are used to avoid electromagnetic fringing effects. The overlap distance in x direction



between the slot centers in a pair of radiating slot  $dx$  and  $p$  are optimized to have sufficiently small reflection (less than -20 dB). Here,  $p$  is the width of parallel-plate structure for one pair of radiating slot. Some samples of slot length  $L_2$  are taken (11.6 mm up to 14 mm, step every 0.2 mm). At each sample, slot length  $L_1$  and vertical slot pair spacing ( $dx$ ) are adjusted as to have sufficient  $S_{11}$ . For slot pair with 100% coupling factor, short position is also optimized. Then, the required  $L_1$ ,  $L_2$  and  $dx$  for targeted coupling factor is obtained. The simulation results of  $S_{11}$  of one pair of radiating slot as function of coupling factor are plotted in fig.3.12. This is utilized to design the length of radiating slot for up to 50% coupling factor at 1-D array of radiating slot design. Here,  $dx = \lambda_p/2$  to minimize undesired mutual coupling. For the last radiating slot pair design with 100% coupling, port 2 of HFSS model in fig.3.11 is replaced by short and then the center of radiating slot pair is located at  $\lambda_p/2$  from this short. Also,  $p = 20$  mm is applied for all radiating slots.

At initial of iteration, the distance between the centers of adjacent radiating slot pairs  $dr_0$  is estimated as”

$$dr_{0,m,m-1} = \lambda_p + \Delta dr_{0,m,m-1},; 2 \leq m \leq M \quad (3.7)$$

where,  $\Delta dr_0(m, m-1)$  is approximated as:

$$\Delta dr_{0,m,m-1} = [\angle S_{21m} + \angle S_{31m-1} - \angle S_{31m}] * \frac{\lambda_p}{2\pi}; 2 \leq m \leq M \quad (3.8)$$

The values of  $\arg. S_{21}$  and  $\arg. S_{31}$  for radiating slots up to 50% coupling factor can be estimated from the graph in fig.3.14. Also, for the last radiating slot ( $m = 1$ ), from HFSS simulation,  $\angle S_{31}$  of  $-180.61^\circ$  is obtained. For 1-D array of radiating slot with total of 26

radiating slots, the average value of  $\Delta dr_0$  is  $-1.8$  mm and the average value of  $dr_0$  is  $0.94\lambda_p$ . The simulation result of 1-D array of radiating slot for the initial iteration is shown in fig. 3.13. Here, the E phase of the radiated wave is plotted. In this graph, the positions of 0 and 700 mm are the positions of input port and shorted end of parallel plate, respectively. The phase data are taken at  $0.25\lambda_0$  below the radiation boundary, which is located at the above radiating slot. Here, the phase is observed along the positive x direction. As to obtain optimum in-phase excitation from the radiating slots, further iterations of spacing adjustment between the centers of adjacent radiating slots are also implemented. Finally, at the first iteration, an average value of spacing between the centers of adjacent radiating slot pairs  $dr$  of  $0.93\lambda_p$  is implemented. The results of simulated  $S_{11}$  for 1-D array of radiating slot are shown in fig.3.14.  $S_{11}$  of  $<-20$  dB is achieved throughout the 300 MHz bandwidth. There are 13 pairs of radiation slots in each half from the center of the antenna panel in the  $\pm y$  direction while there are 33 radiation slot pairs in the x direction. Instead of having tilted slot pairs for circular polarization as in [6] and [7], horizontal slot pairs are designed here for vertical polarization following the methodology described in [14].

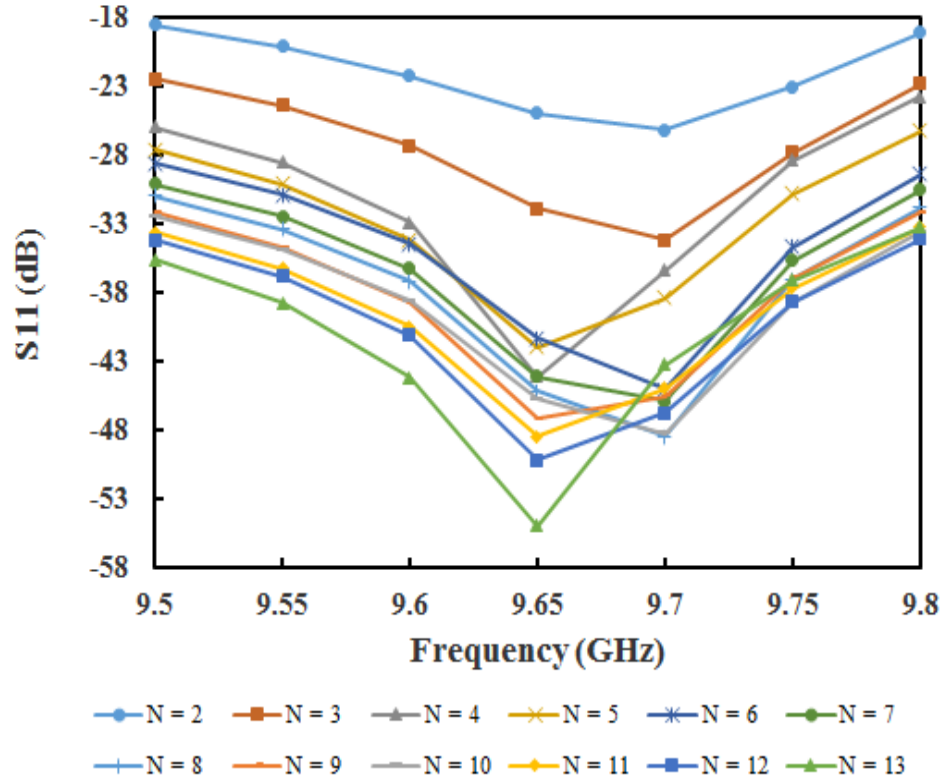


Fig. 3.12. Reflection Coefficients of Designed Radiation Slots

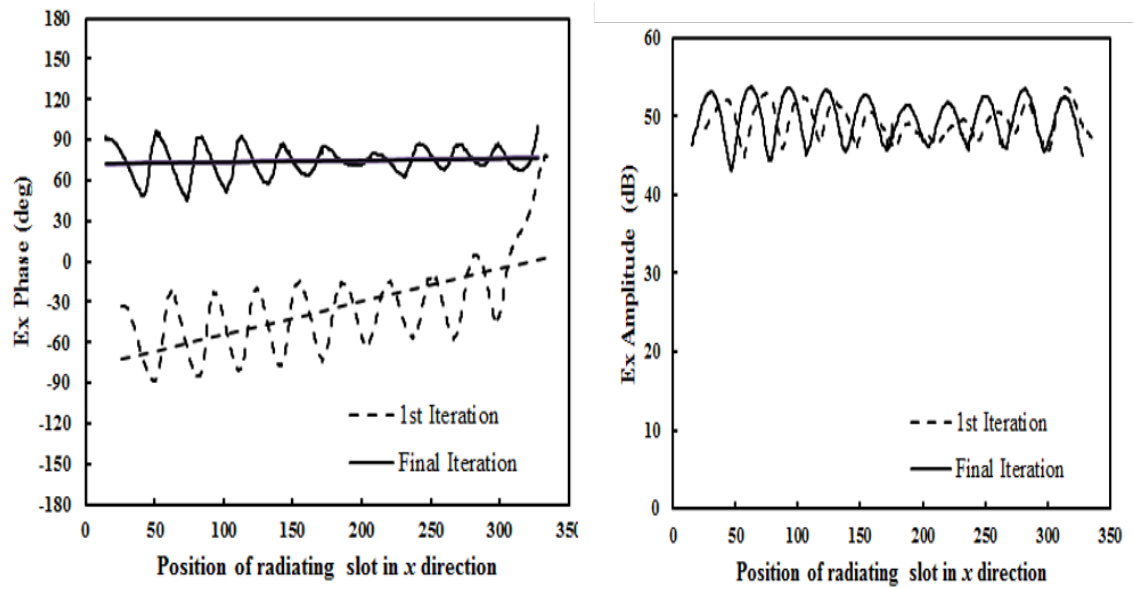


Fig. 3.13. Amplitude and Phase of Radiation Slot 1D Array before and after Optimization

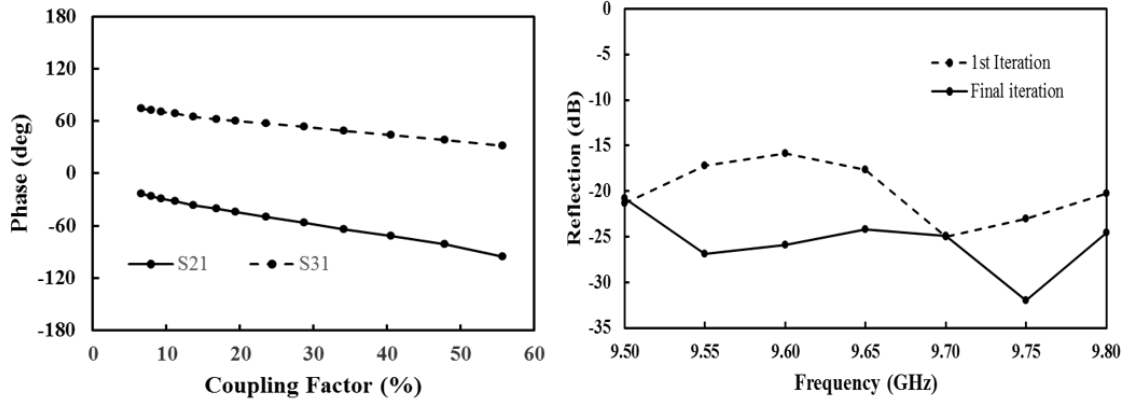


Fig. 3.14. Port Phase and Reflection Coefficient of Radiation Slot 1D Array before and after Optimization

### 3.3 Corporate Edge-feed Scheme

In order to acquire SAR imagery of 1 m resolution at a standard nadir off-set angle of 30 degrees in sliding spotlight mode, the required frequency chirp pulse bandwidth is 300 MHz. It is a known fact that a travelling wave antenna is prone to distortion due to frequency-dependent beam tilting effects. Measurement results of dual polarization antenna beam pattern designed in [7] showed significant beam-shift for chirp bandwidths greater than 250 MHz. To reduce this beam-shift we synthesize a wide-beam antenna by employing corporate-feed in our new waveguide feeder utilizing a two-way power divider called the  $\tau$ -junction designed in [12]. Unfortunately, introduction of coupling slots in the junction significantly increases reflection. In [13], the authors propose a corporate-feed double layer hollow slot-array waveguide model to enhance the bandwidth by making two additional cavities called the ‘iris’ in each T-junction of every layer. Unfortunately, there is no scope of using the T-junction for our waveguide geometry. Moreover, laminating the plates and stacking up layers is too bulky and complicated for small satellite.

Thus, one solution is to modify the  $\tau$ -junction instead by adding an additional inductive wall-pair to see if the bandwidth can be improved. Fig.3.15 shows half of corporate edge feeder network tournament circuit, comprising of all panels. The feeding point is at the edge of the antenna panel. With respect to the coupling slots, the effective feeding point inside the waveguide is at the center of the array of coupling slots, i.e. the window-center of the  $\tau$ -junction which lies in the center of the antenna panel (*along azimuth (x-direction)*). Hence, this feeding scheme is named center edge-feed unlike the conventional end-feed system in [6] and [7] where the feeding point is at one end of the coupling slots array.

Fig.3.16 shows the edge-feed antenna feeding scheme for one panel with the  $\tau$  - junction. There are two feeders at the edge of each panel. Fig.3.16 shows the layered structure of the antenna panel. The electromagnetic wave that is coupled from the two feeders (left and right) travels in to +x and -x direction in the parallel-plate. Here, coupling slots of both feeders are arranged in the same direction. Hence, in z direction, the E field that excited by right feeder should be 180 degrees out of phase with the E field that excited by left feeder. Thus, the wave that travels to +x and -x direction will have same H field orientation, which is a necessary condition for in-phase excitation. Each feeder consists of 15 coupling slots on either side of the  $\tau$ -junction. It is desired that uniform power be transmitted at every single slot, so the required coupling factor of each coupling slot is  $1/n$  where 'n' is the slot number counted from the shortened end of the feeder. It is desired to have uniform power transmitted at every single slot, so the required coupling factor of each coupling slot at the feeder is  $1/n$  where 'n' is the slot number counted from the shortened end of the feeder. Table 3.3 shows the antenna structure dimensions.

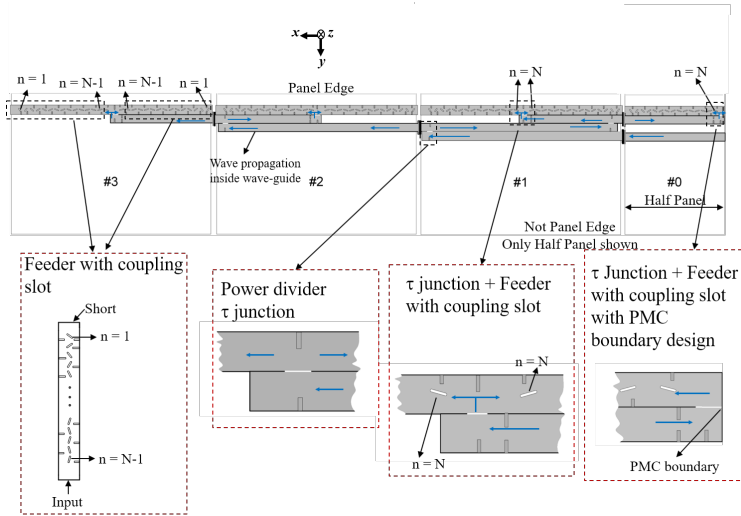


Fig. 3.15. Left Wing of Edge-feed Antenna Network Tournament Circuit

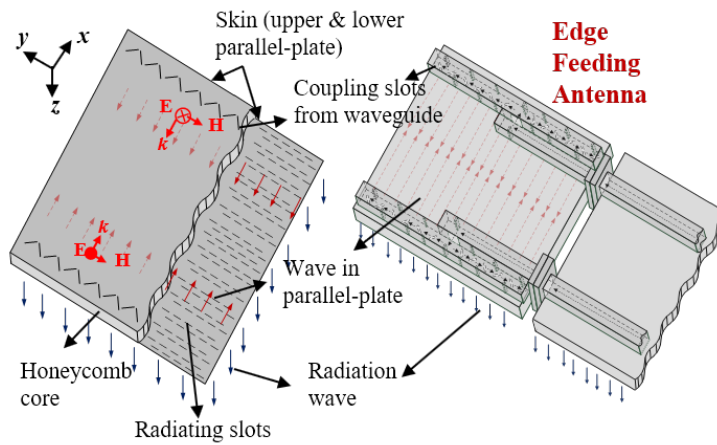


Fig. 3.16. Edge-Feed Design Model Schematic of Antenna Panel 3

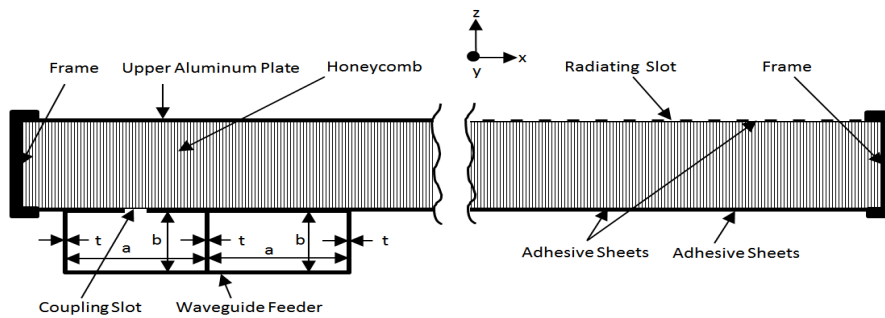


Fig. 3.17. Side-view of Layered Structure of Edge-feed Antenna Panel 3

Table 3.3 MicroX-SAR Antenna Structure Dimensions

Parameter	Dimension (mm)
Antenna Size	700 x 700
Feeder Length	684.24
Feeder Inner Size (a x b)	22.86 x 10.16
Inductive Wall Width	1
Slot Width	2
Slot Radius	1
Hard-wall Width	4.9
Aluminum Skin Thickness	0.3
Honeycomb Core Thickness	6
Feeder Thickness	1
Hard-wall Length	6.3
Adhesive Thickness	0.09

In the following section, we will discuss the steps of our design sequentially and at each step compare the Standing Wave Ratio (VSWR) (measured in terms of the Reflection

Coefficient  $S_{11}$ ) of the waveguide using our modified  $\tau$ -junction with the standard  $\tau$ -junction to demonstrate the effect of double resonance in reducing VSWR and thereby enhancing the bandwidth which is our goal.

### 3.3.1 Coupling Slots Design

Fig.3.19 shows a single coupling slot HFSS design model [6]. This single coupling slot is one unit of coupling slot from one antenna feeder system as described in Fig.3.20. Here, port 1 and port 2 are defined as the feeder input and output port, respectively. Port 3 is the output port which is located at the parallel-plate. As to feed the parallel-plate in phase, the adjacent coupling slots with a spacing of half guided wavelength have opposite inclination orientations. Therefore, the location of the inductive wall also corresponds to the orientation of the coupling slots. However, since periodic boundary condition (PBC) is applied, the simulation using this simplified HFSS model (one inductive wall with its related coupling slot in fig.) is enough. Here, inductive wall is added to cancel reflection.

However, the presence of inductive wall will also contribute a phase enhancement in phase of  $S_{21}$ . Therefore, initially a coupling slot without inductive wall is simulated. The tilt angle ( $\gamma$ ) of the coupling slot is then varied from 5 degrees up to 50 degrees. Here, for every 5-degree increment of  $\gamma$ , the slot length ( $s_l$ ) is tuned so that phase of  $S_{21}$  is 0 degree. A round-edged coupling slot with slot width,  $s_w$  equals to 2 mm and edge-curve radius,  $r_s$  equals to 1 mm are used. After that, the inductive wall is designed for each pair of  $s_l$  and  $\gamma$ . Here, the position ( $i_p$ ) and length ( $i_l$ ) of inductive wall are designed so that sufficiently small reflection of  $S_{11}$  could be obtained ( $< -30$  dB). Here, the inductive wall width,  $i_w$  equal to 1 mm is applied.



Next, each slot ( $\gamma$  and  $sl$ ) and inductive wall ( $ip$  and  $il$ ) parameters are designed up to 50 % coupling factor are designed by utilizing phase results of port 2 and port 3. In the case of the last coupling slot (slot with  $n = 1$ ) design, the slot and inductive wall parameters are obtained by modifying the model in fig.3.19. Here, port 2 is a shorted-end and the center of coupling slot is at the distance  $\lambda_g/2$  from this short.

It is desired that:

$$|S_{21}|^2 = \frac{1}{n}, \quad 1 \leq n \leq N - 1 \quad (3.9)$$

$$|S_{21}| = |S_{31}| \quad (3.10)$$

$$\angle S_{21} = \angle S_{31} \quad (3.11)$$

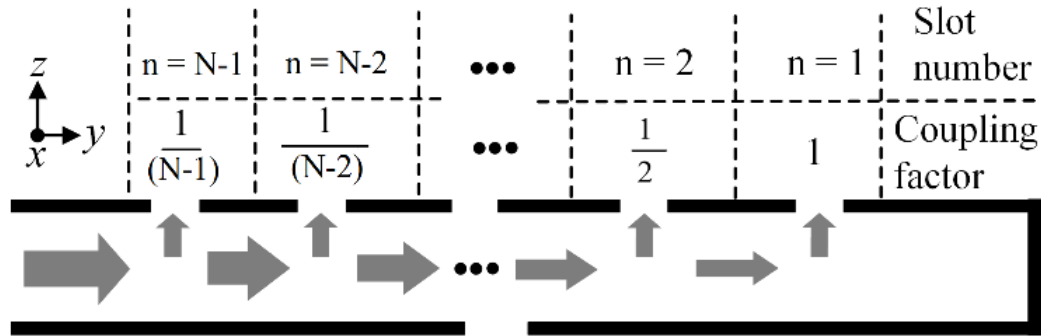


Fig. 3.18. Coupling Factor Computation for Linear 1D Array with Uniform Excitation

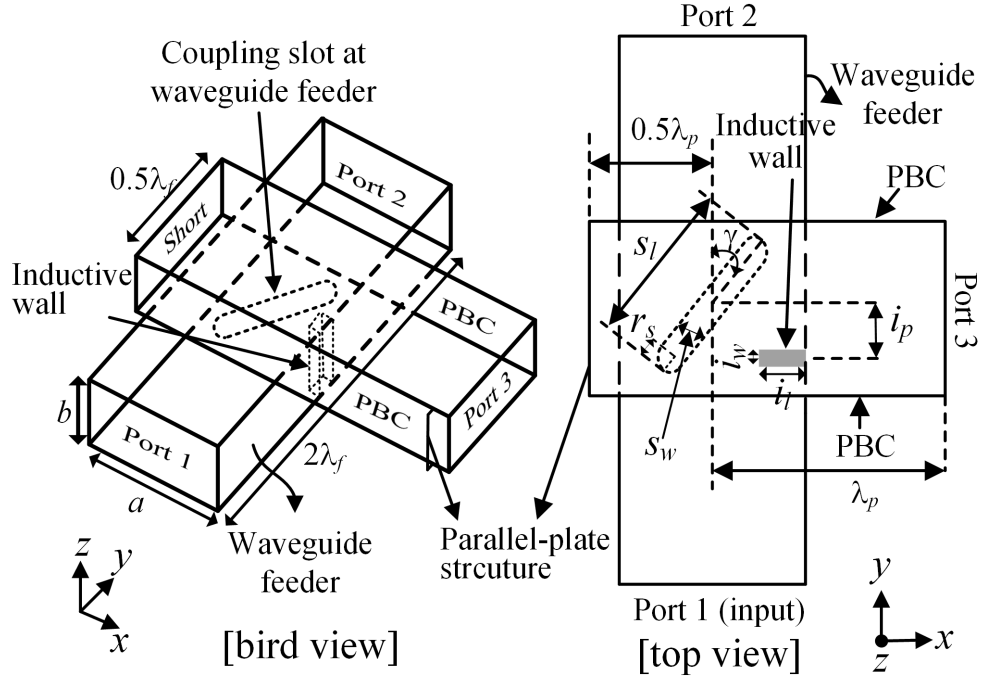


Fig. 3.19. HFSS Single Slot Design Model of Edge-feed Scheme

- *Design of End-feed Array of 'N-1' Slots*

Since slot 'N' is already designed in the previous section, initially the end-feed array of remaining 'N-1' slots designed individually is simulated as shown in fig.3.20. Simulation results show that it does not meet the maximum -15 dB  $S_{11}$  criteria over our desired bandwidth. Thus, inductive walls for the first 3 slots are re-designed from the shorted end (coupling factor 100%, 50% and 33%) using the single slot HFSS model to suppress reflection including hard-wall as shown in fig.3.21 (previously the hard-wall was not taken into consideration for single slot design and 100% coupling slot had no inductive wall). Fig.3.22 shows  $S_{11}$  performance of the original and modified design. Table 3.4 shows the changed parameters in the modified 'N-1' slot end-feed design.

At initial of iteration, the distance between the centers of adjacent radiating slot pairs  $dr_0$  is estimated as”

$$ds_{0n,n-1} = \lambda_g + \Delta ds_{0n,n-1}; 2 \leq n \leq N-1 \quad (3.12)$$

where,  $\Delta dr_0$  (m, m-1) is approximated as:

$$\Delta ds_{0m,m-1} = [\angle S_{21n} + \angle S_{31n-1} - \angle S_{31n}] * \frac{\lambda_g}{2\pi}; 2 \leq n \leq N-1 \quad (3.13)$$

The values of  $\angle S_{21}$  and  $\angle S_{31}$  for coupling slots up to 50% coupling factor can be estimated from the graph in fig.3.22. Also, for the last radiating slot ( $n = 1$ ), from HFSS simulation,  $\angle S_{31}$  of  $-180.61^\circ$  is obtained.

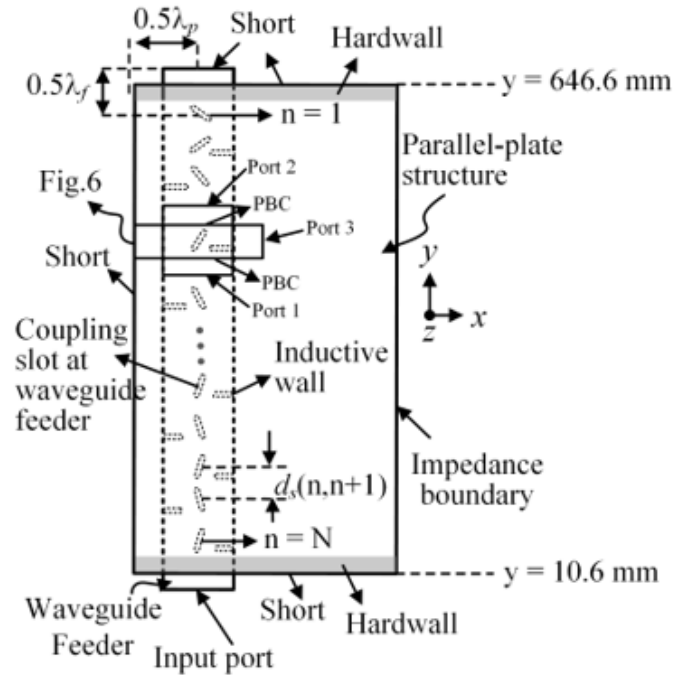


Fig. 3.20. HFSS Design Model of End-feed Array of ‘N-1’ Coupling Slots for Edge-feed

Scheme

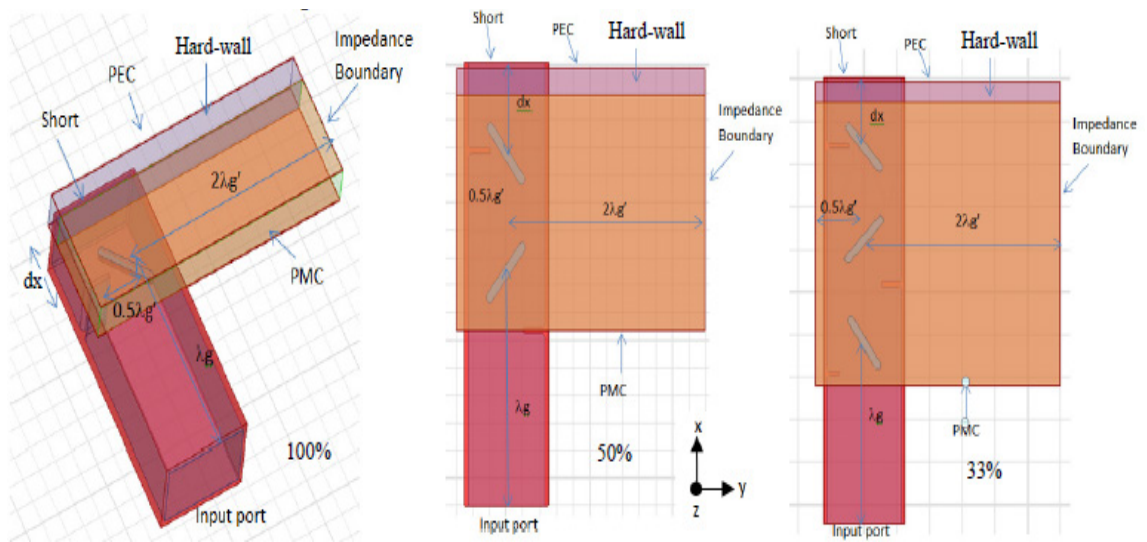


Fig. 3.21. Modified HFSS Design Model of Coupling Slots 1, 2, 3 for Edge-feed Scheme

Table 3.4 New Parameters of End-feed ‘N-1’ Slots Design Model for Edge-feed Scheme

Parameter	Dimension (mm)
Short Position dx	16.6
Wall 1 Length	6.7
Wall 2 Length	10.5
Wall 3 Length	7.35
Wall 1 Position	-0.5
Wall 2 Position	6
Wall 3 Position	3.95

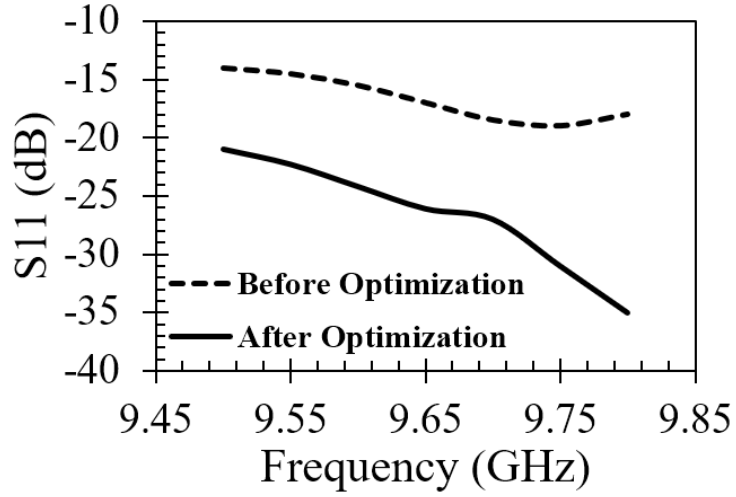


Fig. 3.22. Reflection Coefficient of End-feed Array of ‘N-1’ Coupling Slots before and after Optimization for Edge-feed Scheme

### 3.3.2 Power Divider $\tau$ -junction Design

- *Modification of  $\tau$ -junction without Coupling Slots*

First, the original  $\tau$ -junction is designed for the waveguide feeder as shown in fig.3.23. The length and position of the upper inductive wall (called output wall) are adjusted to have 1:1 power-dividing ratio and phase balance between port 2 and port 3. Next, the  $\tau$ -junction is modified by adding a pair of inductive walls as shown in fig.3.24. The length and position of the walls are adjusted (*the positions of the input and output walls are with respect to the center of the window whereas the position of the smaller wall-pair is with respect to the input wall*). In addition, the window length is also increased. Fig.3.26(a) shows the comparison of the  $S_{11}$  performance of the optimum designs of the original  $\tau$ -junction and the modified  $\tau$ -junction. Adding the inductive wall-pair increases the -10 dB  $S_{11}$  bandwidth from 2.7 GHz to 5.5 GHz, thereby doubling it. This can be

explained by the fact that each wall-pair causes a resonance at a certain frequency which minimizes  $S_{11}$ . Introducing a second smaller wall-pair produces another resonant minimum at a different frequency. The length and position of the smaller walls control the position of the second resonant peak. As seen in fig.3.26(a), in the original  $\tau$ -junction with only one wall-pair (input wall and output wall), there is only one minimum at 9.65 GHz which corresponds to single resonance whereas in the modified  $\tau$ -junction with two wall-pairs, we have a couple of minima in the  $S_{11}$  plot, one at 8.5 GHz and another at 13.4 GHz which corresponds to double resonance.  $S_{11}$  improves significantly at the edge frequencies because of this double resonance thereby significantly enhancing the bandwidth. It is to be noted that although the original  $\tau$ -junction gives a good enough  $S_{11}$  performance in our desired frequency range of 9.5 GHz to 9.8 GHz, as we include the slots, the reflection drastically increases due to the long-line effect and in such a scenario, the additional walls will be critical in increasing the - 20 dB bandwidth.

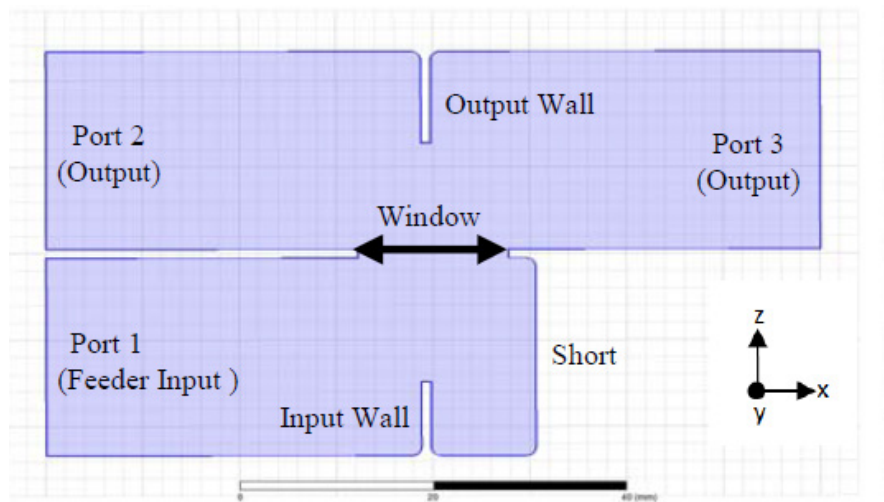


Fig. 3.23. HFSS Design Model of Original  $\tau$ -junction

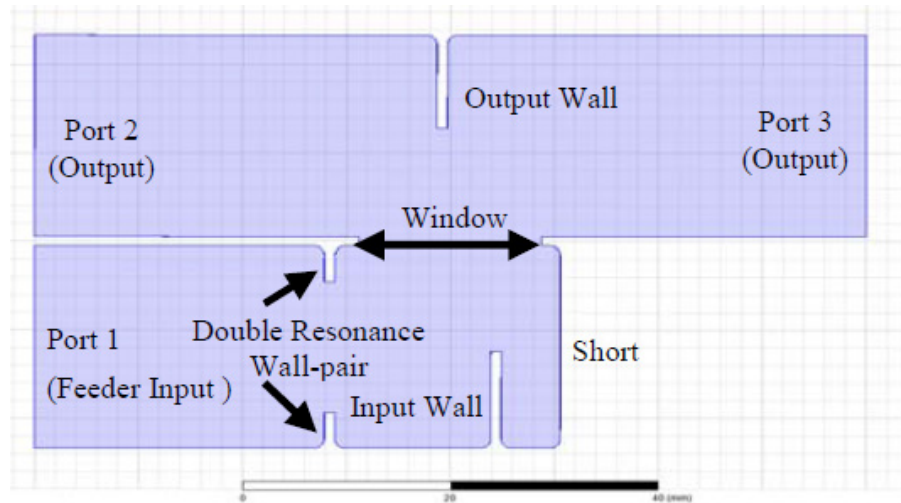


Fig. 3.24. HFSS Design Model of Modified  $\tau$ -junction

Table 3.5 Modified  $\tau$ -junction Design Parameters

Parameter	Dimension (mm)
Input Wall Length	8.52
Input Wall Position	4.4
Output Wall Length	10.58
Output Wall Position	-0.78
Length of double-resonance walls	4
Position of double-resonance walls	16
Window Length	17.6
Short Distance (from window center)	21.2

### 3.3.3 Edge Panel Feeder Design

- *Design of Slot 'N' with Modified  $\tau$ -junction*

Next the modified  $\tau$ -junction is designed including a single slot with coupling factor  $1/N$  on either side [8]. The HFSS model in fig.3.25 shows a port assigned to each slot. Each slot is followed by a small inductive wall (*these wall positions are measured from the corresponding slot centers*) for the purpose of reflection suppression, power ratio adjustment and phase balancing. The length of each port in the x-direction is half the guided wavelength. Keeping the lengths and positions of the window and the double resonance wall-pair unchanged, the other parameters are adjusted to get uniform amplitude and phase balance in ports 2,3,4,5 while simultaneously minimizing  $S_{11}$ . The modified parameters are summarized in Table 3.5.

It is desired along with equations 3.10 and 3.11 that:

$$|S_{41}|^2 = |S_{51}|^2 = \frac{1}{2N}, \quad (3.14)$$

$$\angle S_{41} = \angle S_{51} \quad (3.15)$$

Fig.3.26 shows the comparison of the  $S_{11}$  performance with the modified  $\tau$ -junction and the original  $\tau$ -junction. As seen, using the modified  $\tau$ -junction, the - 20 dB bandwidth is increased from 180 MHz to over 300 MHz. Fig.3.27 shows variation of amplitude and phase characteristics with frequency at the different ports for the double resonance case. It shows good performance in our desired bandwidth of 300 MHz.



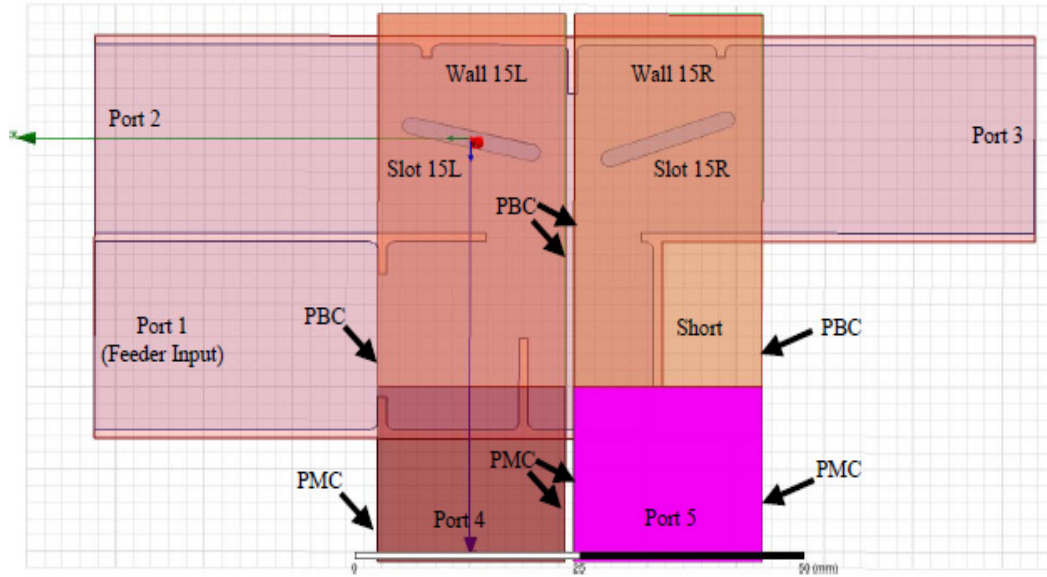


Fig. 3.25. HFSS Design Model of Coupling Slot ‘N’ of Edge-feed Scheme

Table 3.6  $\tau$ -junction with Slot ‘N’ Design Parameters

Parameter	Value
Slot 15L Length	15.91 mm
Slot 15R Length	15.91 mm
Slot 15L Angle	166.8 deg
Slot 15R Angle	19.8 deg
Distance between Slot Centers	22.22 mm

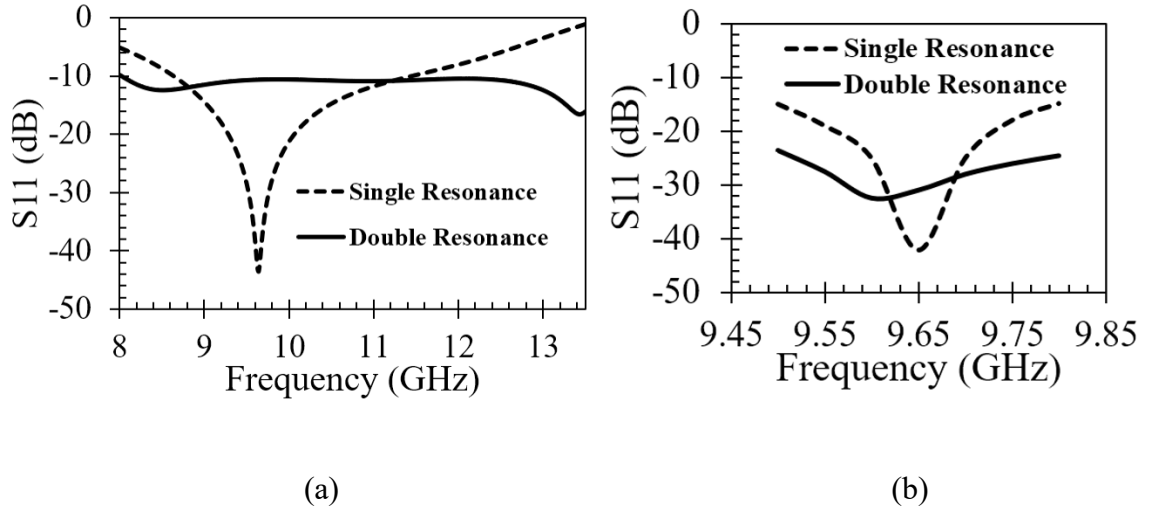


Fig. 3.26. Reflection Coefficient of (a)  $\tau$ -junction only (b)  $\tau$ -junction with Coupling Slot  
'N' of Edge-feed Scheme

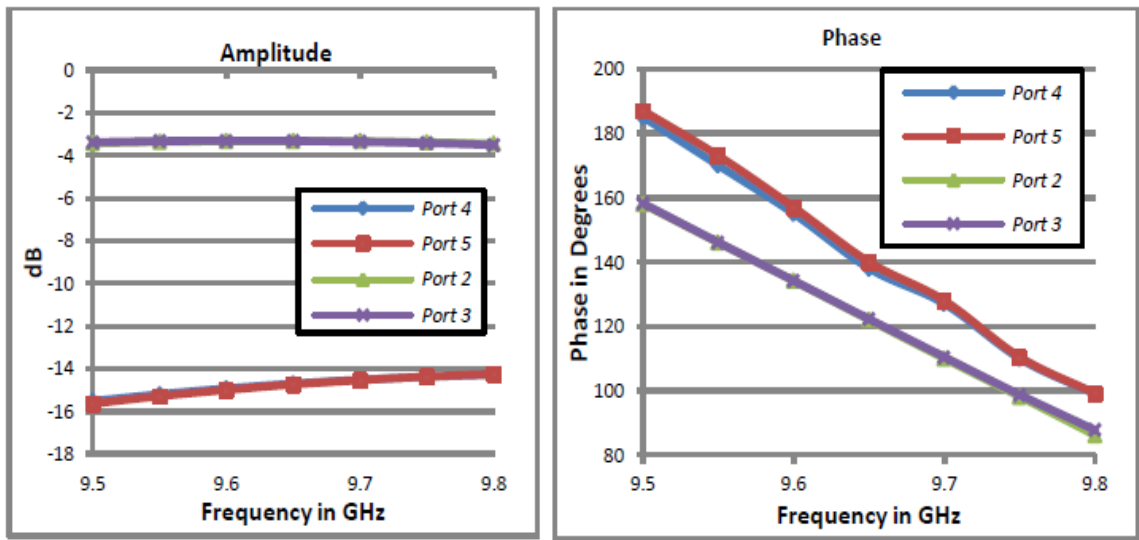


Fig. 3.27. Variation of Port Amplitude and Phase with Frequency

- *Design of Full Feeder with '2N' Slots*

As the final step, the 'N-1' slots end-feed model and slot 'N' with  $\tau$ -junction model are connected to simulate the total feeder waveguide (see fig.3.28). Fig.3.32 compares the

$S_{11}$  performance of the entire system with single resonance and with double resonance. As seen, the latter increases the -20 dB bandwidth from 80 MHz to 300 MHz, which shows the great advantage using the double resonance structure. However, the phase characteristics as a function of distance showed undesirable variations from the center of the window to the end hard-walls as seen in fig.3.30. (*The phase is measured here by means of a polyline in the HFSS model; it is the phase in the center of honeycomb in the parallel plate*). We used both linear and parabolic approximations of the trend-line in excel sheet and calculated a maximum phase variation of 13 degrees. To achieve phase balance, we re-adjust each slot center position by changing the adjacent slot-center distance on both sides of the  $\tau$ -junction by the following equation:

$$d_{sf(n,n-1)} = d_{si(n,n-1)} + \frac{\theta_n - \theta_{n-1}}{2\pi} * \lambda_g, \quad 2 \leq n \leq N \quad (3.16)$$

where  $d_{si}$  and  $d_{sf}$  are the initial and final distances between adjacent slot centers,  $n$  is the slot number,  $\theta_n$  (*calculated from the trend-line equation*) is the phase corresponding to slot number 'n' in degrees.

Fig.3.30 shows that after adjustment the maximum phase variation is reduced to 2.86 degrees and the maximum amplitude variation is only 0.1 dB as seen in fig.3.31 which are well within permissible limits.  $S_{11}$  is below -19 dB throughout the bandwidth as desired as seen in fig.3.32. Fig.3.29 shows the E-field simulated animation. Fig.3.33 shows the fabricated Bread Board Model (BBM) Edge-feed waveguide. Fabrication was done by aluminum deep brazing with manufacturing error less than 0.05 mm.

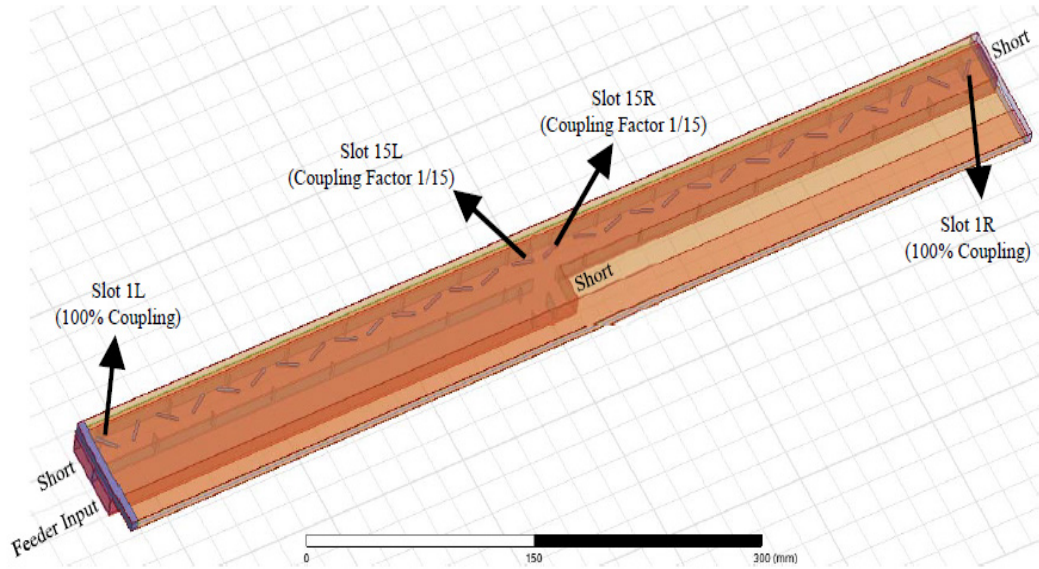


Fig. 3.28. HFSS Design Model of Panel 3 Edge Feeder with '2N' Coupling Slots

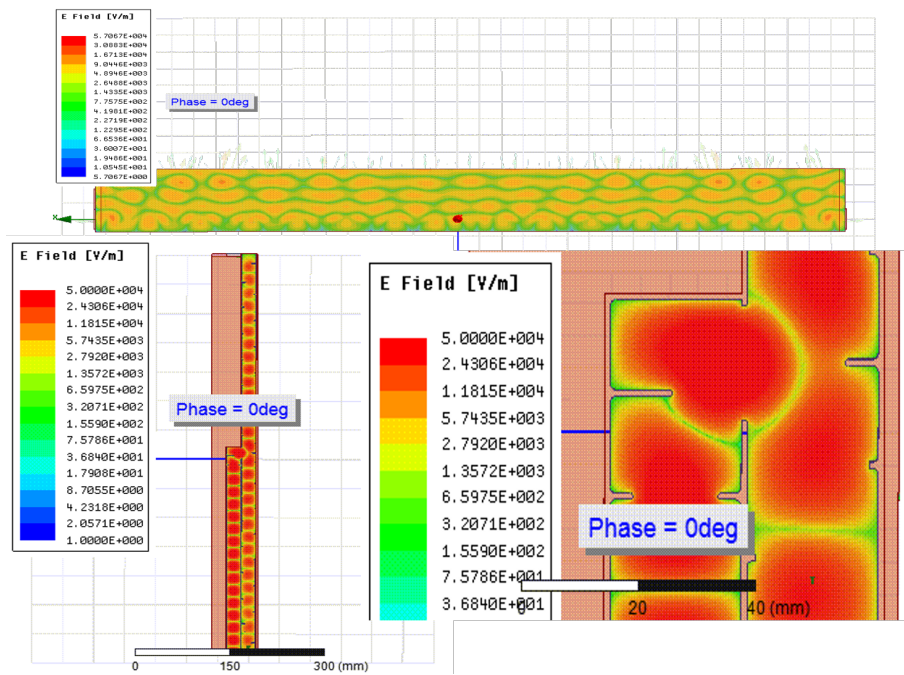


Fig. 3.29. HFSS Animation of Electric Field Propagation inside Edge-feed Waveguide

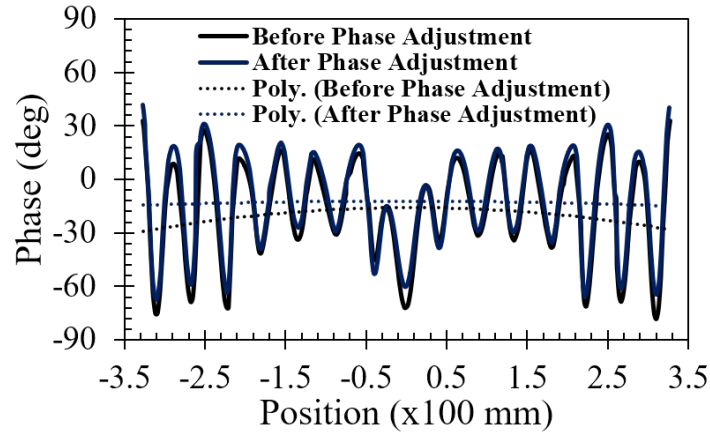


Fig. 3.30. Simulation Amplitude Distribution of Edge Feeder for Panel 3

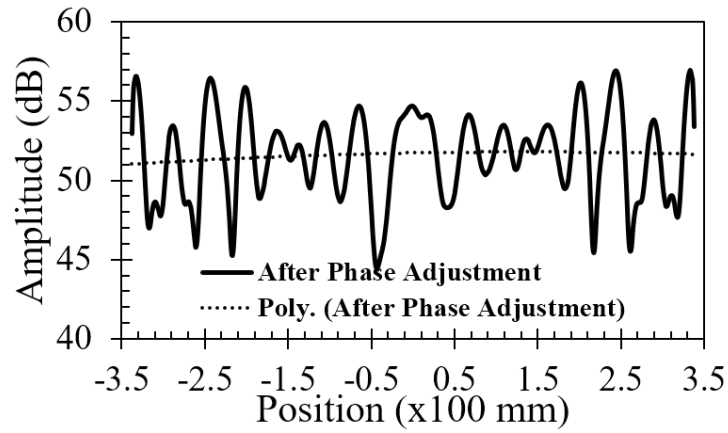


Fig. 3.31. Simulation Phase Distribution of Edge Feeder for Panel 3

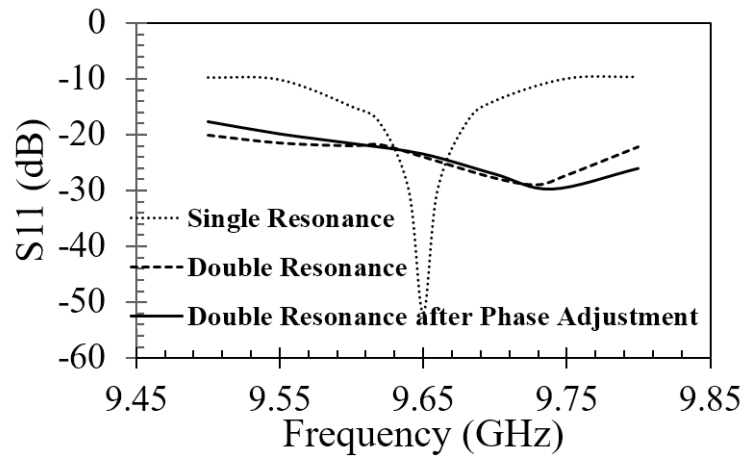


Fig. 3.32. Simulation Reflection Coefficient of Edge Feeder for Panel 3

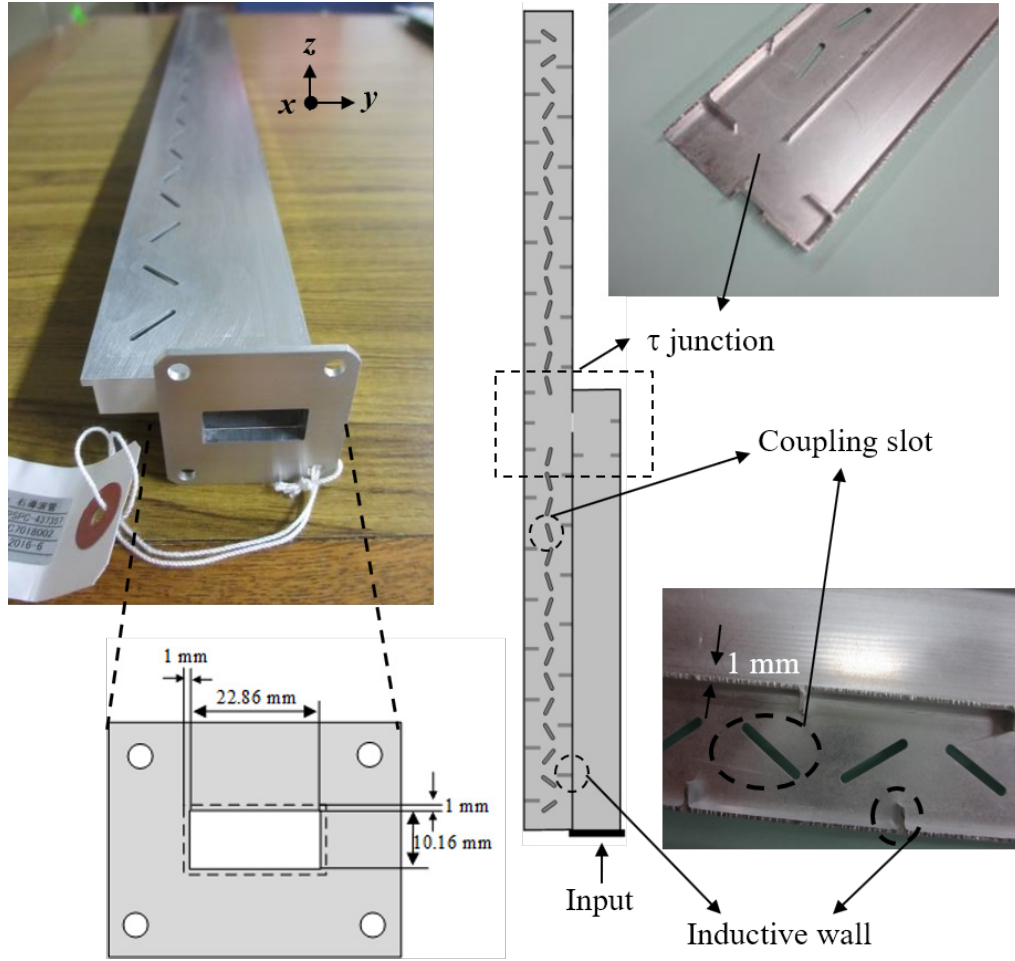


Fig. 3.33 Fabricated Edge-feed Waveguide Feeder for Panel 3

- *Non-identical Feeder Issue of Edge-feed Scheme*

In the edge-feed scheme, there are two feeders at the two corners of each panel. The electromagnetic wave that is coupled from the two feeders (left and right) travels in +x and -x directions in the parallel-plate. The orientation angle of the coupling slots of both feeders must be in the same direction to have the same H field orientation. Thus, designing only one feeder and mirroring its design along the azimuth axis is not permissible since this will change the orientation angle from acute to obtuse and vice-versa which will result in H field being in opposite directions as seen in fig.3.34. Thus, the other feeder needs to be

designed independently [9]. Fig.3.35 shows the HFSS design models of Slot no ‘N’ for the left feeder and right feeder. In order to have  $|S_{41}|=|S_{51}|=1/N$  and equal phase of Port 4 and Port 5 while keeping the slot angle of Slot 15A obtuse and that of Slot 15B acute, the slot length and slot center separation are very different for the left feeder and right feeder as shown in Table 3.7, which is not ideal. Moreover, in z direction, the E field excited by the right feeder should be 180 degrees out of phase with the E field excited by the left feeder. This is a necessary condition to ensure that the wave travelling in the +x and -x directions will have the same H field orientation, which is a critical for in-phase excitation. Since the design parameters are not identical for the two feeders, especially the slot-angle and slot center separation of Slot no 15, the feeder length and excitation phase (from hard-wall to hard-wall outside the waveguide in the middle of the parallel plate, measured by means of a polyline in the middle of the honeycomb layer in the HFSS Model) are different and thus the E-fields excited by the right feeder and left feeder are not perfectly out of phase. Fig.3.36 and fig.3.37 show the excitation amplitude and excitation phase distribution of the two feeders. It is seen that the phase difference between the E fields of the two feeders is about 150 degrees and not 180 degrees as desired. Moreover, since the two feeders will excite the same antenna, it is important that both feeders are of identical length. The length of the right feeder is 684.24mm while that of the left feeder is 683.12mm. Thus, to balance the length of the left feeder without introducing phase taper, the distance of the short position from last slot (100% coupling) has to be increased by 0.56mm on either side of the  $\tau$ -junction, resulting in increase in reflection of the left feeder compared to the right feeder as seen in fig.3.38.

Table 3.7. Designed Parameters of Edge Feeders for Slot ‘N’

Feeder	Slot 15A Length (mm)	Slot15B Length (mm)	d (mm)	Slot 15A Angle (deg)	Slot 15B Angle (deg)
Left	17	17	27.13	166	11
Right	15.91	15.91	22.22	166.6	19.8

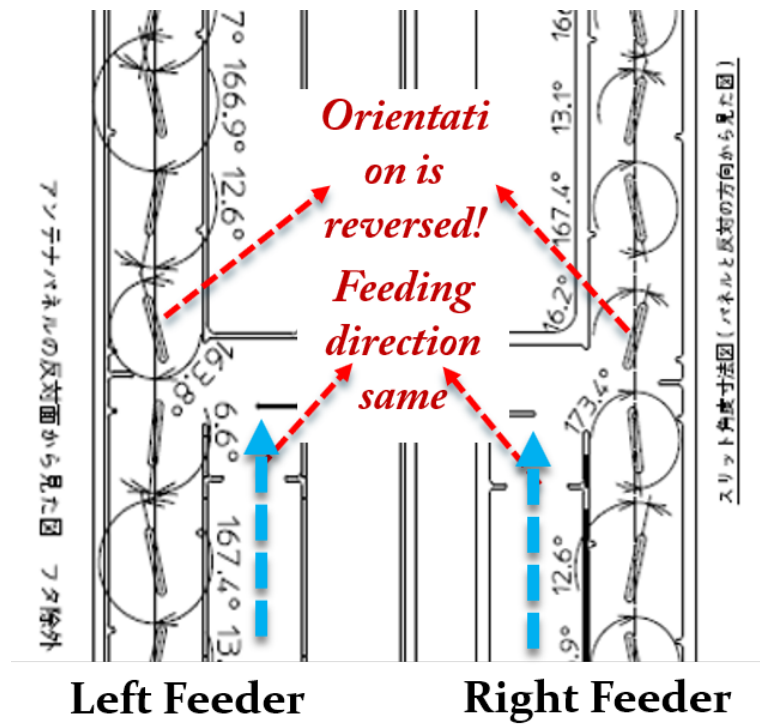


Fig. 3.34. Effect of Mirroring Coupling Slot Design along Azimuth



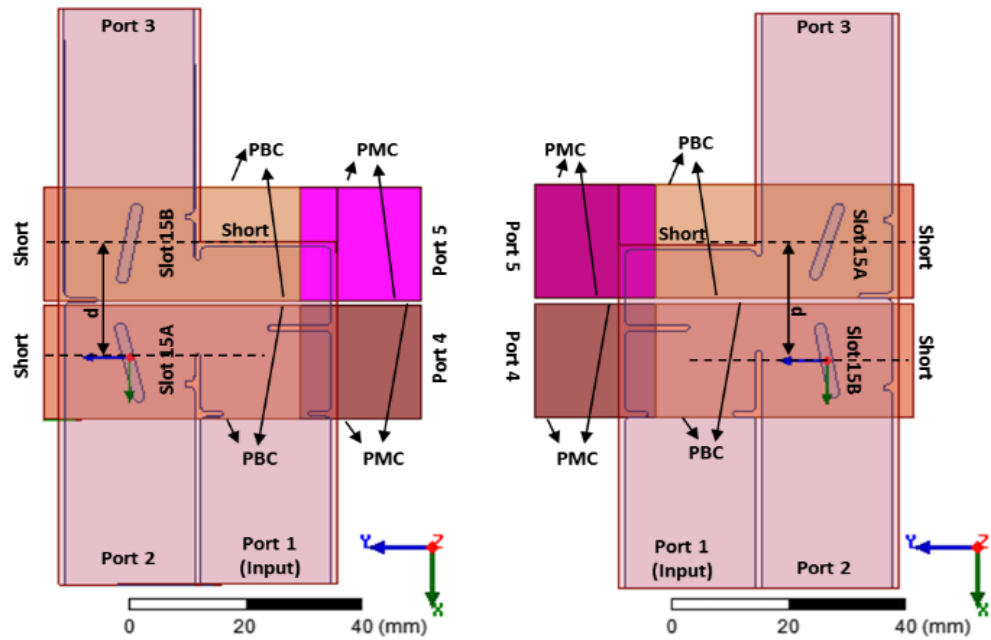


Fig. 3.35. Comparison of HFSS Design Model for Slot ‘N’ of Left Feeder and Right Feeder of Edge-feed Scheme

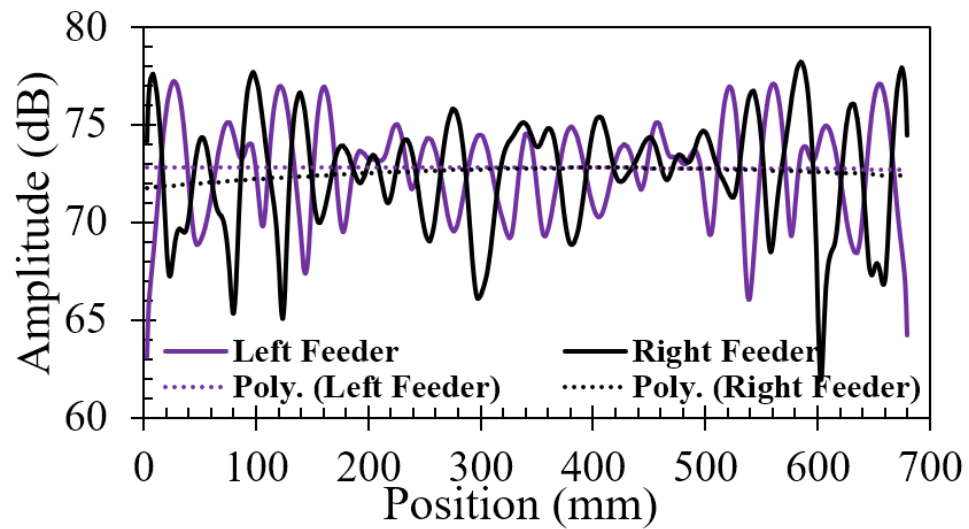


Fig. 3.36. Simulation Amplitude Distribution of Left Feeder and Right Feeder for Panel 3

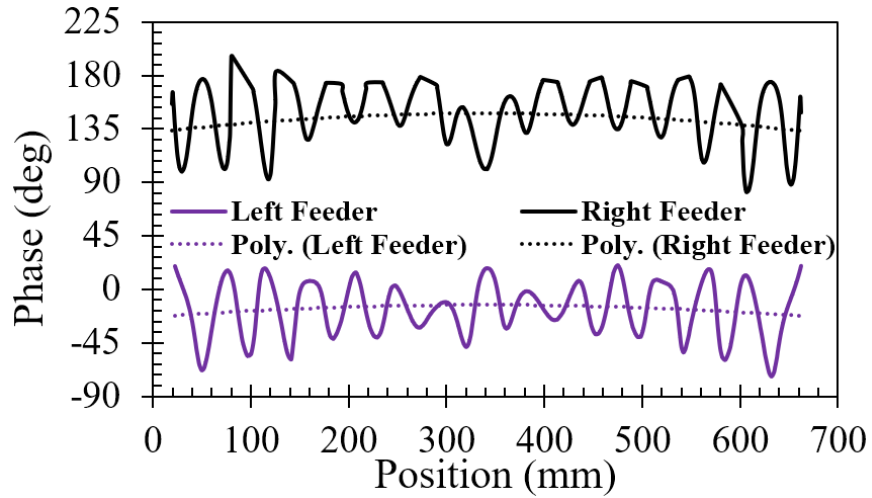


Fig. 3.37. Simulation Phase Distribution of Left Feeder and Right Feeder for Panel 3

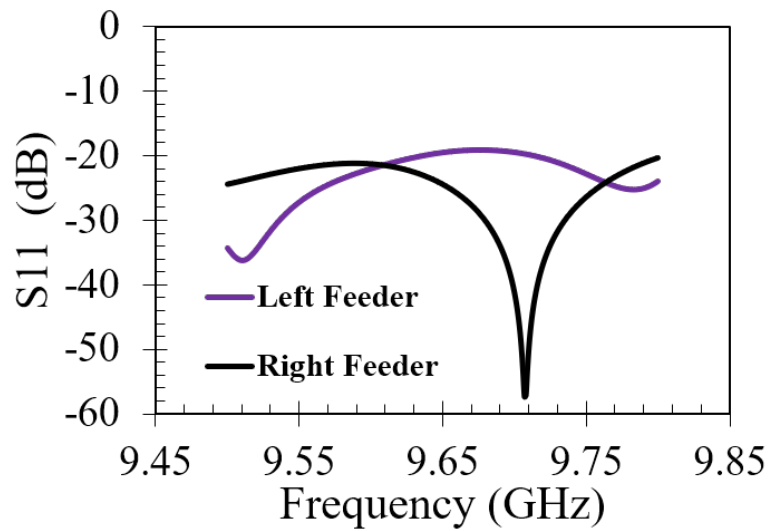


Fig. 3.38. Simulation Reflection Coefficient of Left Feeder and Right Feeder for Panel 3

### 3.3.4 Full Edge Panel Simulation Results

Fig.3.39 shows the full panel 3 HFSS Simulation Model with the two edge feeders. To achieve the desired out-of-phase condition between the two feeders and thereby ensure in-phase excitation, the radiation slots in one half of the antenna panel

must be moved by some distance corresponding to 30 degrees of phase difference. This distance is calculated as:

$$\delta = (\theta/2\pi) * \lambda_p \quad (3.17)$$

For  $\theta = 30$  degrees and  $\lambda_p = 29.68$  mm,  $\delta = 2.5$  mm. Fig.3.40 shows the full panel (*with radiation slots*) near-field simulation results of amplitude and phase of the edge-feed system. The radiation slots corresponding to the left feeder (Port 1) are shifted to the right (away from the feeder) by 2.5 mm to achieve phase difference of 180 degrees. The standard deviations of amplitude and phase are 6.26 dB and 53.2 degrees respectively. Fig.3.41 shows the reflection coefficient of the edge-feed system of full panel. The presence of two feeders increases the active reflection in the two input ports, leading to 2.5 dB degradation in active S of the total system, compared to the reflection of each isolated feeder in fig.3.42.

$$Active S_1 = S_{11} + S_{12} \quad (3.18)$$

$$Active S_2 = S_{21} + S_{22} \quad (3.19)$$

Thus, the desired 300MHz bandwidth is not achieved by the full panel edge-feed antenna although it is wider than the 130MHz bandwidth of the end-feed antenna [3]. Fig.3.42 and fig.3.43 show the simulated full panel antenna gain pattern in range and azimuth. The peak gain is 35.59 dBi, which is 0.69 dBi higher than [6] and the calculated antenna aperture efficiency is 62%, compared to 54% in [6]. Fig.3.44 shows the variation of peak gain with frequency. The maximum gain is at 9.68GHz and the maximum drop in gain in 300 MHz bandwidth is 2.76 dB (less than 3 dB) which confirms wide-band operability.

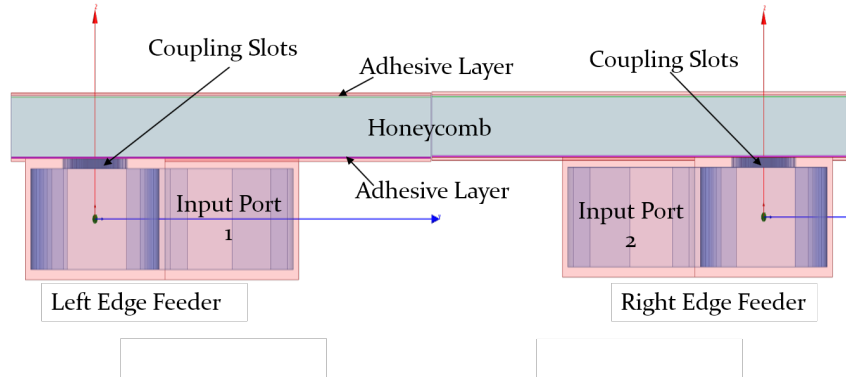


Fig. 3.39. HFSS Simulation Model of Panel 3 with Edge-feed Waveguide Feeders

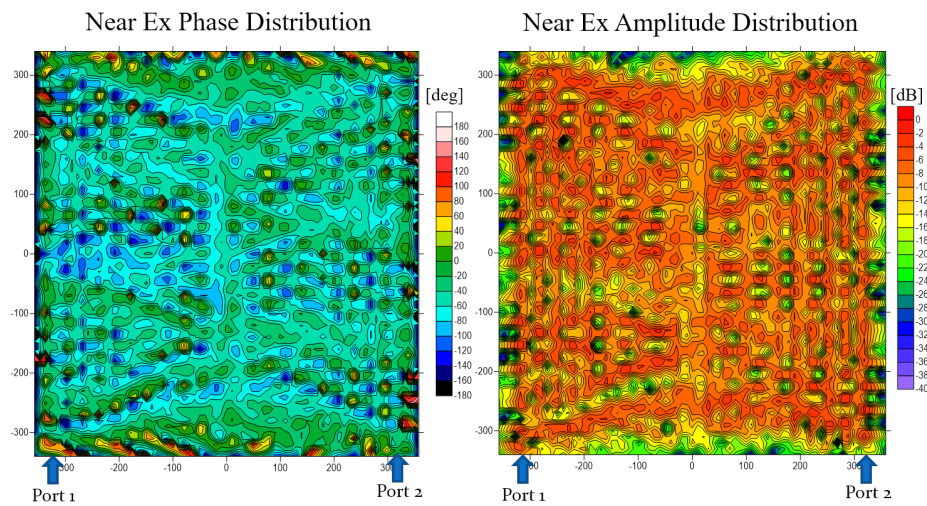


Fig. 3.40. HFSS Simulation Amplitude and Phase of Panel 3 with Edge-feed Scheme

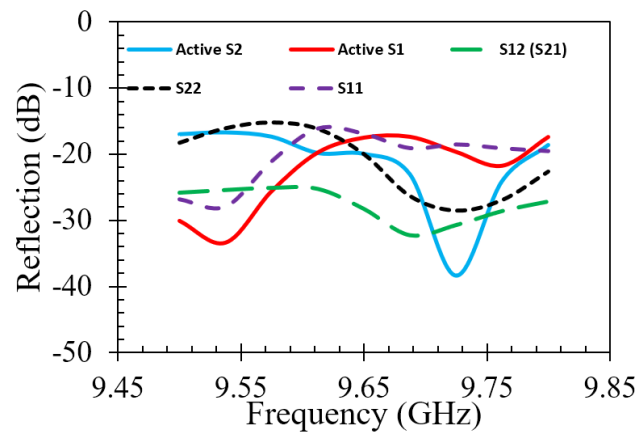


Fig. 3.41. HFSS Simulation Reflection Coefficient of Panel 3 with Edge-feed Scheme

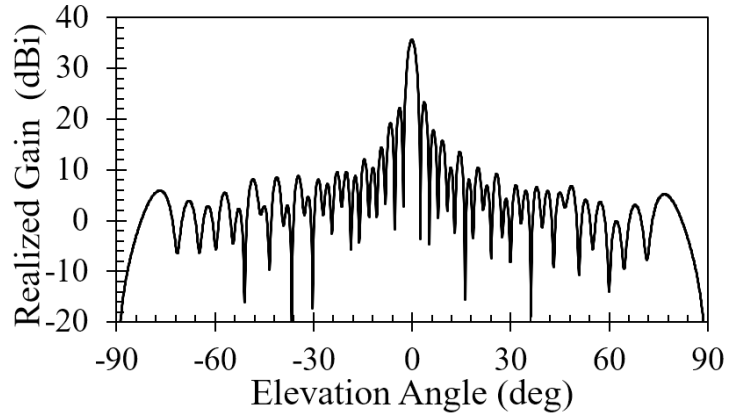


Fig. 3.42. HFSS Simulation Elevation Pattern of Panel 3 with Edge-feed Scheme

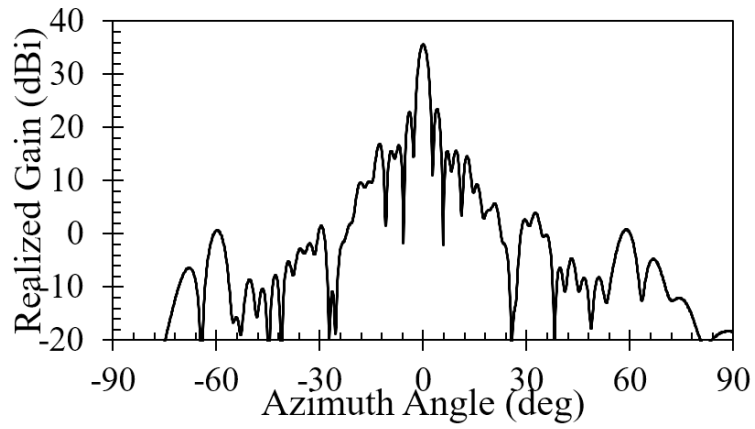


Fig. 3.43. HFSS Simulation Azimuth Pattern of Panel 3 with Edge-feed Scheme

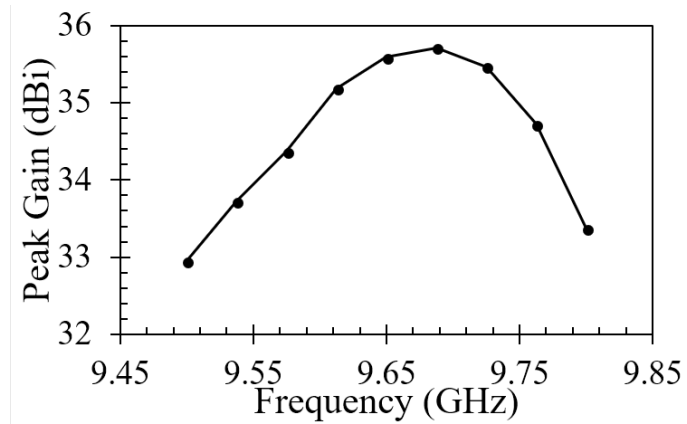


Fig. 3.44. HFSS Simulation Peak Gain vs Frequency of Panel 3 with Edge-feed Scheme

- *Poynting Vector Analysis*

Poynting vector distribution inside the half-panel parallel-plate structure (*without radiating slots*) of the edge-feed system is shown in fig.3.46. The slot angle increases from the panel center towards the hard-wall. Larger the slot angle, greater is the tilt of the Poynting vector from the desired direction of propagation. 30 feeder coupling slots give 30 distinct Poynting vectors. Hard-walls are reflective (*like Perfect H boundary*). Fields from adjacent slots interfere to produce nearly longitudinal component, but since one of the adjacent slots has higher coupling than the other, the resultant Poynting vector is tilted from the desired direction, especially near the hard-wall. However, this tilt is nullified significantly due to reflection from the metal wall. This is because in case of the edge-feed system, the electromagnetic wave radiated from the slot is reflected from the metal wall (*short edge*), which can be considered to act as another closely spaced source. In absence of the metal wall the electromagnetic wave would propagate freely in both directions, thereby significantly increasing the tilt. In absence of the metal wall, there is significant transverse component which is not desired for uniform power distribution as seen in fig.3.45.

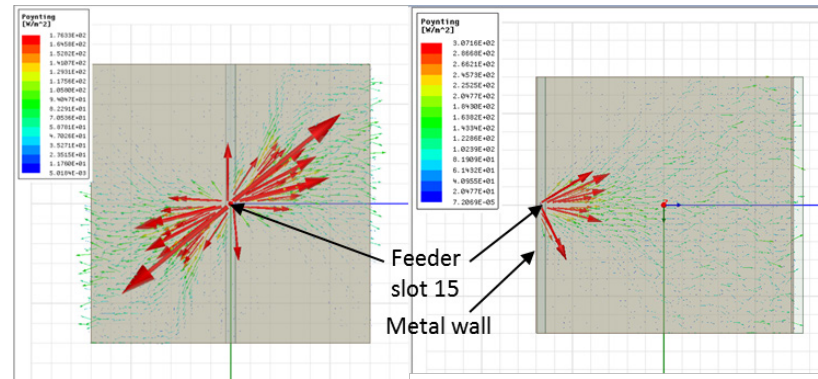


Fig. 3.45. Effect of Metallic Wall on Poynting Vector Distribution of Coupling Slot ‘N’

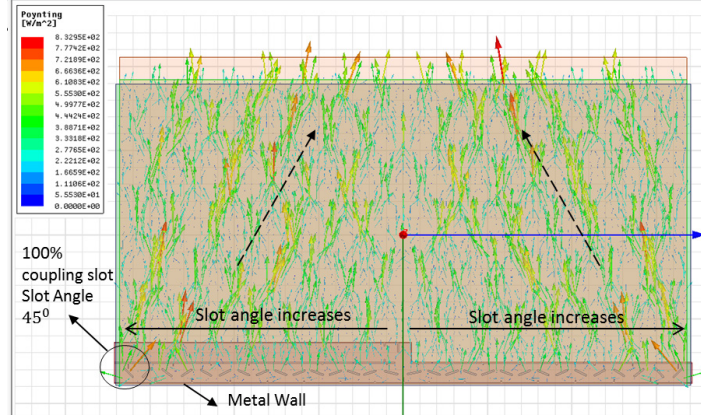


Fig. 3.46. Poynting Vector Distribution of Edge-feed Scheme of Panel 3

### 3.4 Corporate Center-feed Scheme

Although the edge-feed system is successful in enhancing the bandwidth, it requires two non- identical feeding waveguides for each antenna panel leading to structural complexity and difficulty in ensuring the mandatory condition of in-phase excitation by default. Thus, the corporate center-feed tournament network is proposed.

Fig.3.47 shows the deployed configuration of the antenna system. Notations ‘M’ (*for minus*) and ‘P’ (*for plus*) are used to denote the left wing and right wing of the satellite when viewed from front. Fig.3.48 shows the layered structure of outermost antenna panel of the satellite. The rectangular slotted waveguide feeder (WR90) is installed underneath the lower conducting plate. Power is fed through the input port. The waveguide feeder with the lowermost  $\tau$ -junction is placed at the center of each panel. The upper parallel plate antenna structure is identical as before.

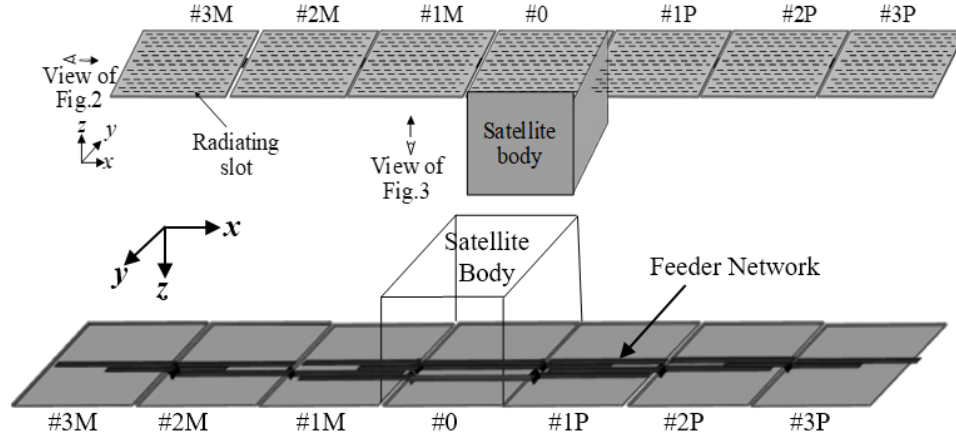


Fig. 3.47. Deployed Configuration of MicroX-SAR Satellite with Antenna

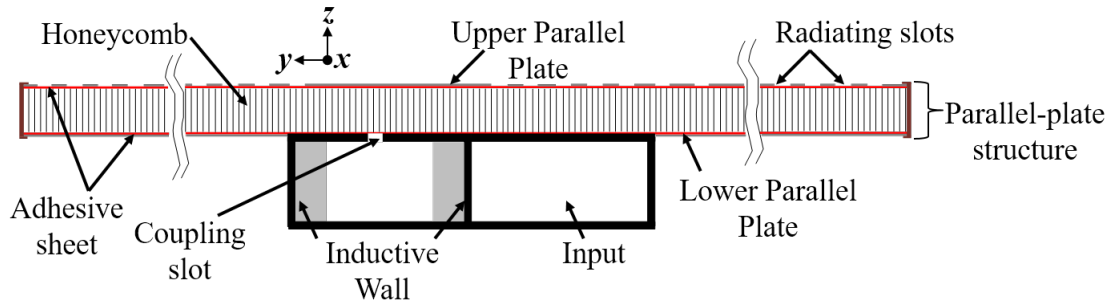


Fig. 3.48. Side-view of Layered Structure of Edge-feed Antenna Panel 3M

Fig.3.50 shows half of corporate feeder network tournament circuit, comprising of all panels [1]. Since the left wing and right wing are identical, we focus on design of the left wing. The feeding point (*Input port in fig.3.48*) is at the center of the antenna panel (*along range (y-direction) in fig.3.48*). With respect to the coupling slots, the effective feeding point inside the waveguide is at the center of the array of coupling slots, i.e. the window-center of the  $\tau$ -junction (*see fig.3.50*) which lies in the center of the antenna panel (*both along azimuth (x-direction) and elevation (y-direction)*). Hence, this feeding scheme is named center-feed.



The feeder of each panel consists of  $2N$  coupling slots,  $N$  on either side of the  $\tau$ -junction, where  $N=15$ . Since we desire uniform power to be transmitted throughout the 7 antenna panels, uniform power must be transmitted at each coupling slot for each panel. Thus, the power transmitted from each coupling slot is  $1/n$  where ‘ $n$ ’ is the slot number counted from the shortened end of the feeder. Panels 1M, 2M and 3M include the  $\tau$ -junction and comprise of 3 ports, 2 ports and 1 port respectively. Panel 2 has one additional layer of  $\tau$ -junction (without coupling slots) which functions as a simple 1:1 power divider. Panel 1 has two additional layers of  $\tau$ -junctions (without coupling slots). The first upper layer functions as a power divider with dividing ratio 2:1 and the uppermost layer functions as a power divider with dividing ratio 4:3. These upper layer power divider  $\tau$ -junctions cannot be placed at the center between two adjacent panels due to presence of the choke flange. Thus, they must be shifted such that the path difference to the panel centers on either side of the  $\tau$ -junctions is an integral multiple of  $\lambda_g$  in order to ensure in-phase excitation of all panels. This requirement makes the design challenging and unique. The coupling slot design and feeder length for panels 1M, 2M and 3M are identical. Panel 0 is the central panel fed from two ports and it is unique since it has no  $\tau$ -junction. All power fed from one port is consumed by the coupling slots on that side. Hence, because of symmetry, we have *Perfect Magnetic Conductor (PMC)* boundary condition instead of *Perfect Electrical Conductor (PEC)* boundary condition in the HFSS design model of panel 0. This also explains why the power dividing ratios of the two upper-layer  $\tau$ -junctions of Panel 1M are 2:1 and 4:3 respectively instead of 1:1 as in the case of Panel 2M. Since the design of coupling slots is identical for Panels 1M, 2M and 3M, in the following section we mainly

focus on Panel 3M and Panel 0. Fig.3.51 shows the HFSS Full Panel Simulation Model of Panel 3M and Panel 0 with coupling slots and radiation slots.

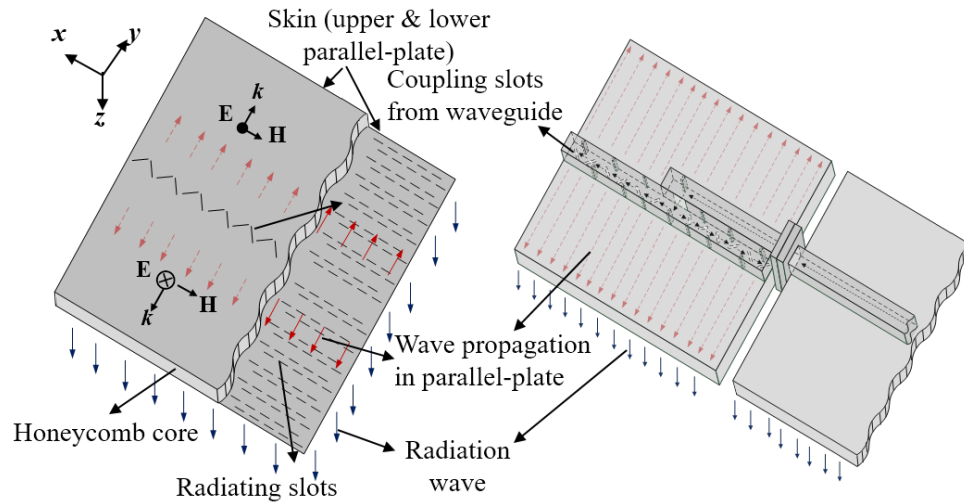


Fig. 3.49. Center-feed Design Model Schematic of Antenna Panel 3P

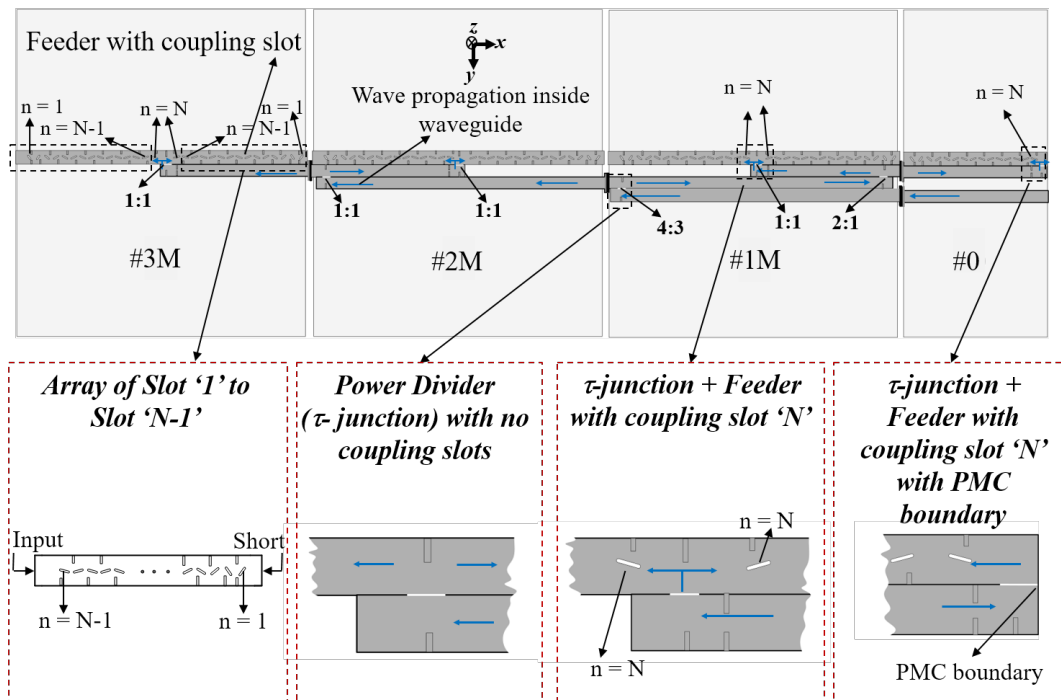


Fig. 3.50. Left Wing of Center-feed Antenna Network Tournament Circuit

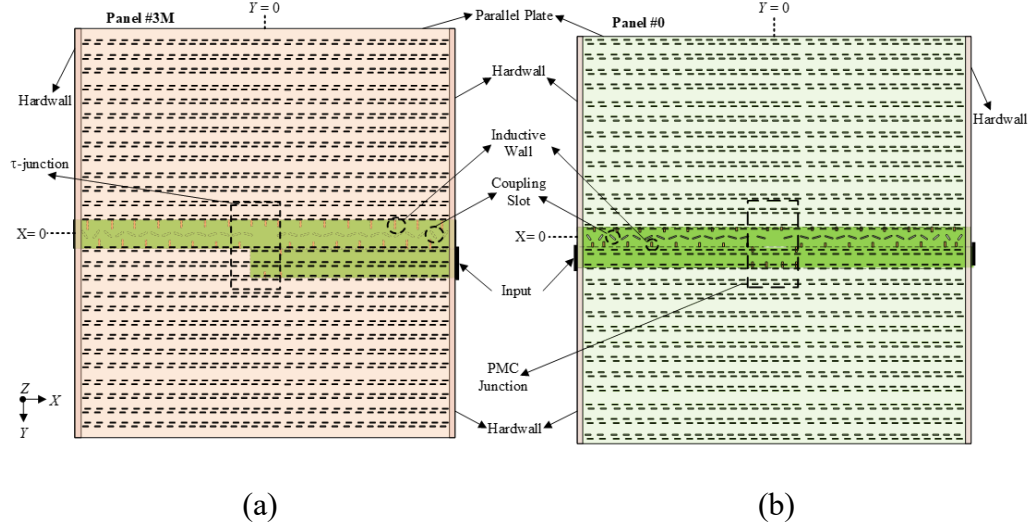


Fig. 3.51. Center-feed HFSS Full Panel Simulation Model of: (a) Panel 3M (b) Panel 0

### 3.4.1 Coupling Slots Design

Fig.3.52(a) and fig.3.52(b) show the HFSS design models of single coupling slot for coupling factors less than 100% (slot ‘2’ to slot ‘N-1’) and 100% coupling factor (slot ‘1’) respectively. Port 1 is the input port and ports 2, 3, 4 and 5 are the output ports. Although the design methodology is similar to the edge-feed scheme, there are differences in the impedance boundaries and the shortened end. Here, there is an additional port 4 in fig.3.52(a) instead of short end with metal wall. *(The additional port is for transmitting power in both directions unlike the edge-feed scheme.)* As RF power is fed through Port 1,  $TE_{10}$  mode is excited and propagates through the waveguide in the x direction. A portion of the power is deflected due to the coupling slot, which propagates through port 3 and port 4, while the remaining power is transmitted to port 2. The distance of port 1 and port 2 from the center of the coupling slot is  $\lambda_g$ . Irrespective of the slot length or slot angle, the power transmitted in ports 3 and 4 are equal in amplitude and 180 degrees out of phase. This is the key feature of the center-feed scheme, which ensures in-phase excitation and

overcomes the trouble of the edge-feed scheme. Fig.3.52(a) is used for designing slots up-to 50% coupling. It is desired that:

$$|S_{31}|^2 = |S_{41}|^2 = \frac{1}{2n}; \quad 2 \leq n \leq N - 1 \quad (3.18)$$

where 'n' is the slot number.

The factor '2' appears since power is deflected in both directions by each coupling slot. Each slot is preceded by an inductive wall for reflection cancelation. The edges of all slots are rounded with radius 1 mm while the edges of all inductive walls are rounded with 0.5 mm radius (not shown in the schematic) to avoid electromagnetic fringing effects at sharp edges. For 100% coupling slot design (slot '1'), fig.3.52(b) is used. Thus, Port 2 of fig.3.52(a) is replaced by short and distance of the short end from the slot-center is reduced to  $\frac{\lambda_g}{2}$ . Since the hard-wall is next to the 100% coupling slot, it will influence reflection and hence must be taken into consideration. Thus, port 3 and port 4 are replaced by impedance boundaries and the *Periodic Boundary Condition (PBC)* of fig 3.52(a) are replaced by *PMC* boundary conditions in fig3.52(b). In case of 100% coupling slots, it has two inductive walls as seen is fig3.52(b). This is because reflection is maximum for 100% coupling and simulations showed best reflection suppression for 2 walls (*of same length and at the same position but on opposite side*) for slot '1'. Fig.3.54 shows the variation of relative slot length (SL) and relative slot angle ( $\gamma$ ) with coupling factor w.r.t. to that of Slot '1'. Wall position is calculated as distance from the slot-center. If the wall is before the slot (as per convention) it is positive. In case of 100% coupling slots, it has two inductive walls as seen is fig.6b. This is because reflection is maximum for 100% coupling and simulations showed best reflection suppression for 2 walls (of same length and at the same position but on

opposite side) for Slot 1 as can be seen in fig.3.53 which shows the reflection profile of all the designed coupling slots.

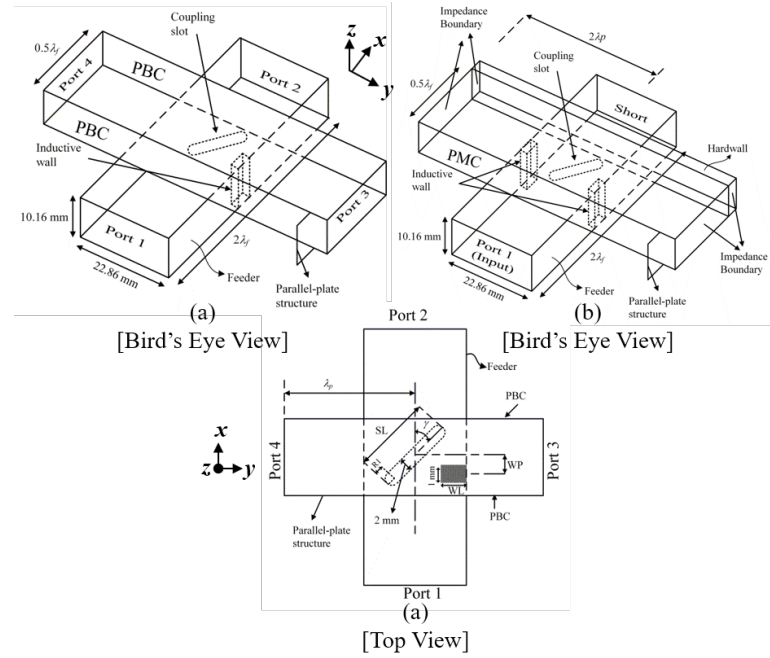


Fig. 3.52. Center-feed Single-slot HFSS Design Model for Coupling Factor: (a) < 100%  
(b) 100%

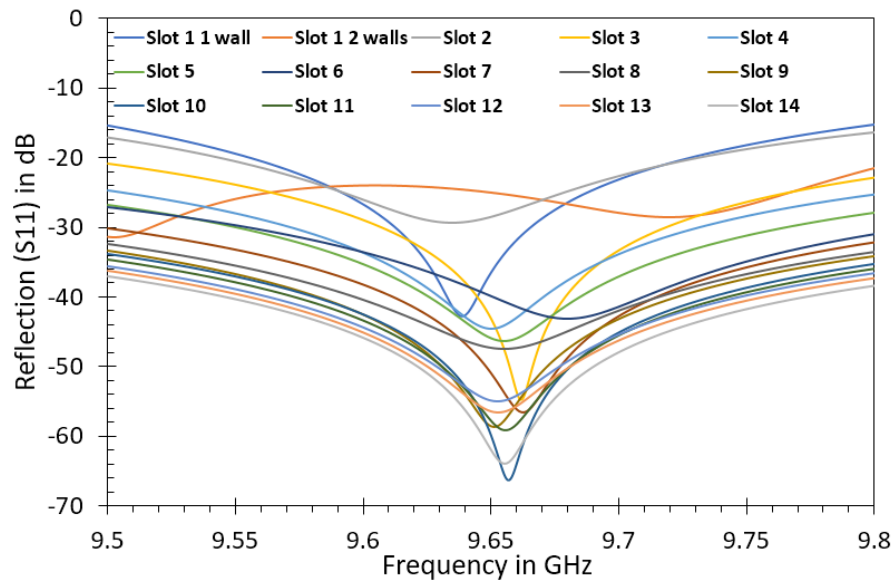


Fig. 3.53. Reflection Coefficient of Designed Center-feed Coupling Slots

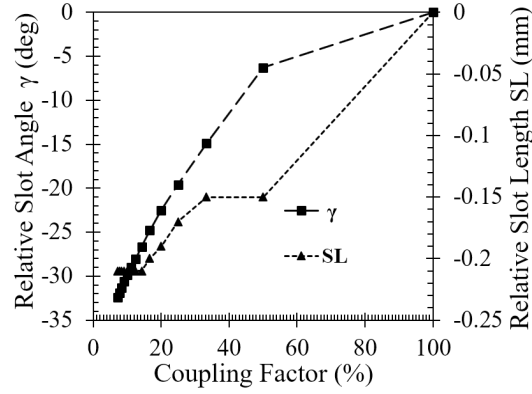


Fig. 3.54. Variation of Center-feed Coupling Slot Parameters with Coupling Factor

### Design of End-feed Array of 'N-1' Slots

An end-feed array of 'N-1' slots is simulated, and the slot positions are optimized using equations like before to get in-phase excitation. Fig.3.55(a) shows the HFSS model and fig.3.55(b) shows the slot separation distance after optimization. Fig.3.56, fig.3.57 and fig.3.58 show the optimized amplitude, phase and  $S_{11}$  respectively. The design of coupling slots '1' to 'N-1' is identical for all panels.

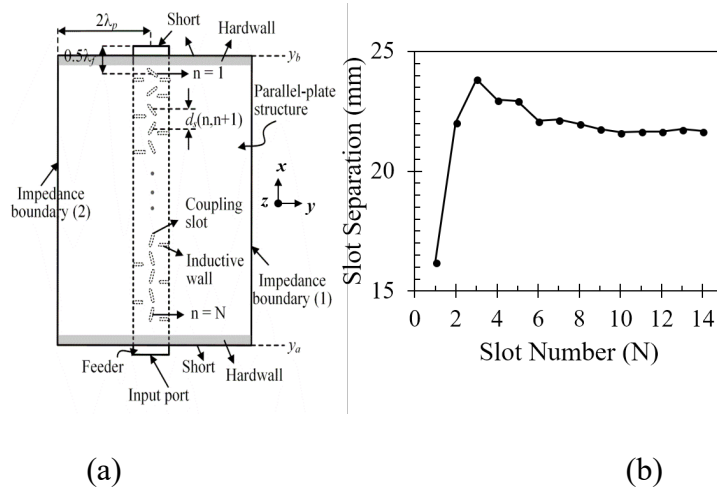


Fig. 3.55. (a) HFSS End-feed 'N-1' slots Design Model and (b) Optimized Slot

Separation for Center-feed Scheme

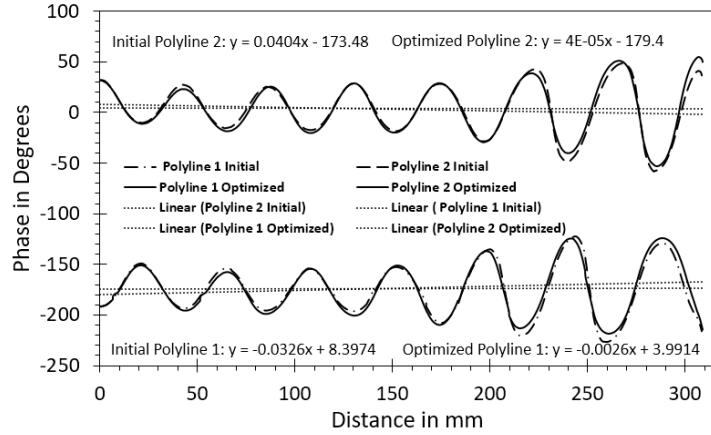


Fig. 3.56. Phase Distribution of End-feed Array of 'N-1' Slots for Center-feed Scheme

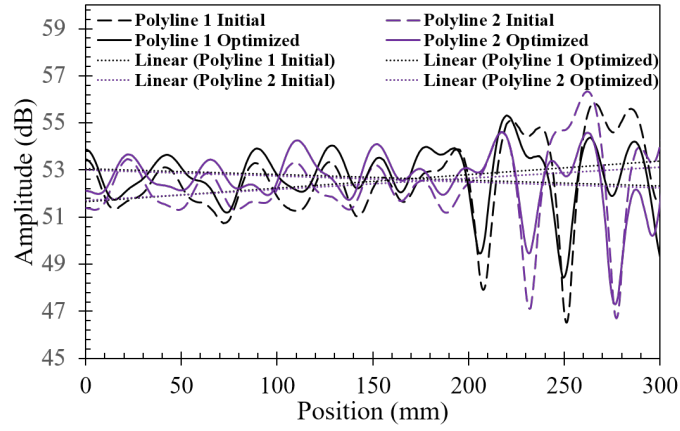


Fig. 3.57. Amplitude Distribution of 'N-1' Slots Array for Center-feed Scheme

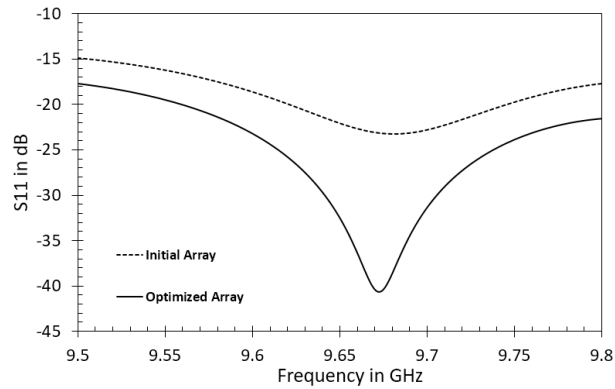


Fig. 3.58. Reflection Coefficient of End-feed Array of 'N-1' Slots of Center-feed Scheme

### 3.4.2 Edge Panel Feeder Design

- *Design of Slot ‘N’ and Slot ‘N-1’ with Modified  $\tau$ -junction*

Fig.3.59(a) shows the HFSS design model for slot ‘N’ with the  $\tau$ -junction with double-resonance inductive walls. Power is fed through port 1 (input). The electromagnetic wave propagates in the x direction, and after reflection at the shortened end of the  $\tau$ -junction, it propagates in -y direction through the window. The window center position determines the power dividing ratio. The  $\tau$ -junction is designed as a 1:1 simple power divider as done for edge-feed scheme. A part of the power is then deflected by the two coupling slots and this power is received at ports 4, 5, 6 and 7. The remaining power is transmitted to port 2 and port 3. It is desired that:

$$|S_{41}|^2 = |S_{51}|^2 = |S_{61}|^2 = |S_{71}|^2 = \frac{1}{4N}, \quad (3.19)$$

$$|S_{21}| = |S_{31}| \quad (3.20)$$

$$\angle S_{41} = \angle S_{51}, \angle S_{61} = \angle S_{71}, \angle S_{21} = \angle S_{31} \quad (3.21)$$

$$\angle S_{41} - \angle S_{61} = \angle S_{51} - \angle S_{71} = \pm 180^\circ \quad (3.22)$$

Equation (3.22) is satisfied by the default center-feed design scheme. Since slot ‘N’ is near the  $\tau$ -junction, it cannot be designed in the usual way as done in Section A.1. Furthermore, although both the slots on either side of the  $\tau$ -junction have the same coupling factor, their design parameters (slot length, slot angle) are not identical as seen in Table 3.8. This is because as the electromagnetic wave bends after being reflected from the shortened end of the  $\tau$ -junction, higher modes are excited near the window and hence its propagation dynamics to the left and right is not identical. Since the two coupling slots are located very close to the window, their design is affected by these higher excitation modes.



Thus, the distance between the centers of the two slots is carefully adjusted to ensure equal amplitude and equal phase in port 4 and port 5. The reflection profile after design optimization is shown in fig.3.68. The window length is initially set to  $\frac{\lambda_g}{2}$  and then optimized to get the best reflection profile.

Fig.3.59(b) shows the HFSS design model for slot ‘N’ and slot ‘N-1’ with the  $\tau$ -junction. Although phase balance condition has been achieved in Section A.2, it is necessary to ensure in-phase condition between slot ‘N’ and slot ‘N-1’ separately using the 4-slot HFSS model. This is done to avoid the phase balance problem (dip or overshoot) at the center of the feeder near the junction as seen in fig.3.30 and fig.3.37 in the edge-feed scheme. The reflection profile after optimization is shown in fig.3.63 Table 3.9 shows the modified design parameters after optimization.

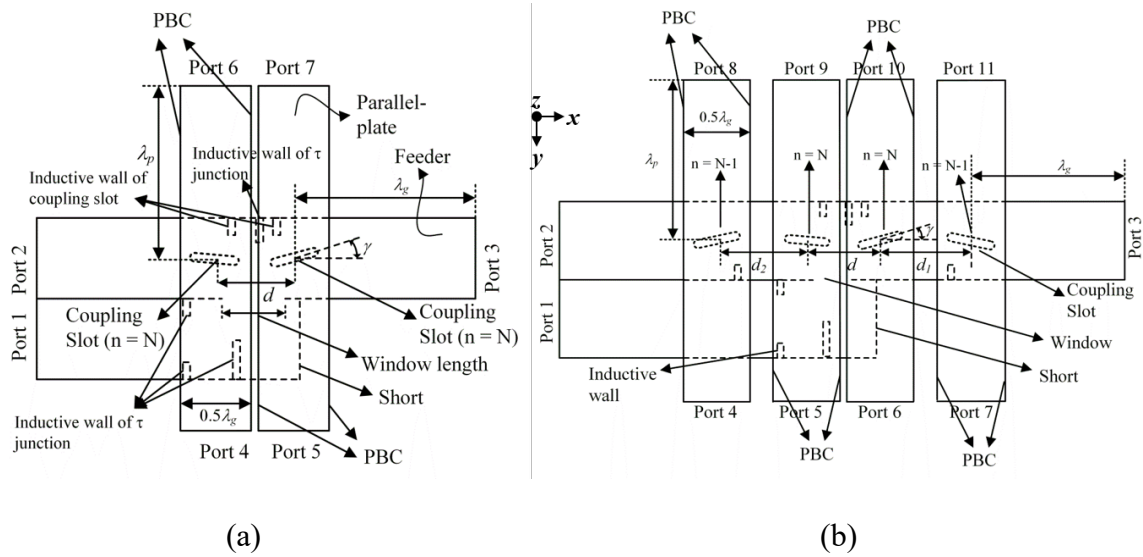


Fig. 3.59. HFSS Design Model with  $\tau$ -junction for Center-feed Scheme of (a) Slot ‘N’ and (b) Slot ‘N’ and Slot ‘N-1’

Table 3.8. Designed Parameters of Slot ‘N’ with  $\tau$ -junction of Center-feed Scheme

Slot Specification	SL (mm)	$\gamma$ (deg)	WL (mm)	WP (mm)	Slot Separation d (mm)
Slot 15 - Left	14.65	173.4	2	-5	23.18
Slot 15 - Right	15.25	16.2	2	-5	
Parameter	S <sub>41</sub>	S <sub>51</sub>	S <sub>61</sub>	S <sub>71</sub>	Window Length (mm)
Amplitude (dB)	-17.71	-17.67	-17.8	-17.75	18
Phase (deg)	-176	-177	3	4	

Table 3.9. Design Parameters of Slot ‘N’ and Slot ‘N-1’ with  $\tau$ -junction of Center-feed

Parameter	S <sub>41</sub>	S <sub>51</sub>	S <sub>61</sub>	S <sub>71</sub>	d (mm)
Amplitude (dB)	-17.68	-17.74	-17.54	-17.64	23.18
Phase (deg)	-60	-59	-59	-58	d <sub>1</sub> (mm)
Parameter	S <sub>81</sub>	S <sub>91</sub>	S <sub>10-1</sub>	S <sub>11-1</sub>	28.38
Amplitude (dB)	-17.77	-17.81	-17.54	-17.63	d <sub>2</sub> (mm)
Phase (deg)	120	120	120	121	28.38

- *Design of Full Feeder with ‘2N’ Slots*

Fig.3.60 shows the HFSS design model of the full feeder with the modified  $\tau$ -junction, formed by cascading the optimized models in section A.3 and section A.4. 1 W RF power is fed to the input port. Fig.3.61 and fig.3.62 respectively show the relative amplitude and phase distribution of the Electric field in the z-direction (measured end-to-end by two polylines on opposite sides in the impedance boundary layers in the middle of

the honeycomb core. A 2<sup>nd</sup> order polynomial trend-line (shown as dotted lines in fig.3.61) and fig.3.62) is used on each polyline to determine its constant amplitude and phase). The constant amplitude levels are nearly equal, with a deviation of only 0.2 dB as seen in fig.3.61. The phase profile is flat as desired. There is a constant phase difference of nearly 180 degrees between the two trend-lines, as seen in fig.3.62. This condition is essential to ensure in-phase excitation. Thus, there is no need to move the radiation slots along the y-direction as required in the edge-feed scheme. Fig.3.63 shows the reflection characteristics of the full-feeder. Good  $S_{11}$  below -20 dB is achieved throughout the 300 MHz bandwidth, thereby ensuring wideband performance as desired.

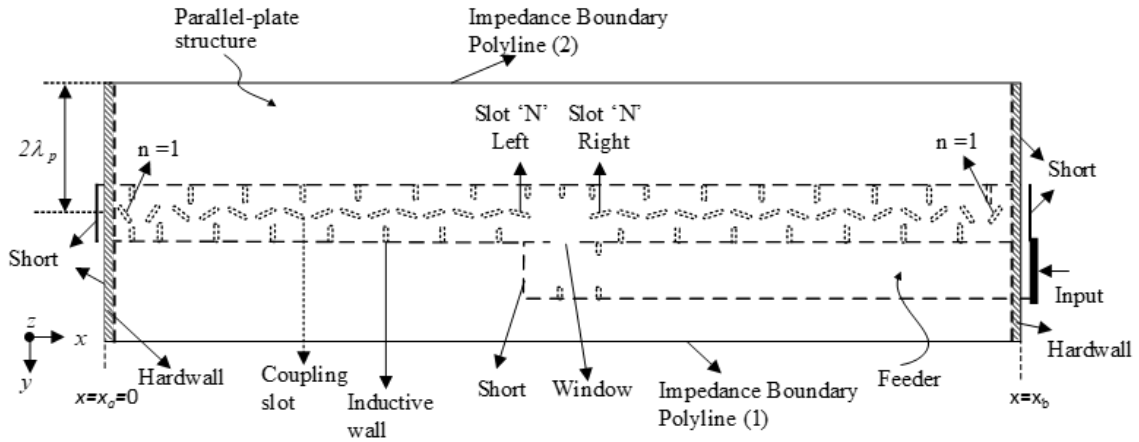


Fig. 3.60. Center-feed Full Feeder HFSS Design Model of Panel 3M

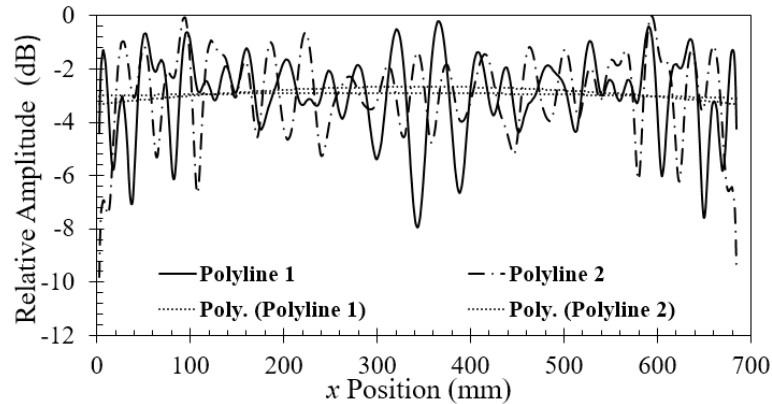


Fig. 3.61. Center-feed Full Feeder Simulation Amplitude Distribution of Panel 3M

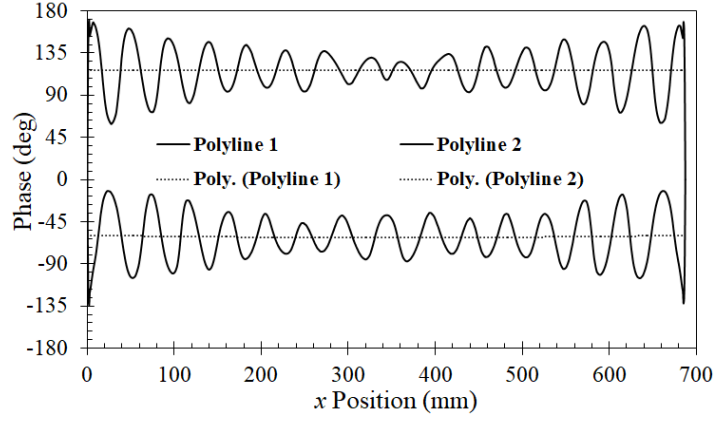


Fig. 3.62. Center-feed Full Feeder Simulation Phase Distribution of Panel 3M

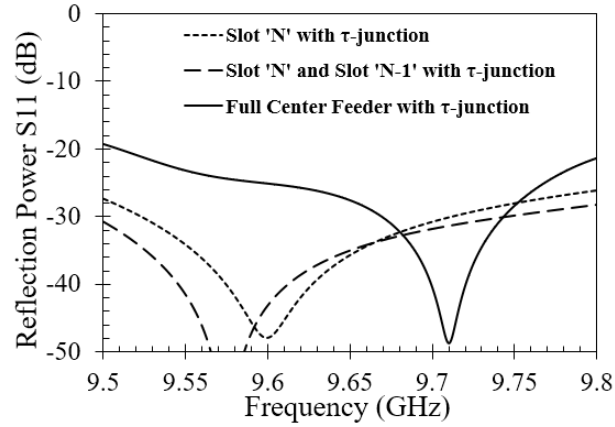


Fig. 3.63. Simulation Reflection Coefficient of Center-feed Feeder of Panel 3M

### 3.4.3 Center Panel Feeder Design

- *Design of Slot 'N and Slot 'N-1' with PMC-junction*

The center panel (Panel 0) on the satellite body has two input ports and no  $\tau$ -junction as shown in fig.3.51(b). Hence, slot 'N' must be designed separately with PMC boundary condition instead of short end of the  $\tau$ -junction to mirror an identical input port. The only difference with Panel 3 feeder is that there is no power divider; hence the factor

$\frac{1}{2N}$  appears in equation (3.23). The HFSS design model for slot ‘N’ and slot ‘N-1’ with PMC boundary condition is shown in fig.3.64. Table 3.10 and Table 3.11 show the design parameters of Slot ‘N’ and Slot ‘N-1’. The reflection profile is shown in fig.3.71. It is desired that:

$$|S_{31}|^2 = |S_{41}|^2 = |S_{51}|^2 = |S_{61}|^2 = \frac{1}{2N} \quad (3.23)$$

$$\angle S_{31} = \angle S_{51}, \angle S_{41} = \angle S_{61} \quad (3.24)$$

$$\angle S_{31} - \angle S_{41} = \angle S_{51} - \angle S_{61} = \pm 180^\circ \quad (3.25)$$

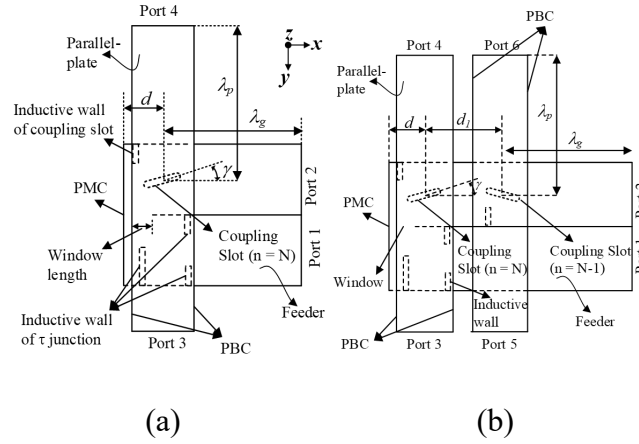


Fig. 3.64. HFSS Design Model with PMC-junction for Center-feed Scheme of (a) Slot ‘N’ and (b) Slot ‘N’ and Slot ‘N-1’

Table 3.10. Design Parameters of Slot ‘N’ with PMC-junction of Center-feed Scheme

Slot Specification	SL (mm)	$\gamma$ (deg)	WL (mm)	WP (mm)
Slot ‘N’	15.5	16.8	6	10
Parameter	$S_{31}$	$S_{41}$	d (mm)	Window Length (mm)
Amplitude (dB)	-14.67	-14.76	13	9
Phase (deg)	-171	-9		

Table 3.11. Design Parameters of Slot ‘N’ and Slot ‘N-1’ with PMC-junction

Slot Specification	SL (mm)	$\gamma$ (deg)	WL (mm)	WP (mm)	d (mm)
Slot ‘N’	14.65	173.4	2	-5	13
Slot ‘N-1’	15.25	16.2	2	-5	
Parameter	S <sub>31</sub>	S <sub>41</sub>	S <sub>51</sub>	S <sub>61</sub>	d <sub>1</sub> (mm)
Amplitude (dB)	-14.73	-14.82	-14.86	-14.86	28.18
Phase (deg)	107	-73	108	-72	

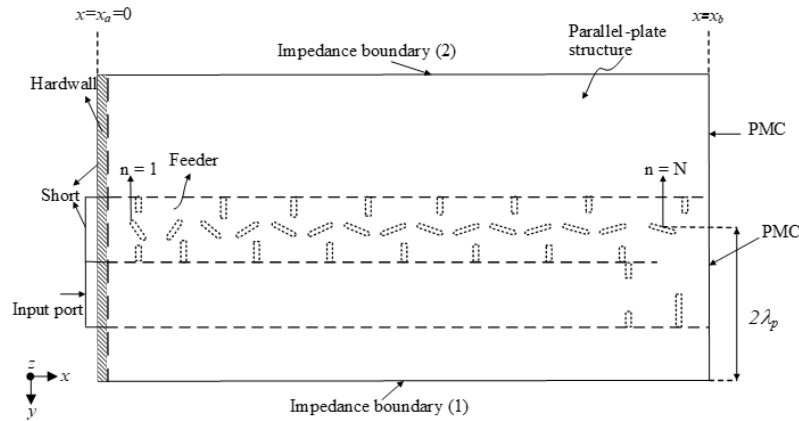


Fig. 3.65. HFSS Half-Feeder Design Model with PMC-junction for Center-feed Scheme

- *Design of Half Feeder with ‘N’ Slots and PMC-junction*

Fig.3.65 shows the HFSS design optimization model for one-half of Panel 0 feeder with PMC boundary condition, constructed by cascading the optimized end-feed slot-array model 3.55(a) with fig.3.64(b). 0.5W RF power is fed to the input port. Fig.3.66 and fig.3.67 respectively show the amplitude and phase distribution. Fig.3.71 shows the reflection characteristics.

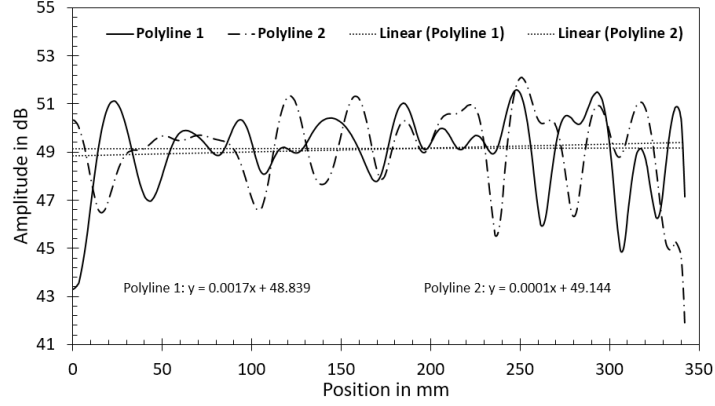


Fig. 3.66. Center-feed Half Feeder Simulation Amplitude Distribution of Panel 0

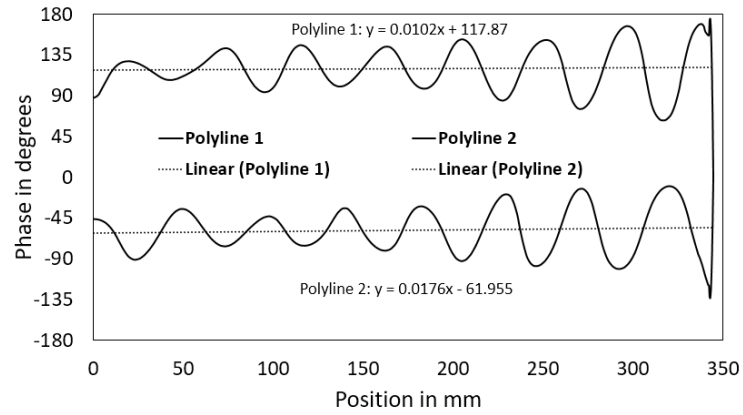


Fig. 3.67. Center-feed Half Feeder Simulation Phase Distribution of Panel 0

- *Design of Full Feeder with '2N' Slots*

Fig.3.68 shows the HFSS design model of full feeder of panel 0 replacing PMC boundary condition with symmetric mirroring. 0.5 W RF power is fed through the two input ports port 1 and port 2 each. Fig.3.69 and fig.3.70 respectively show the relative amplitude distribution and phase distribution of  $E_z$ . Fig.3.71 shows the reflection characteristics. There is good reciprocity and symmetricity and Active  $S_1$  is identical to  $S_{11}$  of half-feeder, which confirms the working principle of design with PMC boundary. The

difference between the constant trendline phases of polyline 1 and polyline 2 is roughly 180 degrees as expected and desired. The constant trendline levels of amplitude and phase in the two polylines are also equal to that of Panel 3 feeder. This is essential since all the panels must be excited with the same phase and same amplitude for uniform excitation. This is achieved by careful design and not by default since the feeder length of panel 0 is different (*longer by 1.62 mm*) than that of panels 1M, 2M and 3M due to different design structure in the center, as summarized in Table 3.12.

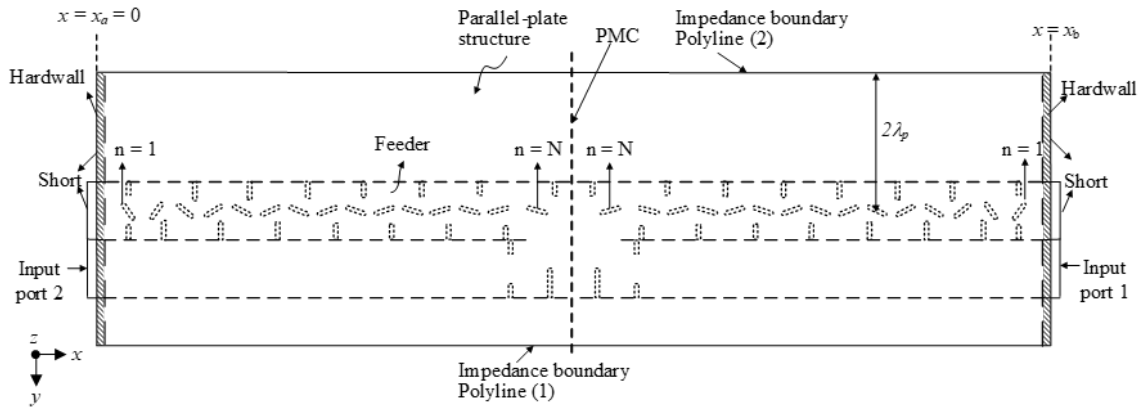


Fig. 3.68. Center-feed Full Feeder HFSS Design Model of Panel 0

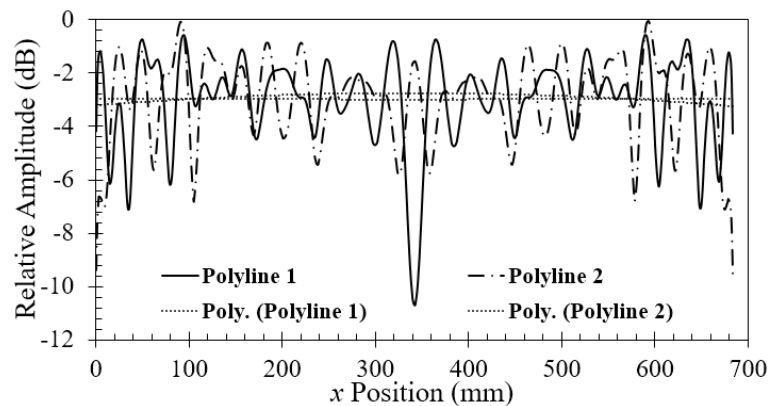


Fig. 3.69. Center-feed Full Feeder Simulation Amplitude Distribution of Panel 0



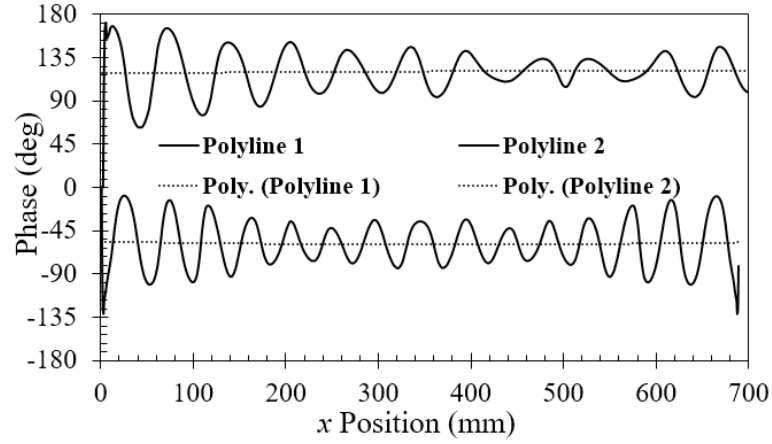


Fig. 3.70. Center-feed Full Feeder Simulation Phase Distribution of Panel 0

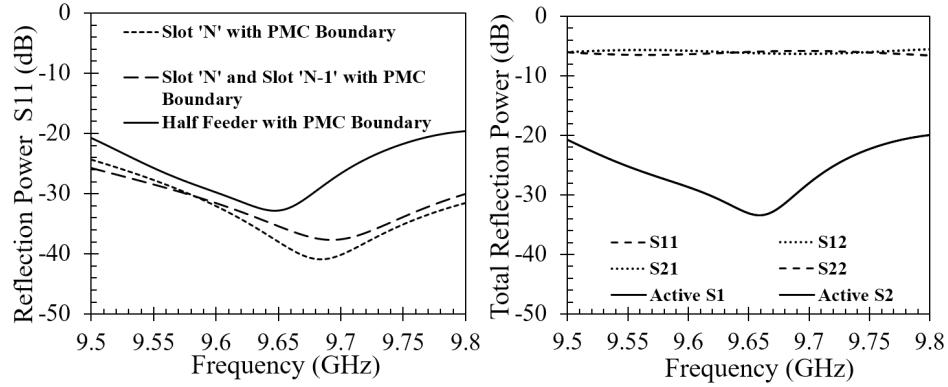


Fig. 3.71. Simulation Reflection Coefficient of Center-feed Feeder of Panel 0

- *Poynting Vector Analysis*

It is interesting to study the Poynting vector simulations to compare electromagnetic field propagation for the center-feed system in comparison to the edge-feed system and using one half-panel antenna without the radiating slots (*since the effect of radiating slots are identical for edge-feed and center-feed system*). Fig.3.73 shows the Poynting vector distribution inside the half-panel parallel-plate structure of center-feed system. As in the case of the edge-feed system, we see that the slot angle increases from the panel center towards the hard-wall. Larger the slot angle, greater is the tilt of the



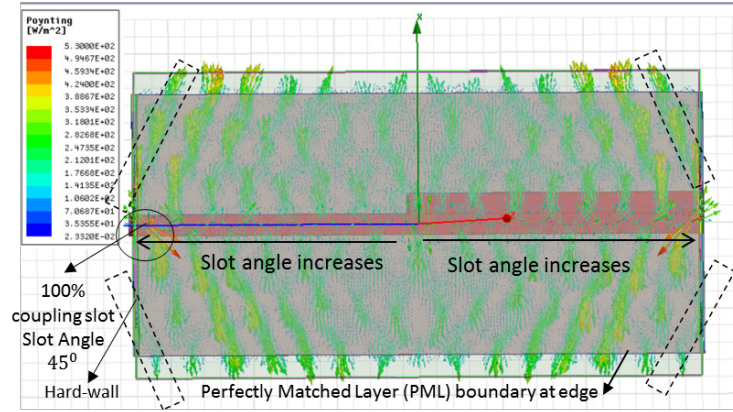


Fig. 3.73. Poynting Vector Distribution of Center-feed Scheme of Panel 3M

Table 3.12. Center Feeder Design Summary of Antenna Panels

Feeder Type	Length (mm)	Amplitude at $f_0$ (dB)		Phase at $f_0$ (deg)	
		Polyline 1	Polyline 2	Polyline 1	Polyline 2
$\tau$ -junction for Panels 3,2,1	688.84	-3.0	-3.3	118.9	-59.4
PMC-junction for Panel 0	690.46	-3.0	-3.2	119.4	-58.7

#### 3.4.4 $N\lambda$ Offset Tournament Feeder Network Design of Upper Layer $\tau$ -junctions

Fig.3.74 shows the HFSS simulation model of the upper layer  $\tau$ -junctions shown in Fig.3.50. Power is fed through T-junction which feeds Panel 1M and Panel 1P on either side. Since we focus on design of the left wing, the input Port 1 position in fig.3.74 is taken after the T-junction output which feeds Panel 1M. Panel 1M feeds Panel 2M and Panel 0 and Panel 2M feeds Panel 3M. Ports 2, 3, 4 and 5 denote the power inputs to Panels 0 (half), 1M, 2M and 3M respectively. The upper  $\tau$ -junction layers  $J_1$ ,  $J_2$  and  $J_3$  must be

carefully designed to ensure equal power arrives at all panels in the same phase. Thus, the desired power dividing ratios at  $J_1$ ,  $J_2$  and  $J_3$  are 2:1.5 (4:3 for  $J_3:J_2$ ), 1:0.5 (2:1 for Port 3 : Port 2) and 1:1 (for Port 5 : Port 4 ) respectively as shown in fig.3.74. Thus, w.r.t. input Port 1, the desired power levels at Ports 2, 3, 4 and 5 are  $1/7$ ,  $2/7$ ,  $2/7$  and  $2/7$  respectively with the same phase. First,  $\tau$ -junctions (*without coupling slots*) is designed for desired power dividing ratios. As an example, fig.3.75 shows the design model of  $J_1$   $\tau$ -junction and fig.3.81 shows the design simulation results.

Then,  $J_1$ ,  $J_2$  and  $J_3$  are connected (*via flat flange and choke flange to simulate the real antenna condition of gap between adjacent panels*) to comprise the  $3\frac{1}{2}$  panel model (*Panels 1M, 2M, 3M and half of Panel 0*) excluding coupling slots with PMC boundary to simulate identical symmetric wing as shown in fig.3.74. The position of the window and inductive walls are carefully adjusted to ensure in-phase excitation to each panel. Ports 2, 3, 4 and 5 are located at the same distance from the center of Panels 0, 1M, 2M and 3M respectively. Fig.3.76 shows the transmitted power and phase. In-phase uniform excitation is achieved as desired.

For further verification, the coupling slots are added to all the feeders in the HFSS design model in fig.3.78 and the HFSS simulation results in fig.3.79, fig.3.80 and fig.3.81 show in-phase uniform excitation with low reflection coefficient as desired.

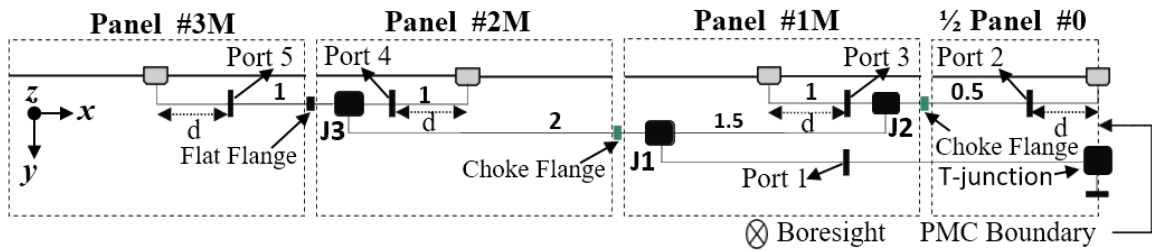


Fig. 3.74. Schematic of Center-feed Power Divider Network Design with  $\tau$ -junctions

**‘Nλ-Offset’ Design Condition:**

$$J_3 P_5 - J_3 P_4 = N\lambda$$

$$J_2 P_2 - J_2 P_3 = N\lambda$$

$$J_1 J_3 - J_1 J_2 = N\lambda$$

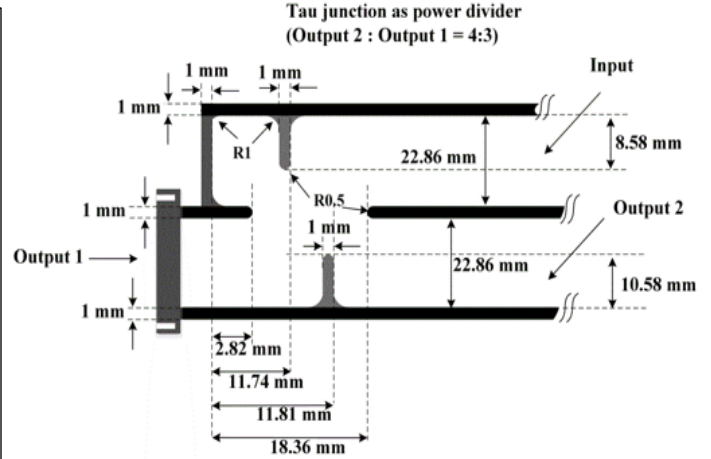


Fig. 3.75. Power Divider  $\tau$ -junction  $J_1$  Design Schematic

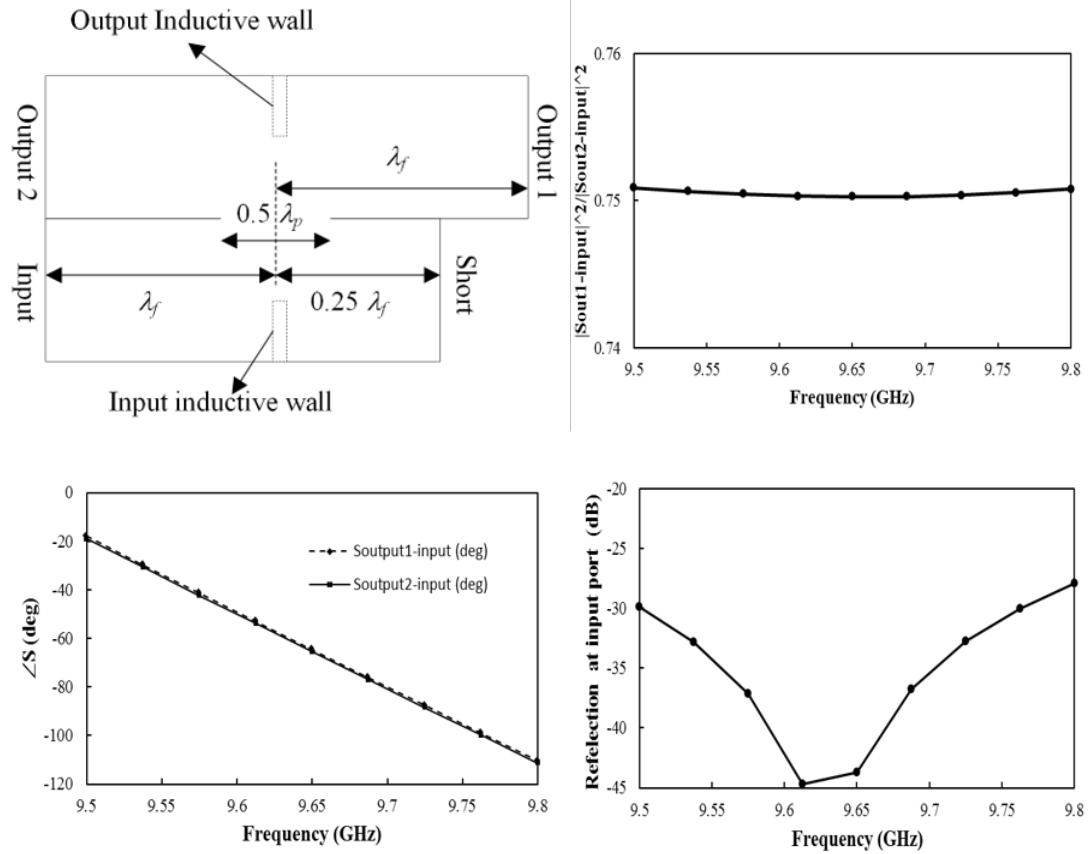


Fig. 3.76. Optimized Design Parameters of Power Divider  $\tau$ -junction  $J_1$

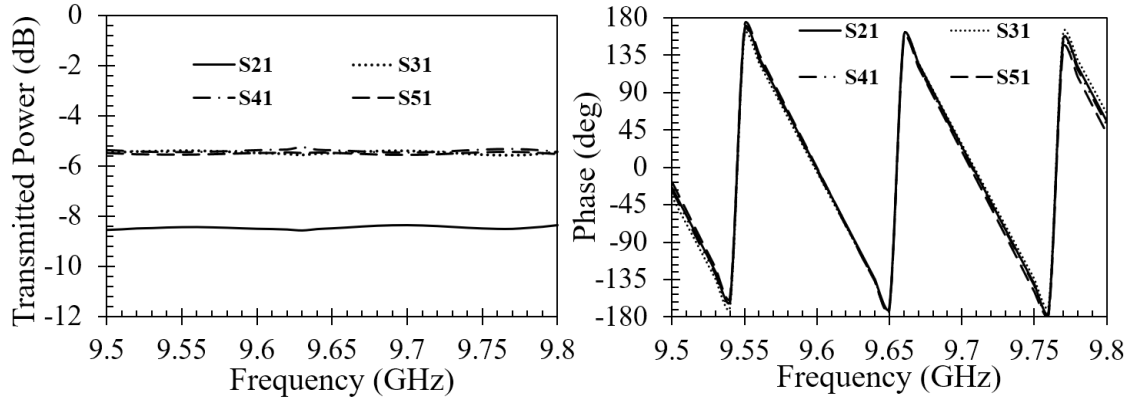


Fig. 3.77. Transmission S Parameters Amplitude and Phase of Designed Power Divider Network

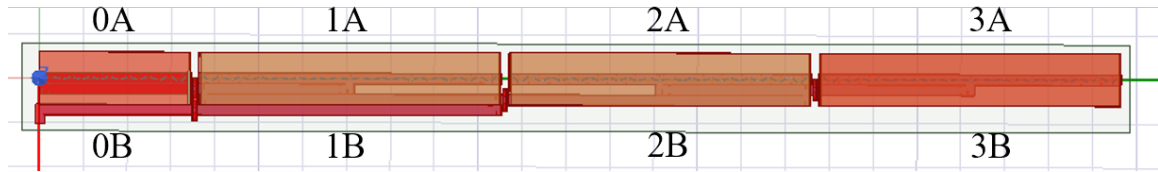


Fig. 3.78. HFSS Design Model of Power Divider Network with Coupling Slots

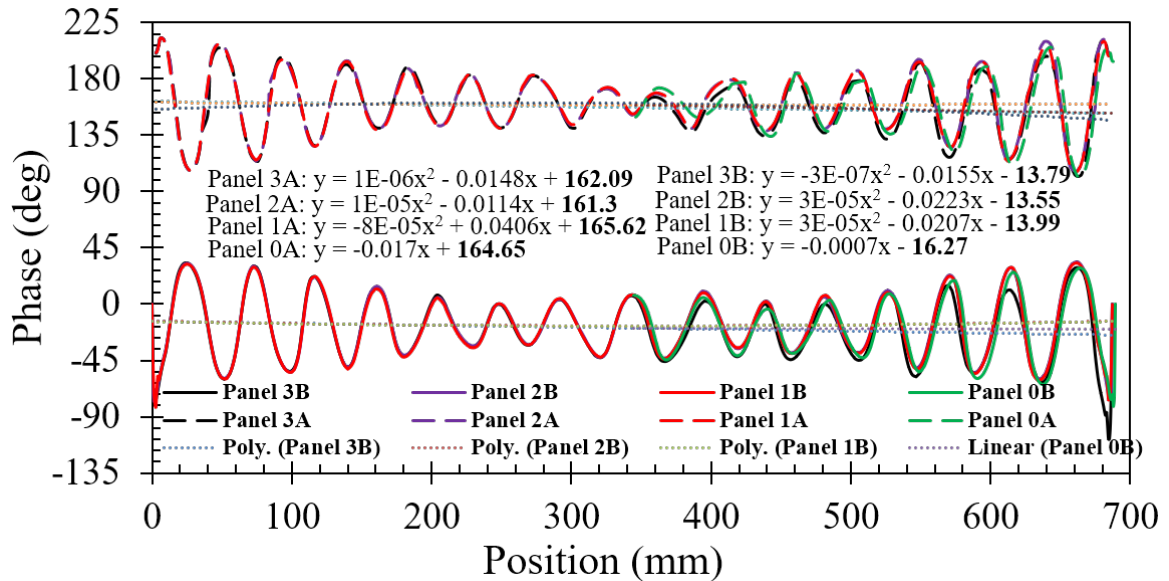


Fig. 3.79. Simulation Phase Distribution of Designed Power Divider Network with Coupling Slots



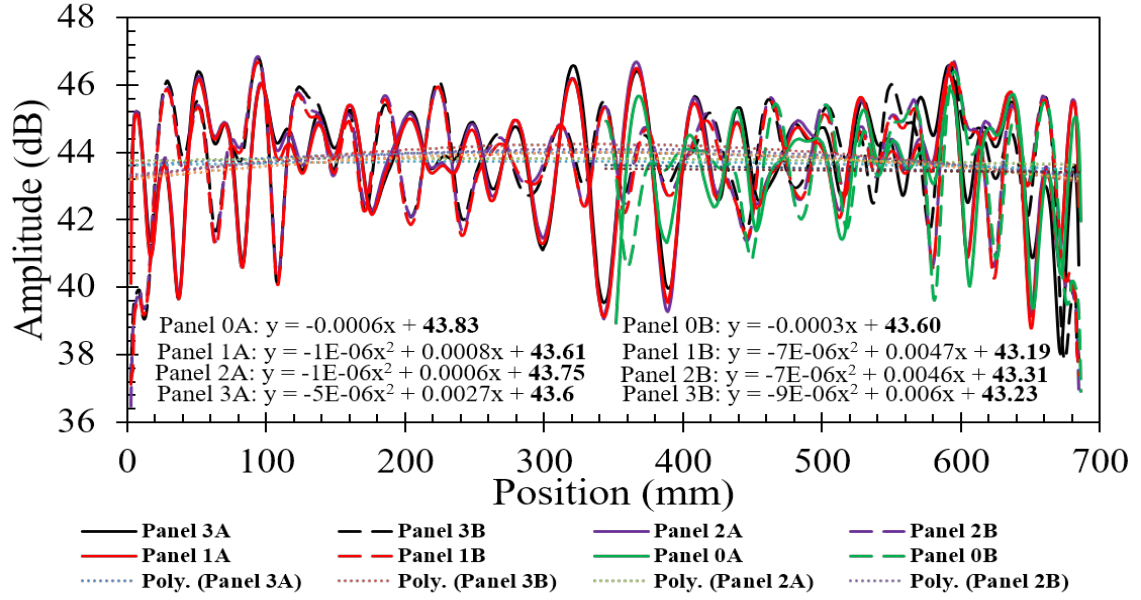


Fig. 3.80. Simulation Amplitude Distribution of Designed Power Divider Network with Coupling Slots

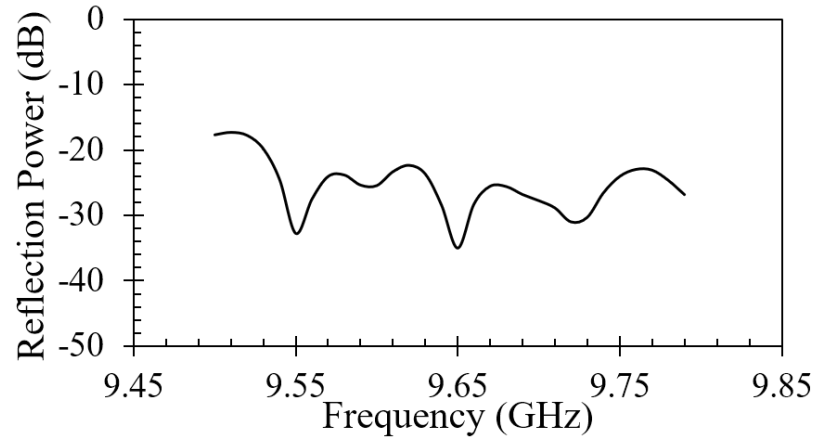


Fig. 3.81. Simulation Reflection Coefficient of Designed Power Divider Network with Coupling Slots

### 3.4.5 Full Panel Simulation Results of All Panels

Full panel antenna is simulated in HFSS including the waveguide feeders and the radiation slots designed in section. ‘Input’ corresponds to Port 1 for all panels. Simulation models of Panel 1M and Panel 2M are similar to fig.3.51(a) with additional upper  $\tau$ -junction layers. Fig.3.82 to fig.3.85 shows the simulated 2D normalized amplitude and phase

distributions of the Electric field in the y-direction ‘ $E_y$ ’ for all panels at center frequency (9.65 GHz). This data is manually obtained by placing a polyline along the feeder ( $y=0$ ) in the azimuth direction and changing its position along the y-direction (range) from -340 mm to +340 mm in steps of 10 mm. Fig.3.89 shows the simulated reflection S parameters. Reflection below -20 dB is achieved throughout the desired bandwidth for all panels. For Panel 2M, Port 2 is the output port which feeds the input port of Panel 3M in fig.3.50. For Panel 1M, Port 2 and Port 3 are the output ports which feed the input ports of Panel 2 and Panel 0 in fig.3.50. From the power dividing ratios shown in fig.3.50, the desired transmission power levels of Panel 1M are  $S_{21} = -2.4 \text{ dB}$  and  $S_{31} = -8.4 \text{ dB}$ , while that of Panel 2M is  $S_{21} = -3.0 \text{ dB}$ . The power dividing ratios are calculated from the S parameters of isolated simulations of Panel 1M and Panel 2M. Unlike fig.3.74 it neglects the influence of reflection from Panel 0 and Panel 3M (see fig.3.50). However, since the reflection levels are below -20 dB, their influence on the actual power dividing ratios is negligible. Full panel reflection profiles of Panel 3M and Panel 0 are nearly identical to that of the reflection profiles of their corresponding waveguide feeders seen in fig.3.63 and fig.3.71. Thus, it can be concluded that the reflection in full antenna panel primarily consists of reflection from the coupling slots in the waveguide feeder. Fig.3.86 and fig.3.87 show the simulated antenna patterns in range (y-z plane) and azimuth (x-z plane) at 9.65 GHz. Fig.3.88 shows the variation of peak directivity and antenna aperture efficiency ( $\eta_{ap}$ ) of all panels with frequency. Panel 1M and Panel 2M have longer feeder waveguide length than Panel 3M due to upper  $\tau$ -junction layers. So, due to long-line effect, they have higher losses. Thus, directivity and aperture efficiency of Panel 1M and Panel 2M are lower than Panel 3M. The simulation results are summarized in Table 3.13.



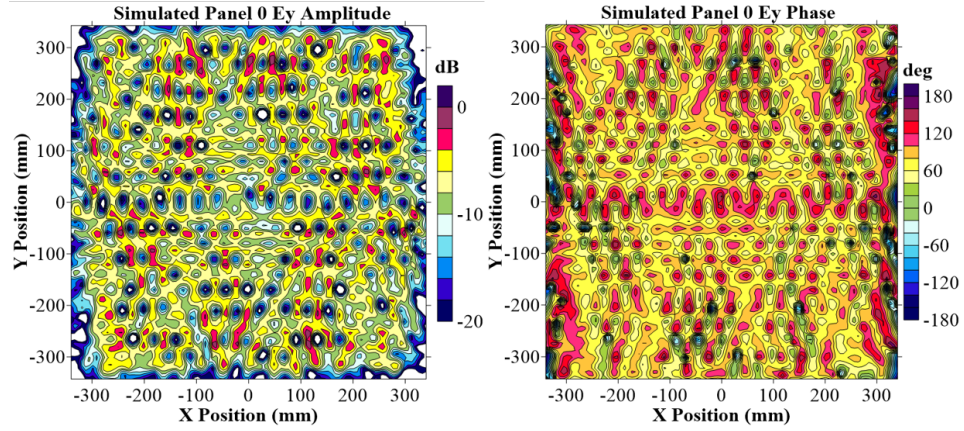


Fig. 3.82. Simulation Amplitude and Phase Distribution of Center-feed Panel 0

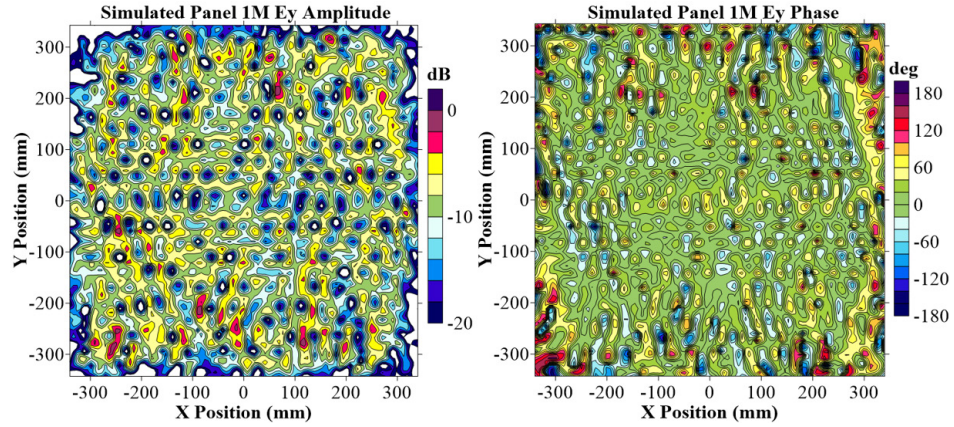


Fig. 3.83. Simulation Amplitude and Phase Distribution of Center-feed Panel 1M

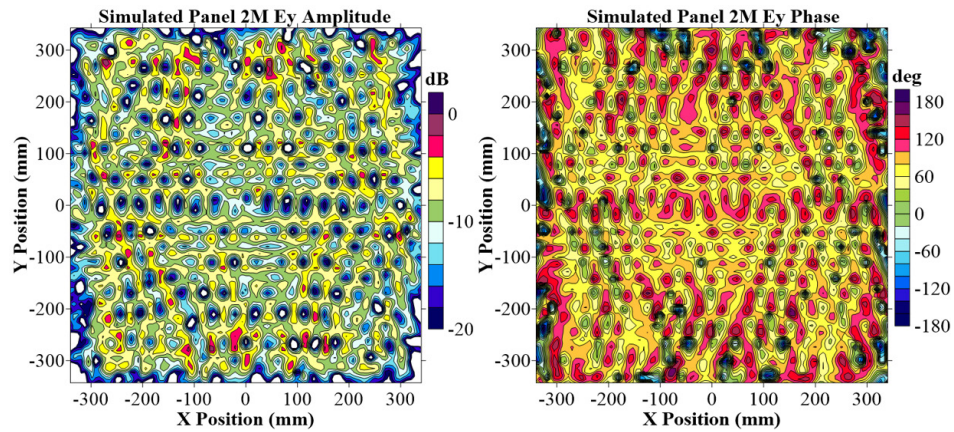


Fig. 3.84. Simulation Amplitude and Phase Distribution of Center-feed Panel 2M

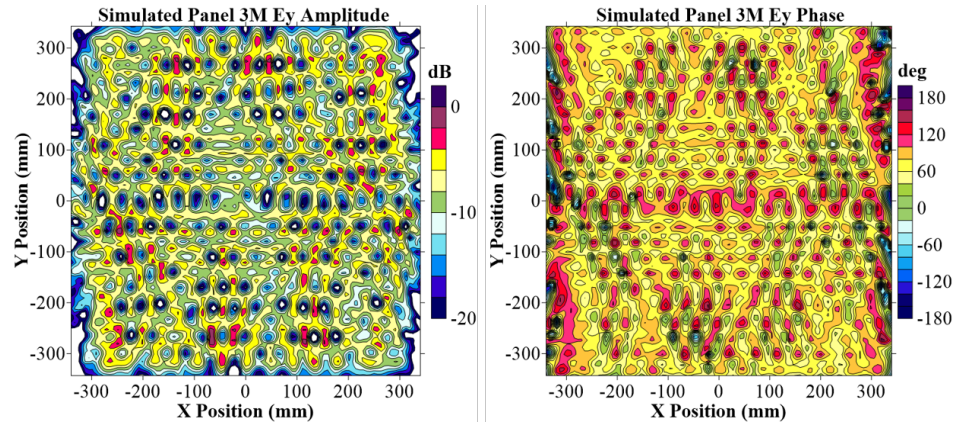


Fig. 3.85. Simulation Amplitude and Phase Distribution of Center-feed Panel 3M

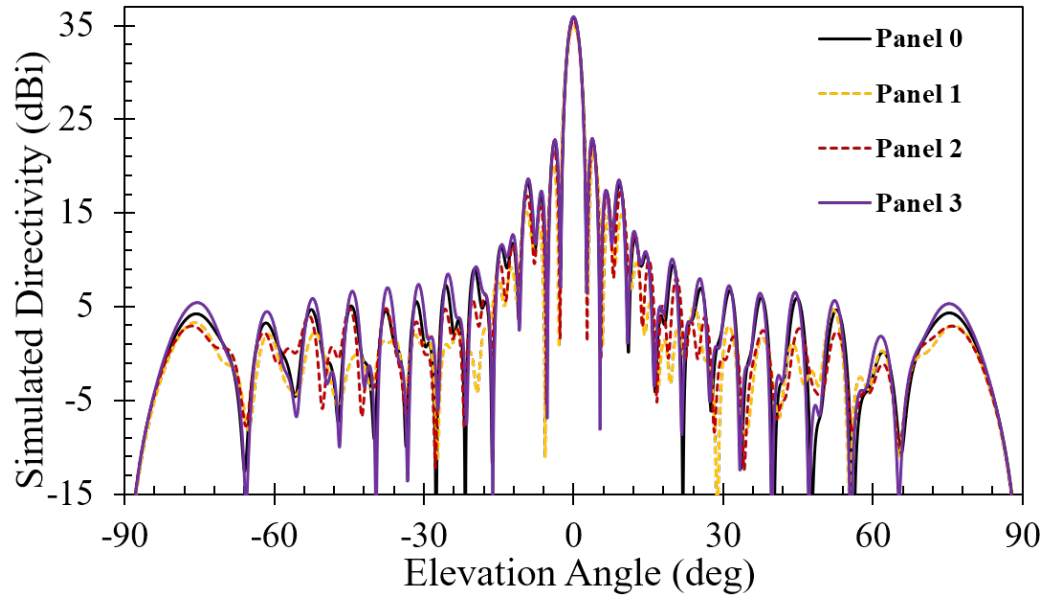


Fig. 3.86. Simulation Elevation Pattern of Center-feed Antenna Panels

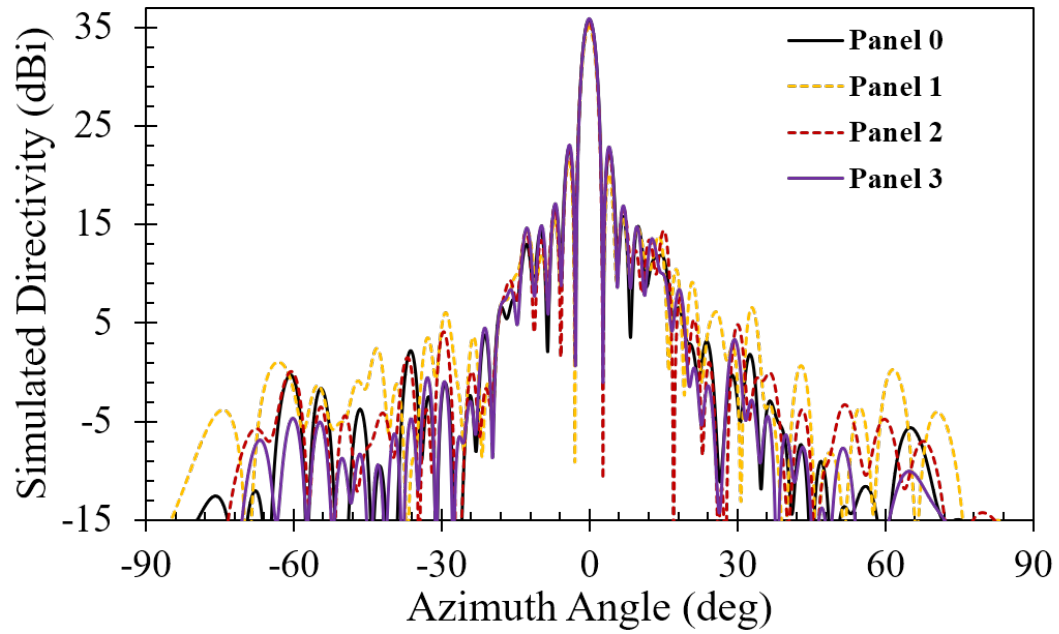


Fig. 3.87. Simulation Azimuth Pattern of Center-feed Antenna Panels

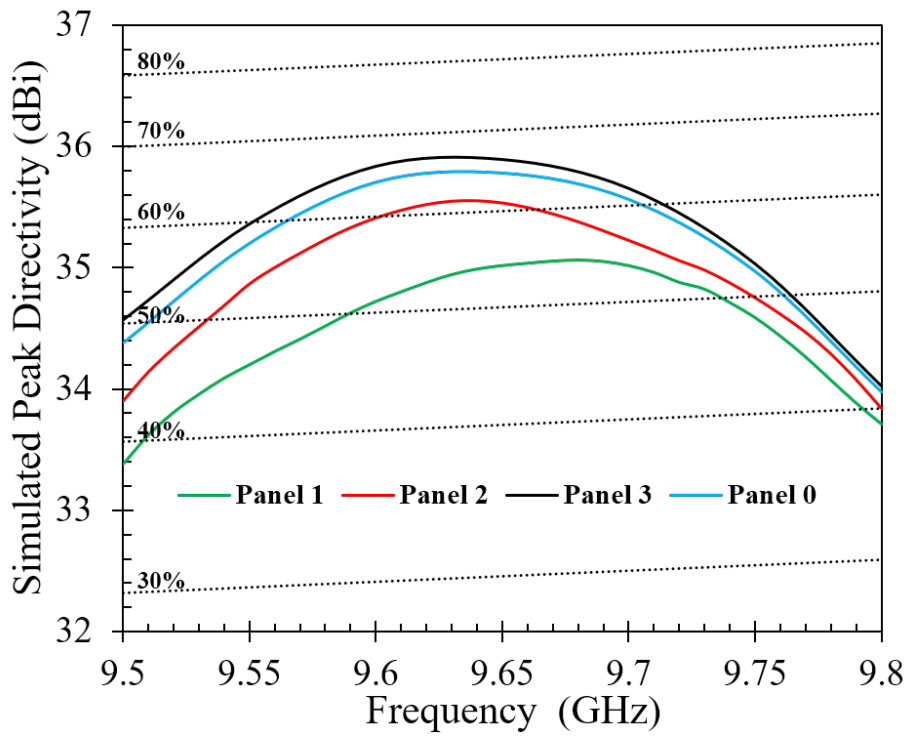


Fig. 3.88. Simulation Peak Directivity of Center-feed Antenna Panels

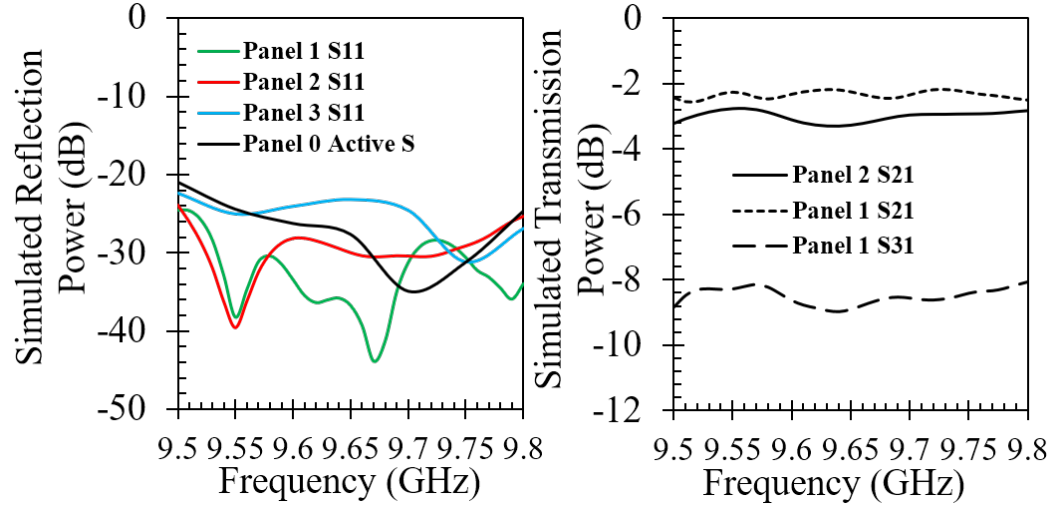


Fig. 3.89. Simulation S Parameters of Center-feed Antenna Panels

Table 3.13. Summary of Center-feed Full Panel Simulation Results

Parameter	Panel 0	Panel 1M	Panel 2M	Panel 3M
Peak Directivity (dBi)	35.8	35.1	35.6	35.9
Aperture Area (cm <sup>2</sup> )	4524.9	4513.9	4513.9	4513.9
Peak Aperture Efficiency (%)	64.3	54.3	61.3	66.2
Amplitude (Std. div) at $f_0$ (dB)	5.6	5.8	5.7	5.4
Phase (Std. div) at $f_0$ (deg)	50.4	54.5	59.6	46.5
Maximum Reflection in $f_{BW}$ (dB)	-20.8	-24.6	-23.8	-22.4

### 3.5 Measurement Results

The designed corporate center-fed Engineering Model (EM) antenna panels were fabricated by machining, welding according to the HFSS design and are shown in fig.3.91. The wooden boards are used for support. Since Panel 0 requires in-phase input power from 2 ports, a 1:1 coaxial cable power divider with Wilkinson phase-shifter is employed for



feeding input power to panel 0. Fig.3.90 shows the Wilkinson power divider cable and fig.3.92 shows its loss characteristics vs frequency.

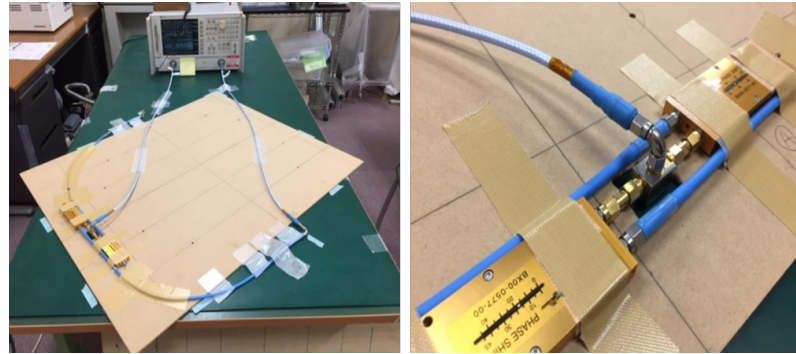
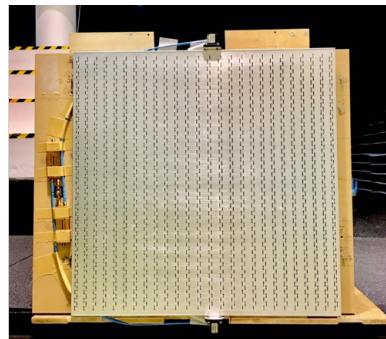
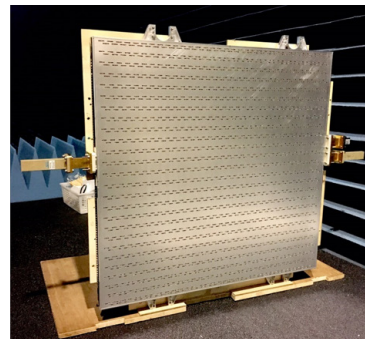


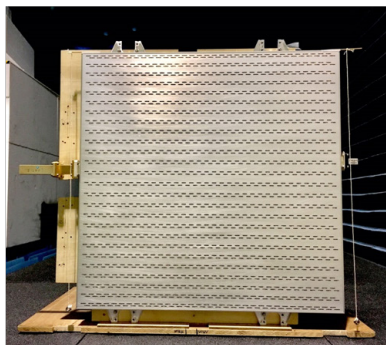
Fig. 3.90. Wilkinson Power Divider with Phase Shifter for Panel 0



*Center-feed EM Panel #0*



*Center-feed EM Panel #1M*



*Center-feed EM Panel #2M*



*Center-feed EM Panel #3M*

Fig. 3.91. Fabricated Center-feed Antenna Panels

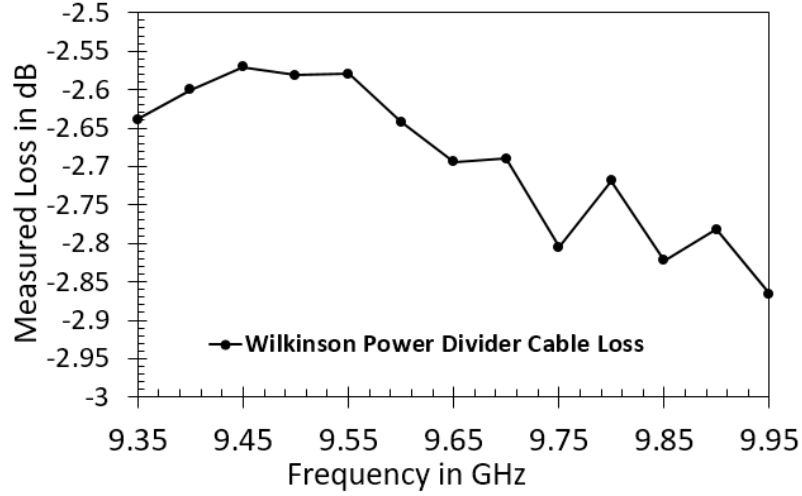


Fig. 3.92. Measured Cable Loss of Wilkinson Power Divider

### 3.5.1 Near-field Tests

The near-field measurement of each isolated antenna panel was conducted in the Anechoic Chamber at Tokyo Institute of Technology, Ookayama Facility. The probe is placed at a height of 15 cm ( $>4\lambda_0$ ) from the AUT as shown in fig.3.93(a). The sampling is done at a spacing of 1.5 cm in both x and y directions, covering 75x75 data points to satisfy the Nyquist sampling criterion for measurement of highest frequency (9.8 GHz) as discussed in [7]. The antenna aperture distributions (amplitude and phase), and directivity are obtained from near-field measurement after considering the probe correction factor. Fig.3.94 to fig. 3.97 show the normalized measured 2-D amplitude and phase distributions of 'E<sub>y</sub>' at 9.65 GHz for all panels. Fig.3.98 shows the 1D phase distribution of Panel 3M and Panel 0 along range and azimuth, measured along the center of the panel. Minimum ripple is observed at 9.6 GHz. The measured directivity of each panel is shown in fig.3.108.

The near-field measurements for the 3-panel antenna array (*Panel 1M to Panel 3M*) and 4-panel antenna array (*Panel 0 to Panel 3M*) were conducted in the anechoic chamber at

Kyoto University. A lift-up table is employed to conduct near-field measurement as shown in fig.3.93(b). The distance of the probe from the AUT is 25.6 cm. The sampling is done at a spacing of 1.5 cm in both x and y directions, covering 227x95 data points for both cases which satisfies the Nyquist sampling criterion. Fig.3.99 to fig. 3.102 show the normalized 2-D amplitude and phase distributions of ‘E<sub>y</sub>’ at 9.65 GHz for the 3-panel and 4-panel arrays. The variation of the measured peak directivity and antenna aperture efficiency with frequency of the 4-panel array is shown in fig.3.109.

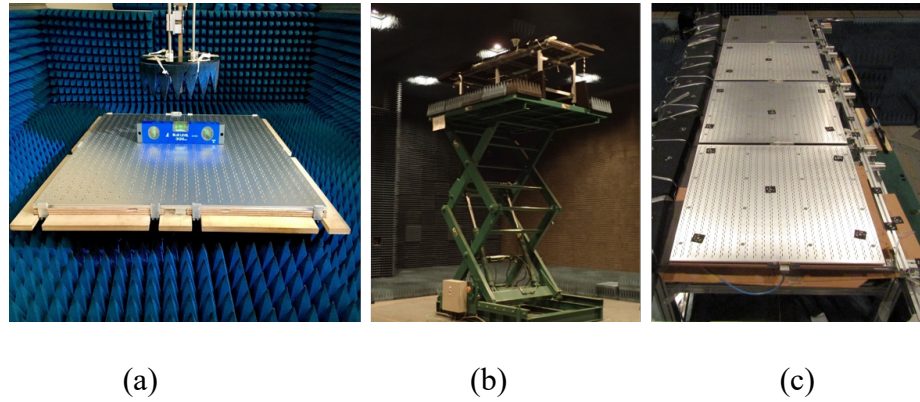


Fig. 3.93. Near-field Measurement Setup: (a): Single Panel at Tokyo Institute of Technology (b), (c): Antenna Panel Array at Kyoto University

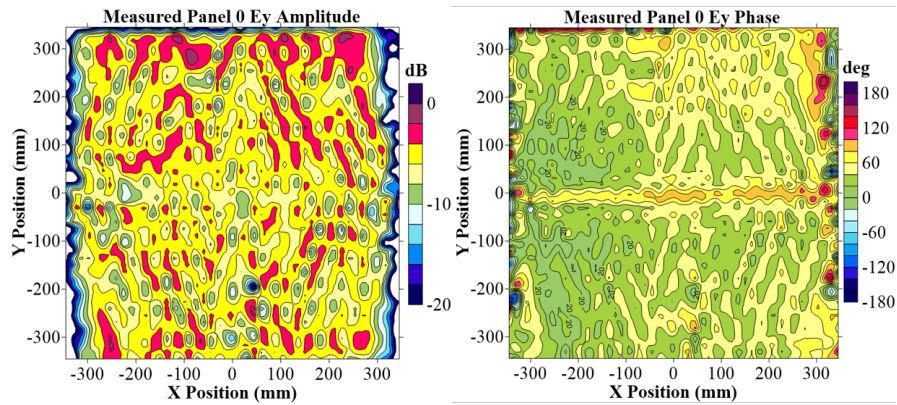


Fig. 3.94. Measurement Amplitude and Phase Distribution of Center-feed Panel 0



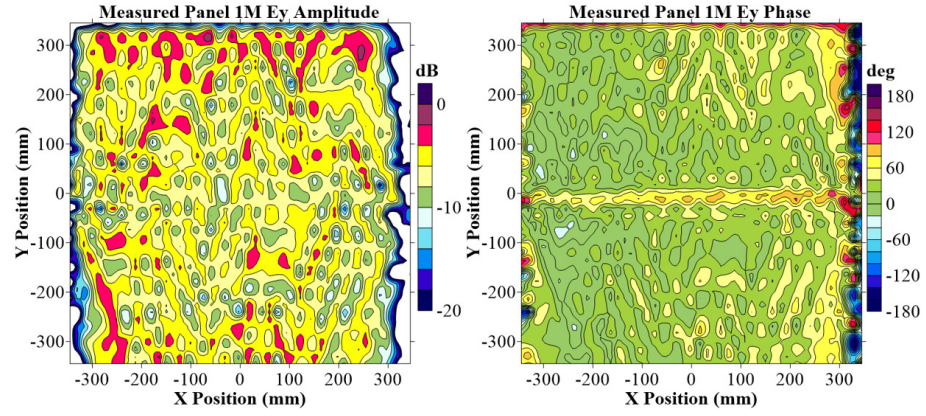


Fig. 3.95. Measurement Amplitude and Phase Distribution of Center-feed Panel 1M

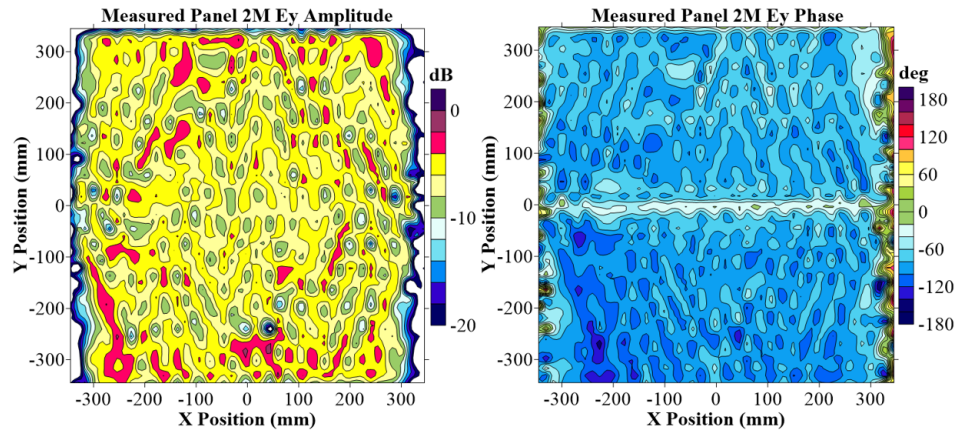


Fig. 3.96. Measurement Amplitude and Phase Distribution of Center-feed Panel 2M

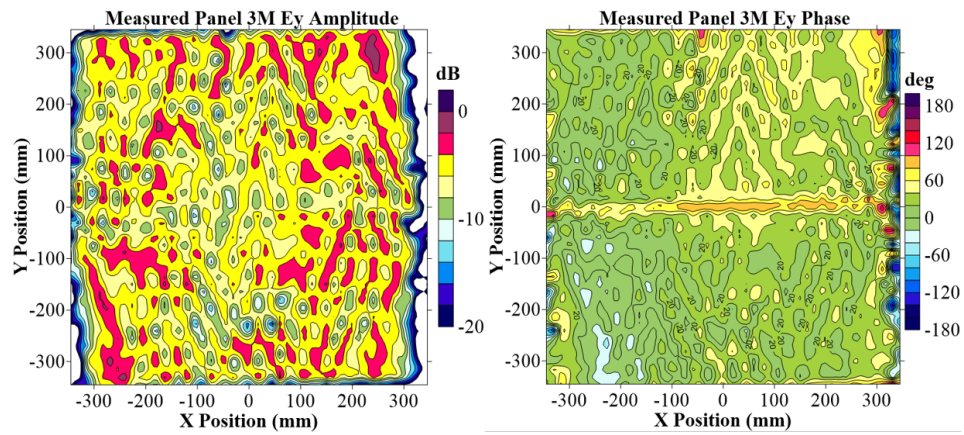


Fig. 3.97. Measurement Amplitude and Phase Distribution of Center-feed Panel 3M



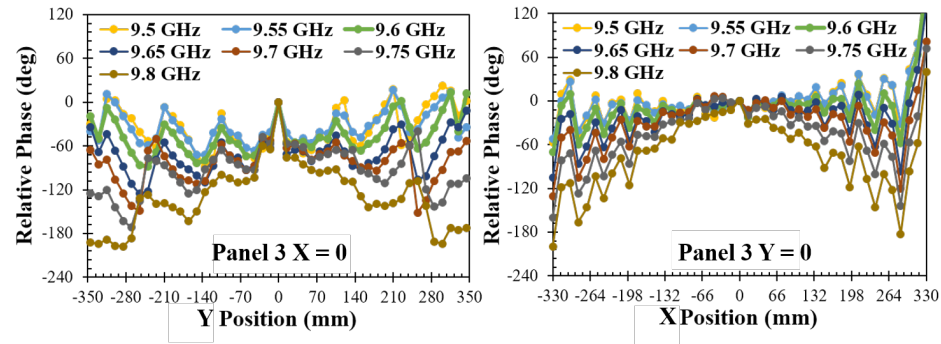


Fig. 3.98. Measurement 1D Phase Distributions along Range and Azimuth at Different Frequencies of Panel 3M

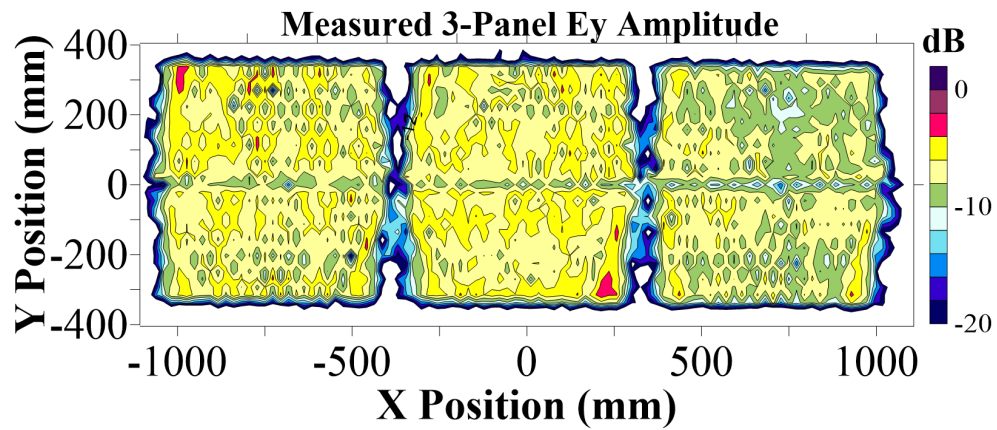


Fig. 3.99. Measurement Amplitude Distribution of Antenna Panel Array 1M-3M

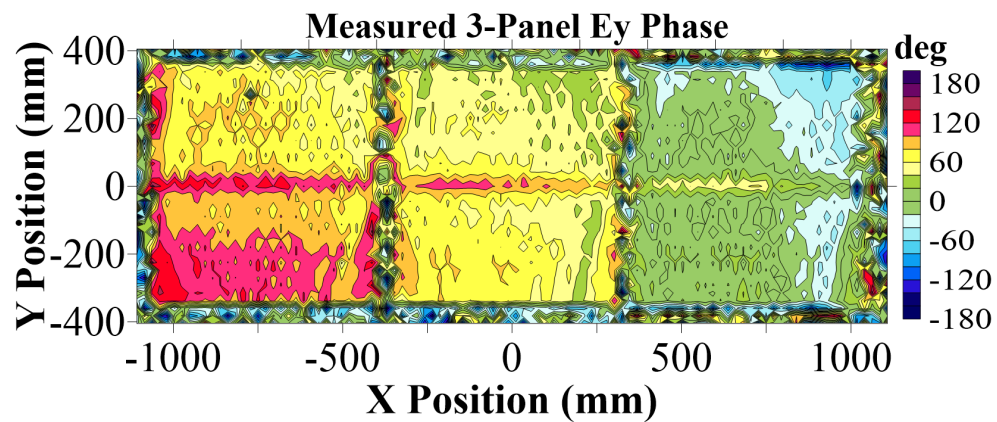


Fig. 3.100. Measurement Phase Distribution of Antenna Panel Array 1M-3M

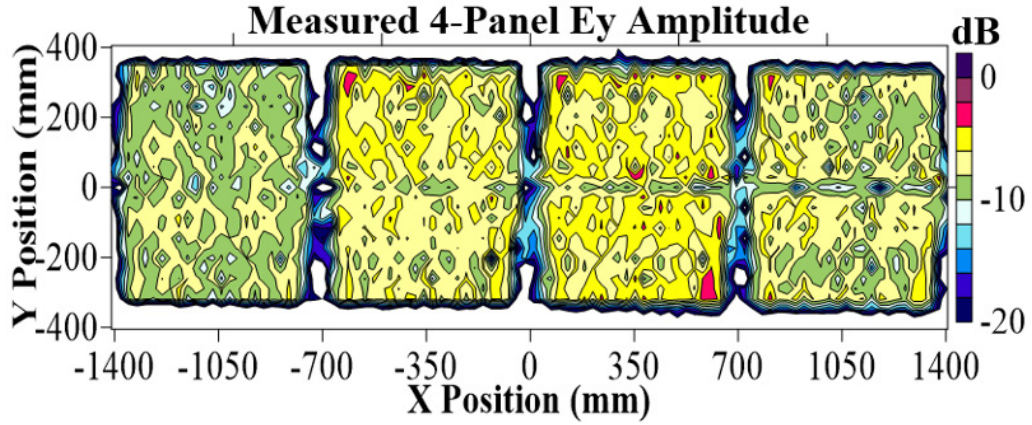


Fig. 3.101. Measurement Amplitude Distribution of Antenna Panel Array 0-3M

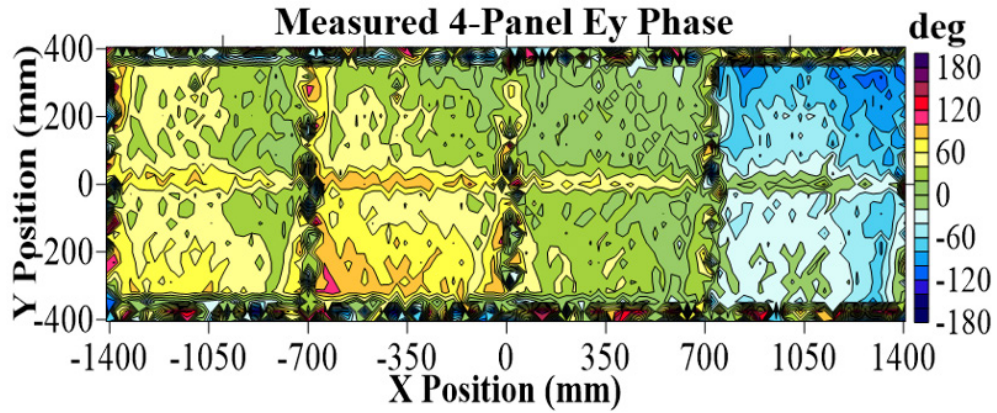


Fig. 3.102. Measurement Phase Distribution of Antenna Panel Array 0-3M

### 3.5.2 Far-field Tests

The single-panel far-field measurements were conducted in the Anechoic Chamber in JAXA Sagami-hara facility as shown in fig.3.103(a) and the antenna panel array far-field measurements were conducted in the Compact-Range Chamber, JAXA Tsukuba Facility as shown in fig.3.103(b).

In ISAS Anechoic chamber, the distance between the receiver horn antenna and AUT (transmitter) is 16.58 meters which is less than the Fraunhofer cut-off distance for far-field

measurement given by  $r \geq 2D^2/\lambda_0$  [6] where D is the largest dimension of the AUT. For panels 1,2 and 3  $D= 973.56\text{mm}$  and  $r \geq 60.97\text{mm}$  while for panel 0,  $D= 974.69\text{mm}$  and  $r \geq 61.14\text{mm}$ . Thus, a correction factor must be added to the measured gain to provide an equivalent far-field gain measurement with distance correction using the same methodology explained in [6] and [7]. Fig.3.109 shows the variation of the Gain Correction Factor (GCF) for each antenna panel in our measurement frequency bandwidth.

In Tsukuba Compact Range Chamber, the Test Zone area is horizontally cylindrical space of 3658 mm (diameter) x 3658 mm (length). The AUT is placed along the range-center line at a distance of 22.04 m from the center of the parabolic reflector. Fig.3.110 and fig.3.111 show the measured antenna gain patterns of all panels in range and azimuth at 9.65 GHz. Fig.3.114 shows the variation of the measured peak gain of each panel (*after corrections*), antenna aperture efficiency ( $\eta_{ap}$ ) and antenna efficiency ( $\eta_a$ ) with frequency. Fig.3.107 shows the normalized measured 3-panel and 4-panel array gain patterns in range and azimuth at 9.65 GHz and fig.3.110 shows the measured peak gain and antenna efficiency of the 3-panel and 4-panel array. Fig.3.108 shows the 3dB beam-width of single panel and 4-panel array. Due to mechanical error and system stability limitations, accuracy is within  $\pm 0.08$  dB and  $\pm 0.2$  dB for single panel and array measurement respectively. The reductions in gain and directivity is less than 3 dB in our desired bandwidth which confirms wideband operation.

The corrected gains of panels 0,1 and 2 are calculated taking into account the Wilkinson power divider cable loss and measured power dividing ratio S-parameters as follows:

$$G_{\#2_{corr}} = \frac{G_{\#2}}{1 - |S_{21\#2}|^2} \quad (3.26)$$

$$G_{\#1_{corr}} = \frac{G_{\#1}}{1 - |S_{21\#1}|^2 - |S_{31\#1}|^2} \quad (3.27)$$

$$G_{\#0_{corr}} = \frac{G_{\#0}}{L_{wc}} \quad (3.28)$$

$$G_{3-Panel-Array_{corr}} = \frac{G_{3-Panel-Array}}{1 - |S_{313-Panel-Array}|^2} \quad (3.29)$$

where  $G_{corr}$  is the corrected gain,  $G$  is the measured gain and  $L_{wc}$  is the Wilkinson cable loss. ‘ $\#n$ ’ denotes the panel number.

The 4-panel arraying efficiency is calculated from the antenna gain measurements as follows:

$$\eta_{AF_{4-Panel-Array}} = \frac{G_{4-Panel-Array}}{G_{\#0_{corr}} + G_{\#1_{corr}} + G_{\#2_{corr}} + G_{\#3}} \quad (3.30)$$

The measured 4-panel arraying efficiency is 91%. The measured antenna loss (*difference between Gain and Directivity*) is 1.2 dBi.

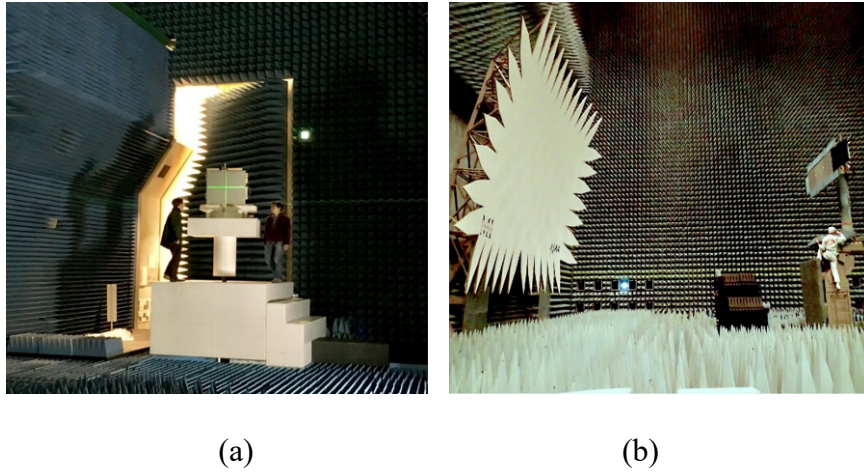


Fig. 3.103. Far-field Measurement Setup: (a): Single Panel at Anechoic Chamber, ISAS JAXA Sagamihara Facility (b) Antenna Panel Array at Compact Range Setup, JAXA Tsukuba Facility

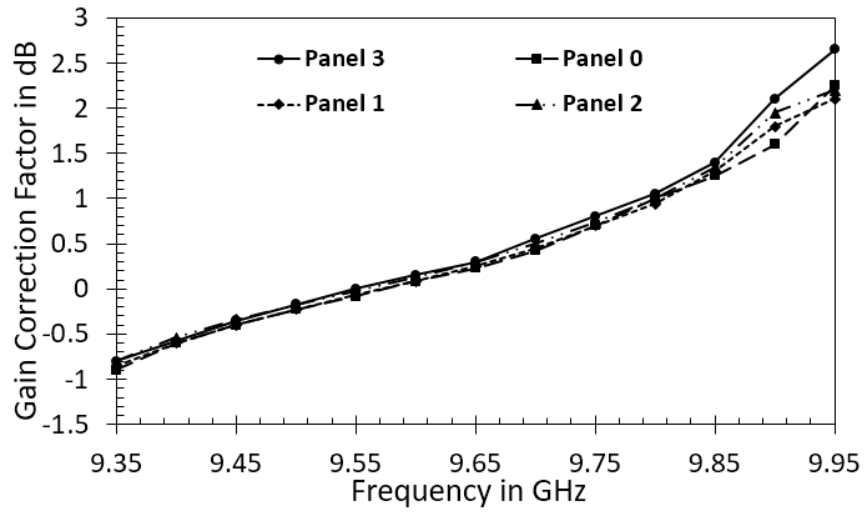


Fig. 3.104. Measured Gain Correction Factor for Far-field Measurement for All Panels

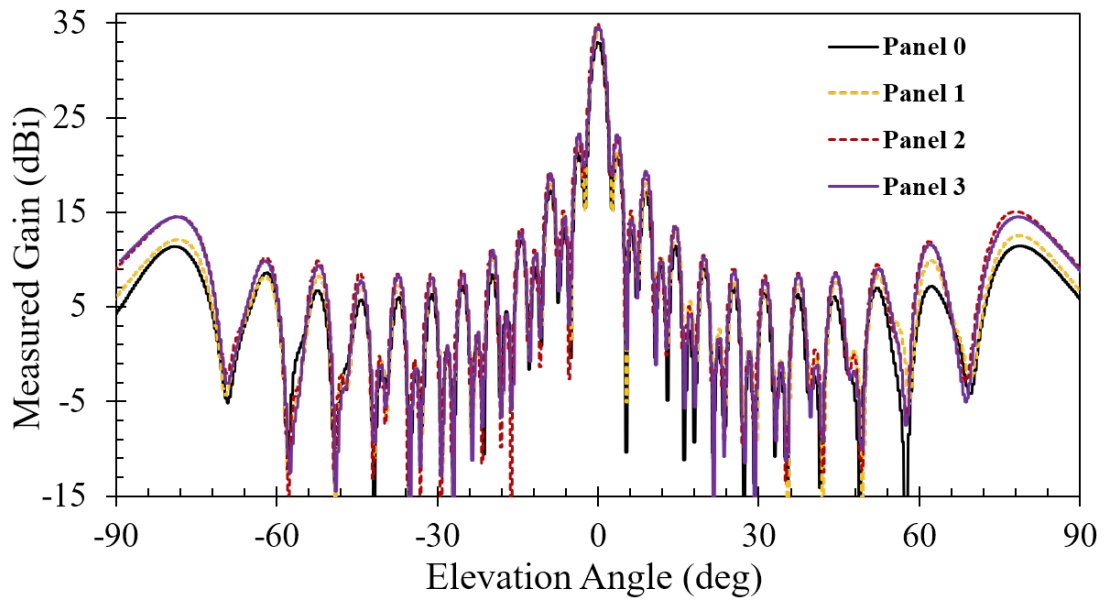


Fig. 3.115. Measurement Elevation Pattern of Center-feed Antenna Panels



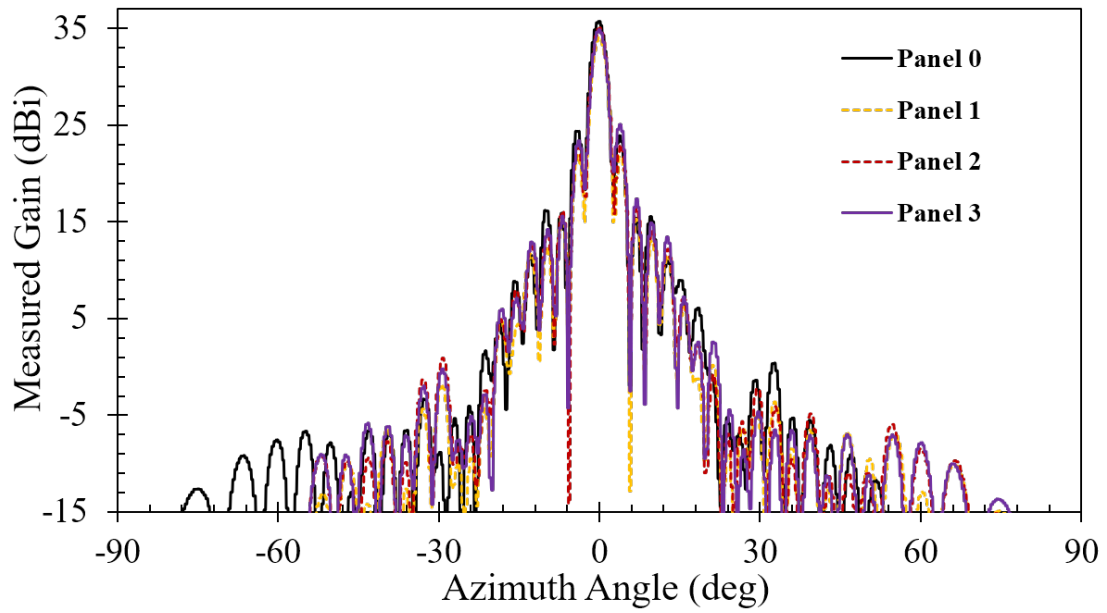


Fig. 3.106. Measurement Azimuth Pattern of Center-feed Antenna Panels

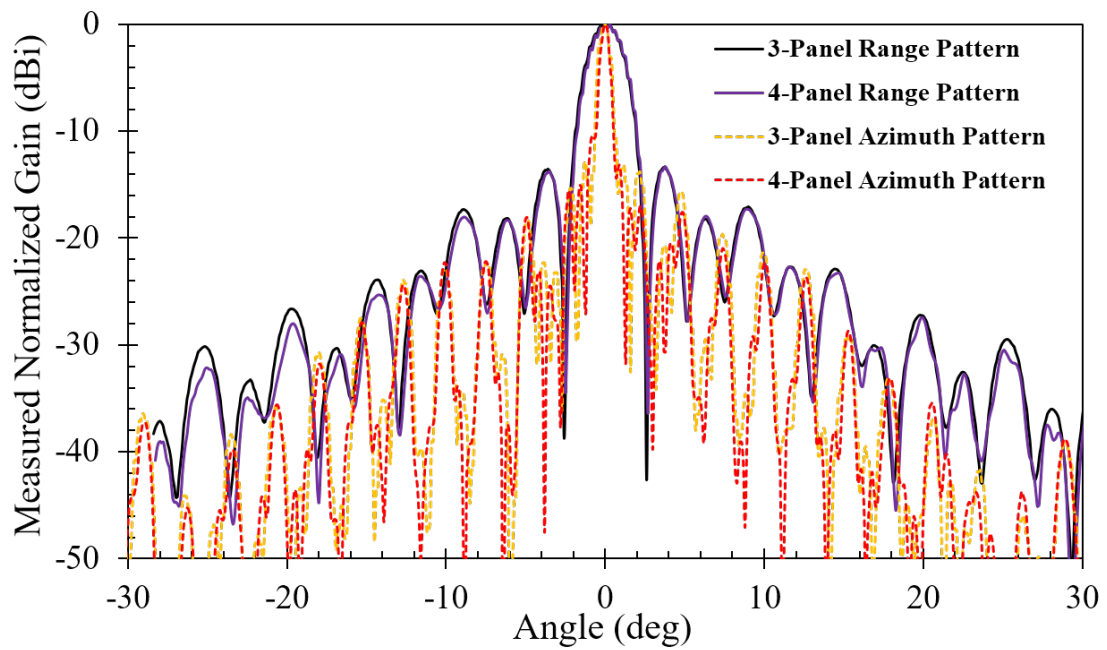


Fig. 3.107. Measurement Elevation and Azimuth Pattern of Antenna Panel Array

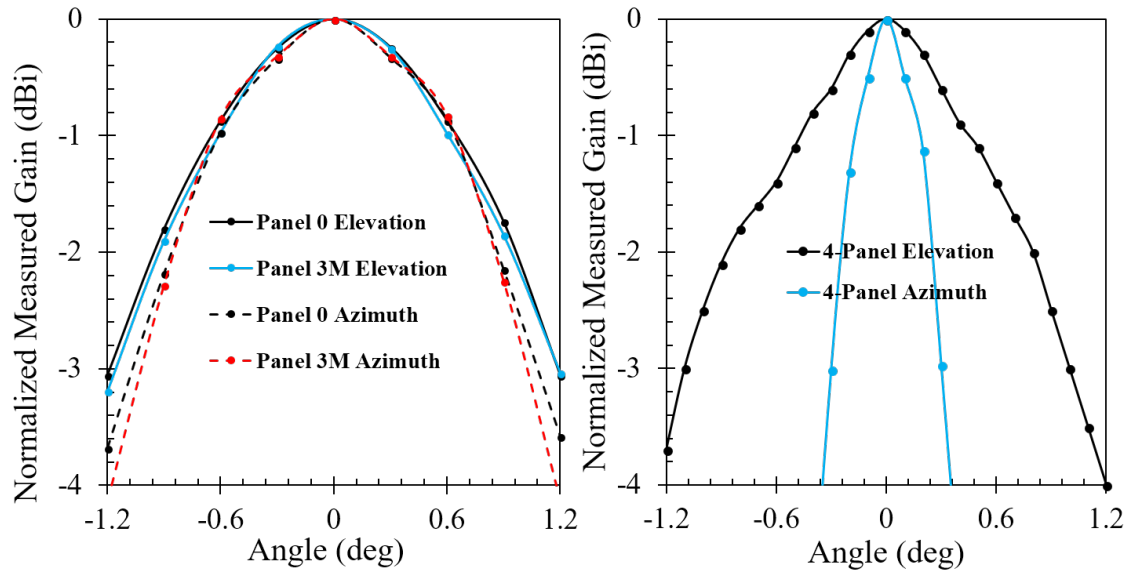


Fig. 3.108. Measurement Elevation and Azimuth 3dB Beamwidth for Panel 0, Panel 3M and 4-Panel Antenna Array

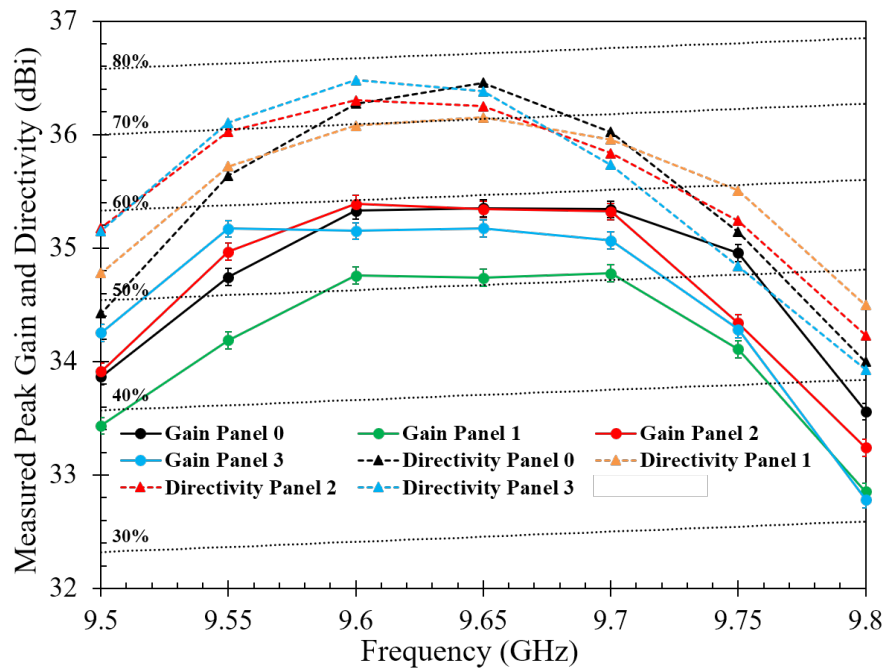


Fig. 3.109. Measurement Peak Gain and Directivity of Center-feed Antenna Panels

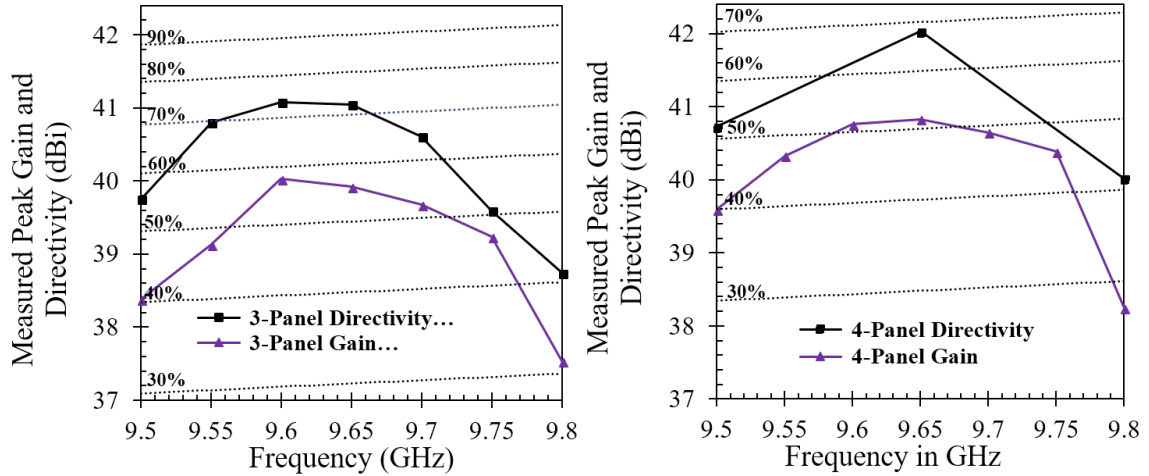


Fig. 3.110. Measurement Peak Gain and Directivity of Antenna Panel Array

### 3.5.3 Vector Network Analyzer Tests

Fig.3.111 shows the VNA measurement setup and fig.3.112 shows the block diagram of S parameter measurement for cascaded antenna array network. Fig.3.113 shows the detailed view of fig.3.112 for Panel 1 and Panel 2. Fig.3.114 and fig.3.115 respectively show the measured reflection and power dividing ratios of the 4 isolated panels using VNA. The lowermost  $\tau$ -junction layer containing coupling slots of panels 1M, 2M and 3M should have the same reflection characteristics, being identical in design. However, the measured reflection levels of panels 1 and 2 are better, respectively below -20 dB and -17.5 dB. This is because for these two panels, only a fraction of the input power goes into the respective antenna panels while the remaining power flows into the terminal loads (*For isolated panel measurements, the ports for transmitting power to the neighboring panels are terminated by standard 50 ohms matched load*).





Fig. 3.111. VNA S Parameters Measurement Setup

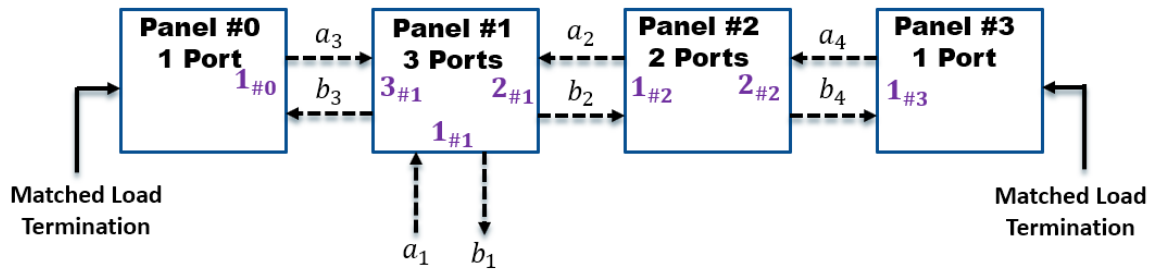


Fig. 3.112. Schematic of S Parameter Computation for Cascaded Antenna Panel Network

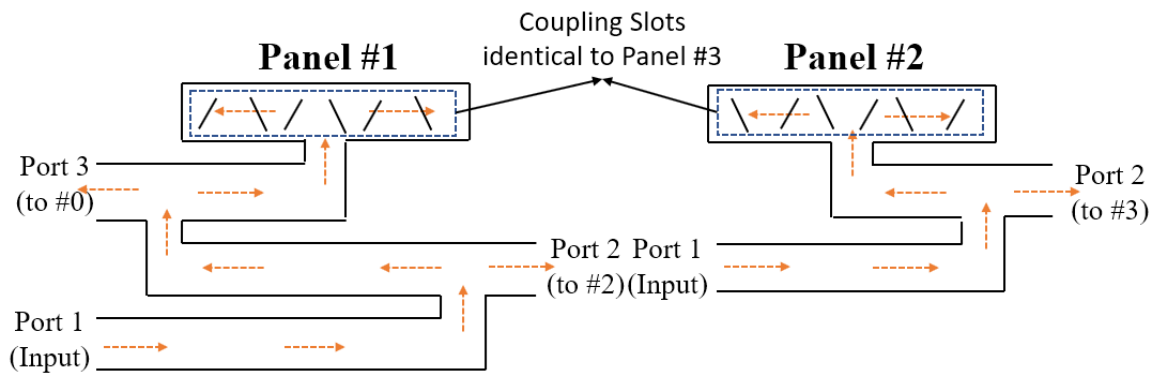


Fig. 3.113. Schematic of S Parameter Calculation for Panel 1 and Panel 2

Assuming reciprocity and neglecting any reflected power from adjacent panels, the  $S_{11}$  of Panel 1M, Panel 2M and the 4-panel antenna array network can be approximately

expressed in terms of measured  $S_{11}$  of Panel 3M and measured power dividing ratios applying energy conservation in the following way:

$$|S_{11\#2_{calculated}}| = \sqrt{(1 - |S_{21\#2}|^2)} |S_{11\#3}| \sqrt{(1 - |S_{12\#2}|^2)} \quad (3.31)$$

$$|S_{11\#1_{calculated}}| = \sqrt{(1 - |S_{21\#1}|^2 - |S_{31\#1}|^2)} |S_{11\#3}| \sqrt{(1 - |S_{13\#1}|^2 - |S_{12\#1}|^2)} \quad (3.32)$$

$$S_{113-Panel\ Array_{calculated}} = S_{11\#1} + S_{21\#1} S_{11\#2} S_{12\#1} + S_{21\#1} S_{21\#2} S_{11\#3} S_{12\#2} S_{12\#1} \quad (3.33)$$

$$S_{114-Panel\ Array_{calculated}} = S_{113-Panel\ Array_{calculated}} + S_{31\#1} S_{11\#0} S_{13\#1} \quad (3.34)$$

Equations (3.31) and (3.32) are derived considering the block diagram shown in fig. 3.113. Equations (3.33) and (3.34) are derived considering cascaded network shown in fig. 3.112. Fig.3.114 shows good correspondence between measured and calculated values of  $S_{11}$  of antenna array. The total network reflection level meets the desired -15 dB limit. All antenna measurement results are summarized in Table 3.14.

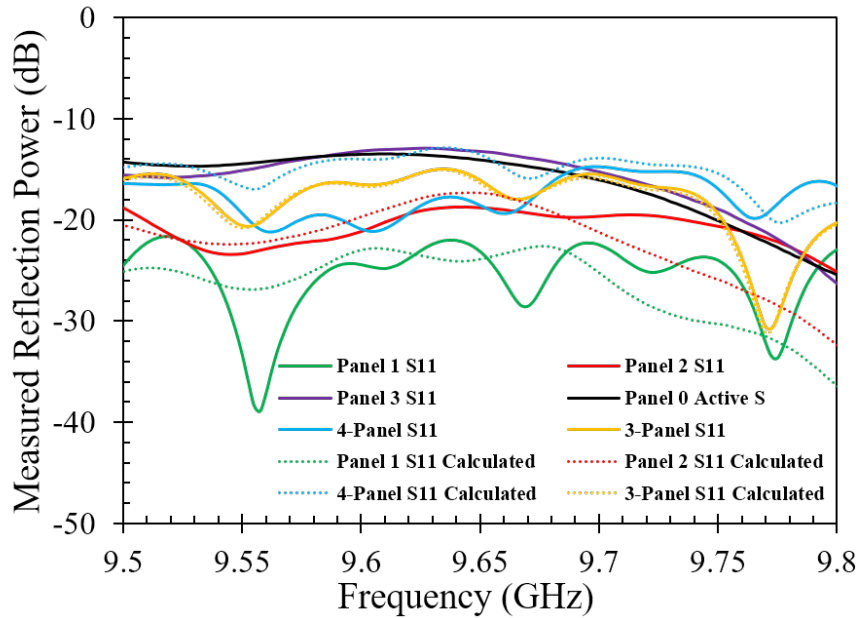


Fig. 3.114. Measured Reflection S Parameters of Each Isolated Panel and Panel Arrays

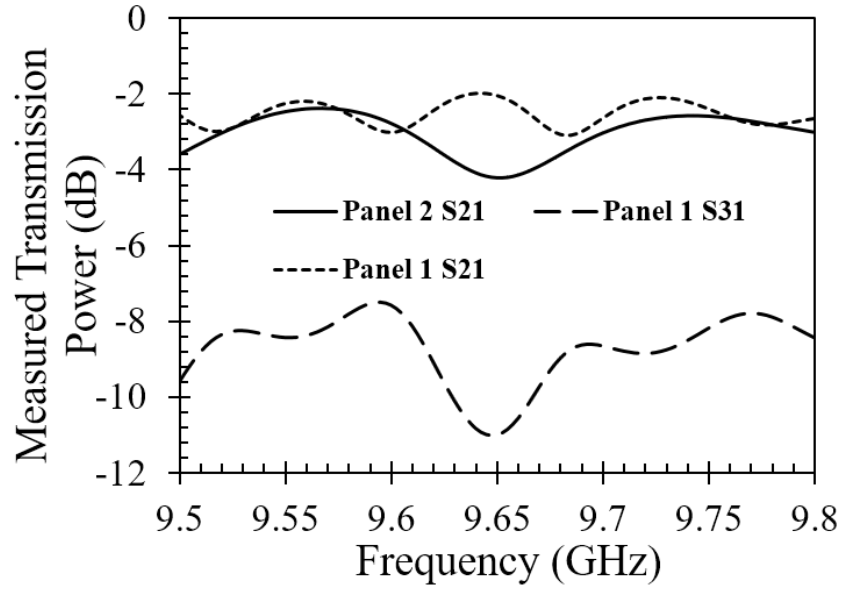


Fig. 3.115. Measured Transmission Power Dividing Ratio S Parameters of Panel 1M and Panel 2M

Table 3.14. Summary of Center-feed Full Panel Measurement Results

Parameter	Panel 0	Panel 1M	Panel 2M	Panel 3M	3-Panel Array	4-Panel Array
Peak Directivity (dBi)	36.5	36.2	36.3	36.5	41.1	<b>42.0</b>
Peak Gain (dBi)	35.3	34.8	35.4	35.2	39.9	<b>40.8</b>
Peak Aperture Efficiency (%)	75.2	70.3	73.5	76.6	73.6	<b>68.0</b>
Peak Antenna Efficiency (%)	58.0	50.9	59.5	55.9	55.1	51.3
Amplitude (Std. div) at $f_0$ (dB)	5.5	5.6	5.6	5.5	5.4	5.1
Phase (Std. div) at $f_0$ (deg)	35.1	42.5	43.8	36.3	58.5	53.6
Maximum Reflection in $f_{BW}$ (dB)	-13.7	-24.6	-23.0	-13.0	-15.0	<b>-14.6</b>

## 3.6 Post Measurement Analysis

### 3.6.1 *Diagnosis of Reflection Degradation*

The measured reflection levels of Panel 3 and Panel 0 are higher than the designed simulation levels by about 7 dB due to positive frequency shift in the reflection profile as seen in fig.3.114. This is undesired since  $S_{11}$  level of -13 dB is very close to the maximum permissible reflection levels of the Low Noise Amplifier (LNA) at the SAR receiver. Also, the measured power dividing ratio levels have fluctuations larger than 1 dB throughout the desired bandwidth unlike the nearly flat simulation results, as seen in in fig.3.115.

One possible reason is the reflected power from Panel 3 and Panel 0 which is not considered in simulation. Since the measured reflection level of Panel 3 and Panel 0 is -13 dB, this effect is not negligible. In Section IV, we concluded that reflection characteristics of full panel antenna is highly dependent on the reflection characteristics of the waveguide feeder. However, since the manufacturing accuracy of all panels was confirmed to be within 0.05 mm, it can be concluded that manufacturing error is not the reason for degraded reflection of the fabricated antenna.

The only parameter which cannot be accurately measured is the thickness of the adhesive layer which is used to attach the honeycomb layer to the parallel plate as seen in fig.3.48. Furthermore, in reality the adhesive layer is not flat (cuboidal) due to surface tension and viscosity effects; but there is no scope to incorporate these factors in the HFSS model. Thus, one possible cause of degradation in reflection may be the inaccuracy in estimation of the effective adhesive thickness during design in HFSS. Thus, we simulated the reflection loss of each antenna panel varying the adhesive layer thickness. Fig.3.116 shows that the simulated reflection profile with adhesive thickness of 0.05 mm matches

very closely with the measured reflection profile of Panel 3. We can make the same conclusion regarding Panel 1 transmission power dividing ratio in fig.3.117. Thus, one possible way to solve the reflection problem would be to redesign the antenna for adhesive thickness 0.05 mm instead of 0.09 mm. However, this would require redesign of each individual coupling slot and radiation slot pair from the beginning which would be a very time-consuming and cumbersome process. Furthermore, adhesive thickness is an uncontrollable parameter since its shape cannot be predicted accurately.

An alternative fast and more effective way to solve this problem would be to change an easily controllable parameter (*e.g. length of the coupling slots in the waveguide feeders*) to compensate the undesired effect of change in an uncontrollable parameter, viz. adhesive thickness. Fig.3.116 shows that decreasing the length of all coupling slots in the waveguide feeders by 0.2 mm produces the same degradation in reflection as changing the adhesive thickness in the parallel plate to 0.05 mm. Thus, to suppress reflection, the length of all coupling slots should be increased by 0.2 mm. Reflection profile and power dividing ratio characteristics with  $t=0.05\text{ mm}$  and  $SL=+0.2\text{ mm}$  are significantly improved and are nearly identical to the original design simulation results as seen in fig.3.116 and fig.3.117. Here, ' $t$ ' is the thickness of the adhesive layer and ' $SL$ ' is the change in slot length (*from original design values*) of coupling slots in the waveguide feeder. The measurement result of newly manufactured Panel 3M with  $SL=+0.2\text{ mm}$  in fig.3.118 validates this approach to improve reflection level. Thus, it can be applied for all panels.

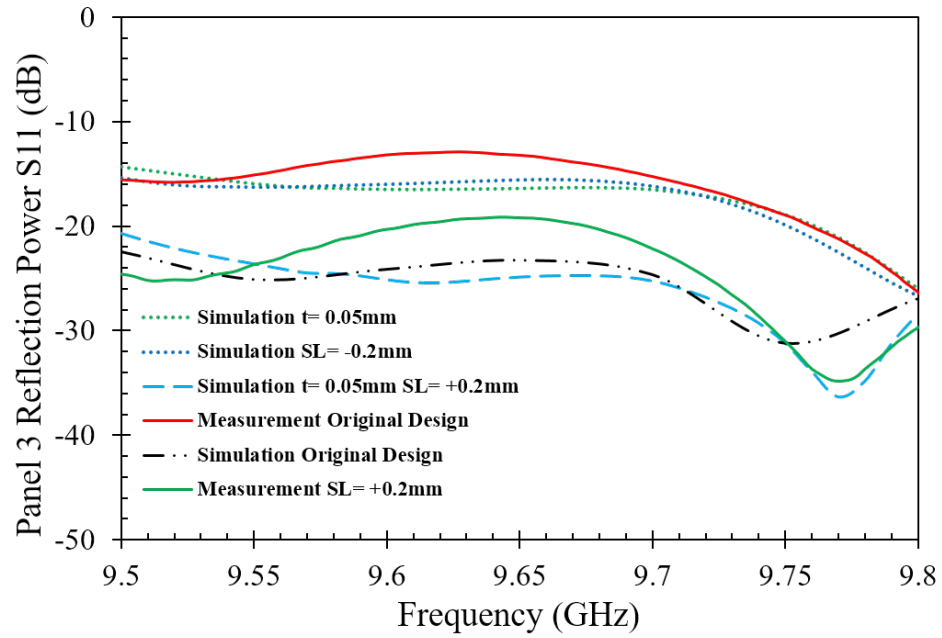


Fig. 3.116. Simulation Reflection S Parameters for Parameter Variations

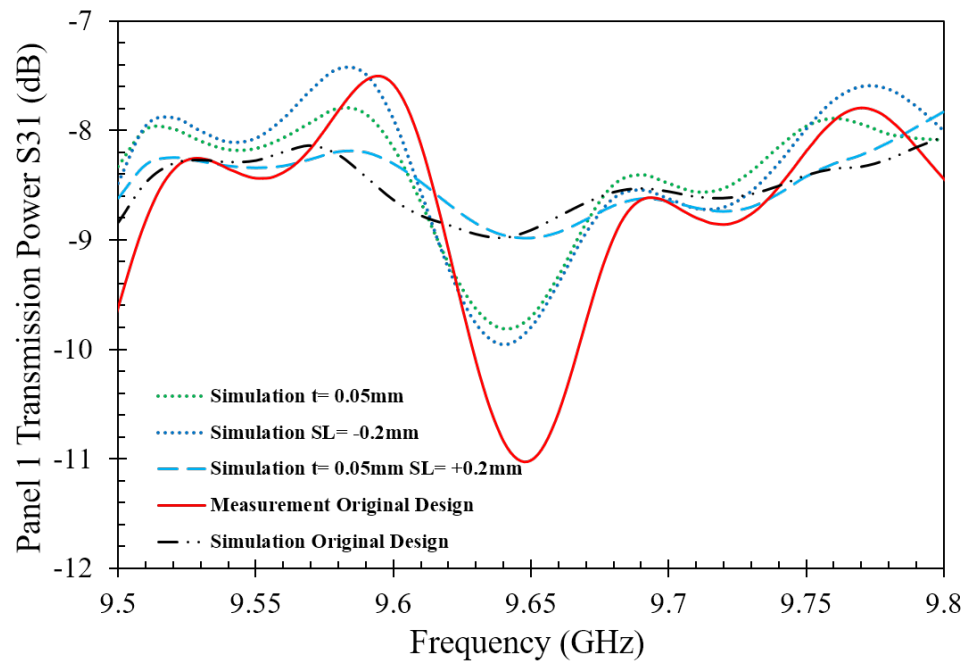


Fig. 3.117. Simulation Transmission Power Dividing Ratio S Parameters for Parameter Variations

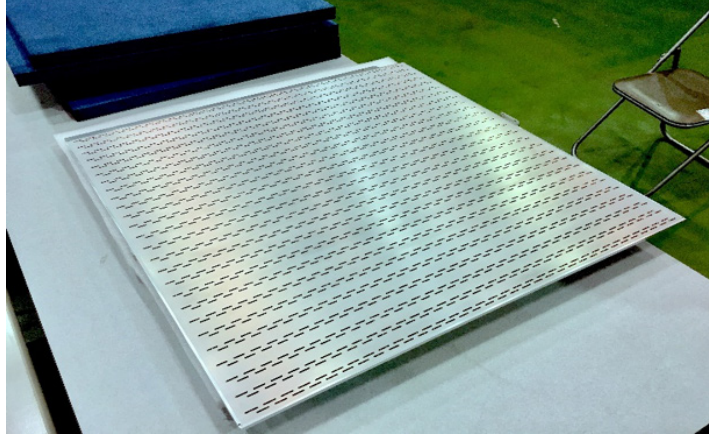


Fig. 3.118. Fabricated New Panel 3M with  $SL = +0.2 \text{ mm}$

### 3.7 Summary

This chapter presented the optimal feeder network design for a parallel-plate slot-array space-borne antenna. Although it was designed for the MicroX-SAR mission, the design principle is general and fundamentally applicable to a more general class of antenna feeder design problems. The key essence of the feeder design is that it is applicable for an odd number of antenna panels where the center panel feeder is unique and different from the other panels. Another novelty of the design is that the upper layer power divider junctions are positioned in such a way that the path difference of the electromagnetic waves to each panel is an integral multiple of the center wavelength which ensures in-phase uniform excitation as desired. Two feeding schemes were proposed: the center-feed technique and the edge-feed technique. The center-feed technique was selected as the optimum design and fabricated antenna measurement results showed good correspondence with HFSS design. The fabricated 4-panel array achieved 40.8 dBi Gain with 68% aperture efficiency and 91 % arraying efficiency. Table 3.15 provides a summary of the benefits and shortcomings of different feeding techniques.

Table 3.15. Pros and Cons of Different Feeding Schemes

<b>Feed Type</b>	<b>Pros</b>	<b>Cons</b>
End-feed	Simple Design, Easy Fabrication, Applicable for Dual-Pol Antenna; Feeders act as hinges	Narrow-band, Narrow-beam antenna, Beam-tilt
Edge-Feed	Wide-band, Wide-beam antenna, Applicable for Dual-Pol Antenna; Feeders act as hinges	Complex asymmetric design, Difficult to fabricate
Center-Feed	Wide-band, wide-beam antenna, lighter (only one feeder per panel), simple symmetric design, No beam-tilt, Easily Fabricated	Feeders do not function as hinges, special spacer design needed





## CHAPTER 4. EGG-CHOKE FLANGE PERFORMANCE ANALYSIS

### 4.1 Background

A choke flange is widely used to avoid degradation of current conduction through a waveguide flange contact due to manufacturing imperfections or oxidization of the flange surfaces [22] [23]. It has a wide range of applications, one of them being in space-borne radars [10]. The motivation behind our choke-flange design was for its application in our MicroX-SAR mission [1] [2] [4]. The satellite bus comprises of seven antenna panels, each of which are fed from below by rectangular WR90 waveguide with the choke flange shown stowed condition in fig.4.1. Thus, it is desired to have contactless waveguide joints for connecting the waveguide feeders of two adjacent antenna panels; hence choke-flange is the ideal type of such a waveguide joint to serve this purpose. In the deployable hinge, RF power is transmitted between two non-contact waveguide flanges, where one is a choke-flange, and the other is a flat cover-flange [6] [11]. Thus, it is difficult to ensure perfect metallic contact. Additionally, due to the possibility of thermal expansion in space, it is necessary to leave a nominal gap of about 0.5 mm to 1 mm between the choke-flange and flat-flange. Furthermore, since there are 6 degrees of freedom, there is always the possibility of both linear and rotational misalignment during practical operation. It is critically important that with the choke-flange, the transmission loss is very low (less than 0.3 dB) taking into account a nominal gap and possible linear and rotational misalignments in the desired bandwidth of 9.5 GHz to 9.8 GHz.

This chapter describes the design methodology, eigen-mode analysis and

measurement results of our specially designed egg-choke flange. Although the initial purpose of its design was its application in 300 MHz bandwidth relevant to the MicroX-SAR project, due to careful intuitive design considerations, the fabricated egg-choke has a much wider operational bandwidth greater than 2.5 GHz, thereby making it robust, unique and useful for several other wide-band applications in X-band.

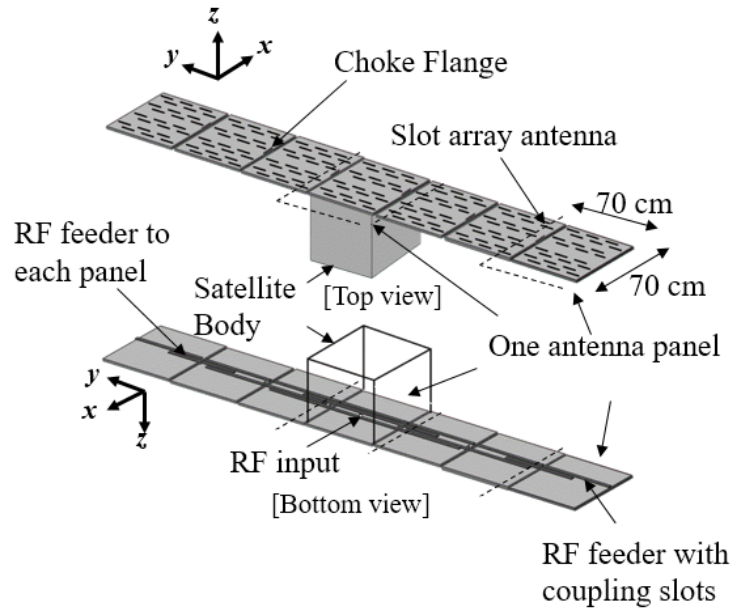


Fig. 4.1(a). MicroX-SAR Deployable Antenna Configuration

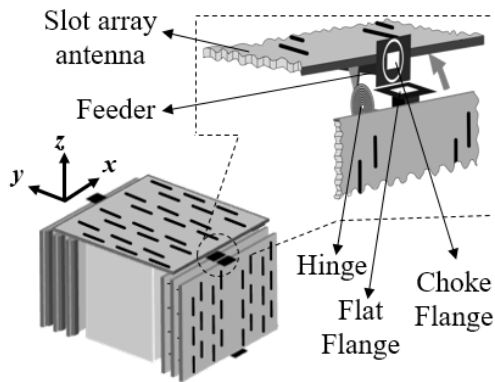


Fig. 4.1(b). MicroX-SAR Antenna in Stowed Condition with Choke Flange

## 4.2 Simulation Results

### 4.2.1 Issues with Standard Circular Choke Flange

The choke-flange HFSS Simulation model 3D view is shown in Fig.4.2(a). Fig.4.2(b) and Fig.4.2(c) show the HFSS simulation models considering possible linear misalignment and rotational misalignments between the choke-flange and the flat-flange during actual operation. The performance of commercially available standard circular choke for WR90 waveguide is first analyzed. Although measurement results of egg-choke will be discussed in detail in Section 4.3, the simulation results of circular choke agree well with the measurement results as seen in Fig.4.3. Using the conventional circular choke-flange, there is high transmission losses greater than 0.5 dB for different gaps between the choke-flange and the flat-flange in our desired bandwidth. Thus, the standard circular choke-flange cannot be used since its resonant frequency lies within our desired bandwidth for a nominal gap of 0.5 mm to 1 mm between the choke-flange and the flat-flange. Hence, it is necessary to design a special choke-flange which meets our desired criteria. Fig.4.4 shows the plot of the resonant frequencies for different misalignments for circular choke as a function of the gap separation ' $\Delta z$ '. The electric field intensity pattern at the resonant frequency is of interest. At the resonant frequency ' $f_R$ ', most of the power is lost to the ring-shaped flange region leading to the formation of standing waves. For circular choke, the number of nodes of the standing wave peaks ' $n$ ' is always equal to 4 as seen in Fig.4.4. The location of the peaks changes for different misalignments as the resonant frequency changes.

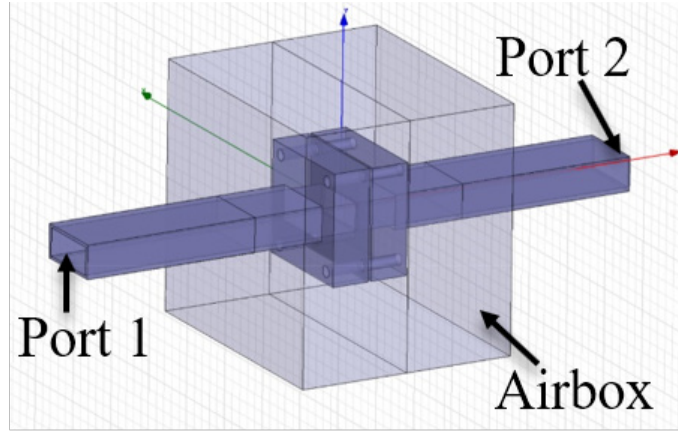


Fig. 4.2(a). 3D View of HFSS Choke Flange Simulation Model

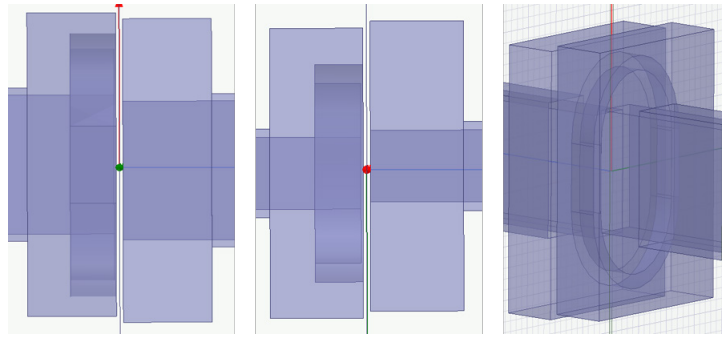


Fig. 4.2(b). HFSS Simulation Model of Egg-choke flange ( $d = 6$  mm) with linear misalignment for  $[\Delta x, \Delta y, \Delta z] = [1, 0, 1]$  mm,  $[0, 1, 1]$  mm and  $[1, 1, 1]$  mm

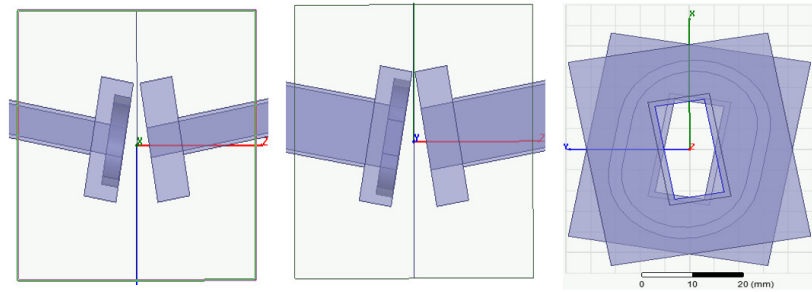


Fig. 4.2(c). HFSS Simulation Model of Egg-choke flange ( $d = 6$  mm) with linear and rotational misalignment with  $[\Delta x, \Delta y, \Delta z] = [0, 0, 10]$  mm for  $[\theta_x, \theta_y, \theta_z] = [10, 0, 0]$  deg,  $[0, 10, 0]$  deg and  $[0, 0, 10]$  deg

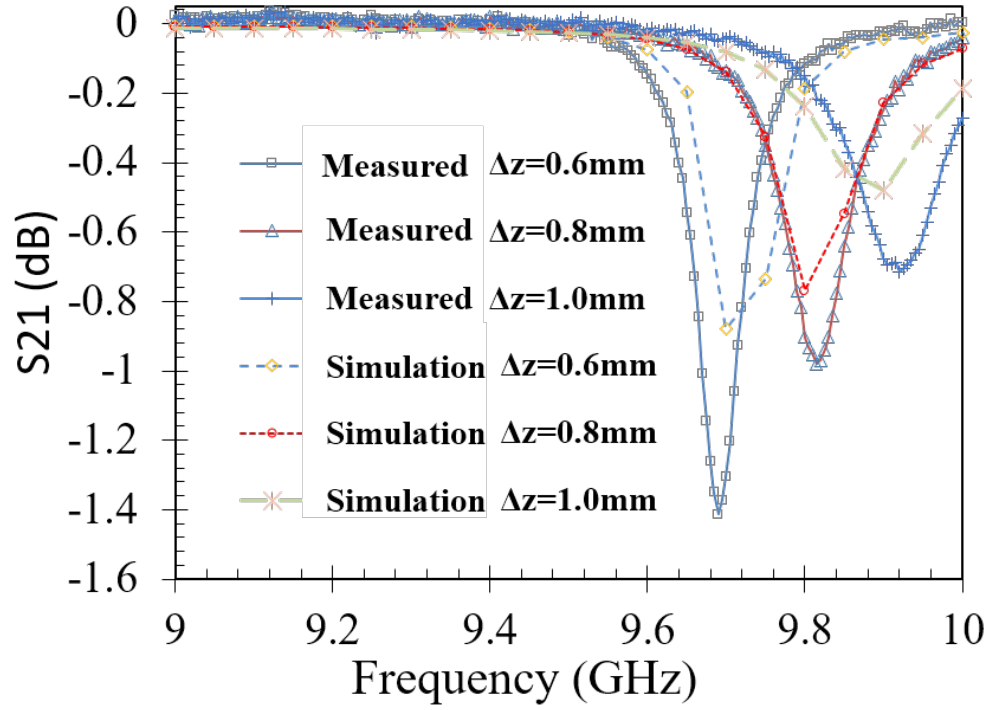


Fig. 4.3. Transmission S Parameter of Circular Choke-Flange for  $(\Delta x, \Delta y) = (1, 0 \text{ mm})$

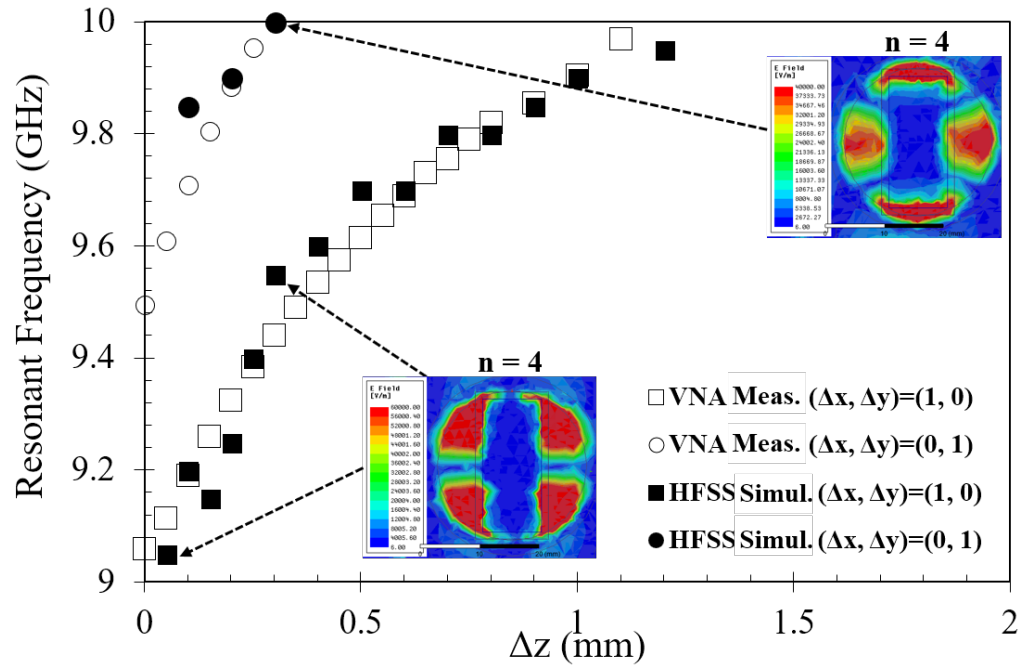


Fig. 4.4. Circular Choke-Flange Resonance Frequency vs  $\Delta z$  for several cases

#### 4.2.2 Egg-Choke Flange Design

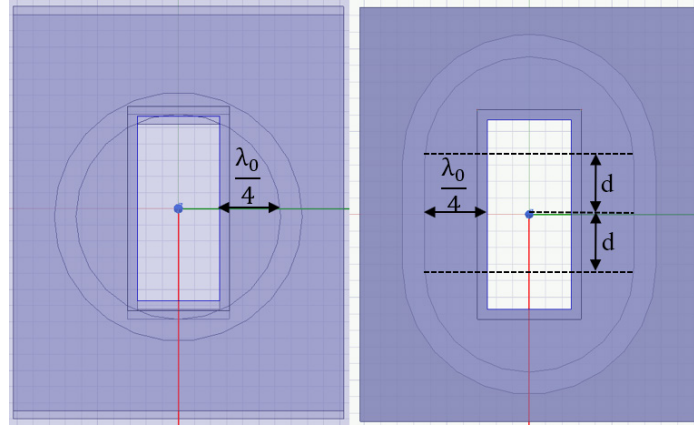


Fig. 4.5. HFSS Simulation Model Cross-sectional view of standard circular-choke (left) and proposed egg-choke (right) for  $d = 6$  mm

Fig.4.5 shows the cross-section of the proposed design model of an egg-shaped choke flange of the HFSS model and fabrication respectively where the shape of the choke changes by varying the parameter ‘d’ [15] [16]. This shifts the resonant frequency outside the desired bandwidth during power transmission.

Fig.4.6 shows the plot of the resonant frequencies varying the parameter ‘d’ for a nominal separation of 0.5 mm between the choke-flange and flat-flange with 1 mm misalignment along the ‘y’ direction. The electric field intensity pattern at the resonant frequency is of interest. At the resonant frequency ‘ $f_R$ ’, most of the power is lost to the ring-shaped flange region leading to the formation of electromagnetic standing waves.

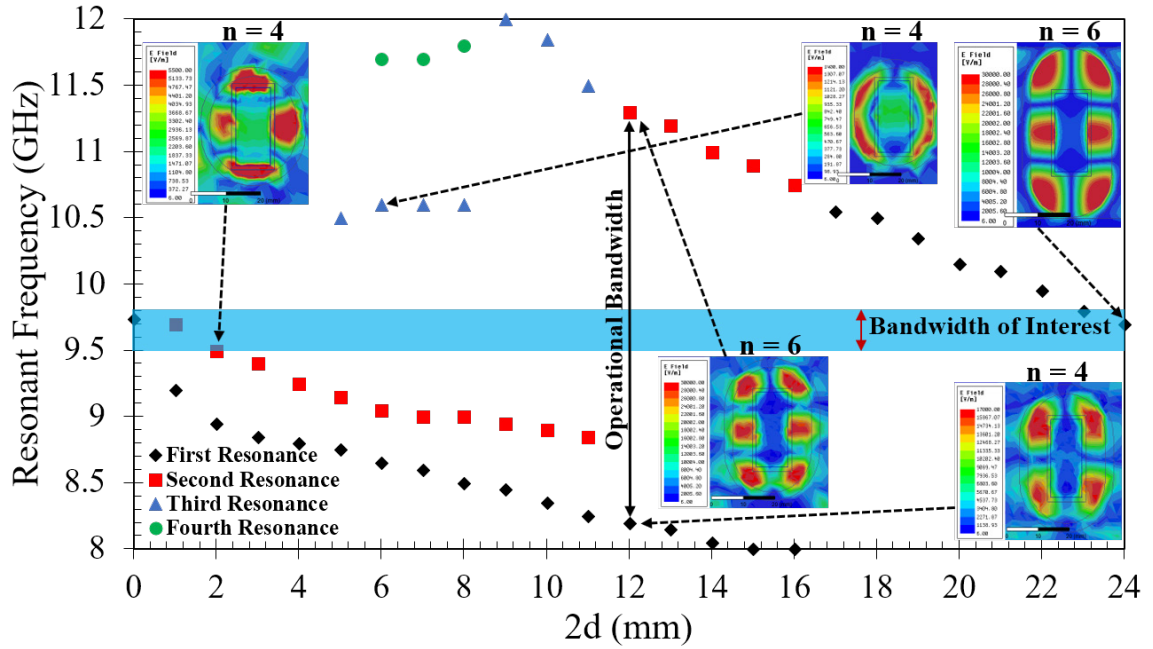


Fig. 4.6 Resonant Frequency vs '2d' for  $[\Delta x, \Delta y, \Delta z] = [1, 0, 0.5]$  mm

In case of the egg-choke ( $2d = 12$  mm),  $n = 4$  at lower resonant frequencies while  $n = 6$  at higher resonant frequencies as seen in fig.4(b). It is interesting to note that for ' $2d$ '=24 mm,  $n = 6$  even though its resonant frequency is the same as that of circular choke for which  $n = 4$ . This is because the distance between two consecutive nodes of electric field standing waves peaks is  $\lambda/2$ . Thus, ' $n$ ' depends on two factors: ' $f_R$ ' and ' $d$ '; ' $n$ ' increases with increase in ' $d$ ' and ' $f_R$ '.

It is desired that the resonant frequencies lie outside our desired bandwidth of 9.5 GHz to 9.8 GHz. The resonant frequencies of the circular choke are near the middle (9 GHz to 10 GHz) of the WR90 bandwidth (8.2 GHz to 12.4 GHz), thereby limiting its operational bandwidth. In contrast, the resonant frequencies of the egg-choke with ' $2d$ '=12mm lie near the lower and upper limits of WR90 bandwidth (around 8.4 GHz and 11.5 GHz). Hence, the operational bandwidth is much larger (more than 2.5 GHz) compared to the desired application bandwidth of 300 MHz. Hence, ' $2d$ '=12 mm is selected as the optimum design



parameter.

Fig.4.7(a) shows the simulation results for different cases of linear misalignment, while Fig.4.7(b) and Fig.4.7(c) show the simulation results considering both linear and rotational misalignment. Misalignment leads to an additional resonance around 8.45 GHz resulting in transmission loss around 0.5 dB and shifts the main resonant frequency around 11.5 GHz. The operational bandwidth considering several combinations of possible linear and rotational misalignment is still 2.5 GHz (8.5 GHz - 11 GHz), thereby showing its robust design.

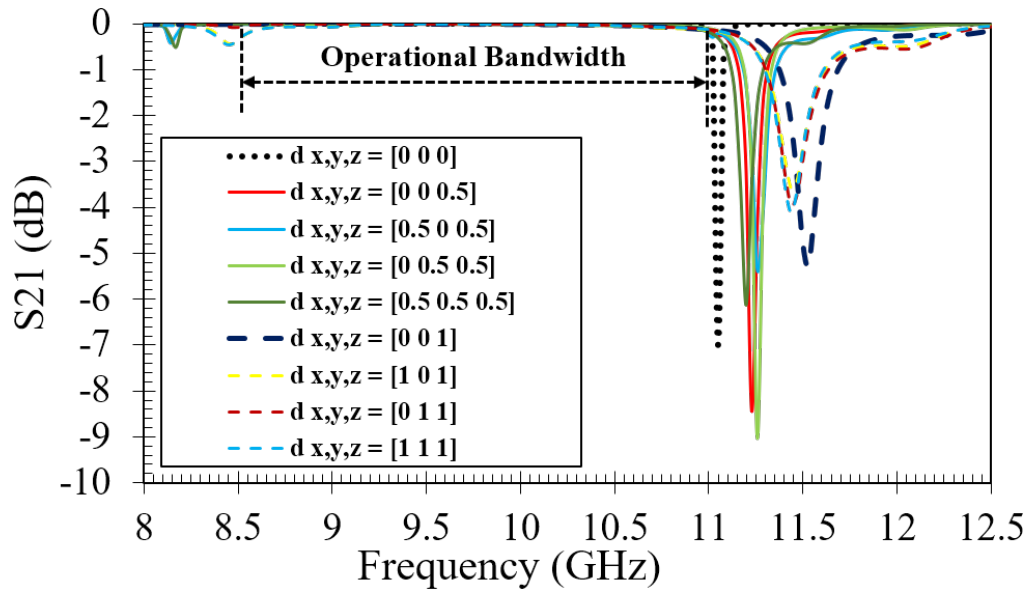
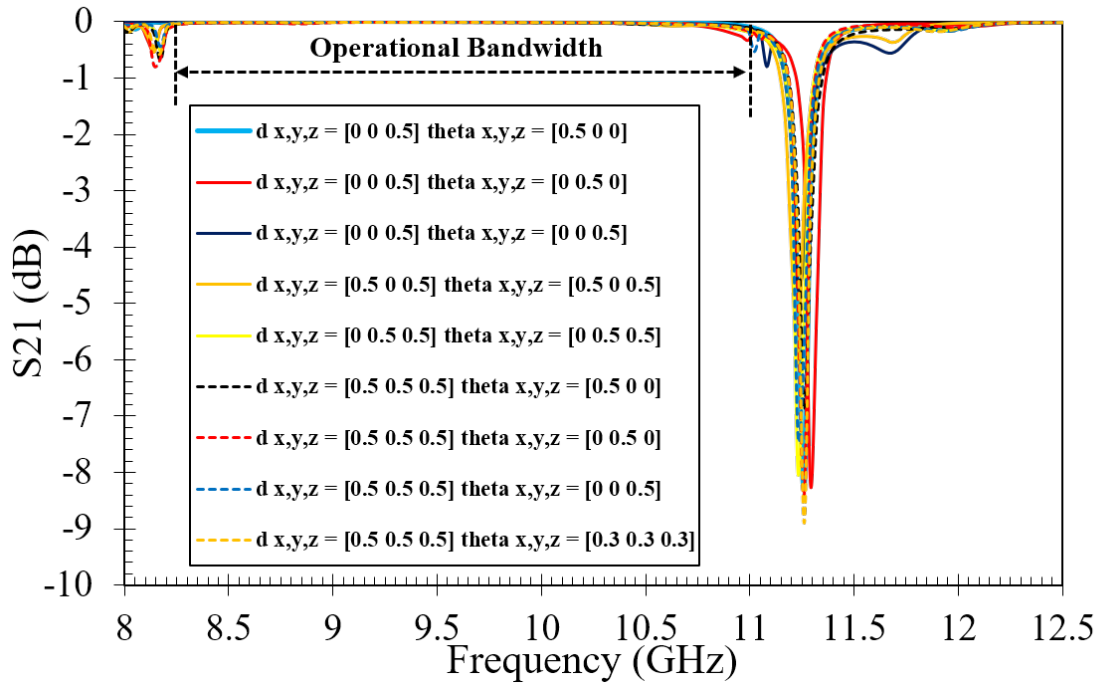
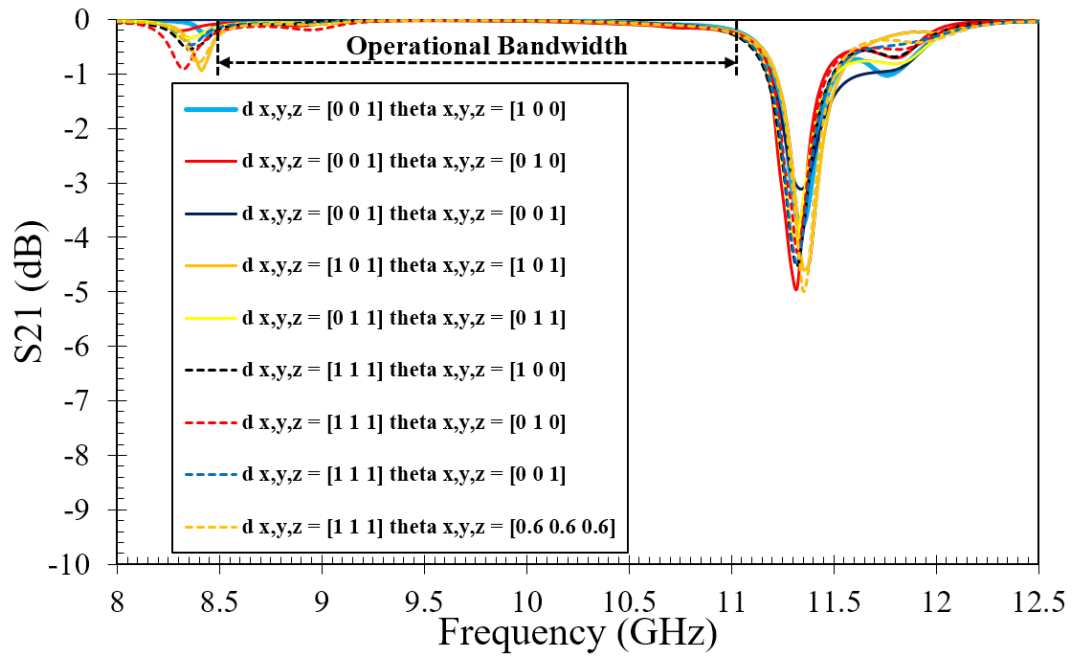


Fig. 4.7. (a) HFSS Simulation Results of Egg-choke flange ( $d = 6$  mm) with linear misalignment. The units are in mm.



(b)



(c)

Fig. 4.7. (b) (c) HFSS Simulation Results of Egg-choke flange ( $d = 6$  mm) with linear and rotational misalignment. The units are in mm and deg respectively.

### 4.3 Measurement Results

Fig.4.8 shows the fabricated egg-choke with its measurement setup block-diagram and the setup with linear and rotational misalignments. The measured co-axial cable loss is 0.1 dB. Fig.4.9(a) shows the measurement results for different cases of linear misalignment, while fig.4.9(b) and fig.4.9(c) show the measurement results with both linear and rotational misalignment. There exists good correspondence with the simulation results shown in Fig.5, and the operational bandwidth with the same combinations of possible linear and rotational misalignment is 2.5 GHz (8.5 GHz to 11 GHz) as expected. Fig.4.9(d) shows the comparison of reflection coefficient for different combinations of flange connections with a nominal separation  $\Delta z = 0.5$  mm between the two flanges (with linear misalignment  $\Delta x = 1$  mm). For the egg-choke, the reflection loss is lower than 20 dB throughout the 2.5 GHz bandwidth and lower than 30 dB in the desired 300 MHz bandwidth from 9.5 GHz to 9.8 GHz. In the center frequency 9.65 GHz, compared to the egg-choke, the reflection loss of the circular choke is higher than 15 dB while that of the flat flange is higher than 18 dB, which shows the better performance of the egg-choke as expected. For a nominal air-gap of 0.46 mm, the reflection loss of panel 1M is lower than -20 dB with the egg-choke.

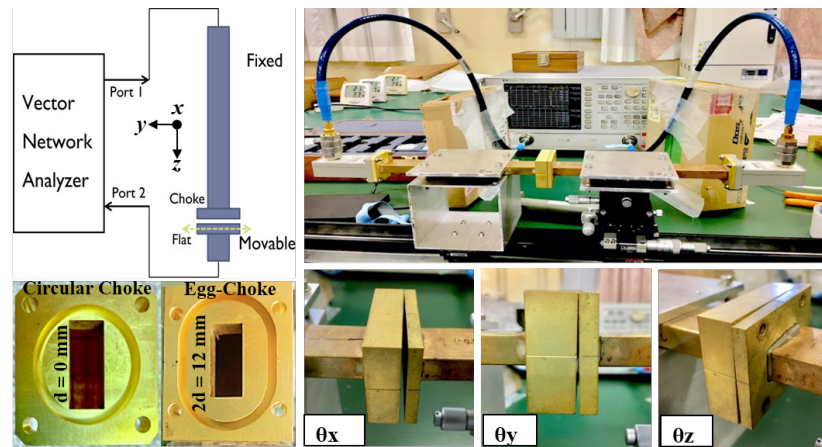


Fig.4.8 Choke Flange Measurement Setup

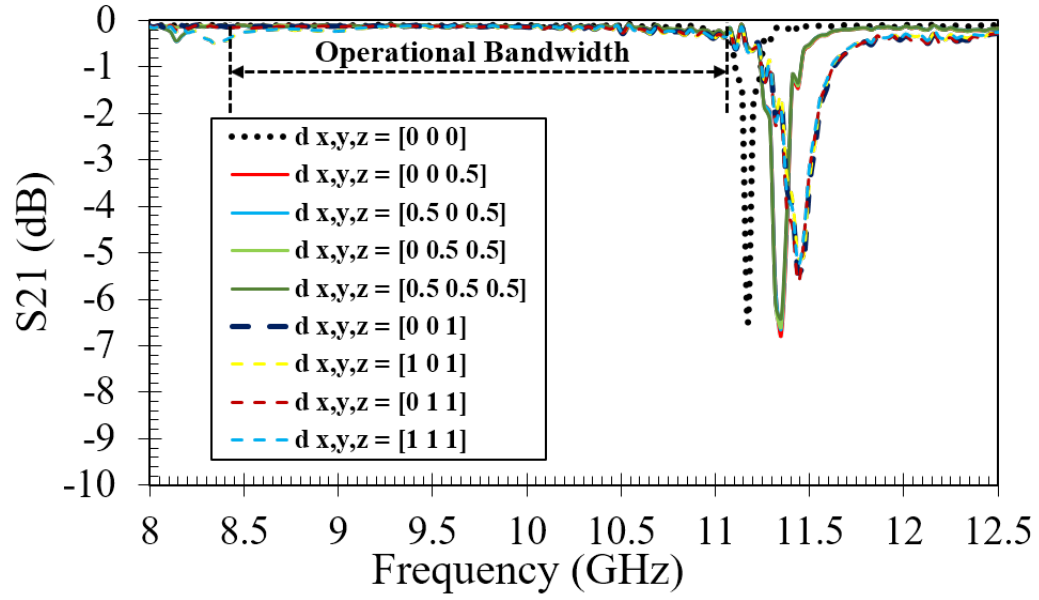


Fig. 4.9. (a) Measurement Results of Egg-choke flange ( $d = 6$  mm) with linear and rotational misalignment. The units are in mm.

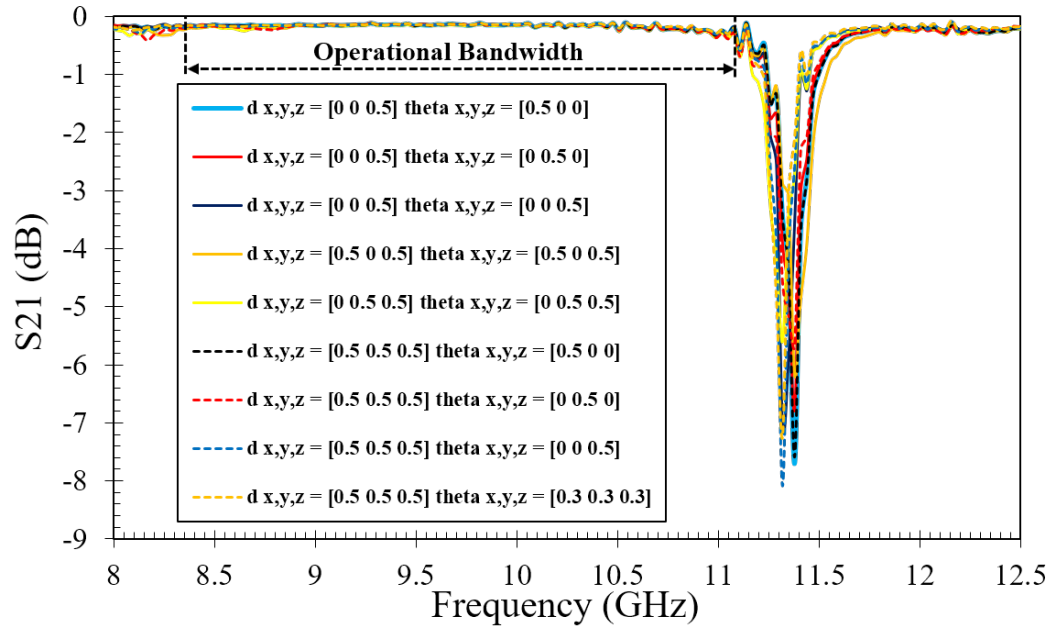


Fig. 4.9. (b) Measurement Results of Egg-choke flange ( $d = 6$  mm) with linear and rotational misalignment. The units are in mm and deg respectively.

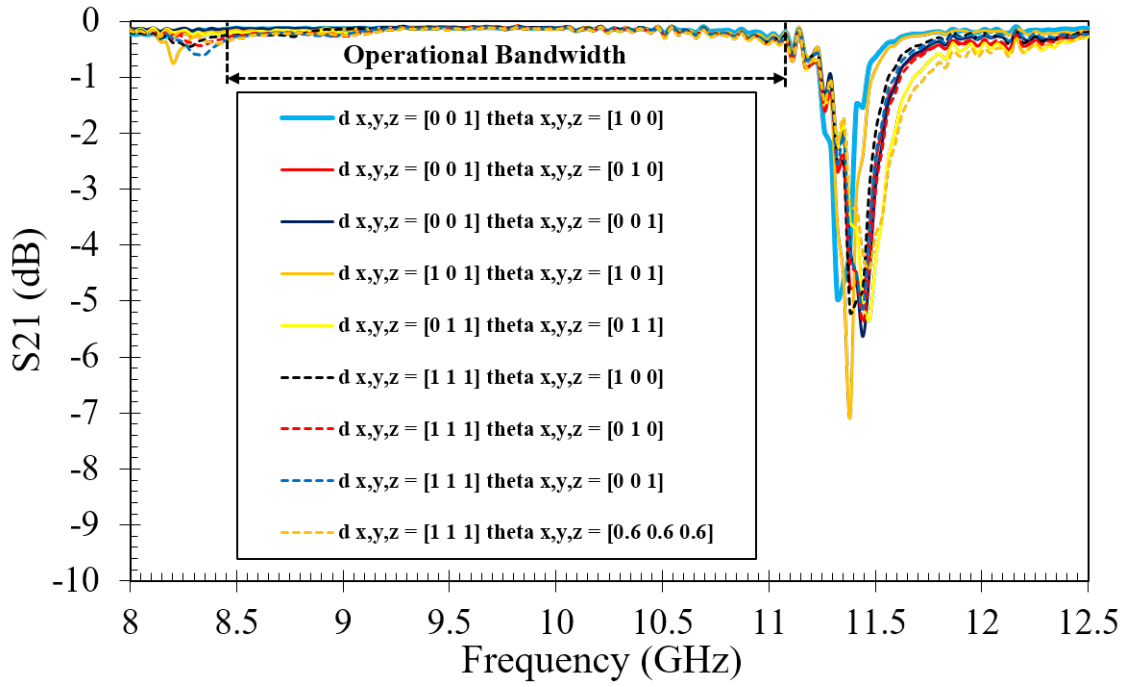


Fig. 4.9. (c) Measurement Results of Egg-choke flange ( $d = 6$  mm) with linear and rotational misalignment. The units are in mm and deg respectively.

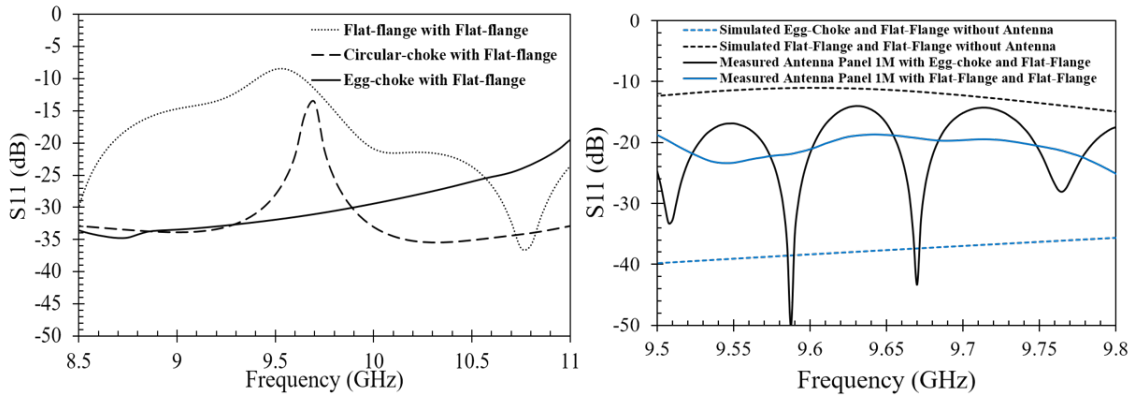


Fig. 4.9(d) Comparison of Reflection Loss for several combinations of flange connections for (left)  $[\Delta x, \Delta y, \Delta z] = [1, 0, 0.5]$  mm without antenna (right) Fabricated Antenna Panel 1M with  $[\Delta x, \Delta y, \Delta z] = [0, 0, 0.46]$  mm

#### 4.4 Eigen Mode Analysis

Fig.4.10 shows a typical propagation of electromagnetic waves in a rectangular waveguide. Although the fundamental mode dominates, higher modes may be generated due to structural geometry. These higher modes can be defined using eigen mode analysis in the following way:

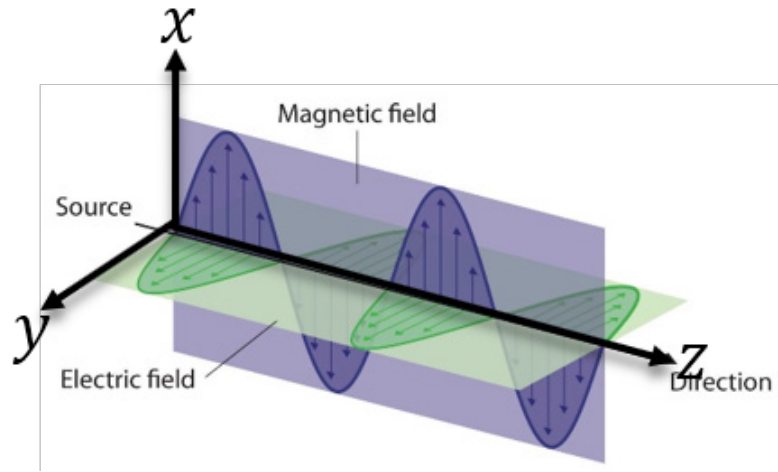


Fig. 4.10. Electromagnetic Field Propagation inside A Rectangular Waveguide

$$\begin{aligned}
 E_x = H_y = & \sum_{m=1}^M \sum_{n=1}^N a_{m,n} \cos\left(\frac{m\pi x}{a}\right) \sin\left(\frac{n\pi y}{b}\right) e^{i\beta_{m,n}z} \\
 & + \sum_{m=1}^M \sum_{n=1}^N b_{m,n} \cos\left(\frac{m\pi x}{a}\right) \sin\left(\frac{n\pi y}{b}\right) e^{-i\beta_{m,n}z}
 \end{aligned} \tag{4.1}$$

$$\begin{aligned}
 E_y = H_x = & \sum_{m=1}^M \sum_{n=1}^N a_{m,n} \sin\left(\frac{m\pi x}{a}\right) \cos\left(\frac{n\pi y}{b}\right) e^{i\beta_{m,n}z} \\
 & + \sum_{m=1}^M \sum_{n=1}^N b_{m,n} \sin\left(\frac{m\pi x}{a}\right) \cos\left(\frac{n\pi y}{b}\right) e^{-i\beta_{m,n}z}
 \end{aligned} \tag{4.2}$$

$$\beta_{m,n}^2 = \left(\frac{2\pi f}{c}\right)^2 - \left(\frac{m\pi}{a}\right)^2 - \left(\frac{n\pi}{b}\right)^2 \quad (4.3)$$

$$f > f_c = \frac{c}{2\pi} \sqrt{\left(\frac{m\pi}{a}\right)^2 + \left(\frac{n\pi}{b}\right)^2} \quad (4.4)$$

where N is the total number of Eigen Modes,  $a_{m,n}$  is the Eigen Mode Forward Propagation Coefficient,  $b_{m,n}$  is the Eigen Mode Backward Propagation Coefficient, a and b are the dimensions of the waveguide in the x and y directions.

TE<sub>10</sub> Mode Propagation for m=1 n=0 is given by:

$$E = E_y = \sin\left(\frac{\pi x}{a}\right) e^{-i\beta_{1,0}z} \quad (4.5)$$

$$H = H_x = \sin\left(\frac{\pi x}{a}\right) e^{-i\beta_{1,0}z} \quad (4.6)$$

$$\beta_{1,0}^2 = \left(\frac{2\pi f}{c}\right)^2 - \left(\frac{\pi}{a}\right)^2 \quad (4.7)$$

Fig.4.11 shows eigen-mode simulation model. PEC Layer isolating the air gap between the choke flange openings and the outside to prevent any leakage. Air box is removed since with airbox eigen modes correspond to phenomenon outside the waveguide, simulation showed no fields inside the waveguide with the airbox. New airbox made (same shape as the waveguide and flange), then inside pec box subtracted with cloning from the new airbox. Finally, after cloning, PEC boxes are deleted. Impedance boundary (500 ohms) replacing the two waveports. No PML boundary to represent radiation since PEC layer isolates the outside leakage.

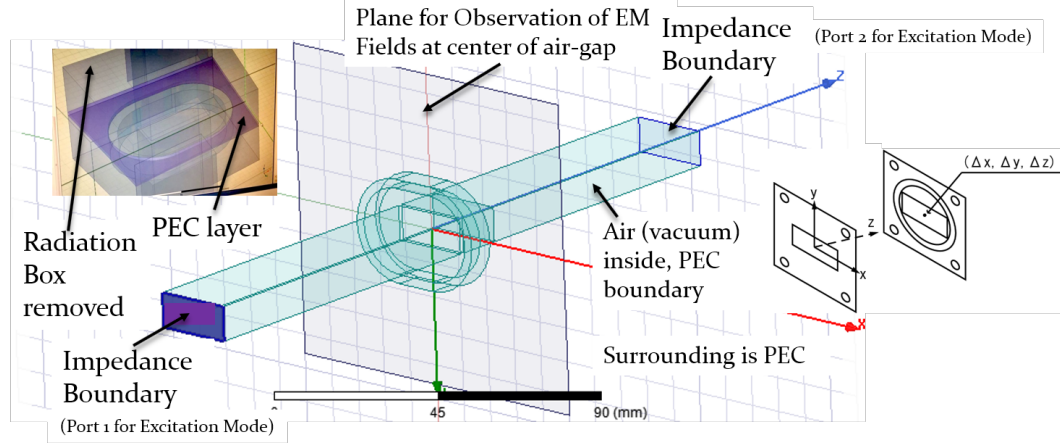


Fig. 4.11. HFSS Eigen-Mode Simulation Model of Choke Flange

Eigen-mode simulation analysis is done for a nominal separation of 1 mm between the choke-flange and flat-flange both two cases:  $[\Delta x, \Delta y, \Delta z] = [0, 1, 1]$  mm and  $[\Delta x, \Delta y, \Delta z] = [0, 0, 1]$  mm. Fig.4.12 shows that for both cases, the transmission loss at the resonant frequency in excitation mode simulation is due to the presence of two higher order eigen-modes with high Quality Factor (Q) near the resonant frequency (*one before the resonant frequency and one after the resonant frequency*). The resonance frequency lies between the two eigen mode frequencies because the resonance effect of the two eigen modes increases the field intensity in the choke ring-flange region and a significant amount of power is leaked out through the choke ring. In HFSS eigen-mode simulation, Q factor is defined as follows:

$$Q_{Higher\ modes} = 2\pi f_E * \frac{E_{FL}}{P_{WG}} \quad (4.8)$$

where ' $E_{FL}$ ' is the energy stored in the ring-shaped flange, ' $P_{WG}$ ' is the fundamental TE<sub>10</sub> Poynting power inside the waveguide and ' $f_E$ ' is the higher mode eigen frequency.



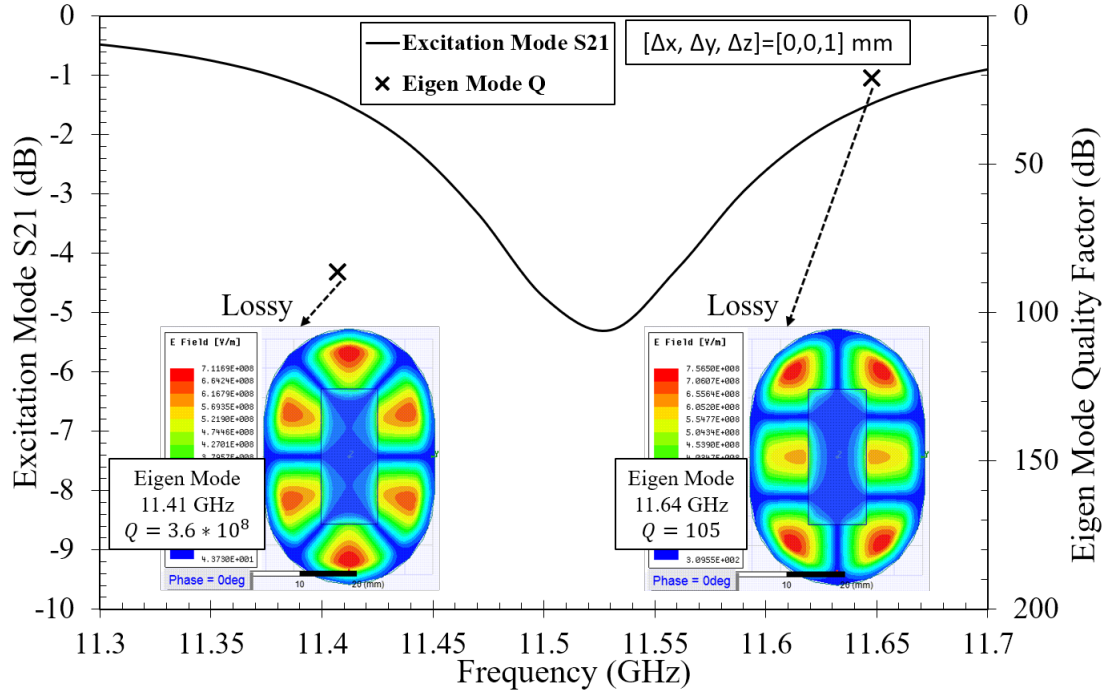


Fig.4.12. (a) Eigen-Mode Analysis of Excitation Mode Simulation of Egg-Choke Flange ( $d = 6 \text{ mm}$ ) for  $[\Delta x, \Delta y, \Delta z] = [0, 0, 1] \text{ mm}$

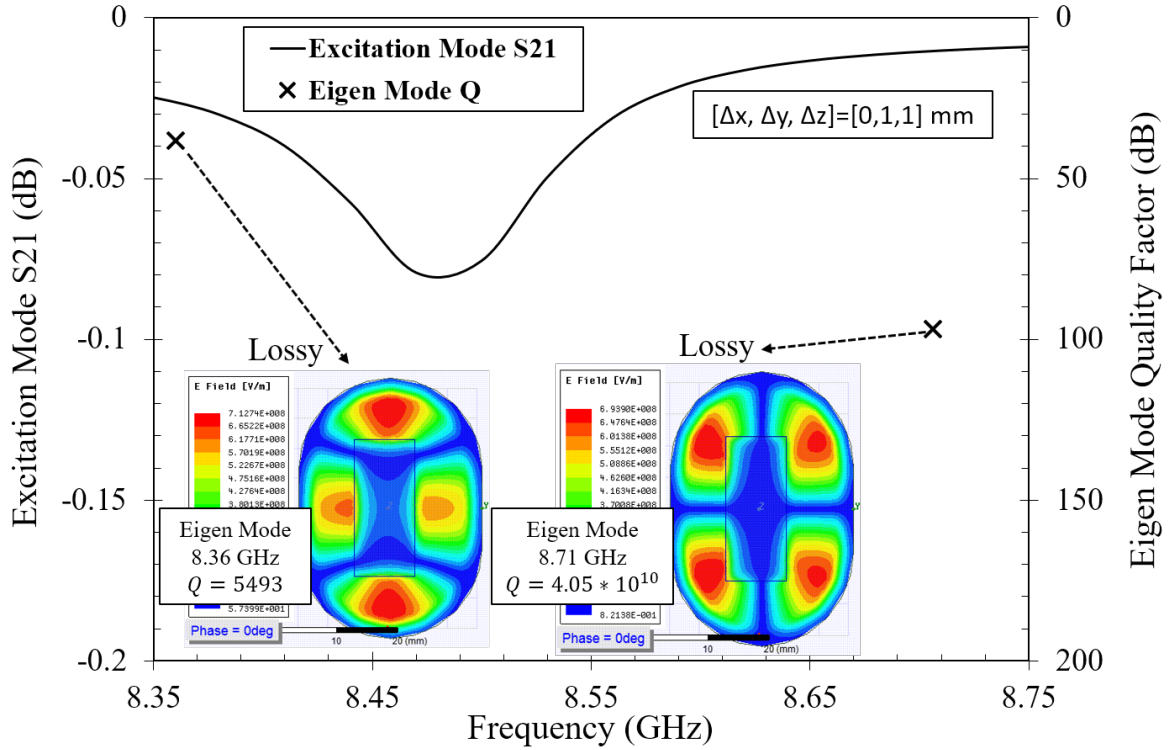


Fig.4.12. (b) Eigen-Mode Analysis of Excitation Mode Simulation of Egg-Choke Flange ( $d = 6 \text{ mm}$ ) for  $[\Delta x, \Delta y, \Delta z] = [0, 1, 1] \text{ mm}$

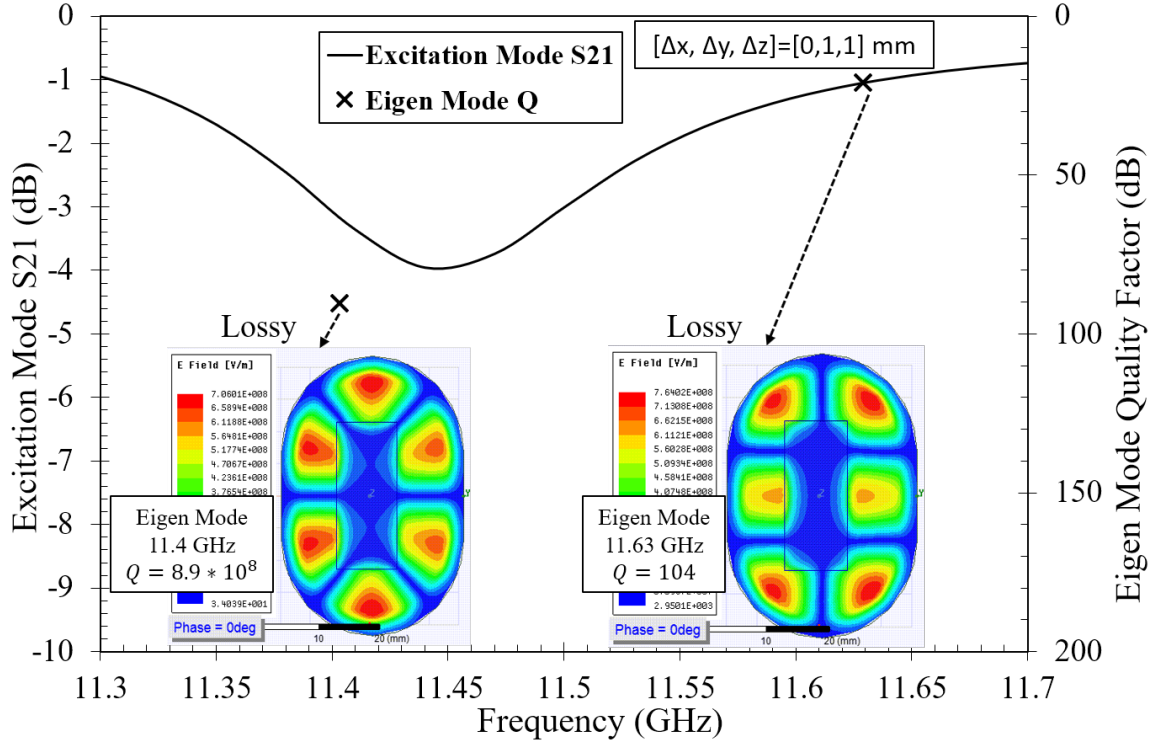


Fig.4.12. (c) Eigen-Mode Analysis of Excitation Mode Simulation of Egg-Choke Flange ( $d = 6$  mm) for  $[\Delta x, \Delta y, \Delta z] = [0, 1, 1]$  mm

Fig.4.13 and Fig.4.14 respectively show the Excitation Mode Poynting Vector and Electric Field intensity of the above two cases:  $[\Delta x, \Delta y, \Delta z] = [0, 1, 1]$  mm and  $[\Delta x, \Delta y, \Delta z] = [0, 0, 1]$  mm. Fig.4.14 shows the mixed mode propagation of the electromagnetic fields at the resonant frequency, which can be decomposed as the vector sum of the fundamental  $TE_{10}$  mode and higher order lossy eigen modes with high Q factor near the resonant frequency shown in fig.4.12.

Standing Waves can be obtained as the superposition of 2 or more Eigen Mode Travelling Waves in the following way considering same amplitude,  $\beta_1 = \beta_2$  (in case of no misalignment) and  $\beta_1 \neq \beta_2$  (in case of misalignment)

$$\begin{aligned}
E &= |E_1| \sin(\omega t - \beta_1 z) + |E_2| \sin(\omega t + \beta_2 z) \\
&= 2A \sin\left(\omega t - \frac{\beta_1 - \beta_2}{2} z\right) \cos\left(\frac{\beta_1 + \beta_2}{2} z\right) = 2A \sin \omega t \cos \beta_0 z \quad (4.9)
\end{aligned}$$

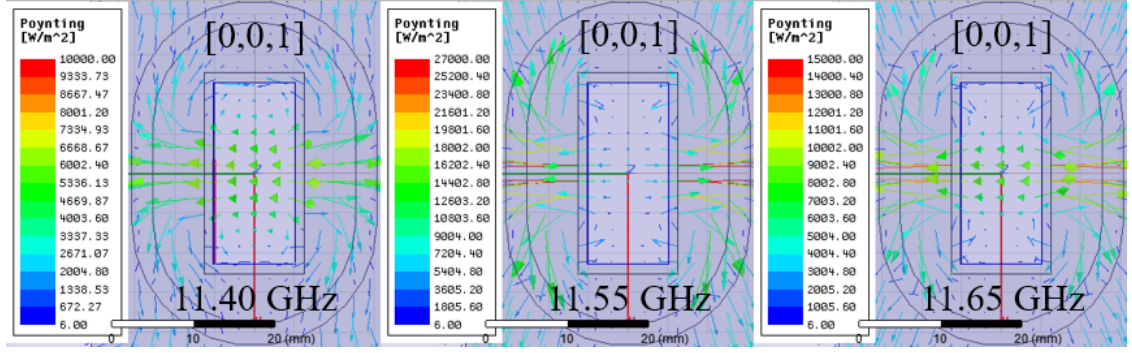
In case of misalignment:

$$\begin{aligned}
E &= |E_1| \sin(\omega t - \beta_1 z) + |E_2| \sin(\omega t - \beta_2 z - 2\theta) \\
&= 2A \sin\left(\omega t - \frac{\beta_1 z + \beta_2 z + 2\theta(\omega)}{2}\right) \cos\left(\frac{\beta_1 z - \beta_2 z - 2\theta(\omega)}{2}\right) \quad (4.10)
\end{aligned}$$

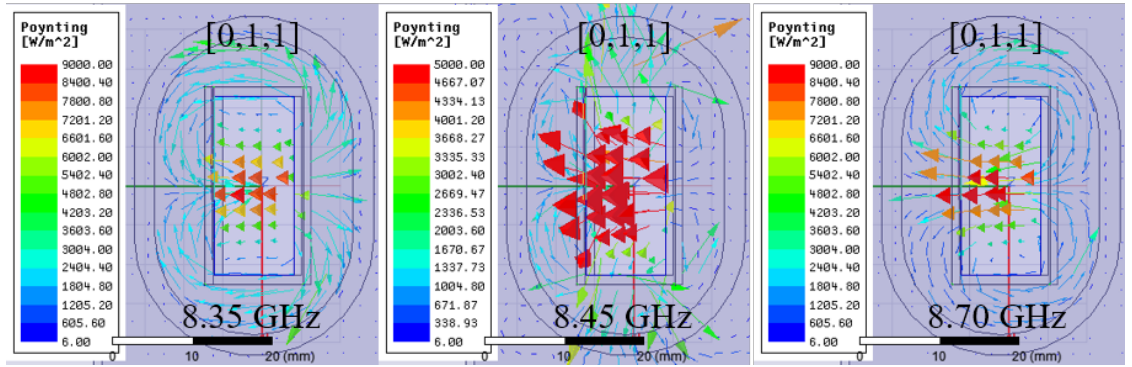
At  $f < f_R$ ,  $2\theta = 0$ : CW rotation. At  $f > f_R$ ,  $2\theta = 180^\circ$ : CCW rotation. At  $f = f_R$ ,  $\beta_1 z + \beta_2 z + 2\theta = 0$ ; thus there is no rotation.

Fig.4.13(a) and Fig.4.14(a) show that in case of no misalignment, due to symmetry, the electromagnetic fields have no preferred direction of motion in the flange region. As a result, there exists standing waves at all frequencies without any rotation. In Fig.4.14(b-c), the arrows show the direction of motion of the electromagnetic fields with high intensity. In case of misalignment, since symmetry is broken, the electromagnetic fields have a preferred direction of motion in the flange region and this direction changes from clockwise (CW) to counter-clockwise (CCW) before and after the resonant frequency; while there is no rotation due to formation of standing waves at the resonant frequency.

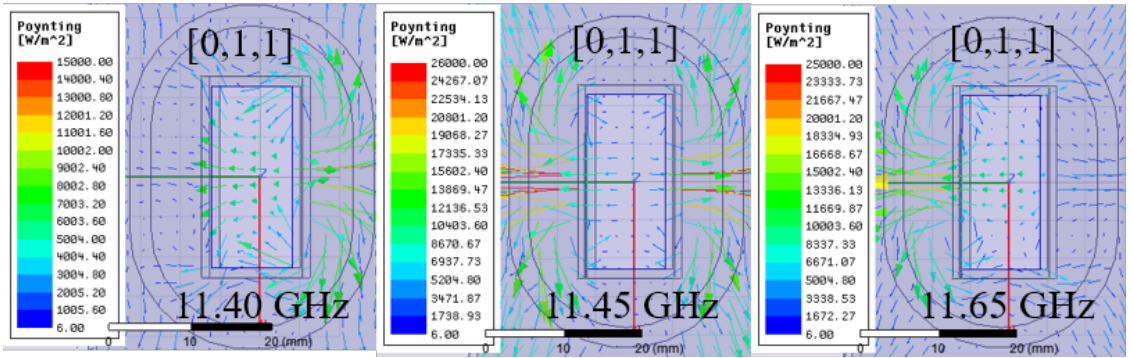
This mixed excitation field rotation before and after the resonance frequency in Fig.4.14(b-c) can be explained as the superposition of two standing eigen-mode Electric fields before and after the resonance frequency shown in Fig.4.12(b-c), whose peak nodes are rotated w.r.t. each other. CCW or CW direction of rotation depends on the phase relationships between these two eigen-mode Electric fields.



(a)



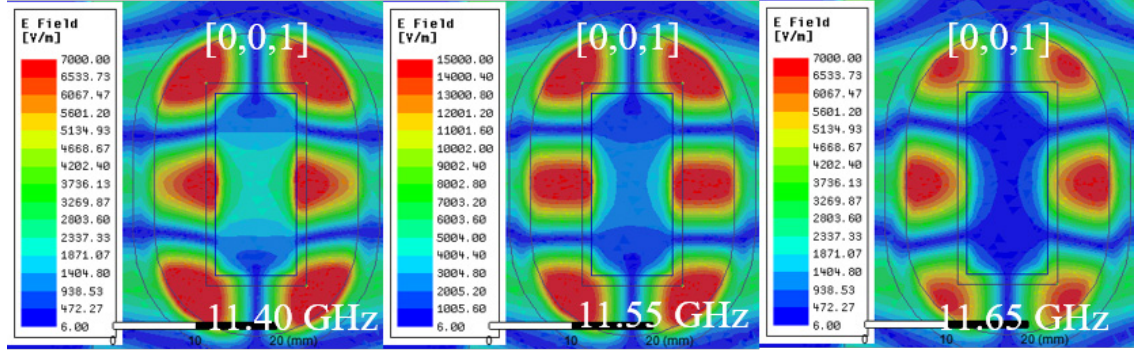
(b)



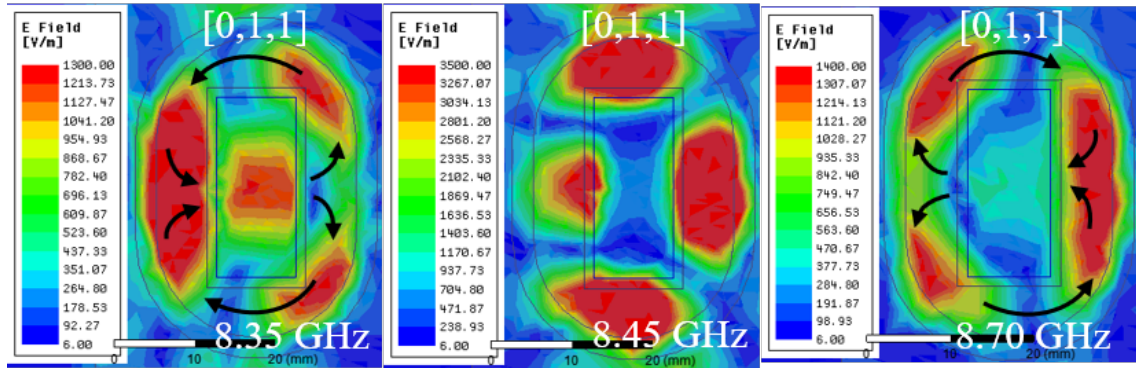
(c)

Fig. 4.13. Simulation Excitation Mode Poynting Vector of Egg-choke Flange ( $d = 6$  mm) for (a) Case  $[\Delta x, \Delta y, \Delta z] = [0, 0, 1]$  mm  $f_R = 11.55$  GHz (b) Case  $[\Delta x, \Delta y, \Delta z] = [0, 1, 1]$  mm  $f_R = 8.45$  GHz (c) Case  $[\Delta x, \Delta y, \Delta z] = [0, 1, 1]$  mm  $f_R = 11.45$  GHz

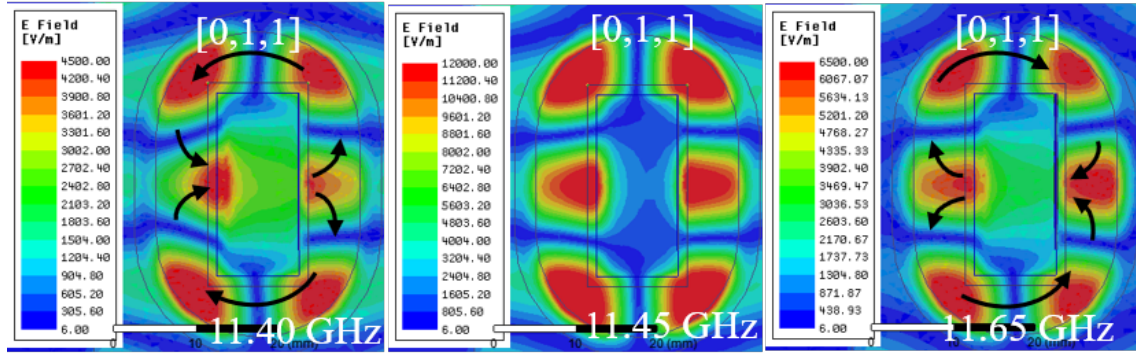




(a)



(b)



(c)

Fig. 4.14. Simulation Excitation Mode Electric Field Intensity of Egg-choke Flange ( $d = 6$  mm) for (a) Case  $[\Delta x, \Delta y, \Delta z] = [0, 0, 1]$  mm  $f_R = 11.55$  GHz (b) Case  $[\Delta x, \Delta y, \Delta z] = [0, 1, 1]$  mm  $f_R = 8.45$  GHz (c) Case  $[\Delta x, \Delta y, \Delta z] = [0, 1, 1]$  mm  $f_R = 11.45$  GHz

## 4.5 Summary

This chapter presented the design concept and performance analysis of an egg-choke flange for connecting adjacent panels of a space-borne antenna array. Although the design was primarily focused for application in MicroX-SAR mission, the design methodology is general and applicable for designing a choke-flange for operation outside the X-band. The key aspect of this choke flange design is that the shape of the choke determines the resonant frequency. Thus, by careful design the device can be operable in the frequency bandwidth of interest. The fabricated egg-choke based on HFSS design showed wide-band operability in the X-band from 8.5 GHz to 11 GHz after taking into consideration possible linear and rotational misalignments during practical operation, thereby showcasing its robust design.



## CHAPTER 5. CONCLUSION

### 5.1 Summary and Discussion

This dissertation work focused on the development of critical microwave technology for realization of a SAR antenna compatible with 100 kg class small satellite.

A passive-array antenna with center-fed waveguide feeding network was proposed as the best candidate for the MicroX-SAR Mission.

The novelty of the proposed feeder network design can be summarized as follows:

- ‘**N $\lambda$ -Offset** Wideband Wide-beam Deployable Antenna Waveguide Feeder Network Design with **Double Resonance  $\tau$ -junction** (for edge-panels) and **Double Resonance PMC-junction** (for 2-input 2-output **odd number center-panel**)’
- **Center-feed Scheme** (1 feeder / panel) for single-pol antenna and **Edge-feed Scheme** (2 feeders / panel) for single / dual-pol antenna
- Reflection Degradation due to Adhesive thickness estimation mismatch solved by increasing the length of all coupling slots by 0.2 mm.
- Fabricated Antenna Panel Array achieved 40.8 dBi Gain with 1.2 dBi loss, 68% aperture efficiency, 91.2% arraying efficiency and 300 MHz bandwidth

Measurement results of each isolated antenna panel and antenna panel arrays of the Engineering Model Prototype Unit showed that wide-beam antenna is achieved with high gain, good antenna aperture efficiency and high arraying efficiency in the desired 300 MHz



bandwidth. Table 6.1 shows the performance comparison of proposed antenna with existing research work

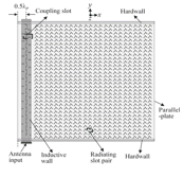
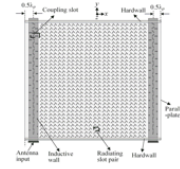
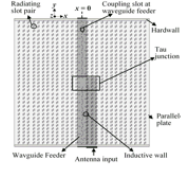
An egg-choke flange was designed for contactless connection between two waveguide feeder joints of adjacent antenna panels during deployed condition of MicroX-SAR Antenna array in space. It was optimally designed for wideband applications in X band

The novelty of the egg-choke design and analysis can be summarized as follows:

- **‘Eigen-mode based Wideband Robust Contactless Egg-Choke Flange Design considering Linear and Rotational Misalignment’**
- The shape of the choke is optimally changed from circular to egg-shape to shift the resonance frequencies outside the desired bandwidth.
- Fabricated Egg-choke showed 2.5 GHz Operational Bandwidth (8.5 GHz to 11 GHz) with transmission loss less than 0.1 dB
- It is explained why **electromagnetic waves change direction of rotation at resonant frequency in case of misalignment due to two higher-mode high Q-factor eigen-modes before and after resonant frequency.**

It is hoped and expected that this dissertation work will lead to the realization of the Flight Model (FM) antenna panels and contribute to successful completion of JAXA’s MicroX-SAR Mission.

Table 5.1. Performance Comparison of Proposed MicroX-SAR Antenna with Existing Research Work

Performance Metrices	End-feed Antenna with 1 feeder [6]	End-feed Antenna with 2 feeders [7]	Proposed Center-feed Antenna with 1 feeder [1]
Structure			
Polarization	Single Circular, RHCP	Dual Circular, LHCP + RHCP	Single Vertical, VV
Operational Bandwidth	130 MHz (9.585 GHz – 9.715 GHz)	130 MHz (9.585 GHz – 9.715 GHz)	300 MHz (9.5 GHz – 9.8 GHz)
SAR Image Resolution	3 meters (Spotlight)– 10 meters (Strip-map)	3 meters (Spotlight)– 10 meters (Strip-map)	1 meter (Spotlight)– 3 meters (Strip-map)
Gain	34.9 dBic	34.5 dBic (LHCP) 34.6 dBic (RHCP)	35.2 dBi
Aperture Efficiency	54%	49.2% (LHCP) 50.1% (RHCP)	76.6%
Side Lobe Level	-12.6 dBic	-12 dBic (LHCP) -13 dBic (RHCP)	-13.2 dBi
NESZ	-17.9 dB (Spotlight) -18.1 dB (Strip-map)	-17.2 dB (Spotlight) -17.4 dB (Strip-map)	-18 dB (Spotlight) -18.7 dB (Strip-map)
Ambiguity to Signal Ratio (PRF=4kHz)	AASR = -24 dB RASR = - 24 dB (with linear FM)	AASR = -28 dB RASR = - 31 dB (with Linear FM)	AASR = -25 dB RASR = -26.5 dB (with Linear FM)

## 5.2 Future Work

Measurement results of EM Antenna panels showed reflection mismatch due to inaccurate estimation of adhesive thickness, which was solved by increasing the length of all coupling slots by 0.2 mm. Flight Model of Antenna Panel 3M was fabricated and VNA measurement validated improvement in reflection coefficient as predicted by HFSS simulations. The other FM panels of the left wing and the entire ring wing panels will be fabricated, and 7-panel near-field measurement needs be done to complete the antenna design for MicroX-SAR Mission.



## **APPENDIX A.    FFT-BASED ANTENNA PATTERN COMPUTATION TOOL**

### **A.1    Background**

A lot of attention is being paid to antenna performance for SAR Mission design, performance evaluation and end-to-end simulations [49]. Practical points of interest are thermos-elastic surface distortions of the antenna surface, iterating on the antenna size, defocusing of antenna patterns and gain losses. Although there are a handful of reliable commercial software for accurate estimation of antenna patterns like Ansys HFSS and GRASP, unfortunately, as the antenna size increases the time taken by them to compute antenna patterns is very long, sometimes even days which make them inefficient for use for efficient performance evaluation from a SAR processing perspective. Moreover, it is not easy to take into account the effect of any irregular surface distortions on the antenna surface, which is a further bottleneck for efficient performance estimation, SAR processing and quick-fire end-to-end simulations. There are several papers in literature where attempts have been made for very fast antenna pattern estimation using Fast Fourier Transforms (FFTs) both planar arrays [54] and reflectors [52] [53] [67] [73] [74], however the results are far from accurate especially in case of the latter while in the former case, FFT-based computations have been done only for uniformly spaced arrays without any surface deformations. In this paper, we propose an FFT-based highly accurate general antenna computation tool for planar arrays with surface distortions and reflectors. For the latter, we combine the methods of Geometrical Optics with FFT for fast and accurate estimation of reflector antenna patterns for different locations of the feed array (off-set and non-offset).

We apply a beam-center approximation method which is highly accurate, unlike the methods available in literature. To validate our methodology, for reflectors, we do a case study of Tandem-L antenna [45] and compare the co-polarization and cross-polarization patterns with the simulation results obtained from GRASP and for planar arrays, we do a case study of MicroX-SAR antenna [1] and compare the computed antenna patterns with Ansys HFSS simulation and hardware measurement results. Furthermore, we study the effect of thermos-elastic surface deformations on MicroX-SAR antenna pattern from software-simulated surface deformation profiles using our Antenna Class Pattern Tool.

This research aims at efficiently computing antenna patterns for reflectors and planar arrays using Geometrical Optics and FFT, while taking into account possible surface deformations in the radiators. As a case study, the 1D and 2D antenna patterns are computed for DLR's Tandem-L (reflector) and JAXA's MicroX-SAR (planar array) using the developed Antenna Class Pattern-Tool in Python, and the simulation results are compared with commercially available tools: GRASP and Ansys HFSS, along with measurement results (for MicroX-SAR). Comparisons showed that the simulation results are accurate within  $\pm 0.1$  dB and the computation time is only a few seconds compared to several hours for GRASP and HFSS.

The rest of this chapter is organized as follows: First, we summarize the duality in space and frequency domain for Array Factor computation taking into consideration surface deformations. We demonstrate our method of combining Geometrical Optics with FFT and the beam-center approximation concept. Next, we provide the detailed methodology of our Pattern Tool computation algorithm for reflector antennas. Finally, we compare our results with software simulation results and discuss our computation accuracy.

### A.1.1 Duality between Space Domain and Frequency Domain

Consider a planar array formed by identical isotropic elements spaced linearly apart with spacing  $dx$  and  $dy$  as shown in fig.A.1 where  $N_{az}$  and  $N_{el}$  are the total number of elements along azimuth and elevation respectively.

A satellite orbiting around the earth will be exposed to thermal stress due to temperature fluctuations depending on the relative position of the satellite w.r.t. the Sun. This leads to antenna surface deformations, primarily along  $z$  direction as shown in fig.A.2.

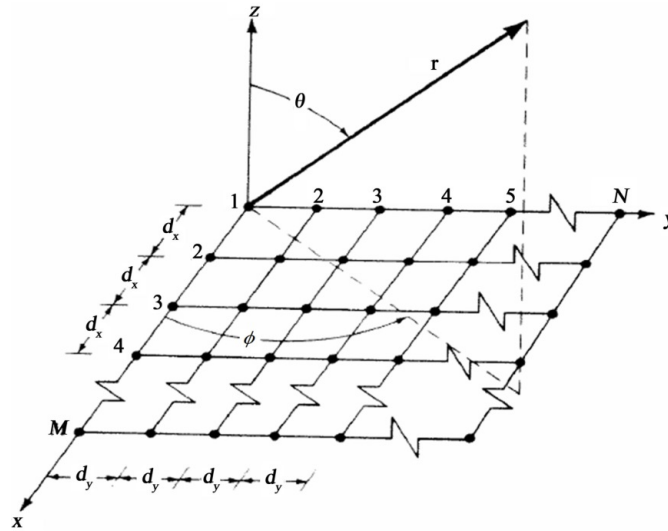


Fig. A.1. Planar Array Geometry

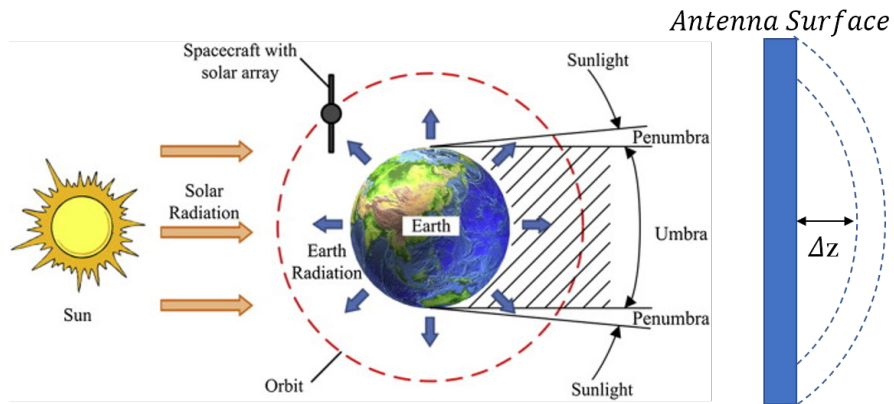


Fig. A.2. Thermo-elastic Surface Deformation of Space-borne Antenna

In the space domain, the normalized array factor can be computed as:

$$AF(\theta, \varphi) = \frac{1}{N_{az}N_{el}} \sum_{n_x=0}^{N_{az}-1} \sum_{n_y=0}^{N_{el}-1} a_{n_x, n_y} e^{-jk r_{n_x, n_y}(\theta, \varphi)} \quad (A.1)$$

$$r_{n_x, n_y}(\theta, \varphi) = n_x d_x u(\theta, \varphi) + n_y d_y v(\theta, \varphi) + \Delta z_{n_x, n_y} w(\theta, \varphi) \quad (A.2)$$

$$k = \frac{2\pi}{\lambda} \quad (A.3)$$

$$u(\theta, \varphi) = \sin\theta \cos\varphi \quad (A.4)$$

$$v(\theta, \varphi) = \sin\theta \sin\varphi \quad (A.5)$$

$$w(\theta, \varphi) = \cos\theta \quad (A.6)$$

where ‘a’ is the complex excitation coefficient corresponding to each element.

In the frequency domain, the same can be computed using FFT in the following way:

$$AF(\theta, \varphi) = \text{FFT}(w_{n_x, n_y}) = \frac{1}{N_{az}N_{el}} \sum_{n_x=0}^{N_{az}-1} \sum_{n_y=0}^{N_{el}-1} w_{n_x, n_y} e^{-j \frac{2\pi k_x n_x}{N_{az}}} e^{-j \frac{2\pi k_y n_y}{N_{el}}} \quad (A.7)$$

$$w_{n_x, n_y} = a_{n_x, n_y} e^{-jk \Delta z_{n_x, n_y}} \quad (A.8)$$

$$\frac{k_x}{N_{az}} = \frac{d_x}{\lambda} u(\theta, \varphi) \quad (A.9)$$

$$\frac{k_y}{N_{el}} = \frac{d_y}{\lambda} v(\theta, \varphi) \quad (A.10)$$

The antenna Gain is obtained by the principle of pattern multiplication assuming each element has identical radiation pattern  $E(\theta, \varphi)$  in the following way:

$$G(\theta, \varphi) = 20 \log_{10}(AF(\theta, \varphi) * E(\theta, \varphi)) \quad (A.11)$$

Assuming that the pattern of each element is not affected by surface deformation, the maximum degradation in gain is equal to the maximum degradation in the array factor

which occurs at the antenna boresight ( $\theta = 0$ ). This drop in peak gain can be approximated applying Taylor series expansion and calculated as follows if equation (A.11) is valid:

$$|k\Delta z_n| \ll 1 \quad (\text{A. 12})$$

$$\Delta AF(\theta, \varphi) = \frac{1}{N_{az}N_{el}} \left( N_{az}N_{el} - \sum_{n_x=0}^{N_{az}-1} \sum_{n_y=0}^{N_{el}-1} e^{-ik\Delta z_{n_x,n_y}} \right) = k^2 \sigma_{\Delta z_{m,n}}^2 \quad (\text{A. 13})$$

## A.2 Planar Arrays

### A.2.1 Case Study with MicroX-SAR Antenna

Antenna patterns are computed for MicroX-SAR 7-panel antenna array [1]. Figure A.3 and fig.A.4 shows the antenna configuration where for each panel  $N_{az} = 33$   $N_{el} = 26$   $dx = dy = \lambda/2$ ,  $f_0 = 9.65$  GHz,  $\lambda_0 = 31.08$  cm. Fig.A.5 shows and fig.A.6 shows the 3D and 2D maximum thermal deformation profile computed by Technosolver Co. Ltd. when the antenna surface is perpendicular to the solar rays. There is only significant deformation along z direction, the deformation along x and y directions are about 0.02 mm, hence negligible and not considered during pattern computation. The deformation profile is symmetric w.r.t. the center panel but the deformation of each panel is not identical. Fig.A.7 and fig.A.8 show the antenna elevation and azimuth patterns computed with the Pattern Tool including the case for thermal deformation and compares the results with the case of no deformation in HFSS and measurement results. The HFSS 7-panel pattern is computed from the HFSS results of each panel with a spacing of 697.5 mm between the center of each panel. Fig.A.9 and fig.A.10 show that the 3dB beam-width and first side-lobe level of the pattern computed with pattern tool match very well with that computed with HFSS.



The 3dB beamwidth error is 0.1 degrees in elevation and 0.01 degrees in azimuth whereas the error in first side-lobe level is 0.25 dB for both elevation and azimuth. The peak gain error is 0.1 dB for both cases assuming an antenna aperture efficiency of 63% which is computed as the product of the antenna arraying efficiency and the average antenna aperture efficiency of each panel obtained from the full panel antenna simulation and measurement results in Chapter 3. Fig.A.11 shows that thermal deformation results in reduction in the peak synthesized gain by 0.14 dB which matches well the approximation computation of 0.15 dB using equation (5.13) for  $\sigma_{\Delta z}=1.04$  mm. Fig.A.9 shows that thermal deformation has negligible effect on the 3dB antenna beamwidth. Fig.A.10 shows that thermal deformation increases the first side-lobe level by 0.7 dB. Fig.A.12 and fig.A.13 shows the 2D antenna patterns (amplitude and phase) computed with the pattern tool with and without deformation. Although the distortion in amplitude is not much, there is significant distortion in the 2D phase as expected. Fig.A.14 shows the comparison of the antenna patterns in 3D space.

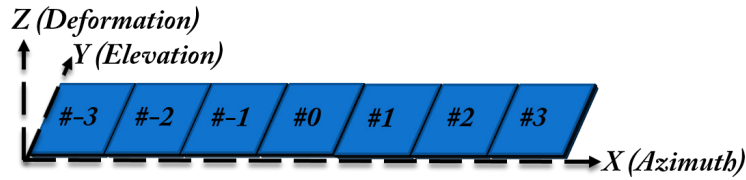


Fig. A.3. Antenna Configuration of MicroX-SAR Satellite

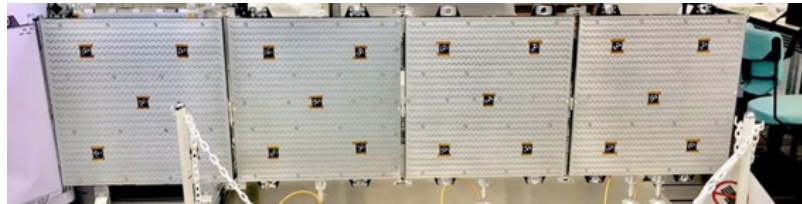


Fig. A.4. Fabricated Left Wing of Antenna Panel Array of MicroX-SAR Mission

### A.2.2 Consideration of Thermo-elastic Surface Deformations

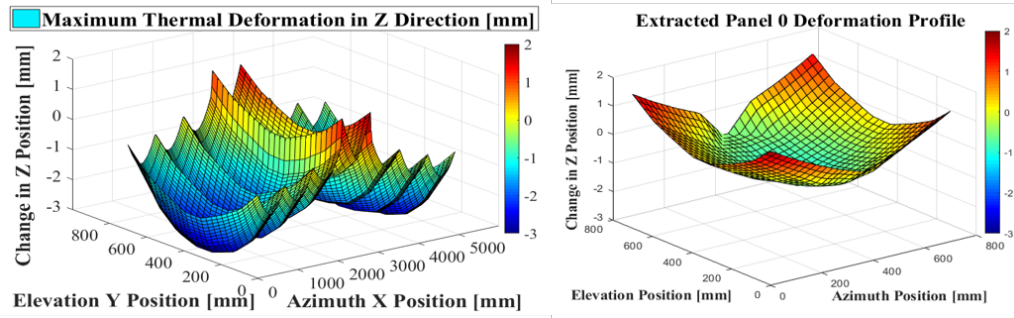


Fig. A.5. 3D Surface Deformation Profile of MicroX-SAR Antenna Array

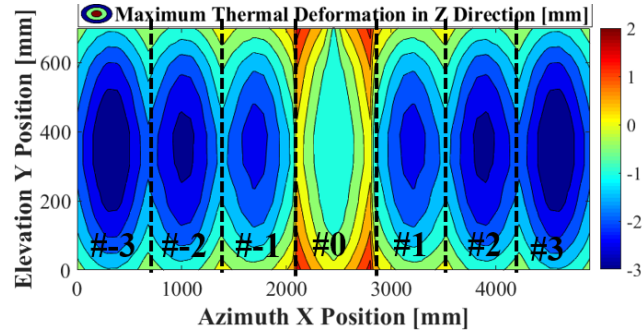


Fig. A.6. 2D Surface Deformation Profile of MicroX-SAR Antenna Array

### A.2.3 Comparison with HFSS Simulations and Measurement Results

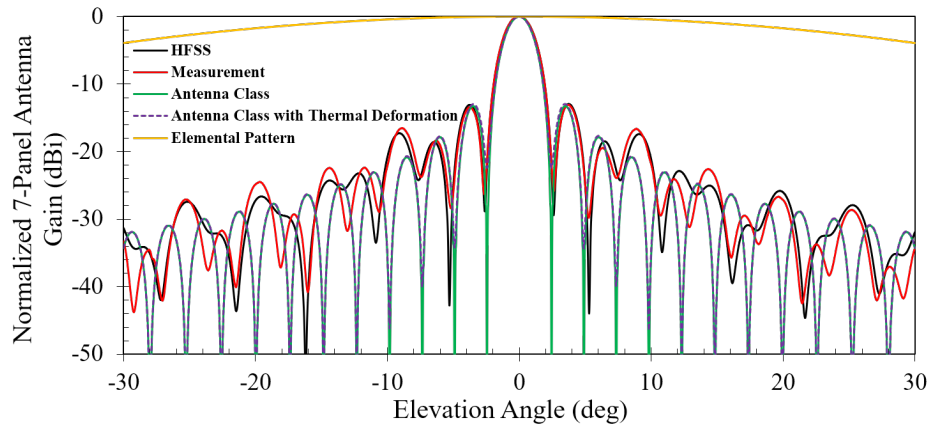


Fig. A.7. MicroX-SAR 7-Panel Antenna Elevation Pattern with Thermal Deformation

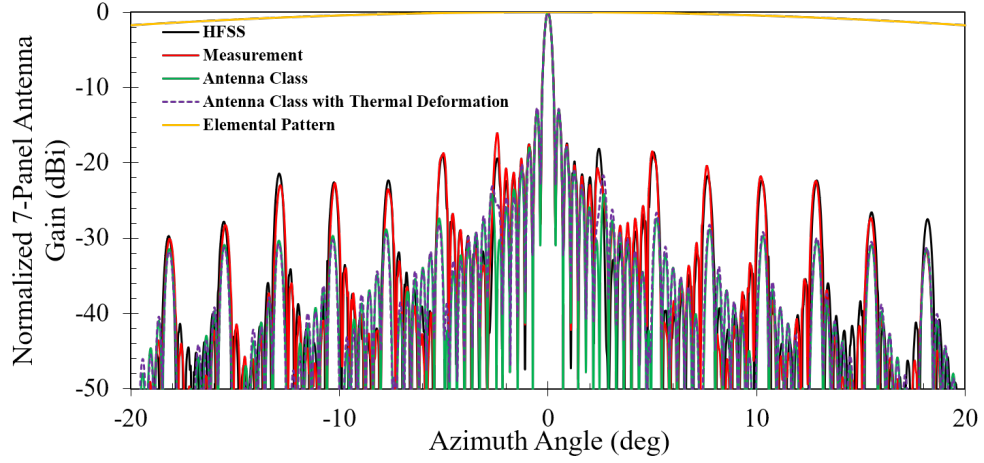


Fig. A.8. MicroX-SAR 7-Panel Antenna Azimuth Pattern with Thermal Deformation

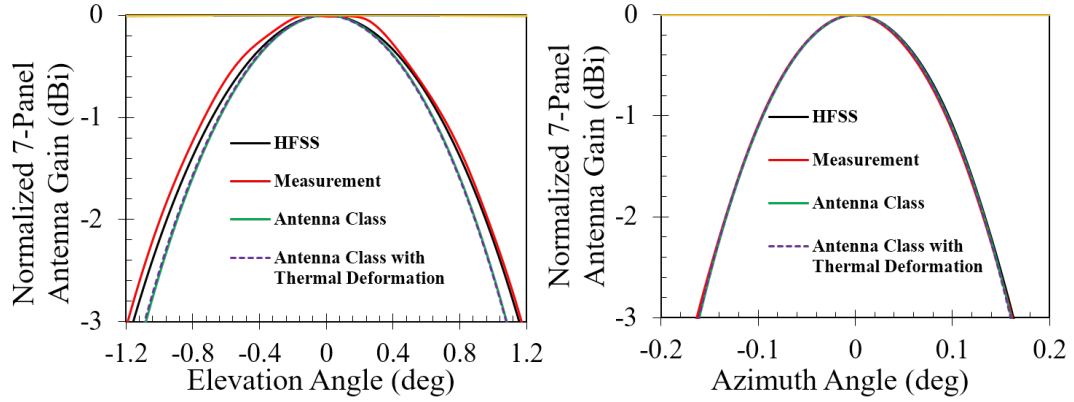


Fig. A.9. Comparison of MicroX-SAR 7-Panel Antenna 3dB Beam-width

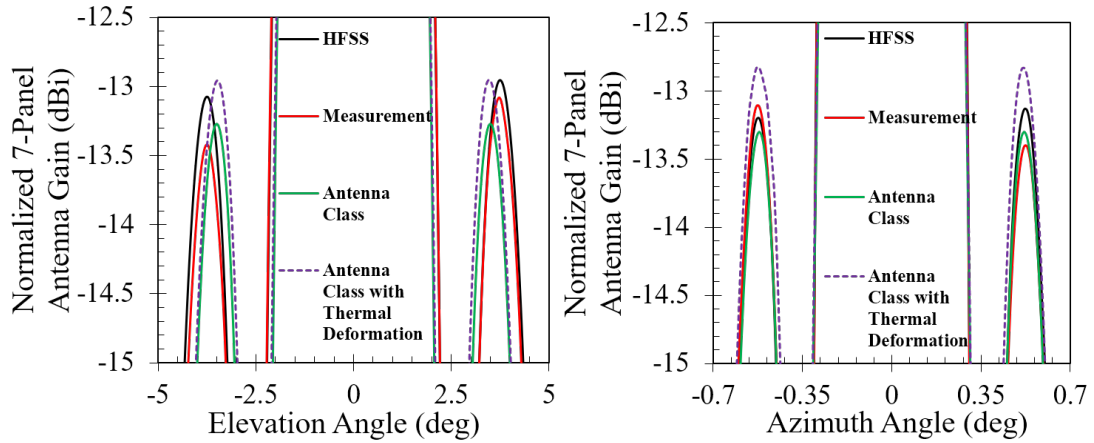


Fig. A.10. Comparison of MicroX-SAR 7-Panel Antenna First Side-lobe Level

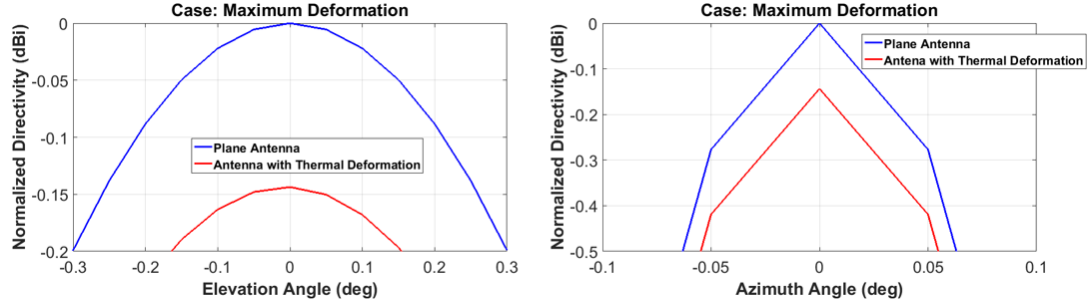


Fig. A.11. Effect of Thermal Deformation on Peak Gain of MicroX-SAR 7-Panel Antenna

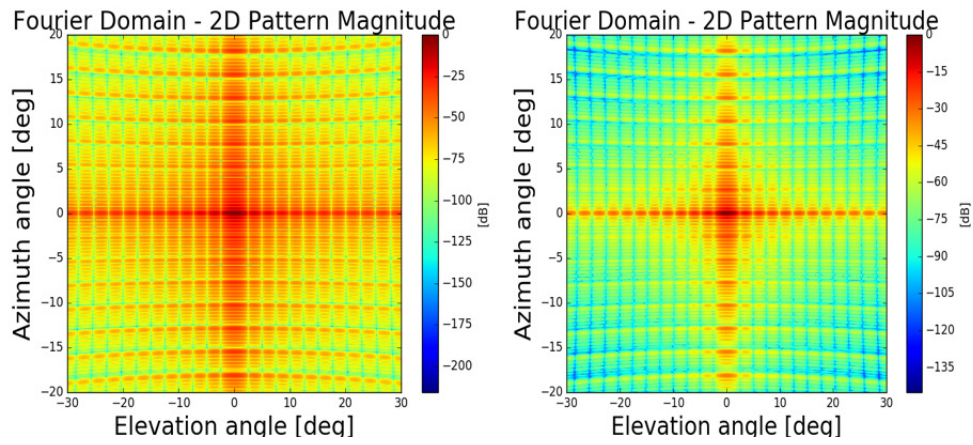


Fig. A.12. Effect of Thermal Deformation on 2D Amplitude of MicroX-SAR 7-Panel Antenna

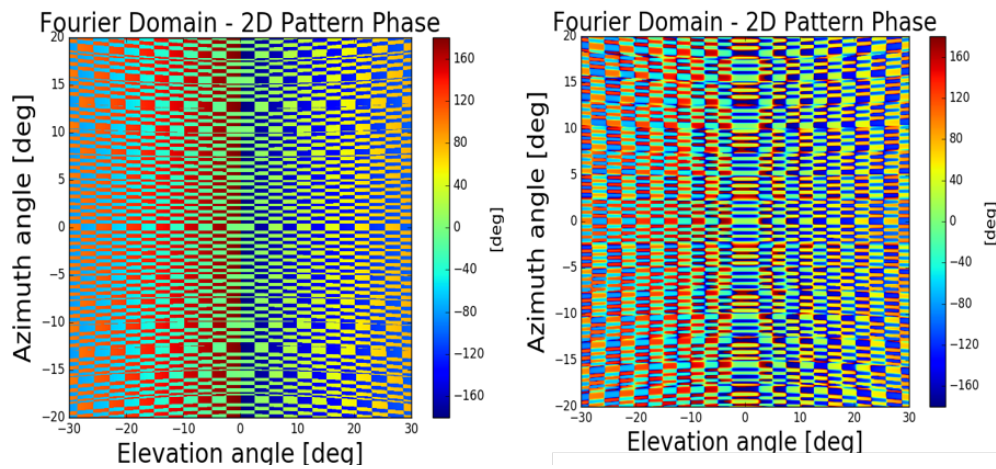


Fig. A.13. Effect of Thermal Deformation on 2D Phase of MicroX-SAR 7-Panel Antenna

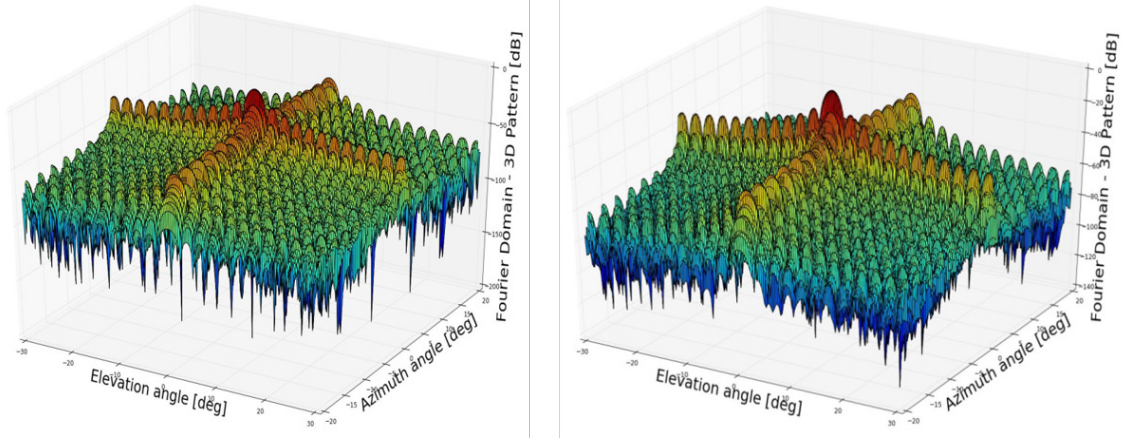


Fig. A.14. Effect of Thermal Deformation on 3D Pattern of MicroX-SAR 7-Panel Antenna

### A.3 Reflectors

Reflector systems for low sidelobe applications use offset parabolic reflectors in either single or dual reflector configurations. Due to the more stringent requirements on the performance of modern radar and satellite reflector antennas, it is necessary that their sidelobe and null locations and levels be predicted accurately. Analytically numerical techniques have been used very successfully in the vector diffraction analysis of reflector antennas, and in recent years, a variety of techniques has been developed [96]. Among these techniques, geometrical optics (GO)/aperture-field and physical optics (PO) methods have been used extensively to analyze the offset parabolic reflectors. In [61] it is stated that the comparison made from both the analytical and numerical viewpoints reveal the appearance of a Fourier transform relation in these methods. The PO integral can be represented as a summation of many Fourier transforms, such that the first term resembles the GO/aperture-field representation. It is stated that the GO/aperture-field method results in approximate description of the sidelobe and null positions and levels, especially for angular regions away from the main beam. In fact, it is stated that for offset parabolic



reflectors and for feeds located at the focal point, the predicted far-field patterns are always symmetric, even in the offset plane. In contrast, the PO method can result in more accurate asymmetric patterns. However, the computational burden and calculation time for PO is much higher than GO, making it inefficient. In [95] a comparison between the PO and GO methods with measurement results showed that PO agree with measured results slightly better than calculations based on GO for the sidelobes known to be influenced by surface pillowing. However, it was concluded that the overall improvement in the agreement to measured results offered by PO/AI over GO/AI for the distorted reflector is not significant. There are several papers which have used FFTs for calculating far-field patterns for reflectors and thereby reduced the computational burden significantly. Unfortunately, even for the simple case of non-offset reflectors, the FFT-based calculations have shown significant deviation from the PO/GO calculations especially at far side lobes and even the 3dB beam-width is not identical.

#### *A.3.1 Combining Geometrical Optics and FFT*

In this section, we propose combination of GO and FFT-based computation method with a beam-center approach to generate highly accurate far-field patterns for reflector antennas with considerations of feed at offset. It is revealed that the proposed beam-center approach is an accurate approximation valid in the far-field and the proposed approach generates accurate patterns while reducing the computation time and computation burden thereby making it very useful for practical purpose. Reflector patterns generated using TICRA GRASP software which uses advanced PO technique are compared with the ones generated by the Python Pattern Tool to validate the beam-center approach.

### A.3.2 Offset and Non-offset Feeds with Spillover

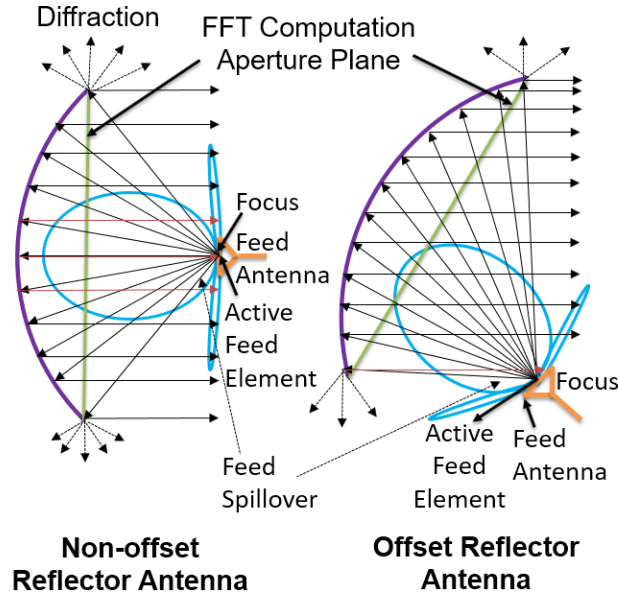


Fig. A.15. Schematic of Reflector Antenna with Different Feed Positions

Fig.A.15 shows the typical geometry of a parabolic reflector antenna with axial feed at offset and non-offset. The fields across the aperture of the parabolic reflector is responsible for this antenna's radiation. The peak gain of a reflector antenna is given by:

$$G_{ref} = \eta \left( \frac{\pi D}{\lambda} \right)^2 \quad (A.14)$$

$$\eta = \eta_r \eta_{ap} \eta_s \eta_o \quad (A.15)$$

where  $D$  is the diameter,  $\eta$  is the total efficiency,  $\eta_r$  is the radiation efficiency,  $\eta_{ap}$  is the aperture efficiency,  $\eta_s$  is the spillover efficiency,  $\eta_o$  are other factors which effect the efficiency like surface errors, cross-polarization, aperture blockage and non-ideal feed phase center.  $\eta$  usually ranges from 0.6-0.8 for a well-designed reflector:

The radiation efficiency is the deals with ohmic losses, as discussed on the efficiency page. Since horn or patch antennas are often used as feeds, and these have very little loss, and because the parabolic reflector is typically metallic with a very high conductivity, this efficiency is typically close to 1 and can be neglected.

The aperture radiation efficiency is a measure of how uniform the E-field is across the antenna's aperture. In general, an antenna will have the maximum gain if the E-field is uniform in amplitude and phase across the aperture (the far-field is roughly the Fourier Transform of the aperture fields). However, the aperture fields will tend to diminish away from the main axis of the reflector, which leads to lower gain, and this loss is captured within this parameter. Aperture efficiency can be improved by increasing the F/D ratio, which also lowers the cross-polarization of the radiated fields. However, increasing the F/D ratio reduces the spillover efficiency.

The spillover efficiency measures the amount of radiation from the feed antenna that is reflected by the reflector. Due to the finite size of the reflector, some of the radiation from the feed antenna will travel away from the main axis at an angle greater than, thus not being reflected. This efficiency can be improved by moving the feed closer to the reflector, or by increasing the size of the reflector.

The most common feed antenna for a reflector is a microstrip patch with length  $L$  and width  $W$  whose radiation pattern is given by [26]:

$$E_{\theta}(\theta, \varphi) = \frac{\sin\left(\frac{kW \sin\theta \sin\varphi}{2}\right)}{\frac{kW \sin\theta \sin\varphi}{2}} \cos\left(\frac{kL \sin\theta \cos\varphi}{2}\right) \cos\varphi \quad (\text{A. 16})$$



$$E_{\varphi}(\theta, \varphi) = -\frac{\sin\left(\frac{kW\sin\theta\sin\varphi}{2}\right)}{\frac{kW\sin\theta\sin\varphi}{2}} \cos\left(\frac{kL\sin\theta\cos\varphi}{2}\right) \cos\theta\sin\varphi \quad (\text{A.17})$$

$$E_{feed}(\theta, \varphi) = \sqrt{E_{\theta}^2(\theta, \varphi) + E_{\varphi}^2(\theta, \varphi)} \quad (\text{A.18})$$

The spill-over efficiency is computed in terms of the antenna beam efficiency which is the ratio of the power illuminating the reflector surface and the power transmitted by the feed antenna as follows [111]:

$$\eta_s = \frac{\int_0^{2\pi} \int_{-\theta_0/2}^{\theta_0/2} E_{feed}^2(\theta, \varphi) \sin\theta d\theta d\varphi}{\int_0^{2\pi} \int_{-\pi/2}^{\pi/2} E_{feed}^2(\theta, \varphi) \sin\theta d\theta d\varphi} \quad (\text{A.19})$$

### A.3.3 Separation of Co-polar and Cross-polar Fields

Cross-polarization is usually unwanted because it leads to polarization losses depending on the transmitting and receiving antennas. If the field transmitted by the test antenna is polarized along the y-axis on boresight, then the co-polar ( $E_{co}$ ) and the cross-polar ( $E_{cx}$ ) field components at an arbitrary point ( $r, \theta, \varphi$ ), can be related to the usual spherical components the following way [97]:

$$E_{co}(\theta, \varphi) = E_{\theta}(\theta, \varphi)\sin\varphi + E_{\varphi}(\theta, \varphi)\cos\varphi \quad (\text{A.20})$$

$$E_{cx}(\theta, \varphi) = E_{\theta}(\theta, \varphi)\cos\varphi - E_{\varphi}(\theta, \varphi)\sin\varphi \quad (\text{A.21})$$

Alternatively, if the total reflected field can be computed, then it can be decomposed into co-polar and cross-polar components in the following way [97]:

$$E_{co}(\theta, \varphi) = E_{Total}(\theta, \varphi) \frac{\sin^2 \varphi \cos \theta + \cos^2 \varphi}{\sqrt{1 - \sin^2 \theta \sin^2 \varphi}} \quad (A.22)$$

$$E_{cx}(\theta, \varphi) = E_{Total}(\theta, \varphi) \frac{\sin \varphi \cos \varphi (1 - \cos \theta)}{\sqrt{1 - \sin^2 \theta \sin^2 \varphi}} \quad (A.23)$$

From equation (5.20), it is obvious that cross-polarization is zero at  $\phi = 0^\circ$  (E-plane) and at  $\phi = 90^\circ$  (H-plane); Cross-polarization is maximum at  $\phi = 45^\circ, 135^\circ$ ; as shown in fig.A.16.

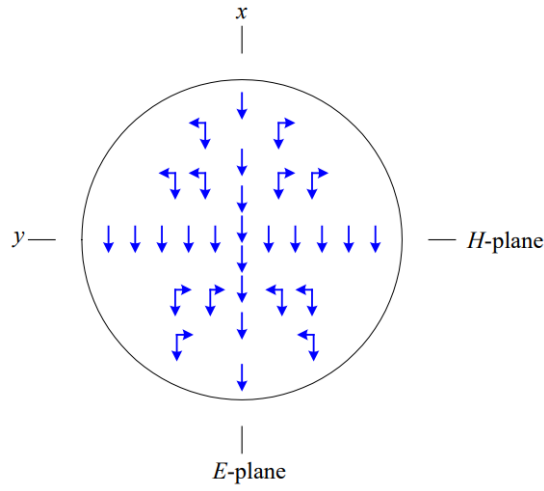


Fig. A.16. Co-polarization and Cross-polarization in Reflector Antenna

#### A.3.4 Beam-center Approximation (BCA) Technique

Fig.A.17 demonstrates the concept of the proposed beam-center approach. Instead of taking the reflections along the normal to the reflector surface during FFT computation as done in all available literature, we consider the incident wave arriving from the active feed-element and compute its reflection from each point on the reflector surface and project it on the FFT computation aperture plane as shown in fig.A.17. This is exact for the center of the antenna beam, hence called the beam-center approach. One critical point of critical

interest which influences the computation accuracy is the selection of the FFT computation aperture plane. Ideally, there will be no approximation error if the pattern were to be computed on the curved reflector surface itself, however, computation of FFT on a 2D curved surface becomes highly complicated and doing so would possibly incorporate other approximation errors which is undesirable. Thus, the FFT plane is selected in such a way that it is closest to the reflector surface while at the same time far enough to be planar and include the reflections from all points on the reflector surface. Hence, the In FFT computation plane is selected to be the plane connecting the two edges of the reflector as shown in fig.A.17 to minimize the error.

A point of critique from a theoretical perspective is that if the radius of curvature of the reflector is very large, then the distance between the proposed FFT aperture plane and the reflector surface will be also large and as a result the proposed beam-center technique will have large errors even close to the beam-center. However, since the radius of curvature of all parabolic dish antennas is quite small in comparison to its radius of curvature, this can never be an issue for the beam-center technique from a practical standpoint. Furthermore, since we are considering the actual reflections of the incident wave from the reflector surface and intersecting them on the FFT plane instead of considering normal incidence, the accuracy is much better than existing literature.

Although this is an approximation far away from the beam-center, it is highly accurate with almost zero errors up-to  $\pm 20$  degrees from the center of the beam which is generally more than sufficient for system design and performance evaluation. Since we are projecting the reflected beam on the FFT plane, irregular to regular interpolation must be done before FFT computation.

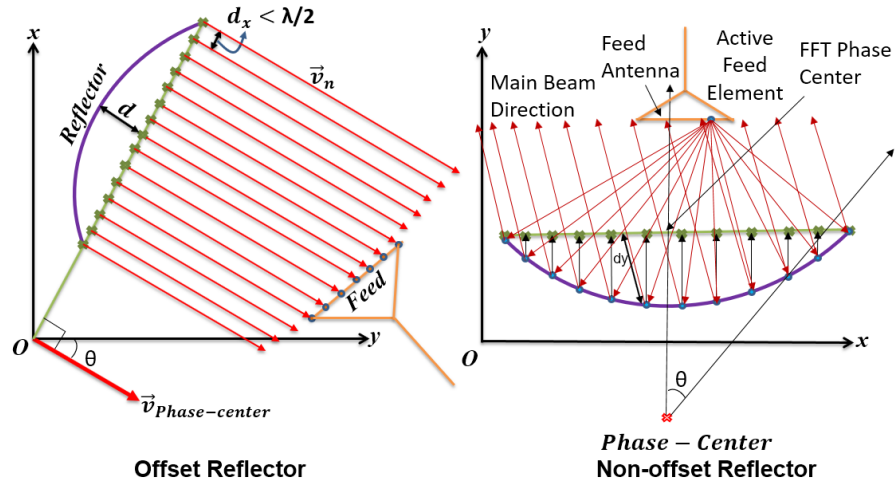


Fig. A.17. Schematic Showing Beam-Center Approach for Reflector Antenna Pattern Computation

- *Computation Algorithm*

Fig.A.18 shows the block diagram of the beam-center-based computation algorithm.

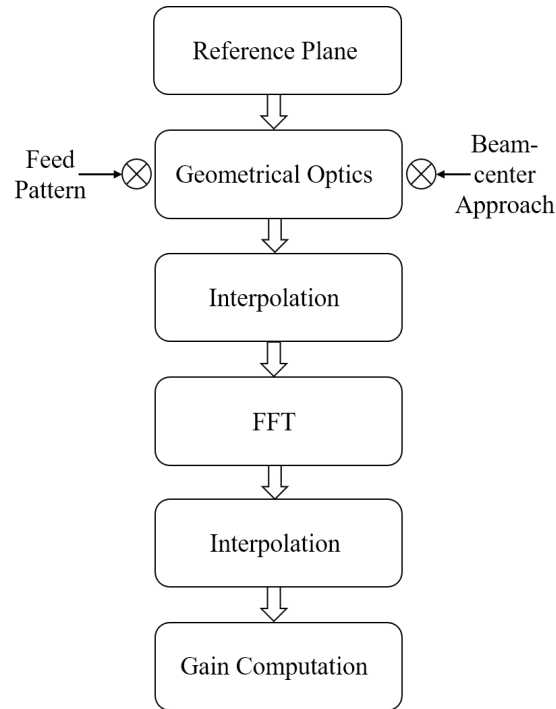


Fig. A.18. Reflector Antenna Pattern Computation Algorithm

### *I. Initialization*

- Define Reflector Parameters and create the reflector surface in Polar/Rectangular Grid.
- Define Feed Antenna Type and its parameters and compute Feed Pattern.
- Define Phase Center.
- Define Output Elevation and Azimuth Angles of Interest and compute desired  $u(\theta, \varphi)$  and  $v(\theta, \varphi)$ .

### *II. Geometrical Optics*

- Compute Incident Field Vectors from Feed to Reflector surface.
- Compute Reflected Field Vectors from normal to Reflector surface.
- Decompose the Reflected Field into Co-Pol and Cx-Pol components.
- Project the Reflected Field Vectors on the FFT Computation Aperture Plane.

### *III. Array Factor Computation*

- Make irregular to regular interpolation of the field intersection points on the FFT plane.
- Compute 2D FFT of interpolated field excitation.
- Interpolate the real & imaginary parts of Computed FFT along  $u(\theta, \varphi)$  and  $v(\theta, \varphi)$ .
- Translate FFT to the desired phase center.
- Normalize the output FFT by the size of field excitation matrix.

#### IV. Antenna Gain Computation

- Multiply the normalized output FFT by the Gain corresponding to square area of FFT Grid.
- Multiply the above gain by aperture efficiency, beam-efficiency and normalized area factor (*since FFT surface is a square grid while the reflector is paraboloidal*).

##### A.3.5 Case Study with Tandem-L Antenna

Antenna patterns are computed for Tandem-L [45] with  $D = 15$  m,  $f_0 = 1.2575$  GHz,  $\lambda_0 = 23.86$  cm, Feed type = patch;  $L = 0.38 \lambda_0$ ,  $W = 0.4 \lambda_0$ ,  $N_{el} = 33$ ,  $N_{az} = 3$ .



Fig. A.19. Demonstration of Tandem-L Reflector Concept

##### A.3.6 Comparison with GRASP Simulation Results

Co-polar and Cross-polar 1D and 2D Patterns are computed for Tandem-L using the Pattern Tool and compared with the patterns generated from GRASP software which uses advanced PO technique. Comparisons are done for two cases: Axial Feed and Offset Feed by 9 meters. For each case, patterns are computed for the combinations of the active feed

elements at the center and edge along elevation and azimuth to ensure the pattern tool is versatile and works for any general case. The antenna aperture efficiency is taken as 78.6% for axial feed and 74.6% for 9 meters offset feed respectively.

Fig.A.20 and fig.A.21 shows the comparison of the 1D Co-polar elevation and azimuth patterns for axial feed. Fig.A.22 and fig.A.23 shows the comparison of the Co-polar 1D elevation and azimuth patterns for feed with 9 meters offset. There is excellent match between the GRASP and Pattern Tool antenna patterns. The maximum peak gain error is 0.2dB for offset edge elements and the average peak gain error is less than 0.1 dB.

Fig.A.24 and fig.A.25 show the comparison of the 3dB beamwidth of the computed antenna patterns with axial feed and 9 meters offset feed respectively. There is zero 3 dB beamwidth error for all cases.

Fig.A.26 shows the comparison of the first side-lobe-level (SLL) of the computed antenna patterns with axial feed. Fig.A.27 shows the comparison of the first side-lobe-level (SLL) of the computed antenna patterns with 9 meters offset feed. The first side-lobe level is of interest since it determines the range and azimuth ambiguity levels. The maximum SLL error is 0.2 dB for offset edge elements and the average peak gain error is less than 0.1 dB.

Fig.A.28 and fig.A.29 shows the comparison of the 2D Co-polar antenna patterns with axial feed. Fig.A.30 and fig.A.31 shows the comparison of the 2D Co-polar antenna patterns with 9 meters offset feed. The comparison patterns are also shown for both amplitude and phase by taking the difference between the pattern tool pattern and the

complex conjugate of the GRASP pattern. Both the amplitude and phase patterns show perfect match.

Fig.A.32 and fig.A.33 shows the comparison of the 1D Cross-polar elevation and azimuth patterns for axial feed. Fig.A.34 and fig.A.35 shows the comparison of the Cross-polar 1D elevation and azimuth patterns for feed with 9 meters offset. Cross-polar gain is very low compared to the co-polar gain which validates the reflector design. The minimum XPD is about 30 dB for active  $N_{az}=2$  and active  $N_{el}=32$  for 9 meters offset feed. For other offset cases, XPD is higher than 40 dB. For all cases of axial feed, XPD is higher than 50 dB, which implies cross-polarization is of minor significance of Tandem-L. The average error in Cross-polarization peak gain computation is 0.2 dB.

Fig.A.36 and fig.A.37 show the comparison of the 2D Cross-polar antenna patterns with axial feed. Fig.A.38 and fig.A.39 show the comparison of the 2D Cross-polar antenna patterns with 9 meters offset feed. The comparison patterns are also shown for both amplitude and phase by taking the difference between the pattern tool pattern and the complex conjugate of the GRASP pattern. The amplitude patterns match well, and the phase patterns show some minor deviations for non-offset case of active edge elements, the reason for which is unclear.



### A. 1D Co-polar Patterns

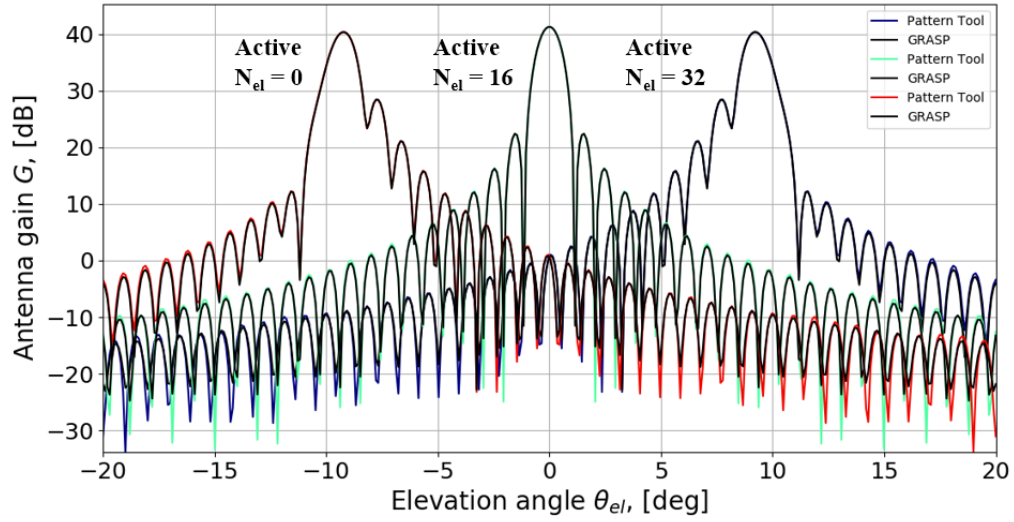


Fig. A.20. (a) Tandem-L Antenna Elevation Pattern Case: Non-Offset Feed Active  $N_{az} = 1$  (Center)

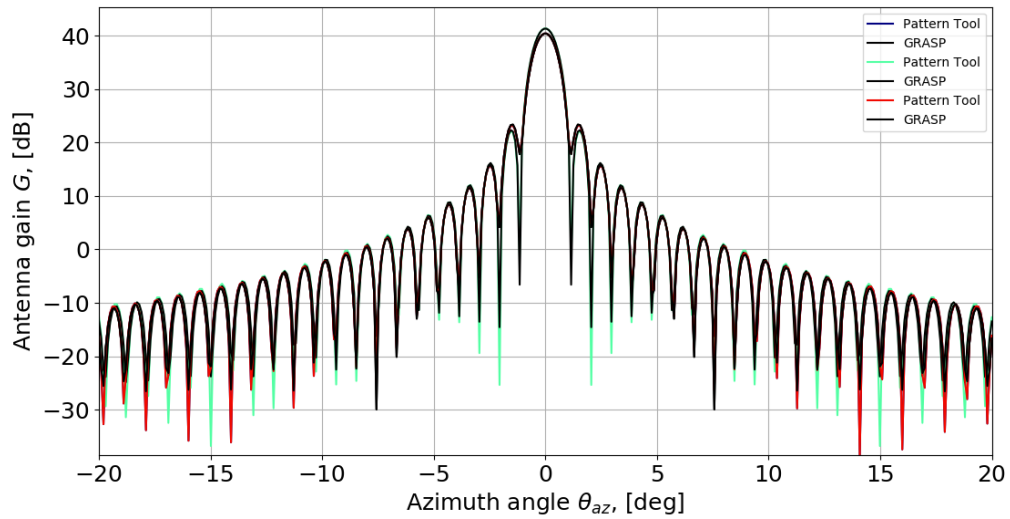


Fig. A.20. (b) Tandem-L Antenna Azimuth Pattern Case: Non-Offset Feed Active  $N_{az} = 1$  (Center)

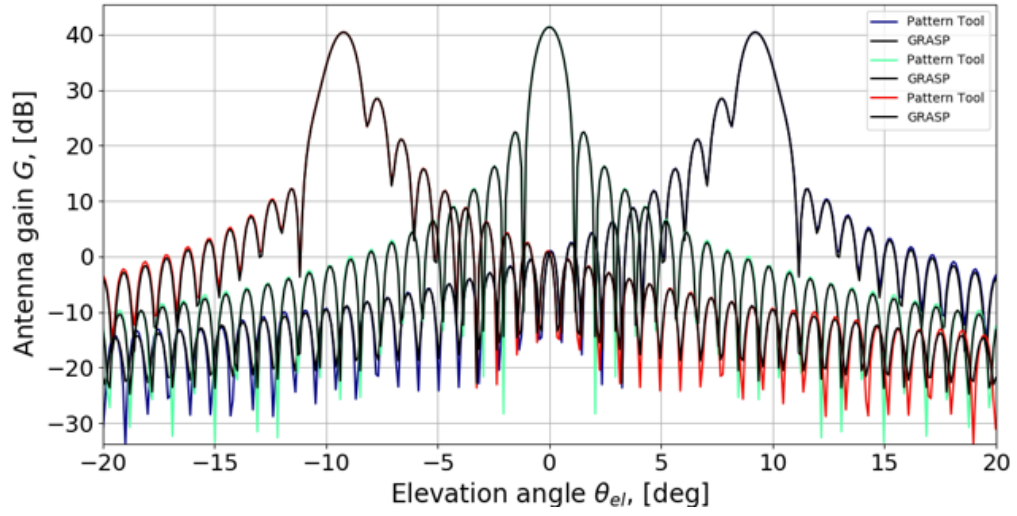


Fig. A.21. (a) Tandem-L Antenna Elevation Pattern Case: Non-Offset Feed Active  $N_{az} = 0$  (Edge)

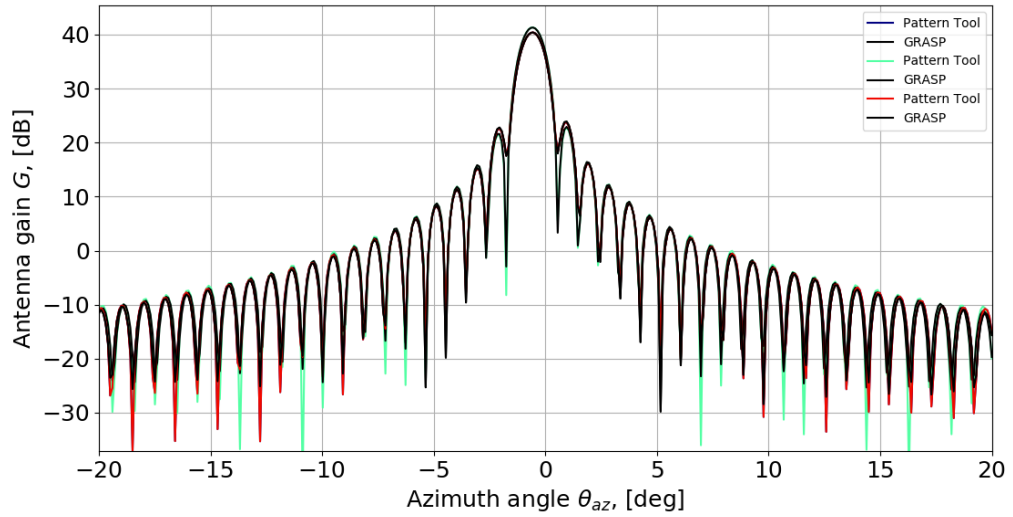


Fig. A.21. (b) Tandem-L Antenna Azimuth Pattern Case: Non-Offset Feed Active  $N_{az} = 0$  (Edge)

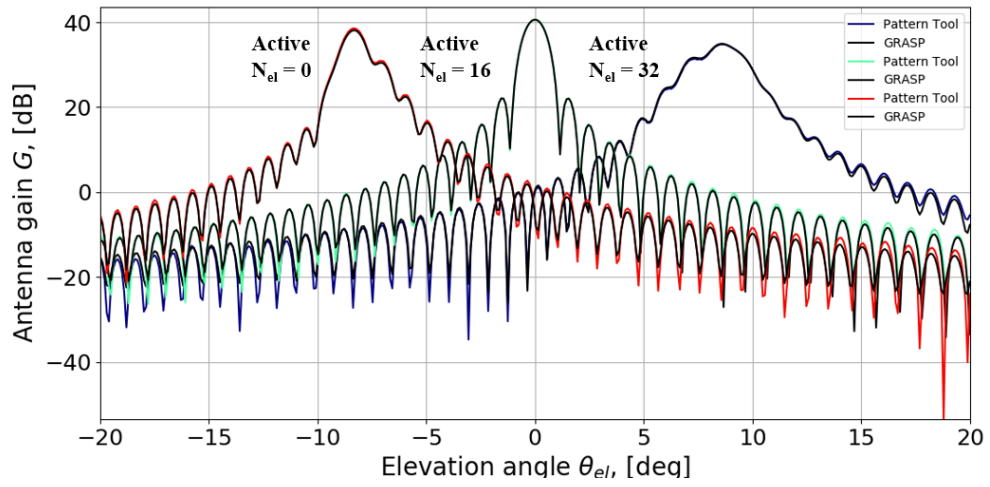


Fig. A.22. (a) Tandem-L Antenna Elevation Pattern Case: 9 meters Offset Feed Active

$N_{az} = 1$  (Center)

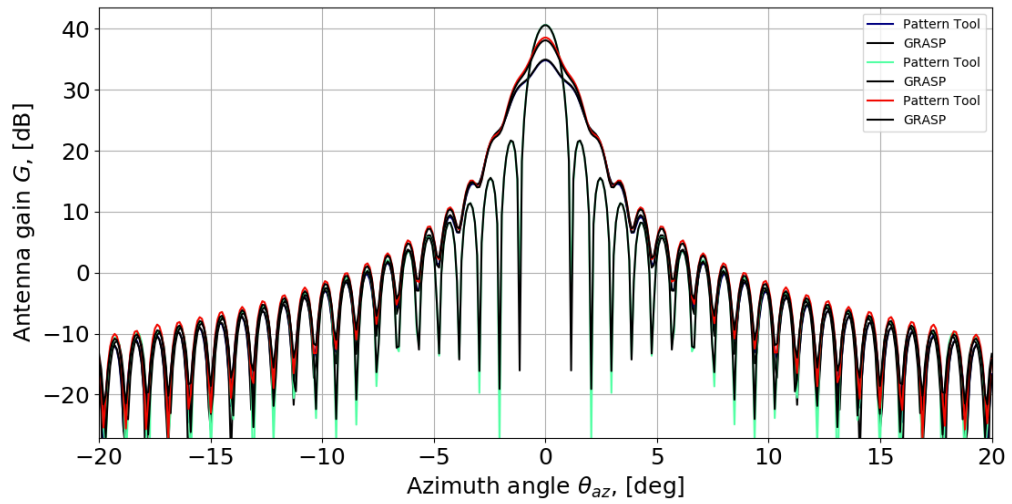


Fig. A.22. (b) Tandem-L Antenna Azimuth Pattern Case: 9 meters Offset Feed Active  $N_{az}$

$= 1$  (Center)

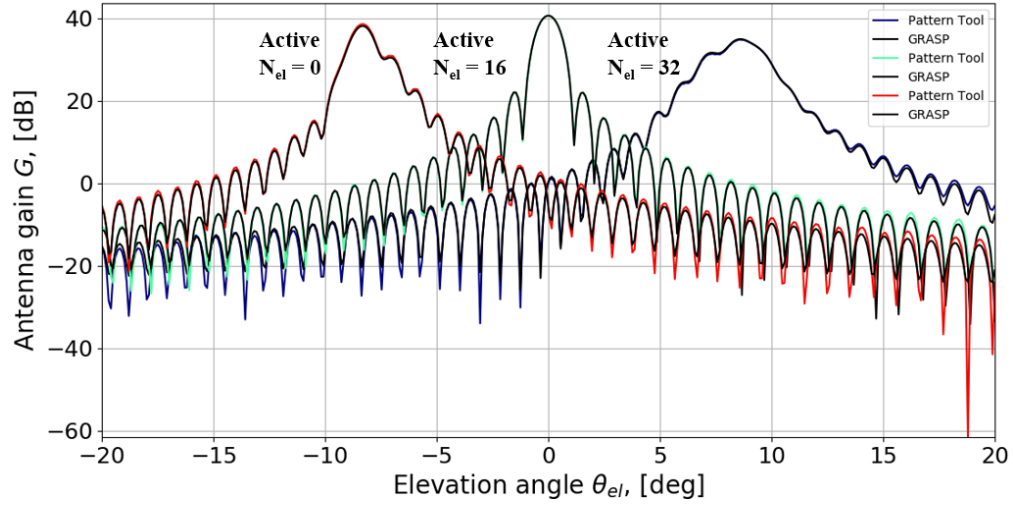


Fig. A.23. (a) Tandem-L Antenna Elevation Pattern Case: 9 meters Offset Feed Active

$N_{az} = 2$  (Edge)

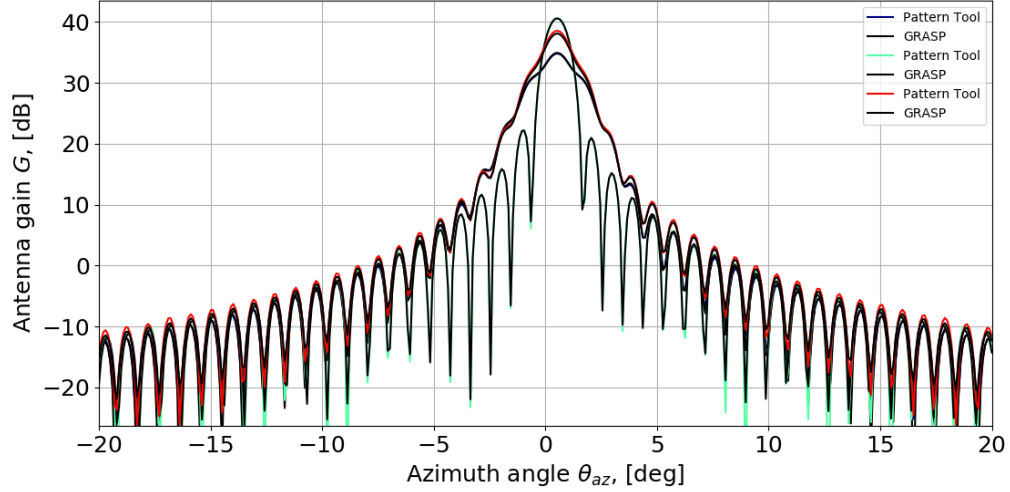


Fig. A.23. (b) Tandem-L Antenna Azimuth Pattern Case: 9 meters Offset Feed Active  $N_{az}$

$= 2$  (Edge)

## B. 3dB Beam-width

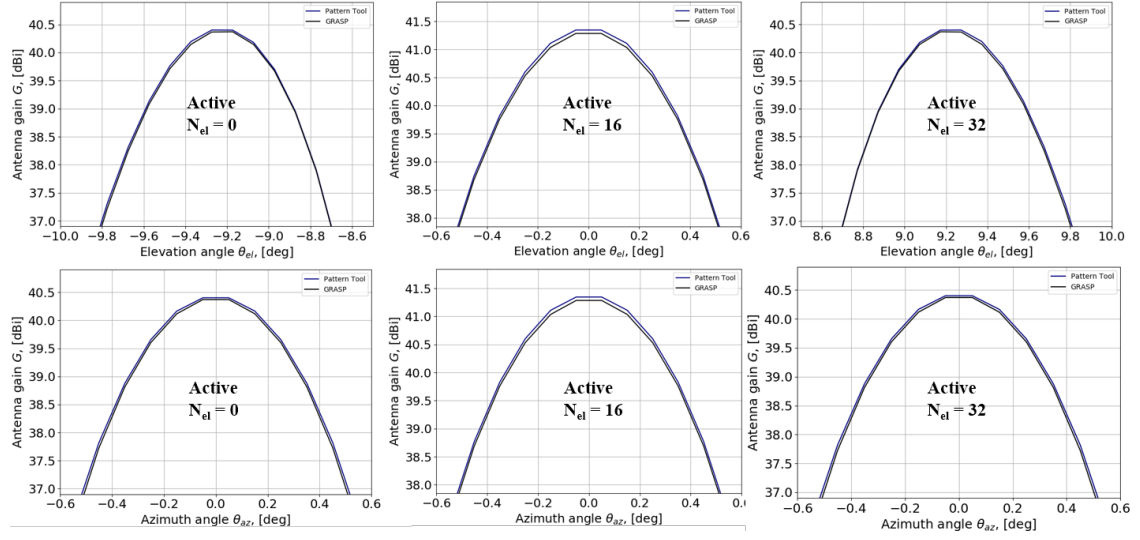


Fig. A.24. Tandem-L Antenna 3dB Beam-width Case: Non-Offset Feed Active  $N_{az} = 1$

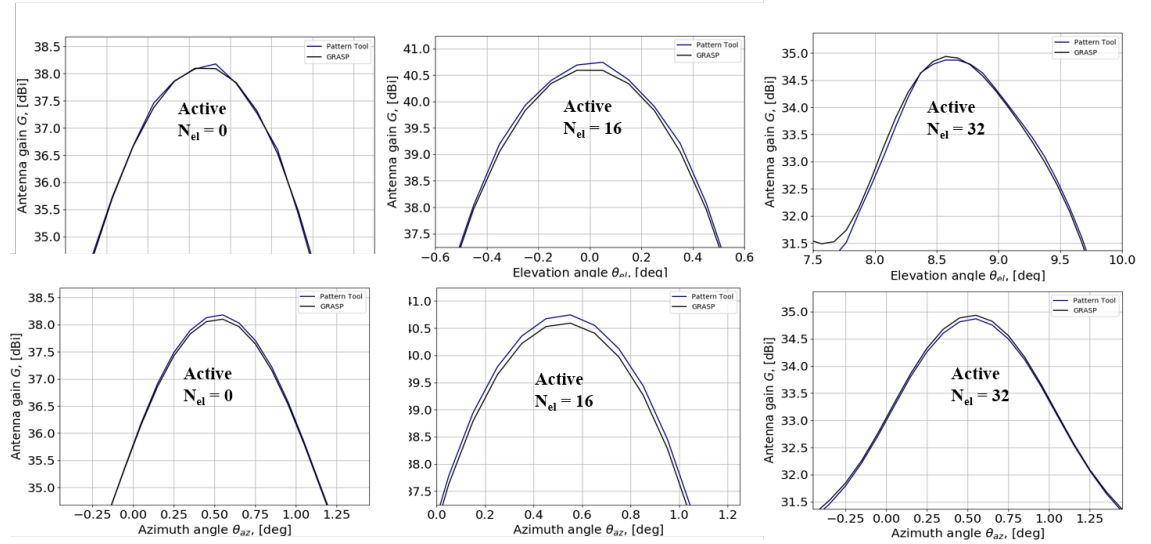


Fig. A.25. Tandem-L Antenna 3dB Beam-width Case: Offset Feed Active  $N_{az} = 2$  (Edge)

### C. Side-lobe Level (SLL)

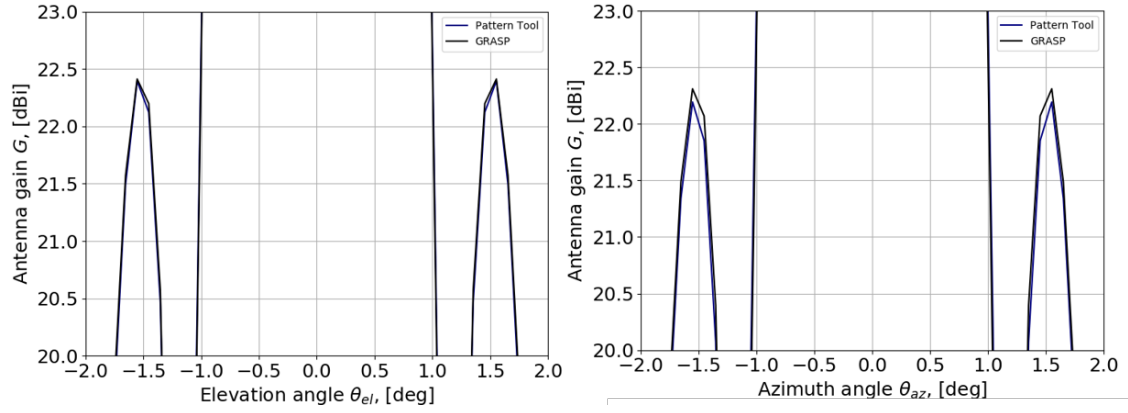


Fig. A.26. Tandem-L Antenna Side-lobe Level Case: Non-Offset Feed Active  $N_{az} = 1$

(Center) Active  $N_{el} = 16$  (Center)

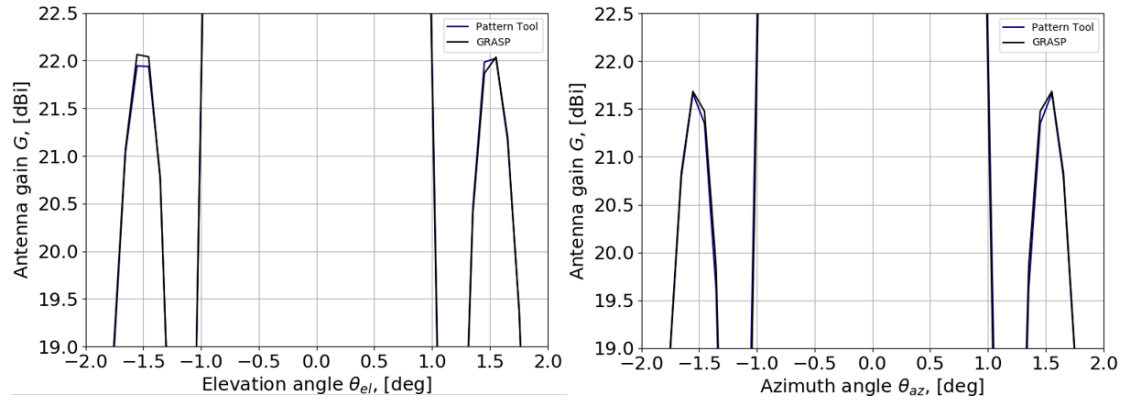


Fig. A.27. Tandem-L Antenna Side-lobe Level Case: Offset Feed Active  $N_{az} = 0$  (Edge)

Active  $N_{el} = 16$  (Center)



### D. 2D Co-polar Pattern

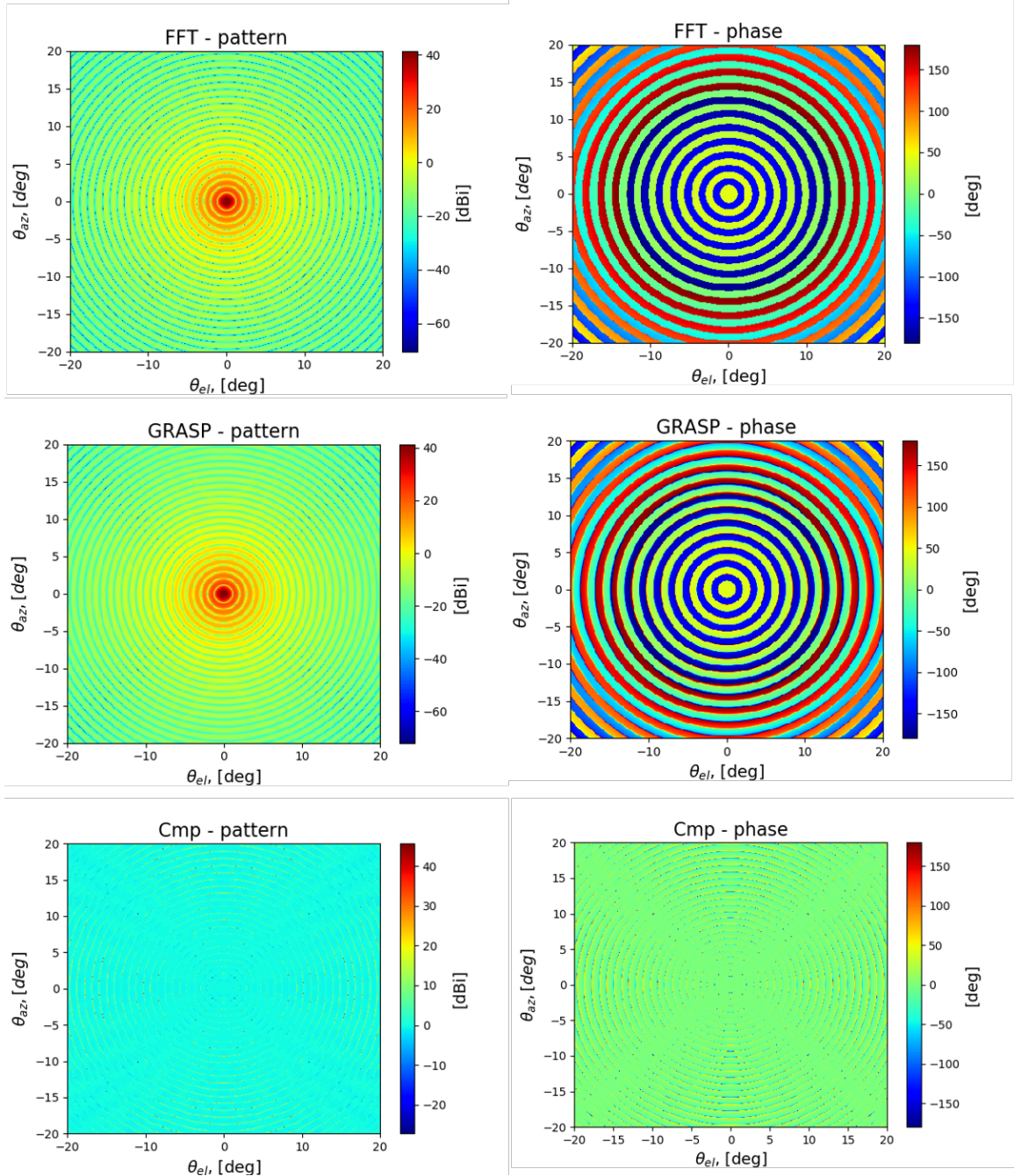


Fig. A.28. Tandem-L Antenna 2D Pattern Case: Non-Offset Feed Active  $N_{az} = 1$  (Center)

Active  $N_{el} = 16$  (Center)

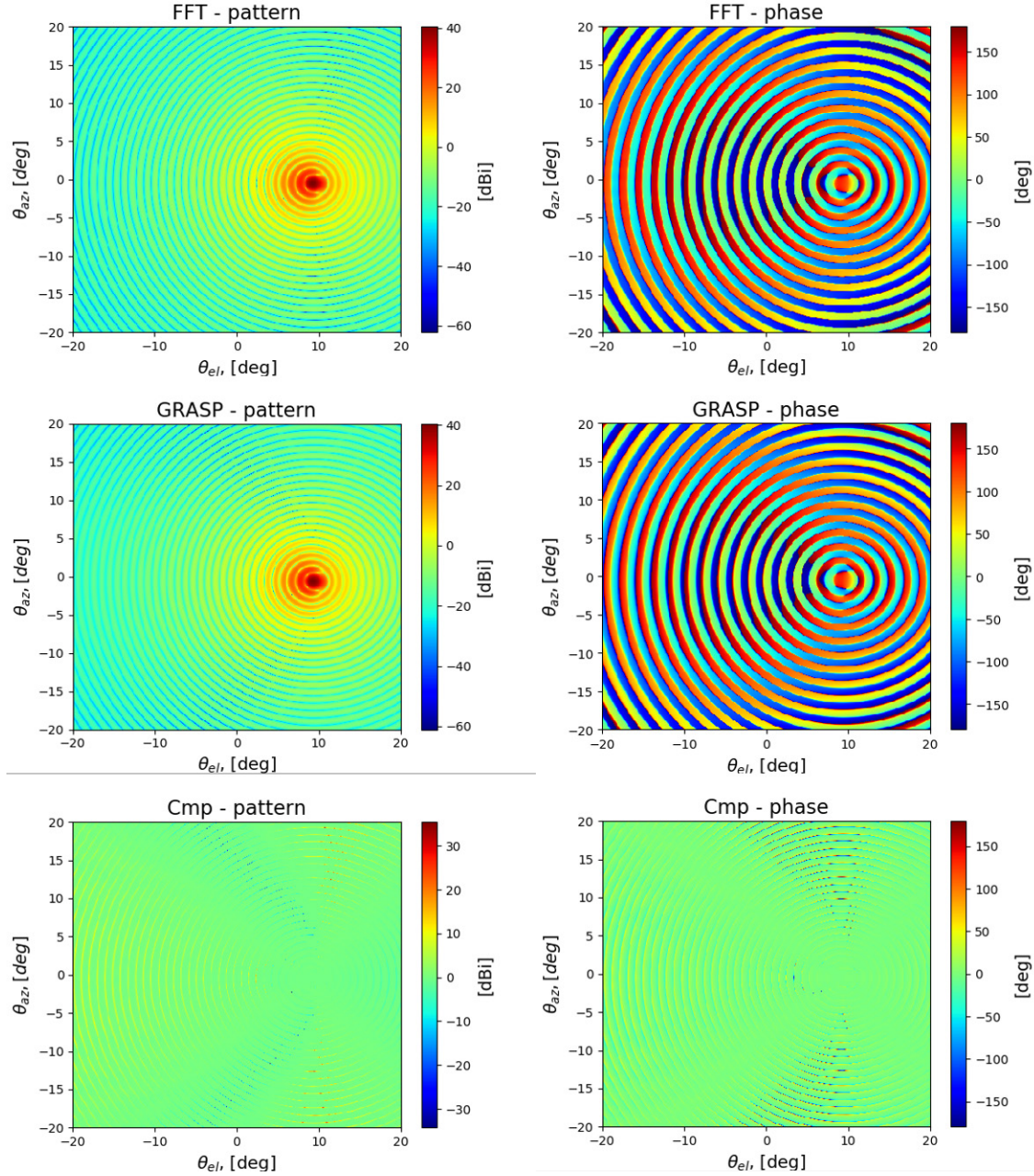


Fig. A.29. Tandem-L Antenna 2D Pattern Case: Non-Offset Feed Active  $N_{az} = 0$  (Edge)

Active  $N_{el} = 0$  (Edge)



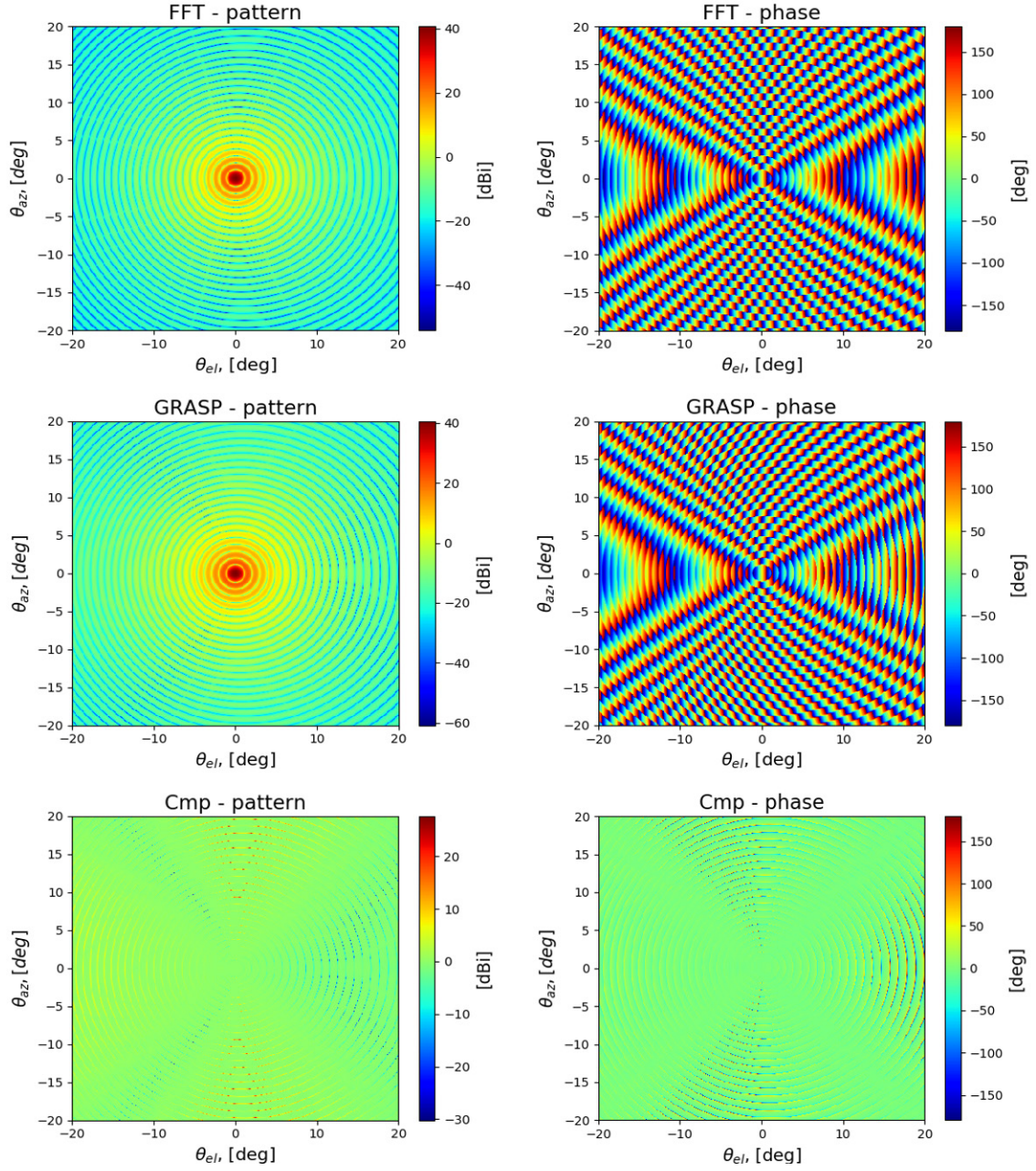


Fig. A.30. Tandem-L Antenna 2D Pattern Case: 9 meters Offset Feed Active  $N_{az} = 1$

(Center) Active  $N_{el} = 16$  (Center)

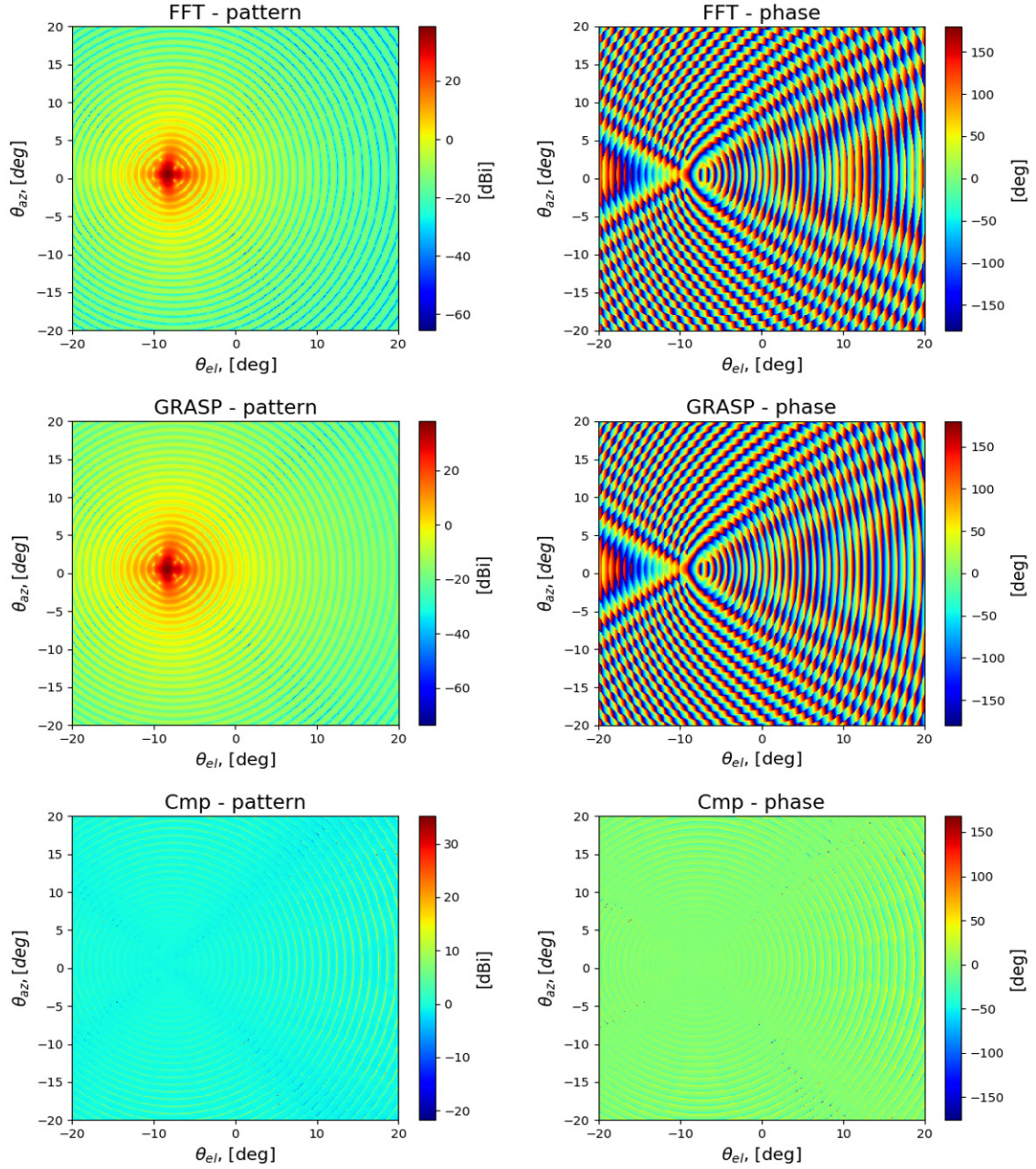


Fig. A.31. Tandem-L Antenna 2D Pattern Case: 9 meters Offset Feed Active  $N_{az} = 2$

(Center) Active  $N_{el} = 32$  (Edge)



### E. 1D Cross-polar Patterns

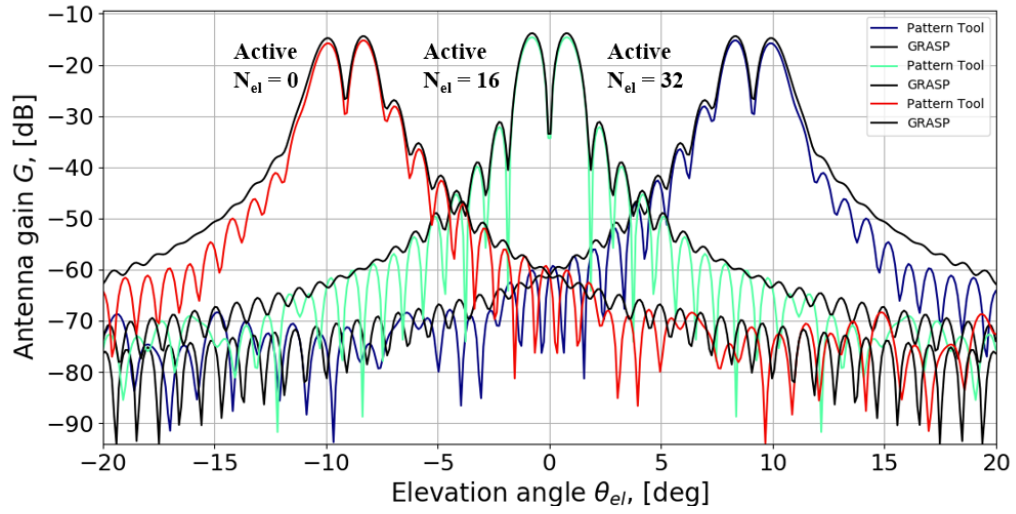


Fig. A.32. (a) Tandem-L Antenna Elevation Pattern Case: Non-Offset Feed Active  $N_{az} = 1$  (Center)

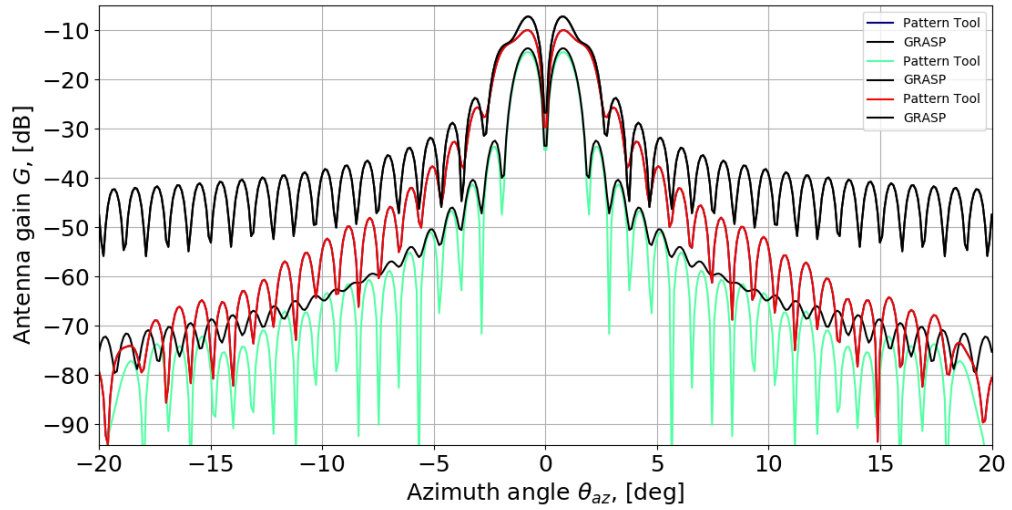


Fig. A.32. (b) Tandem-L Antenna Azimuth Pattern Case: Non-Offset Feed Active  $N_{az} = 1$  (Center)

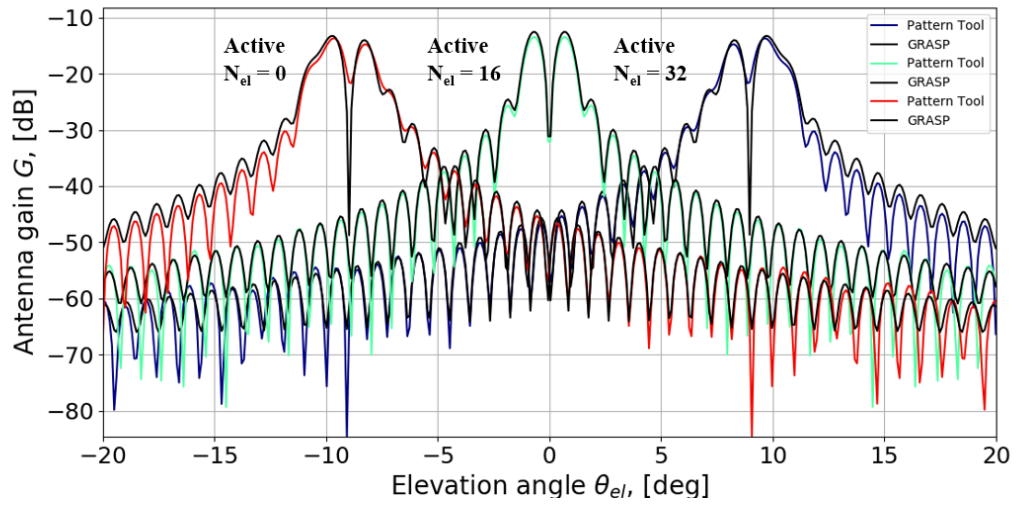


Fig. A.33. (a) Tandem-L Antenna Elevation Pattern Case: Non-Offset Feed Active  $N_{az} =$   
2 (Edge)

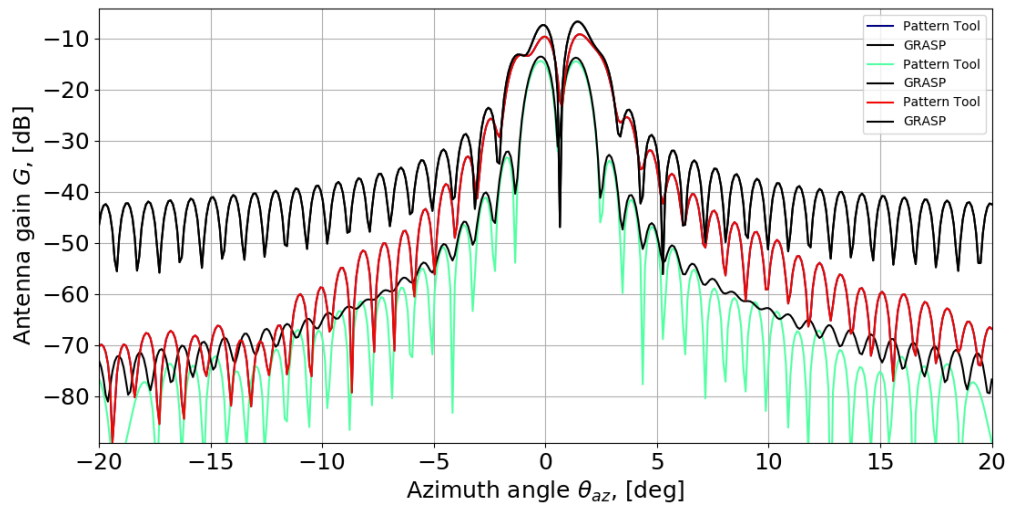


Fig. A.33. (b) Tandem-L Antenna Azimuth Pattern Case: Non-Offset Feed Active  $N_{az} = 0$   
(Edge)

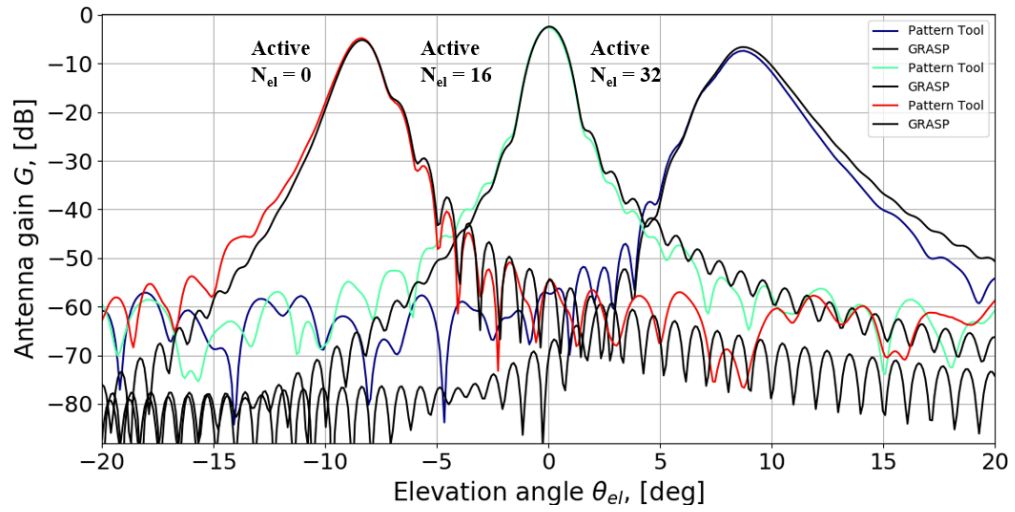


Fig. A.34. (a) Tandem-L Antenna Elevation Pattern Case: 9 meters Offset Feed Active

$N_{az} = 1$  (Center)

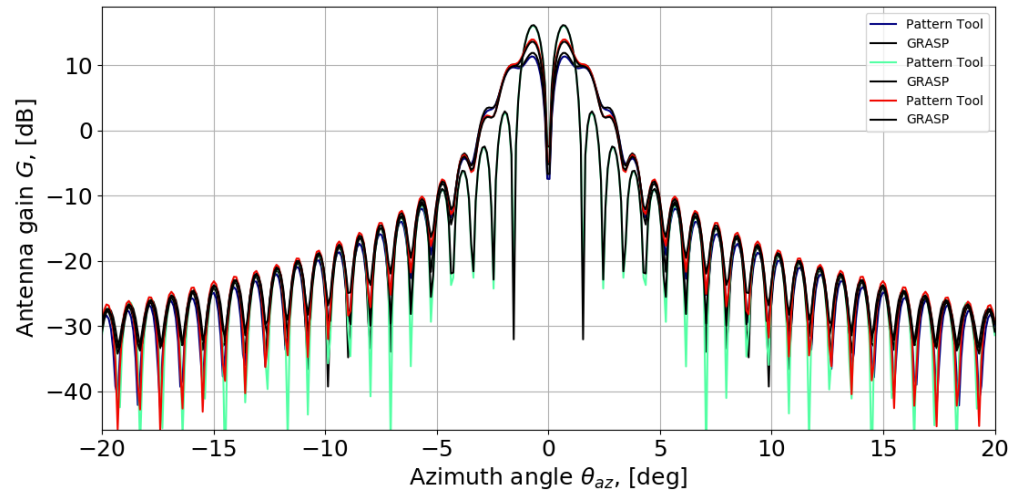


Fig. A.34. (b) Tandem-L Antenna Azimuth Pattern Case: 9 meters Offset Feed Active  $N_{az}$

$= 1$  (Center)

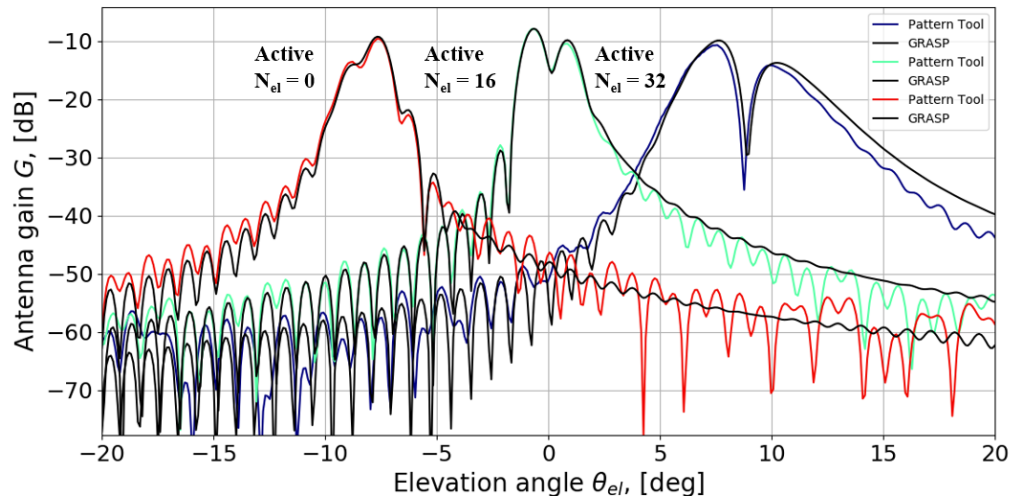


Fig. A.35. (a) Tandem-L Antenna Elevation Pattern Case: 9 meters Offset Feed Active

$N_{az} = 0$  (Edge)

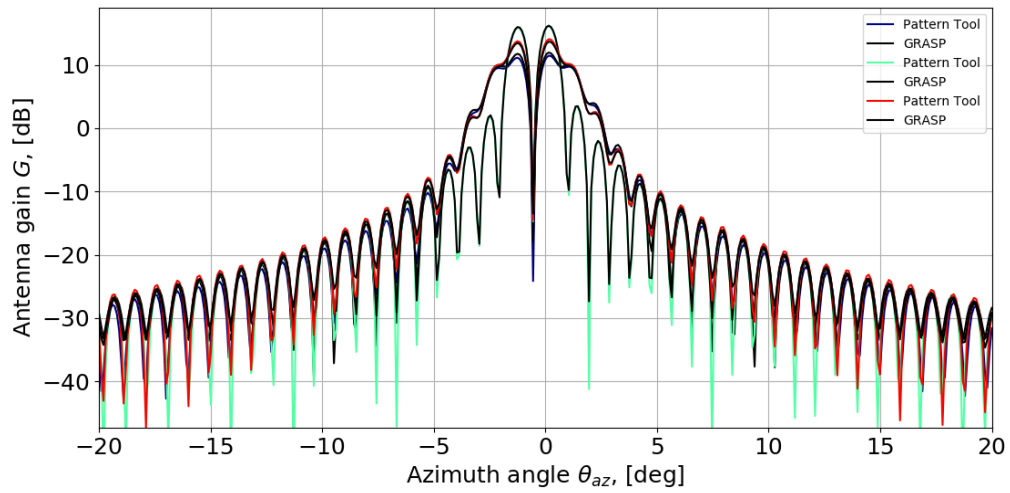


Fig. A.35. (b) Tandem-L Antenna Azimuth Pattern Case: 9 meters Offset Feed Active  $N_{az}$

$= 0$  (Edge)

## F. 2D Cross-polar Pattern

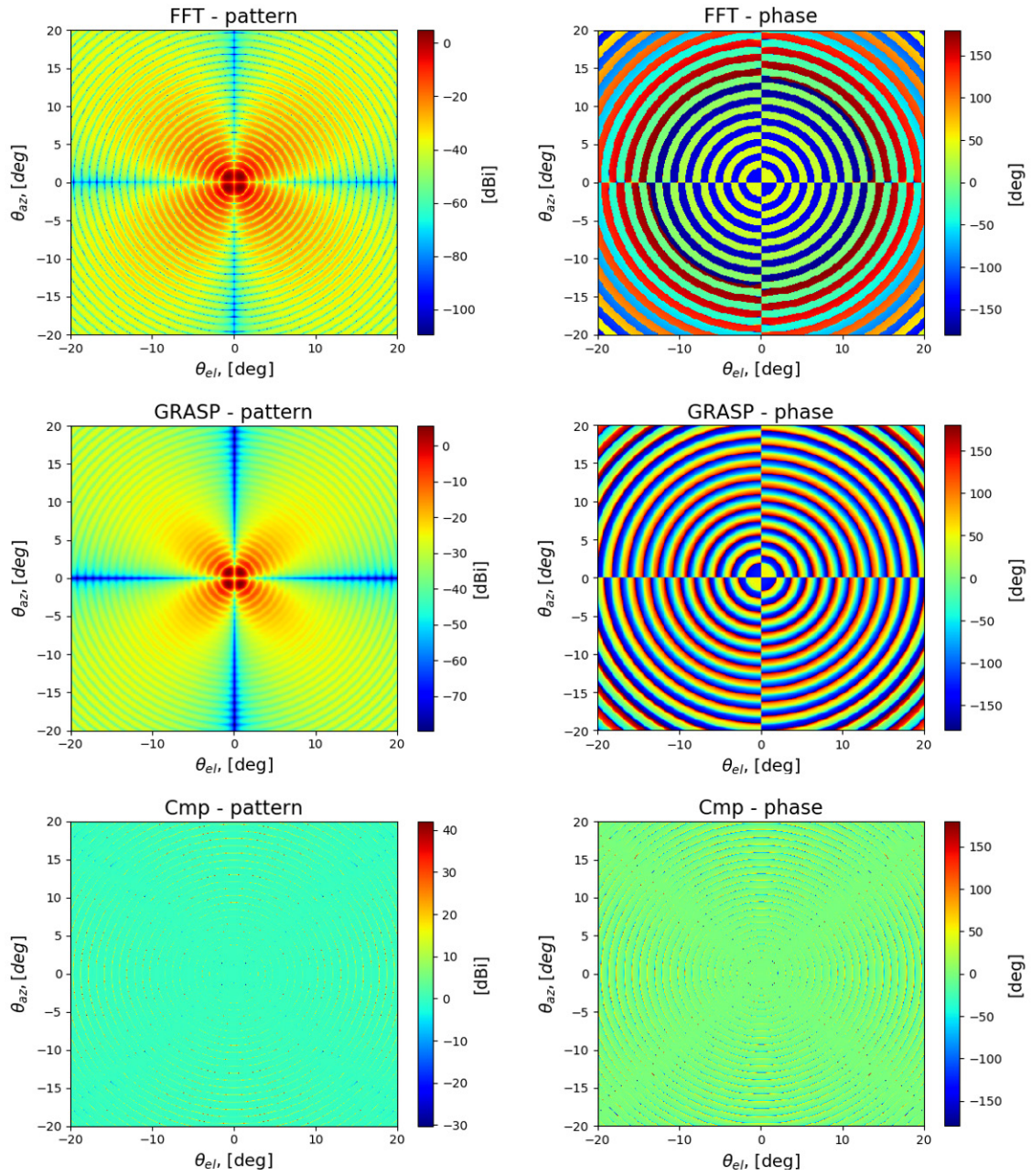


Fig. A.36. Tandem-L Antenna 2D Pattern Case: 9 meters Offset Feed Active  $N_{az} = 1$

(Center) Active  $N_{el} = 16$  (Center)



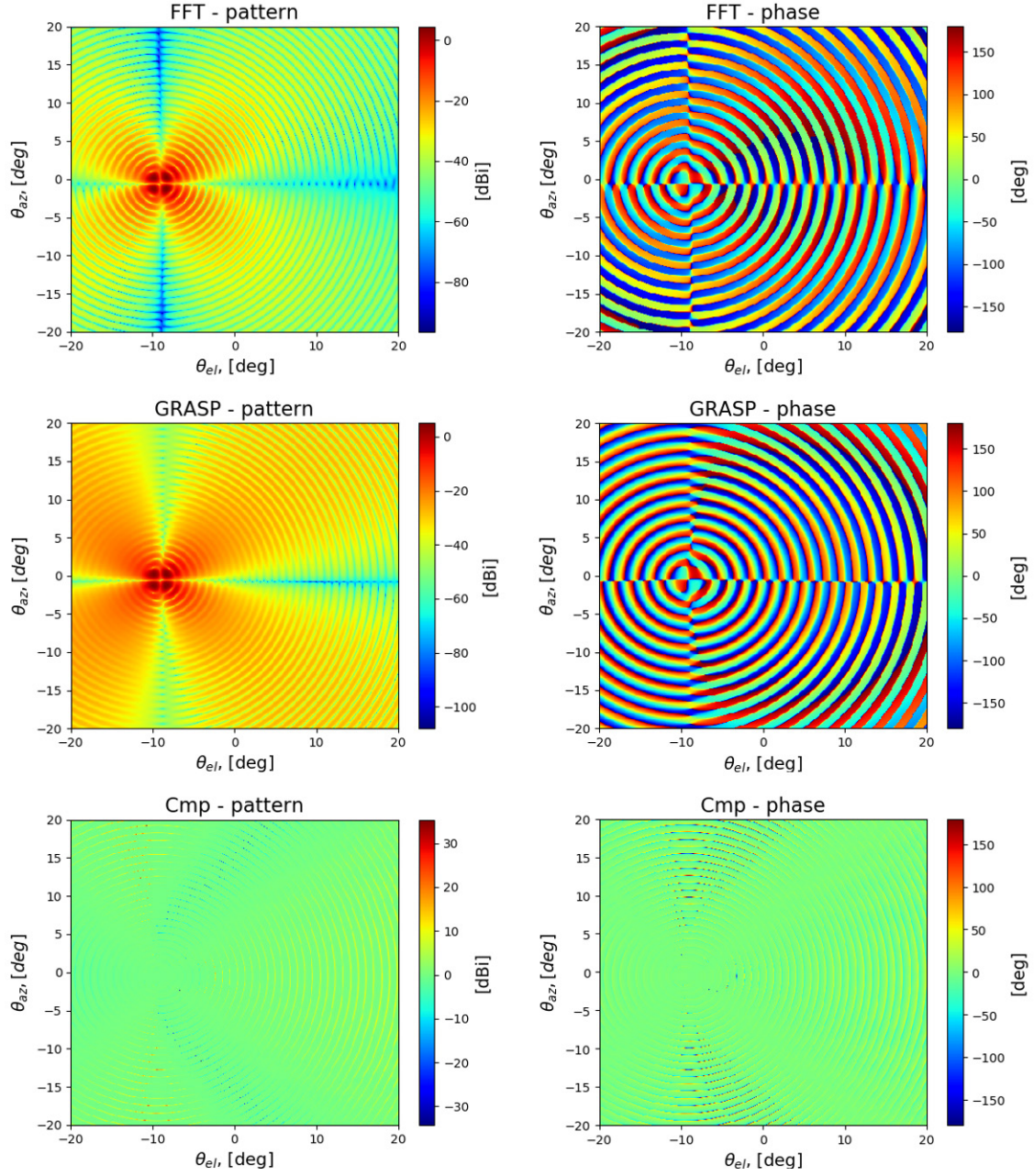


Fig. A.37. Tandem-L Antenna 2D Pattern Case: 9 meters Offset Feed Active  $N_{az} = 0$

(Edge) Active  $N_{el} = 32$  (Edge)



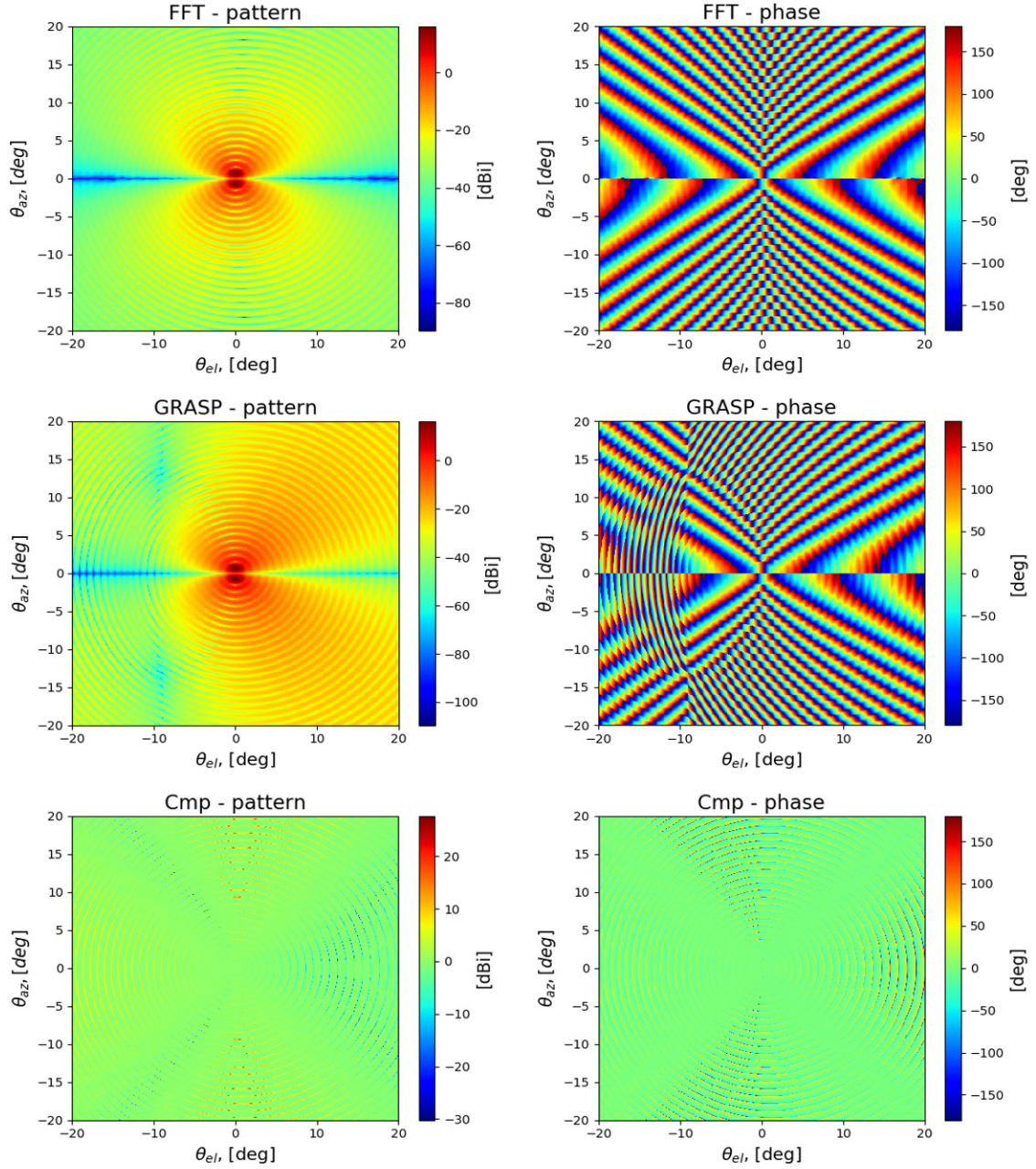


Fig. A.38. Tandem-L Antenna 2D Pattern Case: 9 meters Offset Feed Active  $N_{az} = 1$

(Center) Active  $N_{el} = 16$  (Center)

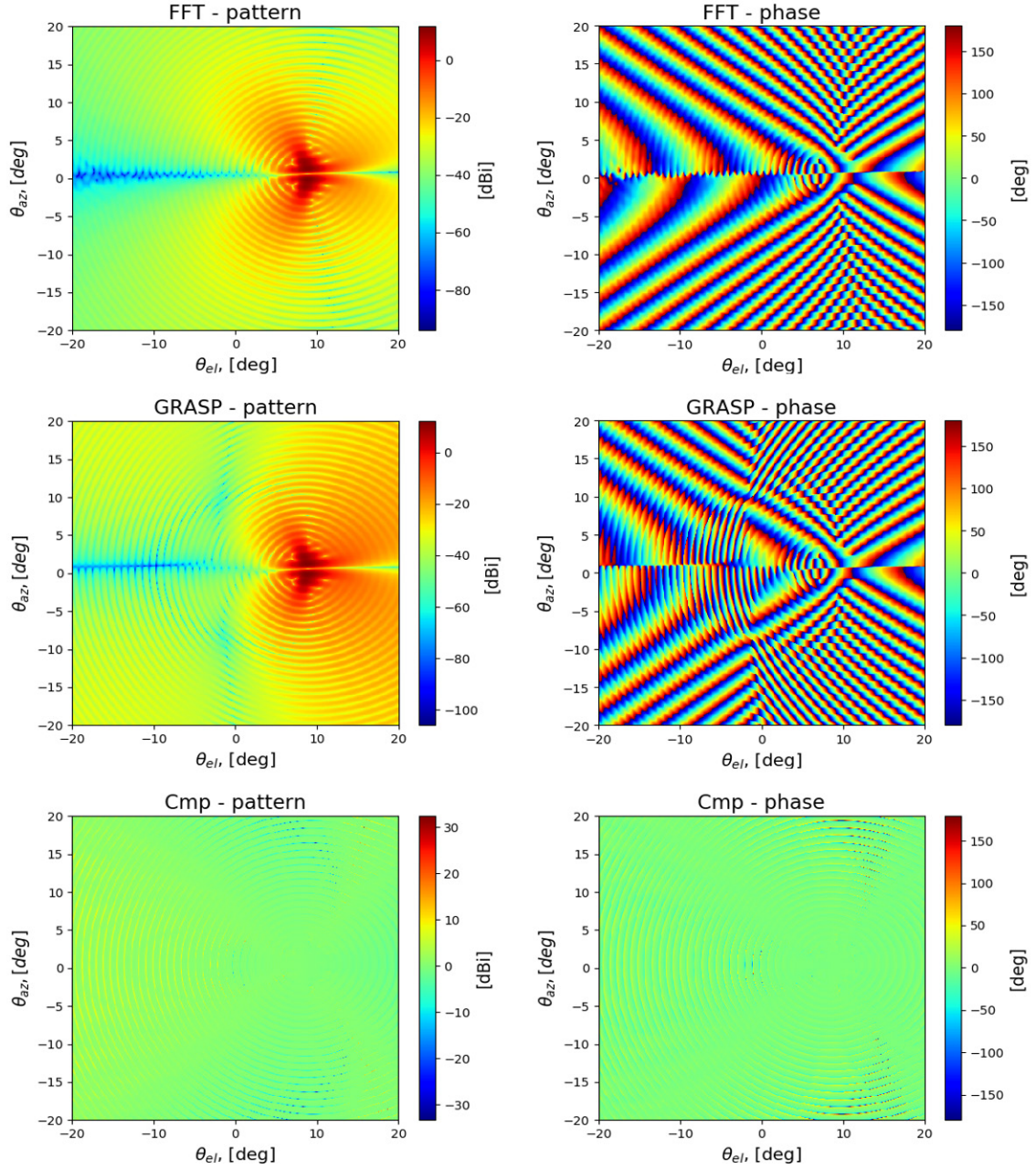


Fig. A.39. Tandem-L Antenna 2D Pattern Case: Offset Feed Active  $N_{az} = 2$  (Edge)

Active  $N_{el} = 0$  (Edge)

#### A.4 Summary and Discussion

This chapter presented the concept for efficient and accurate computation of antenna patterns in Python for non-ideal planar arrays and reflectors.

The novelty of the Pattern Tool can be summarized as follows:

- **FFT-based** Far-field Antenna Pattern computation for **Planar Arrays** with **Thermo-elastic Surface Deformations**
- **Beam Center Approximation** (BCA) Technique for Far-field Axial-fed and Offset **Reflector** Antenna Pattern computation **combining FFT and Geometrical Optics**
- Pattern Tool Computation Time for 1D/2D Co-Pol/Cx-Pol Gain/Phase Patterns only 30-40 seconds with accuracy error within  $\pm 0.1$  dB compared to several hours in GRASP and HFSS electromagnetics software

Results showed that in case of MicroX-SAR planar array, the effect of thermal deformation of the antenna surface reduced the peak gain by 0.14 dB and increased the first side-lobe level by 0.7 dB. In case of Tandem-L reflector, the beam-center approach is highly accurate within  $\pm 0.1$  dB error for Co-polar peak gain and  $\pm 0.2$  dB for Cross-polar peak gain; the 3dB beam-width error was 0 degrees and the error in first side-lobe level was  $\pm 0.1$  dB. The XPD of Tandem-L was found to be greater than 30 dB, thereby the cross-polarization is negligible. 2D patterns also showed good correspondence with GRASP simulations which further validated the proposed beam-center approach. The computation time for the Planar Array Patterns was 7 seconds whereas that for the Reflector Patterns was 30 seconds, in comparison to several hours with HFSS and GRASP software.

## **A.5 Future Work**

In the present state, the Pattern Tool does not take into account feed blockage and multipath reflections which are non-negligible for axial feed reflector systems. One proposal for taking into account blockage and multipath is to consider the optical shadow of the blocked elements on the FFT Plane. Additionally, to further improve the accuracy of the beam-center approach at far angles, one idea is to modify the elemental weights as a function of angle in a way similar to motion compensation in SAR to remove any approximations and get exact far-field patterns for all angles.



## LIST OF RELATED PUBLICATIONS AND PATENTS

### ▪ JOURNALS

- [1] B. Pyne, P.R. Akbar, V. Ravindra, H. Saito, J. Hirokawa, T. Fukami, “Slot-array Antenna Feeder Network for Space-borne X-band Synthetic Aperture Radar”, IEEE Transactions on Antennas and Propagation, July 2018, Vol.66 No.7 pp. 3463-6474.
- [2] B. Pyne, R. Naruse, H. Saito, J. Hirokawa, V. Ravindra, P.R. Akbar, “Robust Contactless Egg-Choke Flange for Wideband Applications”, IEEE Transactions on Microwaves, Theory and Techniques, under review as of July 2018.
- [3] B. Pyne, J. Matar, M. Rodriguez-Cassola, G. Krieger, H. Saito, A. Moreira, “Efficient Fourier-domain Far-field Antenna Pattern Computation for Non-ideal Reflectors and Planar Arrays”, scheduled to be submitted in IEEE Geoscience and Remote Sensing Letters in August 2018.
- [4] H. Saito, P.R. Akbar, H. Watanabe, V. Ravindra, J. Hirokawa, K. Ura, B. Pyne, “Compact X-band Synthetic Aperture Radar for 100kg Class Satellite”, Proceedings of the IEICE Transactions on Communications, Volume E.100-B, No. 9, September 2017, pp. 1653-1660.

### ▪ INTERNATIONAL CONFERENCES

- [1] B. Pyne, P.R. Akbar, H. Saito, M. Zhang, J. Hirokawa, M. Ando, “Design of a Center-feed Waveguide Feeder for Wideband Rectangular Parallel-plate Slot-array Antenna On-board Space-borne X-band SAR System”, Proceedings of the 46<sup>th</sup> European Microwave Conference (EUMC), London, October 2016, pp. 1533-1536.
- [2] B. Pyne, V. Ravindra, P.R. Akbar, H. Saito, J. Hirokawa, “Performance Analysis of Edge-feed Rectangular Parallel Plate Slot-array Antenna Panel for Compact Space-borne X-band SAR System”, Proceedings of the 19<sup>th</sup> International Conference on Electromagnetics in Advanced Applications (ICEAA), Verona, September 2017, pp. 407-410.
- [3] P.R. Akbar, B. Pyne, H. Saito, J. Hirokawa, D. Kim, “Present State of Antenna Design for X-band SAR Sensor on-board 100 kg class satellite”, Proceedings of the 11<sup>th</sup> European Conference on Antennas and Propagation (EUCAP), Paris, March 2017, pp. 2640-2641.

- [4] J. Hirokawa, P.R. Akbar, B. Pyne, H. Saito, “Fabrication of four panels of parallel plate slot arrays for a 100kg-class X-band SAR satellite”, Proceedings of the 12<sup>th</sup> European Conference on Antennas and Propagation (EUCAP), London, April 2018.
- [5] H. Saito, P.R. Akbar, B. Pyne, J. Hirokawa, K. Tanaka, K. Ijichi, H. Watanabe, M. Mita, T. Kaneko, “Engineering Model Results of Compact X-band Synthetic Aperture Radar”, Proceedings of the 4S Symposium, Sorrento, Italy, May 2018.
- [6] H. Saito, P.R. Akbar, K. Tanaka, M. Mita, B. Pyne, T. Kaneko, T. Obata, S. Nakasuka, J. Hirokawa, S. Shirasaka, H. Watanabe, K. Hirako, K. Ijichi, “Engineering-Model Results of X-band Synthetic Aperture Radar for Small Satellite and Its Application to Constellation Mission”, accepted for publication in Proceedings of the 32nd Annual AIAA/USU Conference on Small Satellites, to be held in Utah, USA, August 2018.

#### ▪ PATENTS

- [1] J. Hirokawa, H. Saito, B. Pyne, “Wideband Corporate Feeding System for High Frequency Waves to Deployment Structure”, scheduled to be filed for U.S. and Japanese Patent.
- [2] H. Saito, J. Hirokawa, B. Pyne, R. Naruse, “Robust Contactless Egg-Choke Flange for Wideband Applications in X-band”, scheduled to be filed for U.S. and Japanese Patent.
- [3] M. Rodriguez-Cassola, J. Matar, B. Pyne, G. Krieger, A. Moreira, H. Saito, “Python-based Efficient Antenna Pattern Computation Tool”, scheduled to be filed for European Patent.

## REFERENCES

- [1] B. Pyne, P.R. Akbar, V. Ravindra, H. Saito, J. Hirokawa, T. Fukami, "Slot-array Antenna Feeder Network for Space-borne X-band Synthetic Aperture Radar", IEEE Transactions on Antennas and Propagation, Vol. 66 No. 07, April 24, 2018.
- [2] B. Pyne, R. Naruse, H. Saito, J. Hirokawa, V. Ravindra, P.R. Akbar, "Robust Contactless Egg-Choke Flange for Wideband Applications in X-band", scheduled to be submitted in IEEE Transactions on Microwaves, Theory and Techniques in June 2018.
- [3] B. Pyne, J. Matar, M. Rodriguez-Cassola, G. Krieger, H. Saito, A. Moreira, "Efficient Fourier-domain Far-field Antenna Pattern Computation for Non-ideal Reflectors and Planar Arrays", scheduled to be submitted in IEEE Geoscience and Remote Sensing Letters in August 2018.
- [4] H. Saito, P.R. Akbar, H. Watanabe, V. Ravindra, J. Hirokawa, K. Ura, B. Pyne, "Compact X-band Synthetic Aperture Radar for 100kg Class Satellite", Proceedings of the IEICE Transactions on Communications, Volume E.100-B, No. 9, September 2017, pp. 1653-1660.
- [5] H. Saito, P.R. Akbar, K. Tanaka, M. Mita, V. Ravindra, B. Pyne, J. Hirokawa, S. Shirasaka, H. Watanabe, K. Ura, K. Ijichi, "Development Status of Compact X-band Synthetic Aperture Radar Compatible with a 100kg-class SAR Satellite and its Future Plan", Proceedings of the 31<sup>st</sup> Annual AIAA/USU Conference on Small Satellites", Utah, August 2017, pp. 1-7.
- [6] P.R. Akbar, H. Saito, M. Zhang, J. Hirokawa, M. Ando, "Parallel-Plate Slot Array Antenna for Deployable SAR Antenna Onboard Small Satellite", IEEE Transactions on Antennas and Propagation, May 2016, Vol. 64, no. 5, pp 1661-1671.
- [7] V. Ravindra, P.R. Akbar, M. Zhang, J. Hirokawa, H. Saito, A. Oyama, "A Dual-Polarization X-Band Traveling-Wave Antenna Panel for Small-Satellite Synthetic Aperture Radar", IEEE Transactions on Antennas and Propagation, May 2017, Vol. 65, no. 5, pp 2144-2156.
- [8] B. Pyne, P.R. Akbar, H. Saito, M. Zhang, J. Hirokawa, M. Ando, "Design of a Center-feed Waveguide Feeder for Wideband Rectangular Parallel-plate Slot-array Antenna



On-board Space-borne X-band SAR System”, Proceedings of the 46<sup>th</sup> European Microwave Conference (EUMC), London, October 2016, pp. 1533-1536.

- [9] B. Pyne, V. Ravindra, P.R. Akbar, H. Saito, J. Hirokawa, “Performance Analysis of Edge-feed Rectangular Parallel Plate Slot-array Antenna Panel for Compact Space-borne X-band SAR System”, Proceedings of the 19<sup>th</sup> International Conference on Electromagnetics in Advanced Applications (ICEAA), Verona, September 2017, pp. 407-410.
- [10] P.R. Akbar, B. Pyne, H. Saito, J. Hirokawa, D. Kim, “Present State of Antenna Design for X-band SAR Sensor on-board 100 kg class satellite”, Proceedings of the 11<sup>th</sup> European Conference on Antennas and Propagation (EUCAP), March 2017, pp. 2640-2641.
- [11] H. Saito, P.R. Akbar, B. Pyne, J. Hirokawa, K. Tanaka, K. Ijichi, H. Watanabe, M. Mita, T. Kaneko, “Engineering Model Results of Compact X-band Synthetic Aperture Radar”, accepted for publication in Proceedings of the 4S Symposium to be held in Sorrento, Italy, May 2018.
- [12] K. Fukazawa, J. Hirokawa, M. Ando, N. Goto, “Two-way Power Divider for Partially Parallel Feed in Single Layer Slotted Waveguide Arrays”, Proceedings of the IEICE Transactions on Communications, Vol. E-81 B No 6, June 1998, pp. 1248-1254.
- [13] Y. Miura, J. Hirokawa, M. Ando, Y. Shibuya, G. Yoshida "Double-layer Full-Corporate Feed Hollow Waveguide Slot Array Antenna in the 60-GHz Band", Proceedings of the IEEE Transactions on Antennas and Propagation, Vol. 59 No. 8, August 2011, pp. 2844-2851.
- [14] Jiro Hirokawa, “A Study of Slotted Waveguide Array Antennas”, Doctoral Dissertation, Tokyo Institute of Technology, November 1993.
- [15] R. Naruse, H. Saito, J. Hirokawa, M. Zhang, “Non-contact Wave-feed with Choke-flange Waveguide at the Development Section of the Expansion Antenna for Small Satellite”, Proceedings of the IEICE Technical Report, vol. 114, no. 194, SANE 2014-61, pp. 77-82, Tokyo, August 2014.
- [16] R. Naruse, H. Saito, M. Zhang, J. Hirokawa, “Non-contact Choke-flange Waveguide Power Supply for Antenna Development”, Proceedings of the IEICE General Conference, ISSN 1349-1377, Kusatsu, March 2015.

- [17] B. Pyne, V. Ravindra, H. Saito, "An Improved Pulse Repetition Frequency Selection Scheme for Synthetic Aperture Radar", Proceedings of the 12th European Radar Conference (EURAD), Paris, September 2015, pp. 257-260.
- [18] S.S. Sekretarov, D.M. Vavriv, "A Wideband Slotted Waveguide Antenna Array for SAR Systems", Progress in Electromagnetics Research M, Vol. 11, 2010, pp. 165-176.
- [19] B. Grafmuller, A. Herschlein, and C. Fischer, "The TerraSAR-X antenna system," Proceedings of IEEE International Radar Conference (IRC), May 2005, pp. 222–225.
- [20] G. L. Huang, S. G. Zhou and T. Yuan, "Design of a Compact Wideband Feed Cluster with Dual-polarized Sum- and Difference- Patterns Implemented via 3-D Metal Printing," Proceedings of the IEEE Transactions on Industrial Electronics, vol. 65, no. 9, pp. 7353-7362, Sept. 2018.
- [21] G. L. Huang, S. G. Zhou, C. Y. D. Sim, T. H. Chio and T. Yuan, "Lightweight Perforated Waveguide Structure Realized by 3-D Printing for RF Applications," in IEEE Transactions on Antennas and Propagation, vol. 65, no. 8, Aug. 2017, pp. 3897-3904.
- [22] C. T. Iatrou and M. Cavenago, "Field analysis of rectangular waveguide open junction", IEEE Transactions on Microwave Theory and Techniques, vol. 45, no. 2, pp. 165-172, February 1997.
- [23] G. Addamo, R. Orta, G. Virone, O. A. Peverini and R. Tascone, "Radial Transmission-Line Approach for the Analysis of Ring Loaded Slots in Circular Waveguide", in IEEE Transactions on Microwave Theory and Techniques, vol. 63, no. 5, pp. 1468-1474, May 2015.
- [24] J. J. Bolus and K. Tomiyasu, "Characteristics of a New Serrated Choke", in IRE Transactions on Microwave Theory and Techniques, vol. 4, no. 1, pp. 33-36, January 1956.
- [25] J. Matar, P. Lopez-Dekker and G. Krieger, "Potentials and Limitations of MEO SAR," Proceedings of EUSAR 2016: 11th European Conference on Synthetic Aperture Radar, Hamburg, Germany, 2016, pp. 1-5.
- [26] C. A. Balanis, Antenna Theory Analysis and Design, 3<sup>rd</sup> ed. Hoboken, NJ, USA: Wiley, Sec.2.2.4 and Sec.17.2.4, 2005.

- [27] Merrill Skolnik, "Synthetic Aperture Radar," in RADAR Handbook, 3<sup>rd</sup> ed. McGraw-Hill, 2008.
- [28] K. Tomiyasu, "Tutorial review of synthetic-aperture radar (SAR) with applications to imaging of the ocean surface," in Proceedings of the IEEE, vol. 66, no. 5, pp. 563-583, May 1978.
- [29] D. Bickel, B. Brock, and C. Allen, Spaceborne SAR Study: LDRD 92 Final Report. Sandia National Laboratories, 1993.
- [30] R. L. Jordan, "The Seasat-A synthetic aperture radar system," in IEEE Journal of Oceanic Engineering, vol. 5, no. 2, pp. 154-164, April 1980.
- [31] W. T. K. Johnson, "Magellan imaging radar mission to Venus," in Proceedings of the IEEE, vol. 79, no. 6, pp. 777-790, Jun 1991.
- [32] E. P. W. Attema, "The Active Microwave Instrument on-board the ERS-1 satellite," in Proceedings of the IEEE, vol. 79, no. 6, pp. 791-799, Jun 1991.
- [33] R. K. Raney, A. P. Luscombe, E. J. Langham and S. Ahmed, "RADARSAT [SAR imaging]," in Proceedings of the IEEE, vol. 79, no. 6, pp. 839-849, Jun 1991.
- [34] M. Takeda et al., "Design and implementation of PALSAR Ground Data System at ERSDAC," 2006 IEEE International Symposium on Geoscience and Remote Sensing, Denver, CO, 2006, pp. 1647-1650.
- [35] <https://earth.esa.int/web/eoportal/satellite-missions/s/sar-lupe>.
- [36] K. Ouchi, "Recent Trend and Advance of Synthetic Aperture Radar with Selected Topics", Proc. of the Remote Sensing Journal, Issue 5, Vo. 2, pp. 716-807, 2013.
- [37] S. Riendeau and C. Grenier, "RADARSAT-2 Antenna," 2007 IEEE Aerospace Conference, Big Sky, MT, 2007, pp. 1-9.
- [38] M. Stangl, R. Werninghaus and R. Zahn, "The TERRASAR-X active phased array antenna," IEEE International Symposium on Phased Array Systems and Technology, 2003., 2003, pp. 70-75.

- [39] U. Naftaly and R. Levy-Nathansohn, "Overview of the TECSAR Satellite Hardware and Mosaic Mode," in *IEEE Geoscience and Remote Sensing Letters*, vol. 5, no. 3, pp. 423-426, July 2008.
- [40] A. Moreira, "The TanDEM-X mission: A new measurement of the earth's topography and much more," 2017 18th International Radar Symposium (IRS), Prague, 2017, pp. 1-5.
- [41] P. Capece, L. Borgarelli, M. Di Lazzaro, U. Di Marcantonio and A. Torre, "COSMO SkyMed active phased array SAR instrument," 2008 IEEE Radar Conference, Rome, 2008, pp. 1-4.
- [42] R. Arora, C. Rao, B. Bakori, R. Neelakantan, and J.Vachchani, "Synthetic aperture radar payload on-board RISAT-1: configuration, technology and performance," *Current Science*, vol.104, no.4, p.446, 2013.
- [43] Y. Kankaku, S. Suzuki and Y. Osawa, "ALOS-2 mission and development status," 2013 IEEE International Geoscience and Remote Sensing Symposium - IGARSS, Melbourne, VIC, 2013, pp. 2396-2399.
- [44] M. Cohen, A. Larkins, P. L. Semedo and G. Burbidge, "NovaSAR-S low cost spaceborne SAR payload design, development and deployment of a new benchmark in spaceborne radar," 2017 IEEE Radar Conference (Radar Conf.), Seattle, WA, 2017, pp. 0903-0907.
- [45] S. Huber et al., "Tandem-L: Design Concepts for a Next-Generation Spaceborne SAR System," *Proceedings of EUSAR 2016: 11th European Conference on Synthetic Aperture Radar*, Hamburg, Germany, 2016, pp. 1-5.
- [46] P. Rosen et al., "The NASA-ISRO SAR (NISAR) mission dual-band radar instrument preliminary design," 2017 IEEE International Geoscience and Remote Sensing Symposium (IGARSS), Fort Worth, TX, 2017, pp. 3832-3835.
- [47] [http://space.skyrocket.de/doc\\_sdat/capella-1.html](http://space.skyrocket.de/doc_sdat/capella-1.html).
- [48] A. Moreira, P. Prats-Iraola, M. Younis, G. Krieger, I. Hajnsek and K. P. Papathanassiou, "A tutorial on synthetic aperture radar," in *IEEE Geoscience and Remote Sensing Magazine*, vol. 1, no. 1, pp. 6-43, March 2013.

- [49] M. Rodriguez-Cassola et al., "End-to-end performance analysis of companion SAR missions," 2017 IEEE International Geoscience and Remote Sensing Symposium (IGARSS), Fort Worth, TX, 2017, pp. 153-156.
- [50] D. M. Pozar, *Microwave Engineering*, 4<sup>th</sup> ed. Wiley, 2011.
- [51] R. Sandau, "Status and trends of small satellite missions for Earth observation," *Acta Astronautica*, vol.66, no.1, pp.1–12, 2010.
- [52] O. A. Iupikov, R. Maaskant, M. V. Ivashina, A. Young and P. S. Kildal, "Fast and Accurate Analysis of Reflector Antennas with Phased Array Feeds Including Multiple Reflections Between Feed and Reflector," in *IEEE Transactions on Antennas and Propagation*, vol. 62, no. 7, pp. 3450-3462, July 2014.
- [53] P. Lam, Shung-Wu Lee, C. Hung and R. Acosta, "Strategy for reflector pattern calculation: Let the computer do the work," in *IEEE Transactions on Antennas and Propagation*, vol. 34, no. 4, pp. 592-595, April 1986.
- [54] Y. Liu, X. Huang, K. D. Xu, Z. Song, S. Yang and Q. H. Liu, "Pattern Synthesis of Unequally Spaced Linear Arrays Including Mutual Coupling Using Iterative FFT via Virtual Active Element Pattern Expansion," in *IEEE Transactions on Antennas and Propagation*, vol. 65, no. 8, pp. 3950-3958, Aug. 2017.
- [55] J. L. Gomez-Tornero, A. J. Martinez-Ros and R. Verdu-Monedero, "FFT Synthesis of Radiation Patterns with Wide Nulls Using Tapered Leaky-Wave Antennas," in *IEEE Antennas and Wireless Propagation Letters*, vol. 9, pp. 518-521, 2010.
- [56] Y. Rahmat-Samii and J. M. Kovitz, "Antenna measurements through planar near field apparatus: An educational paradigm linking electromagnetic theory, sampling techniques, and FFT," 2017 XXXII<sup>nd</sup> General Assembly and Scientific Symposium of the International Union of Radio Science (URSI GASS), Montreal, QC, 2017, pp. 1-4.
- [57] P. You, Y. Liu, K. Xu, C. Zhu and Q. H. Liu, "Generalisation of genetic algorithm and fast Fourier transform for synthesising unequally spaced linear array shaped pattern including coupling effects," in *IET Microwaves, Antennas & Propagation*, vol. 11, no. 6, pp. 827-832, 5 12 2017.

- [58] H. V. Bui, S. N. Jha and C. Craeye, "Fast Full-Wave Synthesis of Printed Antenna Arrays Including Mutual Coupling," in *IEEE Transactions on Antennas and Propagation*, vol. 64, no. 12, pp. 5163-5171, Dec. 2016.
- [59] S. N. Jha, S. Hubert and C. Craeye, "Analysis of mutual coupling in large arrays of printed antennas using Contour-FFT," 2015 9th European Conference on Antennas and Propagation (EuCAP), Lisbon, 2015, pp. 1-5.
- [60] D. H. Colvin, "Array factor approximation using physical optics and simple line integration," 2010 IEEE International Symposium on Phased Array Systems and Technology, Waltham, MA, 2010, pp. 833-840.
- [61] R. A. R. de Azevedo and J. Mazzucco, "Fast Calculation of Far-Field Patterns of Reflector Antennas with Fast Fourier Transform," 1980 10th European Microwave Conference, Warszawa, Poland, 1980, pp. 61-66.
- [62] Tao Yuan, Le-Wei Li, Jian-Ying Li, Ning Yuan and Mook-Seng Leong, "A high performance phased antenna array design and analysis using fast algorithm," 2006 IEEE Antennas and Propagation Society International Symposium, Albuquerque, NM, 2006, pp. 533-536.
- [63] Y. Rahmat-Samii, "Microwave holography of large reflector antennas--Simulation algorithms," in *IEEE Transactions on Antennas and Propagation*, vol. 33, no. 11, pp. 1194-1203, November 1985.
- [64] R. Mittra, Wai Ko and M. Sheshadri, "A transform technique for computing the radiation pattern of prime-focal and Cassegrainian reflector antennas," in *IEEE Transactions on Antennas and Propagation*, vol. 30, no. 3, pp. 520-524, May 1982.
- [65] X. Huang, Y. Liu, P. You, M. Zhang and Q. H. Liu, "Fast Linear Array Synthesis Including Coupling Effects Utilizing Iterative FFT via Least-Squares Active Element Pattern Expansion," in *IEEE Antennas and Wireless Propagation Letters*, vol. 16, pp. 804-807, 2017.
- [66] D. R. Prado, M. Arrebola, M. R. Pino and F. Las-Heras, "An Efficient Calculation of the Far Field Radiated by Non-Uniformly Sampled Planar Fields Complying Nyquist Theorem," in *IEEE Transactions on Antennas and Propagation*, vol. 63, no. 2, pp. 862-865, Feb. 2015.

- [67] Z. H. Firouzeh, A. Zeidaabadi-Nezhad and H. Mirmohammad-Sadeghi, "An Optimum Meshing to Compute the Radiation Integrals of Reflector Antennas by FFT Method," 2007 Asia-Pacific Microwave Conference, Bangkok, 2007, pp. 1-4.
- [68] X. F. Ren, A. J. R. Azevedo and A. M. E. S. Casimiro, "Pencil beam pattern synthesis using perturbation technique and fast Fourier transforms," 2007 International Symposium on Microwave, Antenna, Propagation and EMC Technologies for Wireless Communications, Hangzhou, 2007, pp. 680-683.
- [69] A. D. Craig and P. D. Simms, "Fast integration techniques for reflector antenna pattern analysis," in Electronics Letters, vol. 18, no. 2, pp. 60-62, January 1982.
- [70] S. J. Stirland, "Fast Antenna Synthesis by an Iterative FFT Procedure," 1991 21st European Microwave Conference, Stuttgart, Germany, 1991, pp. 745-750.
- [71] O. Bucci, G. D'Elia, G. Franceschetti and R. Pierri, "Efficient computation of the far field of parabolic reflectors by pseudo-sampling algorithm," in IEEE Transactions on Antennas and Propagation, vol. 31, no. 6, pp. 931-937, Nov 1983.
- [72] A. Enneking and F. Aradt, "Fast spectral domain analysis of large finite microstrip patch arrays," IEEE Antennas and Propagation Society International Symposium. 1999 Digest. Held in conjunction with: USNC/URSI National Radio Science Meeting (Cat. No.99CH37010), Orlando, FL, USA, 1999, pp. 2092-2095 vol.3.
- [73] Stephanie Alphonse, "Fast Analysis of a Compound Large Reflector Antenna", Masters' Thesis, Department of Electrical and Electronic Engineering, University of Stellenbosch, March 2012.
- [74] A. Nehzad, Z. Firouzeh, and H. Sadeghi, "A Fast Method to Compute Radiation Fields of Shaped Reflector Antennas by FFT" in book: Advanced Microwave and Millimeter Wave Technologies Semiconductor Devices Circuits and Systems, March 2010.
- [75] T.A. O'Malley, "Computation of Scalar Far-field Patterns of Large Aperture Antennas", NASA Report TMX-3408, June 1976.
- [76] H. Steyskal, R. A. Shore, "Efficient Computation of Reflector Antenna Aperture Distributions and Far Field Patterns", Rome Air Development Center TR-84-45 In-House Report, March 1984.

- [77] W. Zhao, "Retrieval of Free Space Radiation Patterns through Measured Data in a Non-Anechoic Environment", Doctorate Dissertation, Syracuse University, December 2013.
- [78] V. Ravindra, "Dual Polarization Travelling-Wave Antenna with Centralized Radio-Frequency Transmitting/Receiving System for Synthetic Aperture Radar in Small Satellites", Doctorate Dissertation, Department of Electrical Engineering and Information Systems, The University of Tokyo, March 2016.
- [79] V. Ravindra, P. Akbar, H. Saito, M. Zhang and J. Hirokawa, "A parallel plate slot-pair array dual polarization antenna for small satellite SAR," 2015 International Symposium on Antennas and Propagation (ISAP), Hobart, TAS, 2015, pp. 1-4.
- [80] V. Ravindra, H. Saito, P. Akbar, M. Zhang and J. Hirokawa, "Optimal cross-range pattern synthesis using multi-objective genetic algorithm for a passive antenna in small satellite SAR," 2015 International Symposium on Antennas and Propagation (ISAP), Hobart, TAS, 2015, pp. 1-3.
- [81] P. R. Akbar, H. Saito, M. Zang, J. Hirokawa and M. Ando, "X-band parallel-plate slot array antenna for SAR sensor onboard 100 kg small satellite," 2015 IEEE International Symposium on Antennas and Propagation & USNC/URSI National Radio Science Meeting, Vancouver, BC, 2015, pp. 208-209.
- [82] H. Saito et al., "Synthetic aperture radar compatible with 100kg class piggy-back satellite," Conference Proceedings of 2013 Asia-Pacific Conference on Synthetic Aperture Radar (APSAR), Tsukuba, 2013, pp. 88-91.
- [83] P. R. Akbar, J. T. S. Sumantyo, and H. Saito, "Study of synthetic aperture radar sensor on board small satellite," Technical report of IEICE. SANE, vol.112, no.330, pp.31–36, Nov 2012.
- [84] H. Saito, "Compact X-band synthetic aperture radar on 100 kg small satellite," in IAA Symposium on Small Satellites for Earth Observation, April 2015.
- [85] H. Ueda, J. Hirokawa, M. Ando, O. Amano, and Y. Kamata, "Space-use radial line slot antenna in 8 GHz bandwidth honeycomb structure", in 2008 IEEE Antennas and Propagation Society International Symposium, July 2008.
- [86] J. Hirokawa, M. Ando, and N. Goto, "Waveguide-fed parallel plate slot array antenna," IEEE Transactions on Antennas and Propagation, no.2, pp. 218–223, 1992.



- [87] M. Samardzija, T. Kai, J. Hirokawa, and M. Ando, "Single-layer waveguide feed for uniform plane TEM-wave in oversized-rectangular waveguide with hard-surface sidewalls," *IEEE Transactions on Antennas and Propagation*, vol.54, no.10, pp.2813–2819, Oct. 2006.
- [88] K. Sakakibara, Y. Kimura, J. Hirokawa, M. Ando, and N. Goto, "A two-beam slotted leaky waveguide array for mobile reception of dual-polarization DBS," *IEEE Transactions on Vehicular Technology*, vol.48, no.1, pp.1–7, 1999.
- [89] B. Pyne, V. Ravindra, H. Saito "An Improved Nadir Echo Allocation Scheme for Synthetic Aperture Radar", *Proc. of IEICE SANE Technical Report 15*, pp. 21-25, Tokyo 2015.
- [90] P. R. Akbar, B. Pyne, H. Saito, J. Hirokawa, "X-band SAR Antenna On-board Small Satellite", *Proceedings of the 17th Space Science Symposium*, ISAS, JAXA, Sagamihara, January 2017.
- [91] P. R. Akbar, B. Pyne, V. Ravindra, M. Zhang, H. Saito, J. Hirokawa, M. Ando, "X-band SAR Antenna On-board Small Satellite", *Proceedings of the 16th Space Science Symposium*, ISAS, JAXA, Sagamihara, January 2016.
- [92] B. Pyne, V. Ravindra, H. Saito, "Extended Chirp Pulsed Radar (ECMPR) Scheme for MicroX-SAR onboard 100 kg Micro-satellite", *Proceedings of the 16th Space Science Symposium*, ISAS, JAXA, Sagamihara, January 2016.
- [93] H. Saito, P. R. Akbar, M. Zhang, V. Ravindra, R. Naruse, A. Tomiki, J. Hirokawa, M. Ando, "Compact X-band SAR for 100 kg Class Satellite", *Proc. of IEICE SANE Technical Report 14*, pp. 19-24, Tokyo 2014.
- [94] J. Hirokawa, P.R. Akbar, B. Pyne, H. Saito, "Fabrication of four panels of parallel plate slot arrays for a 100kg-class X-band SAR satellite", *Proceedings of the 12<sup>th</sup> European Conference on Antennas and Propagation (EUCAP)*, London, April 2018.
- [95] W. T. Smith and W. L. Stutzman, "A comparison of physical optics and geometrical optics methods for computation of reflector surface error effects," *Southeastcon '89. Proceedings. Energy and Information Technologies in the Southeast.*, IEEE, Columbia, SC, 1989, pp. 214-219 vol.1.

- [96] Y. Rahmat-Samii, "A comparison between GO/aperture-field and physical-optics methods of offset reflectors," in *IEEE Transactions on Antennas and Propagation*, vol. 32, no. 3, pp. 301-306, Mar 1984.
- [97] [www.ece.mcmaster.ca/faculty/nikolova/antenna\\_dload/current\\_lectures/L19\\_Reflector.pdf](http://www.ece.mcmaster.ca/faculty/nikolova/antenna_dload/current_lectures/L19_Reflector.pdf).
- [98] Nurdin A. Adata, "Cross-polarization of Microwave Reflector Antennas", Doctorate Thesis, University of Surrey, 1974.
- [99] T. Ng et al., "Polarization properties of reflector antennas used as radio telescopes," in *Radio Science*, vol. 40, no. 05, pp. 1-12, Oct. 2005.
- [100] D. Ehyaie, "Novel approaches to the design of phased array antennas", Ph.D. dissertation, The University of Michigan, 2011.
- [101] <http://www.jst.go.jp/impact/en/program/13.html>.
- [102] D. Parker and D. Zimmermann, "Phased arrays-part 1: theory and architectures", *IEEE Transactions on Microwave Theory and Techniques*, vol. 50, no. 3, pp. 678-687, mar 2002.
- [103] T. Wanwiwake and C. Underwood, "A Bi/Multi-Static microsatellite SAR constellation", in *Small Satellites for Earth Observation*, H. P. Röser, R. Sandau, and A. Valenzuela, Eds. Wiss.-und-Technik-Verlag, 1996.
- [104] D. Butler, "Many eyes on Earth", *Nature*, vol. 505, no. 7482, pp. 143-144, Jan 2014.
- [105] "Skybox Imaging", [www.skyboximaging.com](http://www.skyboximaging.com).
- [106] S. Gao, Y. Rahmat-Samii, R. E. Hodges and X. X. Yang, "Advanced Antennas for Small Satellites," in *Proceedings of the IEEE*, vol. 106, no. 3, pp. 391-403, March 2018.
- [107] T. Nguyen et al., "An equivalent double layer model for a fast design and analysis of high gain-multilayer radial line slot antennas," *IEICE Trans. Comm.*, vol. E96-B, no. 11, pp. 2891-2900, Nov. 2013.

- [108] R. S. Elliott, *An Introduction to Guided Waves and Microwave Circuits*, Englewood Cliffs, NJ, USA: Prentice-Hall, sec. 2.4, 1993.
- [109] R. S. Jayawardene et al., “Estimation and measurement of cylindrical wave propagation in parallel plate with honeycomb spacer for the use in mm-Wave RLSA,” in *Proc. Asia-Pac. Microwave Conf. Proc. (APMC)*, 2012, pp. 415–417.
- [110] T. Nguyen et al., “Propagation characteristics of honeycomb structures used in mm-wave radial line slot antennas,” *IEICE Trans. Comm.*, vol. E97-B, no. 6, pp. 1139–1147, Jun. 2014.
- [110] T. Nguyen et al., “Propagation characteristics of honeycomb structures used in mm-wave radial line slot antennas,” *IEICE Trans. Comm.*, vol. E97-B, no. 6, pp. 1139–1147, Jun. 2014.
- [111] C. A. Balanis, *Modern Antenna Handbook*, 1<sup>st</sup> ed. Hoboken, NJ, USA: Wiley, 2007.
- [112] H. Saito, P.R. Akbar, B. Pyne, J. Hirokawa, K. Tanaka, K. Ijichi, H. Watanabe, M. Mita, T. Kaneko, “Engineering Model Results of Compact X-band Synthetic Aperture Radar”, *Proceedings of the 4S Symposium*, Sorrento, Italy, May 2018.
- [113] H. Saito, P.R. Akbar, H. Watanabe, V. Ravindra, J. Hirokawa, K. Ura, B. Pyne, “Compact X-band Synthetic Aperture Radar for 100kg Class Satellite”, *Proceedings of the IEICE Transactions on Communications*, Volume E.100-B, No. 9, September 2017, pp. 1653-1660.
- [114] H. Saito, P.R. Akbar, K. Tanaka, M. Mita, B. Pyne, T. Kaneko, T. Obata, S. Nakasuka, J. Hirokawa, S. Shirasaka, H. Watanabe, K. Hirako, K. Ijichi, “Engineering-Model Results of X-band Synthetic Aperture Radar for Small Satellite and Its Application to Constellation Mission”, accepted for publication in *Proceedings of the 32nd Annual AIAA/USU Conference on Small Satellites*, to be held in Utah, USA, August 2018.

\*\*\*\*\*